Ricardo Manuel Martins de Azevedo
Engenheiro Mecânico

CHARACTERIZATION OF THE TURBULENT STRUCTURE IN COMPOUND CHANNEL FLOWS

Dissertação para obtenção do Grau de Doutor em
Engenharia Civil

Orientador: João Gouveia Bento Aparicio Leal,
Assistant Professor, FCT/UNL, Portugal
Professor, Universitetet i Adger, Norway

Co-orientador: Luis R. Rojas – Solórzano
Associate Professor
Nazarbayev University, Kazakhstan

Setembro, 2016

FACULDADE DE CIÊNCIAS E TECNOLOGIA
UNIVERSIDADE NOVA DE LISBOA

Nº de

Arquivo _____

*Copyright*_____

[Characterization of the Turbulent Structure in Compound Channel Flows]

To my parents

Acknowledgments

I would like to thank the Faculty of Science and Technology of New University of Lisbon (FCT/UNL), for accepting me as PhD student. I would like also to acknowledge the University of Beira Interior for providing the necessary conditions to carry out this work.

To my supervisors, Prof. João Leal and Prof. Luis Rojas, for accepting me as a PhD student, for all the dedication and guidance fundamental for the development of this thesis, for all the patience, support, encouraging, and especially for all the knowledge provided. It is a pleasure to work with you! Thank you!

A special gratitude to Prof. Rui Ferreira for his assertive and invaluable advices and help about data processing and turbulence process understanding. Prof. Koji Shiono deserve a special mention for advising me in turbulent flows and LDV measurements. To Prof. Cristina Fael for receiving and providing the necessary conditions at University of Beira Interior.

To Jorge Barros for all the help, support, patience and encouragement when LDV was damaged and I began to get in stress. But above all, thank you for your friendship during this process. You are part of my family! I will be always in gratitude with you.

My thanks to Marina Filonovich for your help, support and understanding. João Fernandes for bring me your help in the filtering data process and Moisés Brito for work with me in the analysis of algorithms built to estimate the turbulent scales and dissipation rate.

Special thanks to Jorge "El Melenu'o" de Oliveira, Alita "La Abuelita" Amorim and Sara "La Doctora" Amorim for your support, advices and relaxing time during this process and especially for all the barbecue and parties moments.

I would also like to express my deep gratitude to my fiancée Manuela Amorim for all the support, encouragement, and help, especially in this last months, to finish this work. Probably, without your presence, this thesis never would be written and this chapter of my life never would be enclosed.

To my parents and sister for all the support through my entire carrier as a student and as investigator. All that I have and I am today, I owe to you. Many thanks!

This work was supported by National Funds from the Foundation of Science and Technology (FCT) through the scholarship SFRH/BD/33646/2009 and through the projects PTDC/ECM/70652/2006 and PTDC/ECM/099752/2008.

Abstract

The main goal of this investigation is to characterize the turbulent structures in compound channel flows considering two geometrical conditions, a simple asymmetric compound channel and the same compound channel but with the placement of rods on the upper bank.

For the simple asymmetric compound channel, three different water depths were analyzed, one corresponding to deep flows and two corresponding to shallow flows. For the compound channel with rods, three different spacing between elements were studied, including two different water depths for each spacing condition.

The measurements were taken with a 2D Laser Doppler Velocimiter, at 9.0 m from the inlet for simple compound channel. For the compound channel with rods, three cross-section around 9.0 m from the inlet of the channel were measured, corresponding to locations downstream of the rod, in the middle of two rods and upstream of the rod. The measurements were performed under quasi-uniform flow condition and streamwise and vertical instantaneous velocity components were obtained.

The raw data was filtered and processed in order to estimate the time-averaged velocities U and W, the turbulent intensities U' and W', Reynolds stress $\overline{u'w'}$, streamwise integral length scale L_x, turbulence dissipation rate ε and Taylor's micro scale λ_x. Taylor's frozen field hypothesis was adopted in order to transform the time record into a space record, using a convection velocity U_c. The autocorrelation function was built and the integral length scale estimated using three different stop methods of the integral: the second zero of the autocorrelation function, the first minimum, and assuming the integral length scale as the wavenumber value when the autocorrelation function reaches $1/e$ (this was concluded to be the most consistent method). For estimating the dissipation rate, the following methods were used: from the third order structure function, from the second order structure function and finally, and from the energy spectrum of the velocity (this was concluded to be the most consistent method).

In the case of a simple compound channel, the deep flows are characterized by macro vortices with streamwise axis between the interface and main channel and between interface and floodplain, having a notable separation in the "main channel vortex" and the "floodplain vortex" meeting, due the double shear layer of the streamwise depth-averaged velocity. Shallow flows are characterized by macro vortices with vertical axis confined between the interface and main channel and originated by the depth average velocity gradient between the main channel and floodplain. A clear linear relation exists between the streamwise integral length scale, L_x, the dissipation rate, ε, and the streamwise turbulent intensity U'. Contrary to 2D

fully developed open-channel flow equations that relation appears to be constant for all water depths.

For the compound channel with rods, new turbulent structures are generated due the interaction between rods and flow. Downstream of rods, the horseshoes-vortex system is perfectly observed and a strong descendant flow dominate both sides of rod, turning invalid the universal laws for 2D fully developed open-channel flows. The integral length scale presents almost constant values in the vertical direction, which indicates that the wakes generated by the rods influence the entire water column. The turbulent microscale and dissipation rate acquire a streamwise variation due to the vortex propagation in the downstream direction, both presenting higher values than the ones corresponding to 2D flows.

Resumo

O principal objetivo desta investigação é a caracterização das estruturas turbulentas em escoamentos em canais de secção composta tendo em consideração duas condições geométricas: um simples e outro com elementos cilíndricos na parte superior do talude.

Para tal, três alturas diferentes de água foram analisadas para o caso do canal simples, uma altura correspondente a escomento profundos "*deep flows*" e dois relativos a escoamentos rasos "*shallow flows*". Para o canal composto assimétrico com elementos cilíndricos, foram estudados três espaçamentos entre cilindros e duas alturas de água para cada um dos espaçamentos. Os espaçamentos estudados foram S_1 = 1m; S_2 = 0.2m; e S_3 = 0.04m, e os elementos cilíndricos colocados foram barras de alumínio de 0.01m de diâmetro e 0.1m de comprimento.

Foi utilizado um Laser Doppler Velocimeter 2D para a realização das medições, as quais foram realizadas a 9.0m da entrada do canal composto simples. No caso do canal composto com elementos cilíndricos, foram medidas três secções transversais localizadas nas proximidades de 9.0 m desde a entrada, sendo uma secção medida à jusante do elemento, outra secção no meio de dois elementos e a última a montante do elemento cilíndrico. As medições foram executadas em condições de escoamento quasi-uniforme, obtendo-se as velocidades instantâneas das componentes longitudinal e vertical.

Depois de medir a secção transversal, os dados foram filtrados e processados de forma a obter uma estimativa da velocidade média temporal U e W, das intensidades turbulentas U' e W', tensões de Reynolds $u'w'$, da macro escala longitudinal L_x, da taxa dissipativa longitudinal ε_x e da micro escala de Taylor's longitudinal λ_x. Para isso, adotou-se a hipótese de Taylor de forma a transformar o registo temporal num registo espacial com a implementação de uma velocidade de convecção U_c. Neste sentido, a função de autocorrelação foi construída, podendo-se estimar o comprimento da macro escala "*integral length scale*" utilizando três métodos para definir o limite superior da integral, nomeadamente, encontrando o segundo zero da função de autocorrelação; encontrando o primeiro mínimo da função de autocorrelação; e assumindo o valor da macro escala integral como o valor do número de onda quando a função de autocorrelação atinge 1/*e*. No caso da taxa de dissipação, foram utilizados três métodos. A estimativa da taxa de dissipação através da função de estrutura de terceiro ordem, através da função de estrutura de segundo ordem e, finalmente, a partir do espectro da velocidade. A micro escala longitudinal de Taylor foi estimada como uma função da taxa de dissipação turbulenta, assumindo um escoamento turbulento isotrópica homogénea incompressível.

No caso do canal composto simples, os escoamentos profundos "*deep flows*" são caracterizados pela existência de macro vórtices de eixo longitudinal entre a zona da interface/leito principal e entre a interface/planície de inundação, existindo uma separação

notável na confluência entre o vórtice do leito principal "*main channel vortex*" e o vórtice da planície de inundação "*floodplain vortex*", devido à dupla camada limite da velocidade média em profundidade. Os escoamentos rasos "*shallow flows*" são caracterizados por macro vórtices de eixo vertical confinados entre a interface e o leito principal, os quais são originados pelo gradiente da velocidade média em profundidade entre o leito principal e a planície de inundação.

Para o canal composto com elementos cilíndricos, novas estruturas turbulentas são geradas devido a interação entre estes elementos e o escoamento. A jusante das hastes, o sistema de vórtices em forma de ferradura "*horseshoes-vortex system*" é perfeitamente observada e um forte fluxo descendente domina o escoamento em ambos os lados da haste. No entanto, este processo é dissipado na direção longitudinal, onde o comportamento do escoamento começa a exibir uma maior interação entre a planície de inundação e o leito principal, até chegar ao encontro do seguinte haste.

Table of Contents

List of Figures

List of Tables

List of Abreviations and Symbols

Latin alphabet

Symbol	Description	Units
A	Cross-section of the flow	[m^2]
B	Channel wide	[m]
B_{MC}	Main channel width	[m]
B_{FP}	Floodplain width	[m]
B_I	Interface width	[m]
C_v	Specific heat	[J/Kg^{o}C]
d_m	Measurement control volume diameter	[m]
D	Rod diameter	[m]
D_{ij}	Second-order velocity structure function	[m^2/s^2]
D_{LL}	Longitudinal second-order structure function	[m^2/s^2]
D_{LLL}	Longitudinal third-order structure function	[m^3/s^3]
D_{NN}	Transversal second-order structure function	[m^2/s^2]
e	Internal energy	[m^2/s^2]
E	Energy spectrum	[m^3/s^2]
f_D	Doppler frequency	[Hz]
Fr	Froude number	[-]
g	Gravitational acceleration	[m/s^2]
h	Interface depth	[m]
H	Water depth	[m]
H_{MC}	Main channel water depth	[m]
Hr	Relative water depth	[-]
k	Thermal conductivity; von Kármán constant	[W/mK]; [-]
k_s	Size of the roughness	[m]
k_w	Frequency spectrum or wavenumber	[1/m]
K	Kinematic energy	[m^2/s^2]
K'	Fluctuation of kinematic energy	[m^2/s^2]
l_m	Measurements control volume length	[m]
L	Macro-scale; channel length	[m]; [m]
L_τ	Integral timescale	[s]
Lx	Longitudinal macro-scale	[m]

n	Manning number	[$sm^{-1/3}$]
N	Total number of measured particles	[-]
p	Pressure	[N/m^2]
q	Heat flux	[W/m^2]
Q	Heat contained into control volume; discharge	[W/kg];
r	Period of space	[m]
R	Autocovariance	[m^2/s^2]
R_h	Hydraulic radius	[m]
Re	Reynolds number	[-]
s	Side slope of the bankfull; period of time	[-]; [s]
S	Spacing between rods	[m]
S_{MC}	Main channel slope	[-]
S_{FP}	Floodplain slope	[-]
S_0	Bed slope	[-]
S'	Skewness	[-]
t	Time; period of time	[s]; [s]
t_{max}	Maximum time in the measurement record	[s]
T	Temperature of the flow	[ºC]
T_0	Period of time	[s]
u	Longitudinal instantaneous velocity	[m/s]
u'	Longitudinal velocity fluctuation	[m/s]
U	Longitudinal time-average velocity	[m/s]
U_c	Convection velocity	[m/s]
U_{CS}	Velocity of the cross-section	[m/s]
U_{max}	Maximum velocity	[m/s]
U_{sup}	Free-surface velocity	[m/s]
U_0	Time-average velocity of the flow	[m/s]
U_*	Friction velocity	[m/s]
$U_{*(y)}$	Local friction velocity	[m/s]
U'; U_{rms}	Longitudinal turbulent intensity	[m/s]
$u'w'$	Reynolds stress	[m^2/s^2]
v	Transversal instantaneous velocity	[m/s]
V	Control volume	[m^3]
w	Vertical instantaneous velocity	[m/s]
w'	Vertical velocity fluctuation	[m/s]
W	Vertical time-average velocity	[m/s]

W'; W_{rms}	Vertical turbulent intensity	[m/s]
x	Longitudinal direction	[-]
y	Transversal direction	[-]
z	Vertical direction	[-]

Greek alphabet

Symbol	Description	Units
δ_{ij}	Delta of Kronecker	[-]
δ_f	Spacing between fringes	[m]
λ	Taylor's micro-scale; wavelength of light	[m]; [m]
λ_x	Longitudinal Taylor's micro-scale	[m]
λ_w	Transversal Taylor's micro-scale	[m]
ε	Dissipation rate of TKE	[m^2/s^3]
ϕ	Angle between LDV beams	[º]
ρ	Density of the fluid; autocorrelation function	[kg/m^3]; [-]
η	Kolmogorov's micro scale	[m]
μ	Dynamic viscosity	[kg/ms]
ν	Kinematic viscosity	[m^2/s]
σ_{ij}	Stress tensor	[N/m^2]
τ	Time macro-scale; time step	[s]; [s]
τ_w	Wall shear stress	[N/m^2]
τ_{ij}	Shear stress tensor	[N/m^2]
Π	Coles' wake strength parameter	

Abbreviations and Acronims

Symbol	Description
DCM	Divided channel method
LDA	Laser Doppler anemometry
LDV	Laser Doppler velocimetry
PDM	Photodetector module
PMT	Photomultiplier tube
SCM	Single channel method
SNR	Signal to noise ratio

TKE	Turbulence kinetic energy
1D, 2D, 3D	One-, two- and three-dimensional

1

Chapter 1

Introduction

Background and Motivation

In most cases, rivers present a compound cross-section constituted by a main channel flanked by floodplains. In natural flood conditions, the flow inundates the floodplains climbing the banks of the main channel. On this regards, and taking into account that in recent years there is an increment in magnitude and frequency of floods, as shown fig. 1.1, the study of this kind of flows is critical to obtain more reliable estimates of flood levels, as well as the characterization of the velocity field of the flow, allowing the identification of floodplains, predict floods in real time or estimate the impact of mitigation measures.

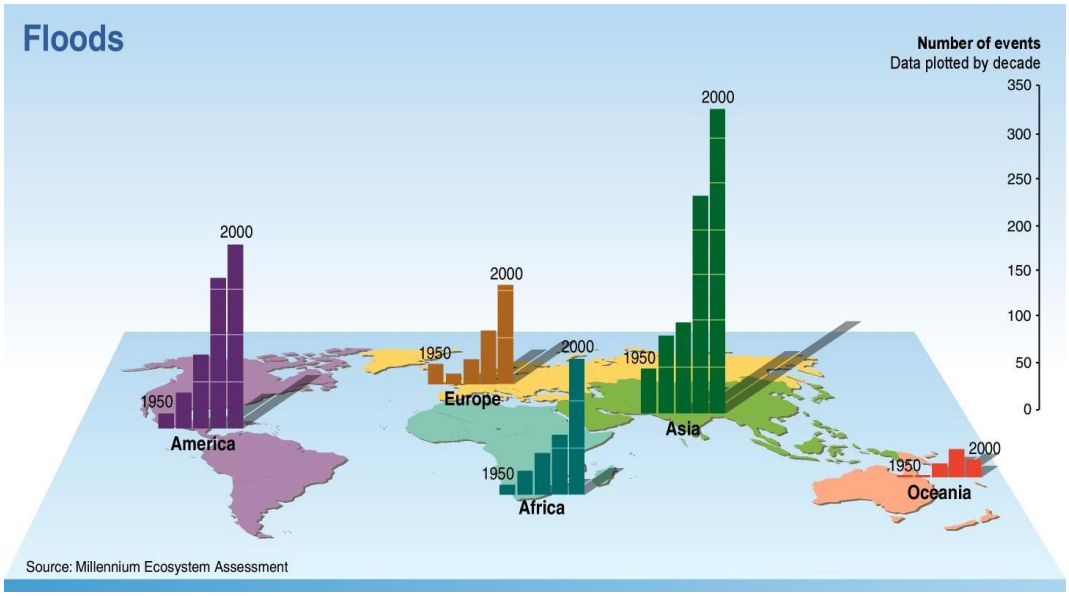

Figure 1.1 Number of floods by decade (Millennium Ecosystem Assesment)

The interaction between the main channel and the floodplains flows originates a complex turbulent flow filed. Due to the flow velocity difference between the main channel and the floodplains, a mixing layer is created which induces horizontal and vertical orientated vortices, as well as mass and momentum transfer, and other kind of phenomena related with the flow acceleration/deacceleration. The phenomenon of momentum transfer was initially observed by Sellin (1964) who identified the presence of vertical orientated vortices in the interface between flows (main channel and floodplains flows). According to Myers (1978), the momentum transfer can be studied as an apparent shear stress caused by the velocity lateral gradient, resulting in turbulent structures that increase the flow resistance.

The complexity of compound channel flow field has attracted the attention of several researchers, and over the last decades there have been an innumerous number of studies regarding this issue. In the 90s, several researchers (Knight and Shiono, 1990; Nezu and Nakayama, 1997) measured the instantaneous velocity using high precision equipments, as

Laser Doppler Velocimeter (LDV). These measurements were one-dimensional (1D) or bi-dimensional (2D) due to equipment limitations. However, they allowed to reveal the presence of complex three-dimensional (3D) turbulent structures of different scales, namely, the presence of helix secondary currents with horizontal axis that overlap the vertical oriented vortices observed by Sellin (1964). The characterization of the turbulent structures is very important since the momentum transfer is not only a function of the lateral Reynolds stresses, but also depends on the secondary currents (Myers, 1978). Although much was achieved in identifying the main turbulent structures within the flow and how they were affected by the water level (Nezu et al., 1997), the detailed characterization of the turbulent field is still missing. The most detailed experimental study is still the one by (Tominaga and Nezu, 1991), where two velocity components were measured using LDV technology. Nevertheless, only turbulent intensities were presented and discussed. As far as the author knowledge, there is not any information available regarding fundamental turbulence quantities such as the integral length scale or the turbulence energy dissipation rate.

Therefore, the renewed interest in studying compound channel flows arises not only from their practical importance, but also from the recent capacity of measuring detail turbulence quantities in the vicinity of the narrow flow regions. These quantities are important to understand the turbulent structures that efficiently transport mass and momentum over larger distances, thus greatly contributing to reducing velocity differences in narrow regions.

Additionally, floodplains are occupied by a plurality of obstacles, namely, natural (*e.g.*, vegetation, topography irregularities) and man-made (*e.g.*, roads, embankments, buildings), that in flood conditions can be partially or totally submerged. On this regards, the roughness of floodplains is usually much higher and more variable than the main channel one, having a fundamental role in the momentum transfer at the interface, since it depends on the velocity difference between the main channel and floodplain flows (Sellin et al., 2003; Shiono, Chan, et al., 2009a, 2009b; Yen, 2002). Therefore, the evaluation of the effect of these obstacles in the turbulence field is important to understand real flow configurations.

Objectives and Methodology

Considering the mentioned before, the main goal of this study is to charaterize in detail the turbulence in compound channel uniform flow and how it is affected by the presence of rigid elements at the interface between main channel and floodplain. To reach this objective, this investigation was focus in the following specific objectives:

1. Characterize the turbulent field and its influence on the momentum transfer between the main channel and floodplain flow for different water depths.
2. Study the influence of different roughness elements density, placed in the upper bank, on the turbulent field.
3. Evaluate different data processing and analisys methodologies to characterize the turbulent field.

To achieve these objectives, instantaneous velocity measurements where carried out in an asymmetric compound channel flow at the hydraulic laboratory of the University of Beira Interior. The measurements were taken using a 2D Laser Doppler Velocimeter System (LDV), which allow to obtain the instantaneous longitudinal u and vertical w velocity components. The LDV has a positioning system which allows the automatic displacement between the measurement points with 0.1 mm accuracy.

To evaluate the mass and momentum transfer, three different relative water depths were tested, corresponding to "deep flows" and "shallow flows" (Nezu and Nakayama, 1997) . These different water depth conditions are expected to originate different turbulent fields, where a stronger mixing layer with vertical oriented vortices will be present for the “shallow flow” and strong secondary currents with streamwise oriented vortices will dominate the “deep flow”.

On the other hand, three different roughness elements density were analyzed in order to study its influence on the turbulent field. The roughness elements selected were aluminum rods with 10 mm of diameter and 100 mm length which simulate trees in flood condition. The spacing between rods were selected according to environment observations, where most spacings founded are around $4 < S/D < 20$, being S the spacing between rods and D the diameter of rods (Esfahani and Keshavarzi, 2010; Notes, 1998; Shiono, Ishigaki, et al., 2009; Terrier, 2010)

To estimate the main turbulent quantities as the integral length scale, the dissipation rate and the micro scale, different methods were used, assuming incompressible homogeneous isotropic turbulent flow. In the integral length scale case, the integral of the autocorrelation function must be defined until a finite value. Thus, three different integral-stop-values were defined, namely, the second zero found on the autocorrelation function, the first minimum found on the autocorrelation function and finally, the wavenumber value when the autocorrelation function

reach 1/*e* (Tropea et al., 2007). In the case of the dissipation rate, three methods were tested. The first method was using the third order structure function, the second method was using the second order structure function and finally, the dissipation rate is also estimate from the spectrum of the velocity. To estimate the longitudinal and vertical micro scale, an equation presented in chapter 2 is used.

Thesis Outline

The present work is divided into five chapters and one appendix, as following:

Chapter 1 introduces the reader to the studied topic, where it is given to know the motivation that carried out the execution of this study. The main goal is presented following, as well the specific objectives. This chapter is finalized with a description of the methodology used and presenting the outline of the thesis.

Chapter 2 aims to inform the reader about the main equations that govern the behavior of the flow in compound channels. Moreover, some partical approaches for modeling of turbulence are also presented. On this regards, this chapter gives to the reader some glimpses on the experimental data processing.

In **chapter 3** an overall description of the laboratory conditions is presented to the reader. Thus, the asymmetric compound channel and the measuring equipments are described. Further, in this chapter the reader can meet with the different roughness conditions studied.

Chapter 4 summarizes the results which will be presented in individual research papers, allowing the reader to have an overall view of the link between research papers and its sequence.

Chapter 5 resumes the main conclusions founded on this investigation and suggests topics for further research.

Appendix A contains the main algorithms developed to process the experimental data. These algorithms were developed using *Matlab*™ software and they are presented with the goal of giving a better understanding on the data processing and also to allow their use by future researchers.

2

Chapter 2

Literature Review

A thorough analysis of the hydrodynamic behavior of flow streams encountered in compound channels, requires to review fundamental concepts and the state of the art in turbulence measurements, especially in anisotropic conditions as expected in this investigation.

Therefore, this chapter begins describing the fundamental equations of fluid mechanics written in differential form, namely mass, momentum and energy conservation equations. Additionally, it will present the decomposition of Reynolds as a valid approach to analyze turbulent flow properties. Afterwards, the Reynolds decomposition concept will be introduced into the governing differential equations, accounting for all relevant involved variables (velocity, pressure, etc.). Further, the concept of statistically stationary processes will be introduced, in order to present the function that correlates events that occur at different periods of time and/or space.

Next, Kolmogorov´s energy cascade theory will be introduced. Through this theory, the energy transfer between different turbulent scales is explained, as well as, the relation between the Reynolds number and the characterization in time, space and frequency of those scales. Particularly, the -5/3 Law of Kolmogorov and its respective hypotheses will be revised to support the explanation of conditions for energy transfer among the different eddy scales.

In following section, it will be presented how direct measurements will be processed and analyzed either in temporary or spatial domain by adopting the frozen field hypothesis or Taylor hypothesis, which establishes a convection velocity that allows the transformation of the time record (corresponding to the measured data of the velocity) to the space domain.

The structure functions will be defined in the next section. On this regard, the concept of the autocorrelation function is used to correlate two and three points spaced by a distance r, so as to obtain expressions that are related with the energy dissipation rate between eddies in the inertial sub-range, assuming locally isotropic flow.

Once the expressions for the large scales and dissipation rate are introduced, it will be introduced expressions for the smaller scales, which are strongly associated to viscous effects.

Finally, the expressions to characterize the behavior of the mean flow in fully developed 2D flow will be presented, which will be used as a base for comparison with the 3D compound channel flows studied in this study.

2.1. Differential Conservation Equations

In this section, a brief review of the fundamental equations of fluid mechanics are presented, assuming that the fluid properties are describe as a function that varies uniformly with time and position, as $\vec{u} = \vec{u}(x, y, z, t)$. The notation used trhough the thesis can either be referred to the standard Cartesian coordinates or to tensorial notation (for example, the space coordinate vector $\vec{x} = (x, y, z) = x_i = (x_1, x_2, x_3)$ or the velocity vector $\vec{u} = (u, v, w) = u_i = (u_1, u_2, u_3)$).

For an incompressible fluid, where the density variations are neglected, the mass conservation equation can be written (*e.g.* Pope 2000)

$$\frac{\partial u_i}{\partial x_i} = 0 \tag{2.1}$$

where u is the instantaneous velocity and subscript i represents each spatial direction and its repetition means summation.

For Newtonian and incompressible fluids, the momentum equation (Newton's 2nd law) also known as Navier-Stokes equations can be written:

$$\rho\left(\frac{\partial u_i}{\partial t} + u_j \frac{\partial u_i}{\partial x_j}\right) = \rho g_i - \frac{\partial p}{\partial x_i} + \mu\left(\frac{\partial^2 u_i}{\partial x_j \partial x_j}\right) \tag{2.2}$$

The RHS term represents the inertia or the total variation of momentum in time (including a local time variation term and a convection term). The first term in the LHS represents the contribution of the volume (body) external forces (where only gravity is considered). The second and third terms in the LHS represent the external surface forces.

The total energy balance (1st law of thermodynamics), including the thermal and kinetic contributions, can be written (White, 2011):

$$\rho\left(\frac{\partial e}{\partial t} + u_j \frac{\partial e}{\partial x_j}\right) + \rho\left[\frac{\partial}{\partial t}\left(\frac{u_i^2}{2}\right) + u_j \frac{\partial}{\partial x_j}\left(\frac{u_i^2}{2}\right)\right] = \rho Q - \frac{\partial q_j}{\partial x_j} - \frac{\partial}{\partial x_j}(p u_j) + \rho g_j u_j + \frac{\partial}{\partial x_j}(\sigma_{ji} u_i) \tag{2.3}$$

where $\sigma_{ji} = \mu\left(\frac{\partial u_j}{\partial x_i} + \frac{\partial u_i}{\partial x_j}\right)$ is associated to the stress tensor corresponding to the work that generates surface deformations, e is the internal energy, Q and q are related to the heat flux

changes. This expression is constituted by two parts, a first part corresponding to the thermal energy balance

$$\rho\left(\frac{\partial e}{\partial t}+u_j\frac{\partial e}{\partial x_j}\right)=\rho Q-\frac{\partial q_j}{\partial x_j}-p\frac{\partial u_j}{\partial x_j}+\sigma_{ji}\frac{\partial u_i}{\partial x_j} \tag{2.4}$$

and a second part corresponding to the kinetic energy balance

$$\rho\left[\frac{\partial}{\partial t}\left(\frac{u_i^2}{2}\right)+u_j\frac{\partial}{\partial x_j}\left(\frac{u_i^2}{2}\right)\right]=-u_j\frac{\partial p}{\partial x_j}+\rho g_j u_j+u_i\frac{\partial \sigma_{ji}}{\partial x_j} \tag{2.5}$$

All the three conservation laws (mass, momentum and energy) were presented for instantaneous quantities. To describe the behavior of the variables of the flow, regardless of their condition (laminar or turbulent), Osborne Reynolds (1894) decomposed each of the variables associated to the fluid motion as a function of two terms: average and fluctuation.

In this investigation, *U*, *V* and *W* denote the components of mean (or time-averaged) velocity in the *x*-direction (streamwise with the origin at the channel entrance), *y*-direction (spanwise with the origin at the windows side) and *z*-direction (vertical with the origin at the channel bottom), respectively, *u*, *v* and *w* represents the instantaneous velocity, *u'*, *v'* and *w'* the velocity fluctuations and *U'*, *V'* and *W'* denote the turbulence intensities or r.m.s.

In this regard, the time-averaging function, represented by an overbar, is defined as:

$$U_i=\overline{u}_i=\frac{1}{T_0}\int_0^{T_0}u_i dt \tag{2.6}$$

where T_0 is a period of time long enough to include any period of the fluctuations. However, since the measurement technique used to obtain the velocity field was a Laser Doppler Velocimeter (LDV), the time-averaged velocity calculated through eq. 2.6 will present a bias associated to the high velocity particles detected by LDV. One way to diminish this bias for the streamwise component, is calculating the time-averaged velocity from eq. 2.7, were the low velocity particles have more weight (McLaughlin and Martin, 1975)

$$U=\overline{u}=\left(\frac{1}{N}\sum_{n=1}^{N}u_n^{-1}\right)^{-1} \tag{2.7}$$

where *N* is the total number of measured particles.

Further, the fluctuation for the same turbulent function is defined as the deviation of *u* from its average value.

$$u' = u - U \tag{2.8}$$

Importantly, by definition, the average of the fluctuations is zero, as shown in eq. 2.9, while the mean square of the fluctuations is different from zero, which is considered as a way to obtain a measure of turbulent intensity, eq. 2.10. However, to ensure the validity of eq. 2.9, the time-averaged velocity must be calculated from eq. 2.6 and not from eq. 2.7.

$$\overline{u'} = \frac{1}{T_0}\int_0^{T_0}(u - U)dt = U - U = 0 \tag{2.9}$$

$$\overline{u'^2} = \frac{1}{T_0}\int_0^{T_0} u'^2\, dt \neq 0 \tag{2.10}$$

On the other hand, since the *w* instantaneous velocity varies around zero (in most of the cases studied in this investigation), the equation used to calculate the *w* time-averaged velocity was always eq. 2.6.

Clarified the Reynolds decomposition, the three conservation laws presented above, can be rewritten in terms of time-averaged and fluctuations. In this regards, the *mass conservation equation* eq. 2.1 is given by

$$\frac{\partial U_i}{\partial x_i} = 0 \tag{2.11}$$

where, U_i represents the *i*-th time-averaged velocity component

In the case of *momentum equation* (eq. 2.2), it takes the following form applying the Reynolds decomposition and taking the time-averaging of each term (Pope, 2000) :

$$\rho\left(\frac{\partial U_i}{\partial t} + U_j\frac{\partial U_i}{\partial x_j}\right) = \rho g_i - \frac{\partial \overline{p}}{\partial x_i} + \mu\left(\frac{\partial^2 U_i}{\partial x_j \partial x_j}\right) - \rho\frac{\partial}{\partial x_j}\left(\overline{u'_i\, u'_j}\right) \tag{2.12}$$

The last term in the equation are the so called Reynolds stress that arise from the fluctuanting velocity field.

Finally, applying the Reynolds decomposition on the *kinetic energy equation* (eq. 2.15), the two following expressions are obtained, one for the time-averaged kinetic energy due to the mean flow ($U_i^2/2$) and the other for the turbulence kinetic energy (TKE) due to turbulent fluctuations ($k = \overline{u'^2_i}/2$) (Nikora and Roy, 2012).

$$\rho\left[\frac{\partial}{\partial t}\left(\frac{U_i^2}{2}\right)+U_j\frac{\partial}{\partial x_j}\left(\frac{U_i^2}{2}\right)\right]=\rho g_i U_i-\frac{\partial}{\partial x_j}\left(\overline{p}U_j\right)-\rho\frac{\partial}{\partial x_j}\left(U_i\overline{u'_i u'_j}\right)+\mu\frac{\partial^2}{\partial x_j^2}\left(\frac{U_i^2}{2}\right)+\rho\overline{u'_i u'_j}\frac{\partial U_i}{\partial x_j}-\mu\overline{\left(\frac{\partial U_i}{\partial x_j}\right)^2} \quad (2.13)$$

$$\rho\left(\frac{\partial k}{\partial t}+U_j\frac{\partial k}{\partial x_j}\right)=-\rho\overline{u'_i u'_j}\frac{\partial U_i}{\partial x_j}-\frac{\partial}{\partial x_j}\left(\overline{p'u'_j}\right)-\rho\frac{\partial}{\partial x_j}\left(\frac{\overline{u'_i u'_i u'_j}}{2}\right)+\mu\frac{\partial k^2}{\partial x_j^2}-\mu\overline{\left(\frac{\partial u'_i}{\partial x_j}\right)^2} \quad (2.14)$$

This last equation, can also be written as:

$$\frac{\partial k}{\partial t}+U_j\frac{\partial k}{\partial x_j}=P-\frac{1}{\rho}\frac{\partial}{\partial x_j}\left(\overline{p'u'_j}\right)-\frac{\partial}{\partial x_j}\left(\frac{\overline{u'_i u'_i u'_j}}{2}\right)+\nu\frac{\partial k^2}{\partial x_j^2}-\varepsilon \quad (2.15)$$

where $P=-\overline{u'_i u'_j}\frac{\partial U_i}{\partial x_j}$ is the production of TKE and $\varepsilon=\nu\overline{\left(\frac{\partial u'_i}{\partial x_j}\right)^2}$ is the dissipation rate of TKE. Considering a homogeneous and isotropic turbulent flow, the dissipation rate of TKE can be simplified through eq. 2.16.

$$\varepsilon=15\nu\overline{\left(\frac{\partial u'_1}{\partial x_1}\right)^2} \quad (2.16)$$

2.1.1 *Momentum balance equation for compound channel flow*

Given the expressions obtained for the conservation laws using the Reynolds decomposition, eq. 2.17 shows the combination of momentum and continuity equations in compound channel flows for steady ($\partial/\partial t=0$) uniform ($\partial/\partial x=0$) turbulent flow in the streamwise direction (*cf.* Shiono and Knight 1991), as shown in fig. 2.1.

$$\rho\left[\frac{\partial}{\partial y}(UV)+\frac{\partial}{\partial z}(UW)\right]=\rho g S_o+\frac{\partial}{\partial y}\left(-\rho\overline{u'v'}\right)+\frac{\partial}{\partial z}\left(-\rho\overline{u'w'}\right) \quad (2.17)$$

where $S_o=-\partial z_b/\partial x$ is the bed slope, being z_b the bed elevation.

A depth integration of this equation can be found in Shiono and Knight (1991), where experimental data from straight compound open cannel were conducted, rendering

$$\frac{\partial}{\partial y}\left[H(\rho UV)_d\right]=\rho g H S_o+\frac{\partial}{\partial y}\left[H\left(\tau_{yx}\right)_d\right]-\tau_b\left(1+\frac{1}{s^2}\right)^{1/2} \quad (2.18)$$

where H is the flow depth, τ_b is the bed shear stress, s is the side slope, $(\rho UV)_d=\frac{1}{H}\int_0^H\rho UV dz$ and $\left(\tau_{yx}\right)_d=\frac{1}{H}\int_0^H\left(-\rho\overline{u'v'}\right)dz$ are depth-averaged quantities

which are referenced with a subscript d . A physical interpretation of eq. 2.18 corresponding to the turbulent field skecteched in fig. 2.1, renders that the LHS term represents the secondary flows, the first term on the RHS account for the gravity contribution, the second term represents the momentum transfer by the interface vortices and the last one accounts for bed friction.

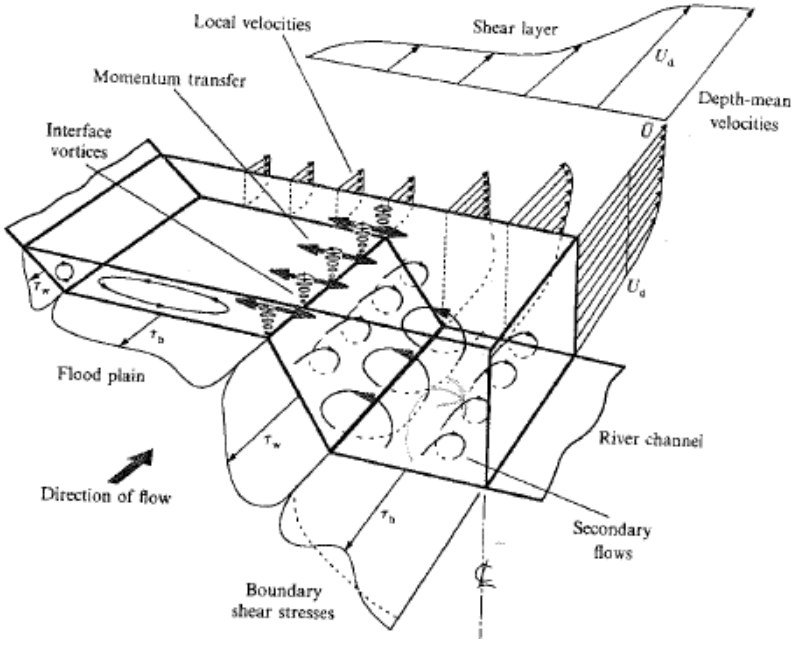

Figure 2.1 Flow field associated with a straight compound channel (Shiono and Knight, 1991).

2.2 Modeling of Turbulence

For a physical phenomenon to occur steadily in space and time it is not sufficient to verify the conservation laws. It is necessary that the flow parameters are stable to small perturbations. Sometimes, these perturbations can grow to reach a new state. This new state, at the same time, could be unstable to other perturbations, generating again a new state and so on. Finally, the flow becomes a conjunction of many random instabilities non-linearly interconnected, which is known as turbulent flow.

However, the presence of perturbations is not a sufficient factor to explain the random behavior of the turbulent flow. In fact, most of the laminar flows are subject of numerous perturbations. The generation of a turbulent flow is triggered by combination of these perturbations, which can be associated with small changes in initial conditions, boundary conditions or/and properties of materials, in presence of a high Reynolds number flow, resulting into chaotic behavior Lorenz (1963).

In practical words, this means that despite repeated uncountable times the same experiment, under similar initial and boundary conditions, an identical behavior of the variables in time is never obtained, as shown fig. 2.2. Thus, it is practically impossible to predict the exact value of the velocity or pressure of the flow under certain conditions. On the contrary, it is much more realistic to determine the range of values that these variables can achieve under these conditions, or the probability that they can reach a certain value.

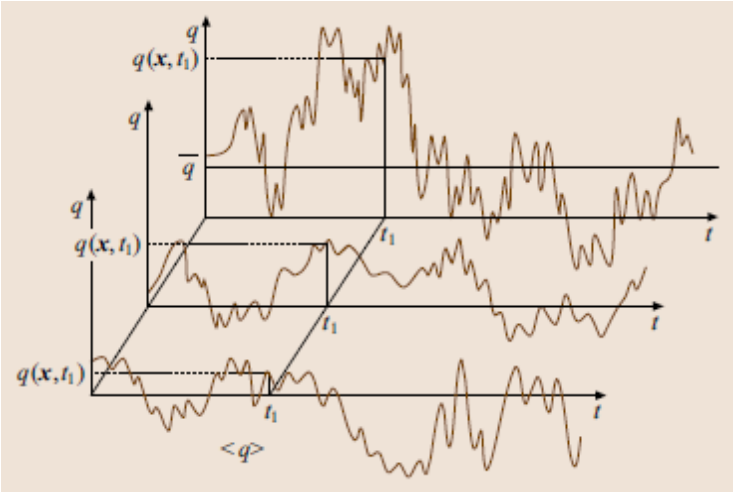

Figure 2.2 Ensemble of repeated experiments under similar initial boundary conditions. (Tropea et al., 2007)

One way to characterize the behavior of a random variable is calculating the probability density function (PDF) of the variable itself, which describes the relative probability that this variable takes a particular value or be located in a given range of possible values. However, to fully characterize a random process, it is necessary to know for every instant of time the PDF, which is an impossible task.

For a deeper reading in characterizing random variables through the probability functions, the reference Pope (2000) , Chap. 3 is recommended.

2.2.1 *Statistically Stationary Processes*

In the case of stationary processes, in which most of the turbulent flows can be encountered, the behavior of the variables reaches a statistically steady state after an initial transition period where, although the variables vary in time, are statistically independent from it. Assuming that fig. 2.2 shows the behavior of the velocity $u(t)$ of a statistically stationary process, the behavior of the time-average velocity and the variance, after an initial transition period, is independent of time, as shown in fig. 2.3 ($t \geq 5$).

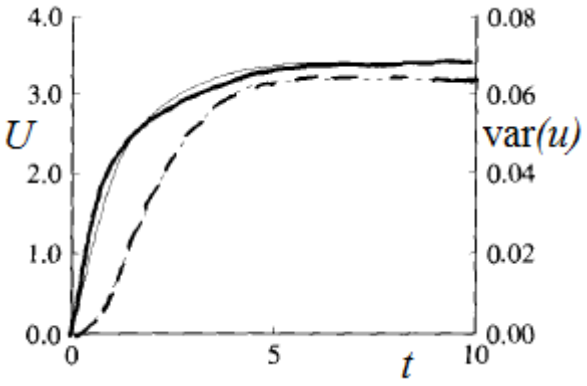

Figure 2.3 Mean $U(t)$ (solid line) and variance $\mathrm{var}(u)=\overline{u'(t)^2}$ from three repetitions of a turbulent-flow experiment (Pope, 2000)

Further, in turbulent flows the occurrence of certain phenomena (especially eddies/vortices) that occur with a certain frequency is usually observed. Specifically in compound channel flows, these phenomena occur by the interaction between main channel flow and floodplain flow (causing vortices of longitudinal and vertical axis), or by the interaction between main channel/floodplain flows and roughness placed over the floodplain region, where the roughness geometry (roughness diameter, spacing between rough elements, etc.) have an important role to play on the eddies propagation.

The study of such flows has been focused on understanding the frequency with which vortices are originated and how they interact with the flow. For this purpose, it is necessary to analyze the correlation existent in the behavior of a same variable for different intervals of time and/or space. The autocorrelation function verifies the correspondence between events occurring at different periods of time/space, being able to analyze the frequency and lengthscale of these events. The autocorrelation function in normalized form can be expressed as (*e.g.* Pope 2000):

$$\rho(s)\equiv\frac{\overline{u'(t)u'(t+s)}}{\overline{u'(t)^2}} \tag{2.19}$$

where $u'(t)=u(t)-U(t)$. Equation 2.19 provides a correlation coefficient between lagged process in time/space *t* and *t*+*s*. For $s=0\rightarrow\rho(0)=1$, whereas that for $s>0\rightarrow\rho(s)<1$. In the case of periodic functions with periodicity T_0 ($f(t)=f(t+T_0)$), the autocorrelation function also present a periodic behavior. Figure 2.4 shows, the behavior of the autocorrelation function for some known signals.

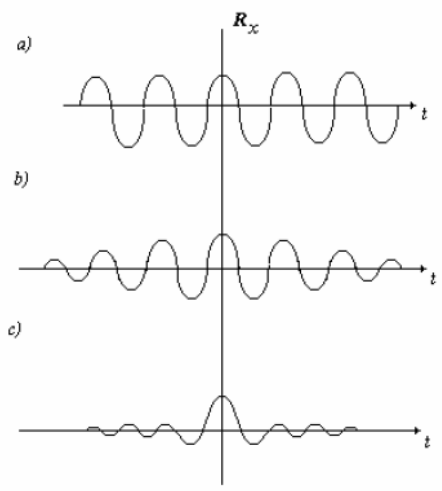

Figure 2.4 a) Sine function. b) Narrowband random noise. c) Broadband random noise

In general, the autocorrelation function can be correlated to events in space and time with one, two or three components of the reference system, obtaining nine combinations of the flow field. Thereby, events occurred in one direction can be correlated with events occurred in other directions (Tropea et al., 2007).

$$\rho_{u'_i u'_j}(r,s) = \frac{\overline{u'_i(x,t)u'_j(x+r,t+s)}}{\overline{u'_i(x,t)u'_j(x,t)}} \tag{2.20}$$

The real expected behavior of the autocorrelation function is as shown in fig. 2.5, where the events correlation decrease rapidly as the intervals of time (*s*) or space (*r*) increase, and where the correlation coefficients start to exhibit oscillations due to poor statistics and to the random nature of the phenomenon. The duration time of the process is defined as the integral timescale (eq. 2.21) or the integral length scale (eq. 2.22). However, in practical terms, the integral of the autocorrelation function must be defined until a finite value. In this investigation, different integral-stop-values were used in order to analyze the behavior of the integral length scale under several conditions (see section 4.4). The integral-stop-values used were:

1º Method: the integral-stop-value is defined as the second maximun found on the autocorrelation function.

2º Method: the integral-stop-value is defined as the first minimun found on the autocorrelation function.

3º Method: the integral length scale is defined as the wavenumber value when the autocorrelation function reaches 1/*e*, *i.e*., the value expected if an exponential decay of the autocorrelation function is assumed.

4º Method: the integral length scale is defined bycalculating the power spectrum of the autocorrelation function when its tends to zero, as shown in eq. 2.23 (Nezu and Nakagawa, 1993).

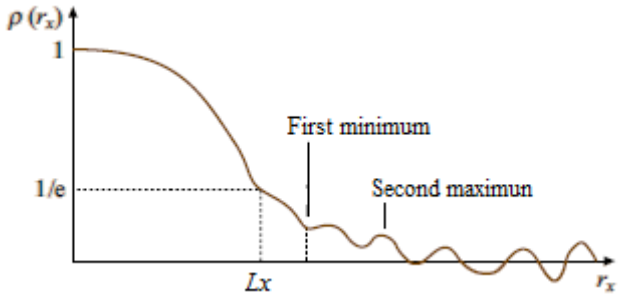

Figure 2.5 The integral-stop-values used to determine the macro-scale. $\rho(r_x)$ autocorrelation function; r_x intervals of space in the longitudinal direction (Tropea et al., 2007).

$$\bar{\tau} \equiv \int_0^\infty \rho(s)ds \tag{2.21}$$

$$L_x \equiv \int_0^\infty \rho(r)dr \tag{2.22}$$

$$L_x = \frac{\pi}{2}\lim_{k_w \to 0} E(k_w) \tag{2.23}$$

The non-normalized autocorrelation funtion (autocovariance) of the signal $R(s) \equiv \overline{u'(t)u'(t+s)} = \overline{u'(t)^2}\rho(s)$, is associated with the frequency spectrum $E(k_w)$ of the same signal, forming a Fourier transform pair:

$$E(k_w) \equiv \frac{1}{\pi}\int_{-\infty}^{\infty} R(s)e^{-ik_w s}ds = \frac{2}{\pi}\int_0^\infty R(s)\cos(k_w s)ds \tag{2.24}$$

$$R(s) = \frac{1}{2}\int_{-\infty}^{\infty} E(k_w)e^{ik_w s}dk_w = \int_0^\infty E(k_w)\cos(k_w s)ds \tag{2.25}$$

Both eqs. 2.24 and 2.25, contain the same information but expressed in different ways, which allows rewriting the integral timescale as: (Nezu and Nakagawa, 1993)

$$L_\tau = \frac{\pi E(0)}{2\overline{u'^2}} \tag{2.26}$$

2.2.2 *The energy cascade and Kolmogorov hypotheses*

Andrey Kolmogorov (1945) did the first relevant effort in quantifying turbulence and his work, which is valid for all isotropic and homogenous turbulent flows, describes the energy content distribution between eddies (energy cascade). The energy cascade suggests the existence of different scales through which the energy is flowing from larger ones to smaller ones until it dissipates as heat due to viscosity. Most of the kinetic energy of turbulent motion is in the larger structures, where aspects such as the system geometry, define the size and shape of the vortices (production sub-region/small wave numbers). These larger structures are broken down into smaller structures (inertial sub-region / larger wave numbers) until the energy is dissipated by viscous effects (viscous sub-region / larges wavenumbers).

In a turbulent flow, the Kolmogorov´s hypotheses state that the correlation of velocities between two points separated by a distance "*l*", into the inertial sub-region, is equal to $C\left(\bar{\varepsilon} l\right)^{2/3}$, where *C* is a universal constant and $\bar{\varepsilon}$ is an average flow of energy per unit mass.

Also, the Kolmogorov´s hypotheses propose the existence of an interval of scales where the turbulent behavior is universal, *i.e.*, the flow is homogeneous, isotropic and statistically stationary. This last attribute indicates that, on average, the state does not change in time (statistically), *i.e.*, the flow only depends on two parameters to describe the energy dissipation, the energy flow ($\bar{\varepsilon}$) and the viscosity (ν). The size of the larger scales, where the friction effects still have an important role, is given by the combination between the energy flow and viscosity, so as to form a length scale. This scale is denoted as Kolmogorov's scale η.

$$\eta = \varepsilon^{-1/4} \nu^{3/4} \tag{2.27}$$

$$u_\eta = \left(\varepsilon \nu\right)^{1/4} \tag{2.28}$$

$$\tau_\eta = \nu^{1/2} \varepsilon^{-1/2} \tag{2.29}$$

Generally, the different vortices scales existing in any turbulent flow can be grouped in three scale regions. The first region is bounded by the integral length scale, which is associated with larger vortices and the Reynolds number is the same as the main flow:

$$\mathrm{Re}_L = \frac{UL}{\nu} \tag{2.30}$$

Then, there is an intermediate region where energy production still exists, and finally a last region that starts at the so-called micro-scale (λ), that is the smaller scale, having an isotropic character and for which the energy is dissipated into heat.

Doing an analysis of the Kolmogorov´s hypotheses for larger vortices (integral length scale), the energy contained per unit of time is given by:

$$e_L = \frac{U^2/2}{T} \approx U^2 T^{-1} \approx U^3 L^{-1} \tag{2.31}$$

at the same time, the specific energy dissipated per unit of time in the integral length scale is:

$$\Phi_L \approx \nu \left(\frac{\partial U_i}{\partial x_j} \right)^2 \approx \nu \frac{U^2}{L^2} \tag{2.32}$$

The relation between the energy contained and the energy dissipation is:

$$\frac{e_L}{\Phi_L} = \frac{U^3 L^{-1}}{\nu U^2 L^{-2}} \approx \frac{UL}{\nu} \approx \mathrm{Re}_L >> 1 \tag{2.33}$$

With this last relation, it is deduced that the energy dissipation is negligible in the larger scales region. Therefore, all the energy is transferred to the vortices of the intermediate scales region.

$$e_L \approx e_\lambda \Rightarrow U^3 L^{-1} \approx u^3 \lambda^{-1} \tag{2.34}$$

In the intermediate scales region, the relation between the energy contained and the dissipation is also equal to the Reynolds number associated to this scale,

$$\frac{e_\lambda}{\Phi_\lambda} = \frac{u^3 \lambda^{-1}}{\nu u^2 \lambda^{-2}} \approx \frac{u\lambda}{\nu} \approx \mathrm{Re}_\lambda \tag{2.35}$$

$$\mathrm{Re}_\lambda \approx \mathrm{Re}_L \left(\frac{\lambda}{L} \right)^{4/3} \tag{2.36}$$

Since the ratio between the length scales is not negligible, the Reynolds number associated to these scales still has a significant value, so that the energy dissipation is still negligible. Therefore, it can be stated that:

$$e_L \approx e_\lambda \Rightarrow U^3 L^{-1} \approx u^3 \lambda^{-1} \tag{2.37}$$

$$\frac{e_\lambda}{\Phi_\lambda} = \frac{u^3 \lambda^{-1}}{\nu u^2 \lambda^{-2}} \approx \mathrm{Re}_\lambda = \mathrm{Re}_L \left(\frac{\lambda}{L} \right)^{4/3} \tag{2.38}$$

As the energy contained is of the same order as the energy dissipated,

$$\frac{e_\lambda}{\Phi_\lambda} \approx 1 \Rightarrow \mathrm{Re}_L \left(\frac{\lambda}{L} \right)^{4/3} = 1 \tag{2.39}$$

$$\frac{\lambda}{L} \approx \mathrm{Re}_L^{-3/4} \tag{2.40}$$

This last equation relates the characteristics length scales of the micro-scale with the integral length scale. Notably, as the Reynolds number present in the main flow increases, the difference between the micro-scale and integral length scale increases.

Using a similar analysis, the velocity and time terms of the Kolmogorov's and integral length scales can be related. Using the initial nomenclature, the expressions that relate the Komogorov's scale with the integral length scale are:

$$\frac{\eta}{L} \approx \mathrm{Re}_L^{-3/4} \tag{2.41}$$

$$\frac{u_\eta}{U} \approx \mathrm{Re}_L^{-1/4} \tag{2.42}$$

$$\frac{\tau_\eta}{T} \approx \mathrm{Re}_L^{-1/2} \tag{2.43}$$

Being $T = L/U$, eq. 2.43 can be rewritten as follows:

$$\tau_\eta \approx \frac{L}{U} \mathrm{Re}_L^{-1/2} \tag{2.44}$$

The previous equation is very useful because it provides a reference value of the temporal Kolmogorov's scale or, in other words, the minimum frequency of data acquisition if the study of this scale is desired.

The diagram of the energy cascade explained above is represented in fig. 2.6.

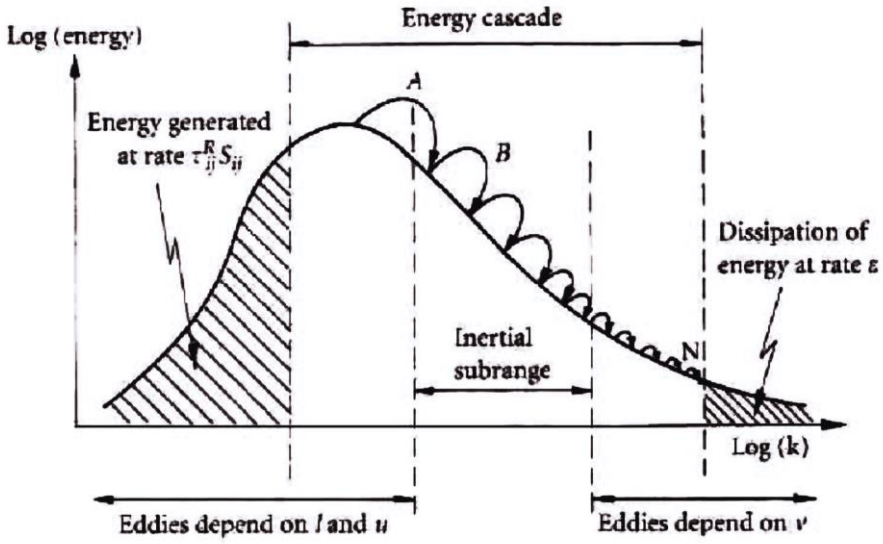

Figure 2.6 Schematic representation of the Energy Cascade.

Figure 2.6 shows how the energy contained in the vortices of large scale (integral length scale) is transferred to smaller scale vortices, until this energy is dissipated into heat by viscous effects (micro-scale). As mentioned above, the integral length scale only depends on the mean average velocity of the flow and of the system geometry (in compound channel flow, for a given channel this is represented by the depth of the main flow stream), while the micro-scale depends only on the viscosity of the fluid.

In the inertial sub-range, the energy spectrum is given by the known law of -5/3 of Kolmogorov and its expression is (Pope, 2000):

$$E(k) \approx C\varepsilon^{2/3} k_w^{-5/3} \tag{2.45}$$

The power law -5/3 corresponds to the inertial range where the integrals of k_w and ε converge. For larger wavenumbers, the energy contained in vortices decreases following the relationship $k_w^{-\alpha}$, with $\alpha < 5/3$, while for lower wavenumbers, the energy dissipation follows a similar relationship, but with $\alpha > 5/3$.

Figure 2.6 does a schematic exemplification of vortices arising when the flow pass through a grid, as well as the different types of power spectra obtained depending of the area in which the measurements are perform.

As shown in fig. 2.7, in the first stage eddies are originate and a transition of the flow until a fully developed turbulent flow occurs. In the next two stages (stage ii and stage iii), a fully developed turbulent flow exists. However, in the last stage the turbulence in the flow decreases since the smaller eddies are dissipated by viscous effects (energy cascade).

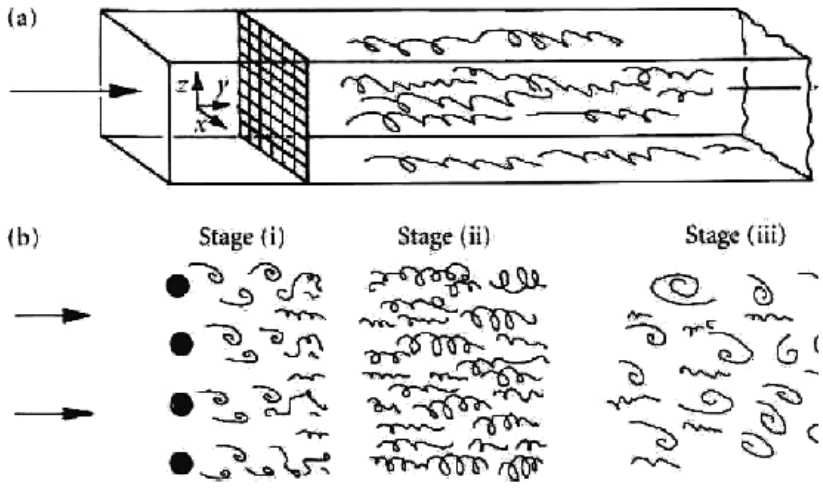

Figure 2.7 Turbulence generated through a grid. b) Development of the different stages of the turbulence. Stage(i) Transition to a fully developed turbulent flow. Stage (ii) and (iii) Fully developed turbulent flow. Stage (iii) Dissipation of the smallest eddies.

The power spectra for each of these stages (see fig. 2.8) shows the variation of the kinetic energy contained. The first stage (fig. 2.8a), where the turbulence is generated, is characterized by a large presence of large eddies (macro-vortexes) transporting large amounts of energy, and by absence of smaller vortices. In the second stage (fig. 2.8b), vortices of large and small scales are found, having an energy transfer from largest vortices towards smallest vortices. That is why in the second stage a smoother decay of energy due to the transfer of energy for different wavenumbers (existence of a variety of sizes of vortices) is visualize. For the first stage, the energy decay is not so smooth because in this stage there is not a variety of sizes of vortices and therefore, the wavenumber is limited. In the third stage (fig. 2.8c), the power curve is similar to the curve obtained in the second stage, however, as in this stage the vortices have a smaller scale, the specific energy transported by them will be smaller (but distributed among many more eddies).

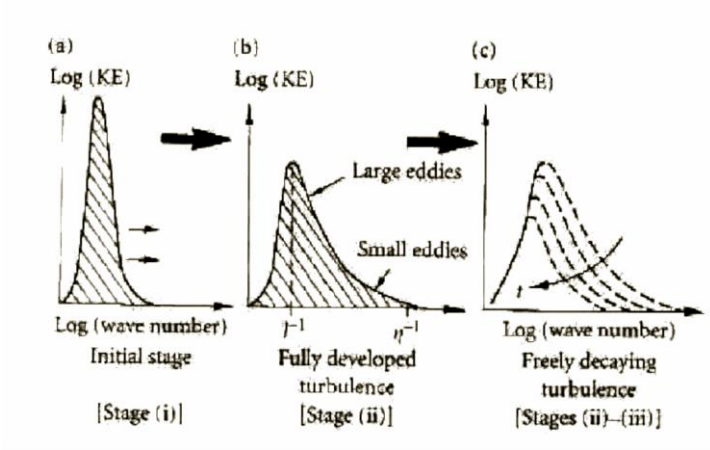

Figure 2.8 Variation of the kinetic energy for the different stages of flow.

2.2.3 *Taylor's or Frozen-Field Hypothesis*

Taylor's hypothesis allows us to relate the behavior of a variable in space and time considering only a convection velocity U_c, *i.e.*, when measurements are made only as function of time, convection velocity allows transforming the time-record to a space-record. In this way, the spatial autocorrelation function can be determined through the temporal autocorrelation function.

$$\frac{\partial q}{\partial t} + U_C \frac{\partial q}{\partial x_1} = 0 \tag{2.46}$$

Despite being a hypothesis that fits quite well to most flow conditions, the great challenge is to define the convection velocity that best fits all scales of flows. As a first approximation, the convection velocity can be taken between $0.7U$ and $0.9U$, where U represents the time-average velocity of the flow, depending on the distance between the measurement point and the wall.

The convection velocity for different scales, according to Tropea et al. (2007), can be estimated as:

$$U_c = \begin{cases} U \rightarrow \text{Large scales} \\ Uf(I) \rightarrow \text{Intermediate scales} \\ U\,\mathrm{Re}_L^{1/4} \rightarrow \text{Small scale} \end{cases} \tag{2.47}$$

where *f(I)* is the ratio between the root-mean-square of the fluctuations and the mean velocity and the Reynolds number is based on the large scale. If the turbulent intensity is less than 20%, the convection velocity can be considering as the one for large scales. In the present

investigation the time-average velocity of each measurement point (*U*, *V* and *W*) was assumed as the convection velocity.

2.2.4 *Structure Functions*

Second-order Structure Function

By definition, the second-order velocity structure function is the velocity covariance between two points separated by *r*, which is expressed as,

$$D_{ij}(r,x,t) \equiv \overline{\left[U_i(x+r,t)-U_i(x,t)\right]\left[U_j(x+r,t)-U_j(x,t)\right]} \tag{2.48}$$

A flow can be considered locally isotropic, in a small domain and in a turbulent flow at high Reynolds numbers, if the behavior of the turbulence does not have a favorite direction, *i.e*., if the energy transfer and the fluctuation statistics are the same in all directions. For this, the flow domains should not be near boundaries or singularities.

In this case, eq. 2.48 is independent of *x*, and D_{ij} will just depend only on *r*, as shown in fig. 2.9. Thus, the correlation between the components of the velocity field can be express in terms of the longitudinal and transversal correlation functions, as shown in eq. 2.49 (Pope, 2000).

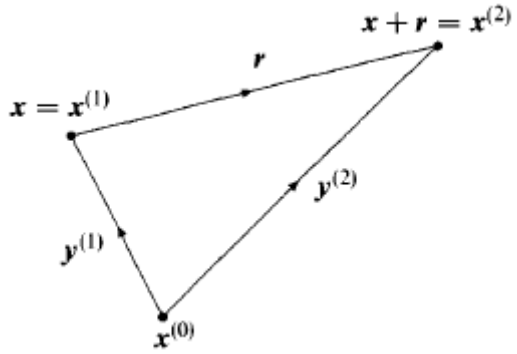

Figure 2.9 Sketch showing the points *x* and *x*+*r* in terms of $x^{(n)}$ and $y^{(n)}$.

$$D_{ij}(r,t) = D_{NN}(r,t)\delta_{ij} + \left[D_{LL}(r,t) - D_{NN}(r,t)\frac{r_i r_j}{r^2} \right] \tag{2.49}$$

where D_{LL} and D_{NN} are the longitudinal and transversal structures function, respectively, δ_{ij} is the delta Kronecker and r_i and r_j are the coordinates along the reference axis of the first and second point, separated by a distance *r*. However, when considering an incompressible flow, and as a result of the equation of continuity, $\partial D_{ij}(r,t)/\partial r_i = 0$, the transversal correlation function can be expressed solely in terms of the longitudinal function, as follows:

$$D_{NN}(r,t) = D_{LL}(r,t) + \frac{1}{2} r \frac{\delta}{\delta r} D_{LL}(r,t) \tag{2.50}$$

At the same time, and considering the Kolmogorov's hypotheses, for values of *r* in the inertial subrange, where *r* is much larger than the Kolmogorov's scale and much smaller than the integral length scale, $(\eta << r << L)$, the longitudinal structure function is independent of ν and can be calculated as:

$$D_{LL}(r,t) = C_2(\varepsilon r)^{2/3} \tag{2.51}$$

where C_2 is a universal constant that does not depend on the Reynolds number. Further, the transversal structure function is given by:

$$D_{NN}(r,t) = \frac{4}{3} C_2(\varepsilon r)^{2/3} \tag{2.52}$$

Figure 2.10 shows the second order structure functions for the three components, longitudinal D_{11} and transversal D_{22} and D_{33}, as well as, the way to calculate the constant C_2.

The Kármán-Howarth equation

Using the Navier-Stokes equations and deriving the double-point correlation, an expression with three kind of terms is obtained: the convection term, the pressure gradient and the viscous term. However, for isotropic incompressible turbulent flows, the pressure term disappears and an expression that depend on functions of double and triple velocity correlations arises as (Pope, 2000):

$$\frac{\partial}{\partial t}\left(\overline{u'^2} f\right) - \overline{u'^2}^{3/2} \frac{1}{r^4} \frac{\partial}{\partial r}\left(r^4 k\right) = 2\nu \overline{u'^2} \frac{1}{r^4} \frac{\partial}{\partial r}\left(r^4 \frac{\partial f}{\partial r}\right) \tag{2.53}$$

where *f* and *k* represent the double and triple correlations, respectively. However, using the second and third-order structure functions, an equivalent expression is obtained, as shown in eq. 2.54.

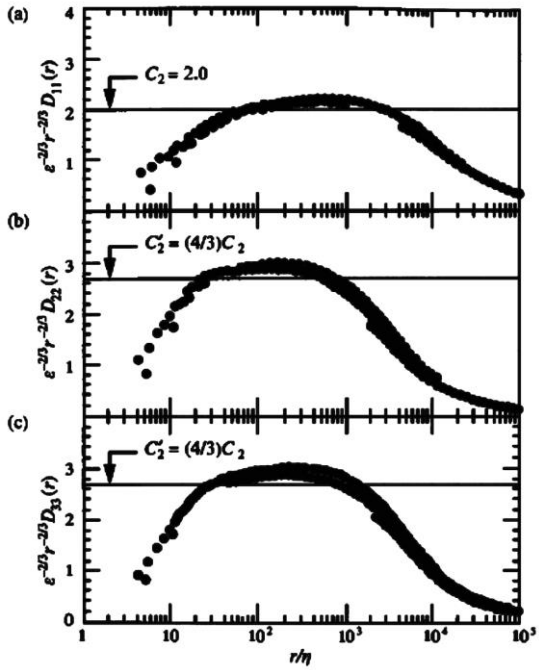

Figure 2.10 Second-order velocity structure functions. Horizontal lines show the predictions of the Kolmogorov hypotheses in the inertial subrange, eqs. 2.51 and 2.52. (Pope, 2000)

$$\frac{\partial}{\partial t}D_{LL} + \frac{1}{3r^4}\frac{\partial}{\partial r}\left(r^4 D_{LLL}\right) = \frac{2\nu}{r^4}\frac{\partial}{\partial r}\left(r^4\frac{\partial D_{LL}}{\partial r}\right) - \frac{4}{3}\varepsilon \tag{2.54}$$

Integrating eq. 2.54 renders:

$$\frac{3}{r^5}\int_0^r s^4\frac{\partial}{\partial t}D_{LL}(s,t)ds = 6\nu\frac{\partial D_{LL}}{\partial r} - D_{LLL} - \frac{4}{5}\varepsilon r \tag{2.55}$$

For a local isotropic flow, the term in the right side of eq. 2.55 is zero and the viscous term can be neglected in the inertial sub-range, so that the third-order structure function is equal to:

$$D_{LLL}(r,t) = -\frac{4}{5}\varepsilon r \tag{2.56}$$

Further, Kolmogorov showed that the skewness is constant and it is related with the second and third-order functions as:

$$S' \equiv D_{LLL}(r,t) \Big/ D_{LL}(r,t)^{3/2} \tag{2.57}$$

Substituting from eq. 2.56, leads to:

$$D_{LL}(r,t)=\left(\frac{-4}{5S'}\right)^{2/3}(\varepsilon r)^{2/3} \tag{2.58}$$

Considering the hypothesis of similarity in the inertial sub-range, the energy spectral function is:

$$E(k_w)=C\varepsilon^{2/3}k_w^{-5/3} \tag{2.59}$$

where C = 0.53 - 1.5 is the universal constant of Kolmogorov and k_w is the wavenumber.

2.2.5 *Taylor microscales*

The Taylor microscale is the largest scale for which vortices are still strongly affected by the viscosity of the fluid. To determine the value of the Taylor microscale, an expansion of the Taylor series of the spatial autocorrelation function $\rho(r)$ near the origin is required, which gives:

$$\rho_{u_i'^2}(x,r,t)=\rho_{u_i'^2}(x,0,t)+\left(\frac{\partial\rho}{\partial r}\right)_{r=0}r+\left(\frac{\partial^2\rho}{\partial r^2}\right)_{r=0}\frac{r^2}{2}+o(r^3) \tag{2.60}$$

Considering that $\rho_{u_i'^2}(x,0,t)\equiv 1$ and neglecting the values greater than r^2, an approximation of the parabola equation for the autocorrelation coefficient is obtain,

$$1+\left(\frac{\partial\rho}{\partial r}\right)_{r=0}\lambda_x+\left(\frac{\partial^2\rho}{\partial r^2}\right)_{r=0}\frac{\lambda_x^2}{2}=0 \tag{2.61}$$

Taking into account that the first derivative of the autocorrelation function at r = 0 is equal to zero $(\partial\rho/\partial r=0)$, and that the second derivative at r = 0 is negative, then it is obtain:

$$\lambda_x^2=\frac{-2}{\left(\frac{\partial^2\rho}{\partial r^2}\right)_{r=0}} \tag{2.62}$$

Therefore, the behavior of the autocorrelation function can be approximate to the following expression:

$$\rho_{u_i'^2}(x,r,t)=1-\left(\frac{r^2}{\lambda_x^2}\right) \tag{2.63}$$

Thus, as shown in fig. 2.11, the parabola intersects the axis at $r=\lambda_x$

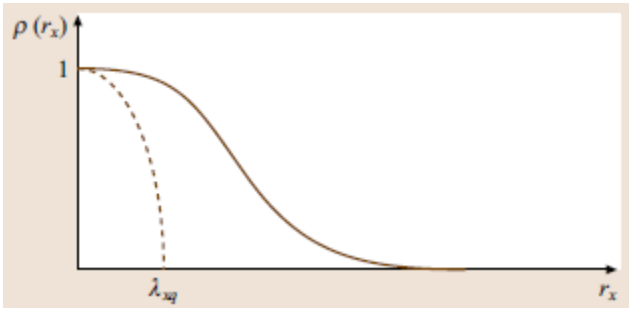

Figure 2.11 Evaluation of Taylor's microscale. Tropea et al. (2007)

Another way to express eq. 2.62, is calculating directly the second derivative of the autocorrelation function, as:

$$\left(\frac{\partial^2 \rho}{\partial r^2}\right)_{r=0} = \left[\frac{\partial^2}{\partial r^2}\left(\frac{\overline{u'_i(x,t)u'_i(x+r,t)}}{\overline{u'^2_i(t)}}\right)\right]_{r=0} = -\frac{\overline{\left(\frac{\partial u'_i(t)}{\partial r}\right)^2}}{\overline{u'^2_i(t)}} \tag{2.64}$$

Substituting in the eq. 2.62, it leads to:

$$\lambda_x^2 = \frac{2\overline{u'^2_i}}{\overline{\left(\frac{\partial u'_i}{\partial r}\right)^2}} \tag{2.65}$$

For an incompressible homogeneous isotropic turbulent flow, and using eq. 2.16, the longitudinal Taylor microscale can be express as a function of the turbulent dissipation ε, as follows:

$$\lambda_x^2 = \frac{30\nu\overline{u'^2_i}}{\varepsilon} \tag{2.66}$$

Moreover, the square of the transversal Taylor microscale is given as the half of the square of the longitudinal microscale $\lambda_x^2 = 2\lambda_w^2$.

2.2.6 *Dissipation Rate*

Once the integral length scale, second- and third-order velocity structure functions and Taylor microscale have been introduced, the next variable to characterize is the dissipation rate. In this investigation, six methods are used to estimate it, assuming an isotropic turbulent flow.

1º Method: this relation is useful in evaluating the TKE dissipation rate from the large-scale variable:

$$\varepsilon = \frac{\left(\overline{u'^2}\right)^{3/2}}{L_x} \tag{2.67}$$

2º Method: the dissipation rate is calculated from eq. 2.16.

3º Method: the dissipation rate is calculated from eq. 2.66.

4º Method: the third-order velocity structure function, *i.e.*, eq. 2.56.

5º Method: the second-order velocity structure function, *i.e.*, eqs. 2.51 and 2.52.

6º Method: considering the second hypothesis of similarity in the inertial sub-range, *i.e.*, eq. 2.59.

2.3 Two-Dimensional Flow Structures

2.3.1 *Flow Velocity*

In 1930, an investigation carry out by Prandtl concluded that the behavior of U should be independent of the boundary layer thickness, following a similar behavior of eq. 2.68, where $U_* = \left(\tau_b/\rho\right)^{1/2}$, being τ_b the wall shear stress and U_* the friction velocity.

$$U^+ = \frac{U}{U_*} = F\left(\frac{zU_*}{\nu}\right) \tag{2.68}$$

On the other hand, von Kármán concluded in 1933 that the behavior of the time-averaged velocity of the flow in the outer region, must be independent of the viscosity, and its difference with the free-surface velocity U_{sup}, should depend on the boundary layer thickness δ and other properties. In this sense, the behavior of the outer region obeys the following expression, which is denominated the velocity defect relation:

$$\frac{U_{\text{sup}} - U}{U_*} = G\left(\frac{z}{\delta}\right) \tag{2.69}$$

After determining the expressions for the mean velocity in the near wall region (viscous sublayer) and in the region near the free-surface (free-surface region), Millikan showed in 1937 that, in order to have both expressions engaging smoothly, the velocity distribution must have a logarithmic behavior, given by the following expression,

$$\frac{U}{U_*} = \frac{1}{\kappa}\ln\left(\frac{zU_*}{\nu}\right) + A \tag{2.70}$$

where the von Kármán constant is $\kappa \approx 0.41$.

More recent research, conducted by Coles in 1956, determined that eq. 2.70 is valid solely in the wall region ($z/H < 0.2$), while for $z/H > 0.2$, the time-averaged velocity behavior is fitted adding a wake function as shown in eq. 2.71.

$$\frac{U}{U_*} = \frac{1}{\kappa}\ln\left(\frac{zU_*}{\nu}\right) + A + wake\left(\frac{z}{H}\right) \tag{2.71}$$

Coles proposed empirically that the wave function $wake(z/H)$ can be considered as:

$$wake\left(\frac{z}{H}\right) = \frac{2\Pi}{\kappa}\sin^2\left(\frac{z\pi}{2H}\right) \tag{2.72}$$

where Π is Coles' wake strength parameter. Basically, eq. 2.71 represents the difference between eq. 2.70 and the real behavior of the velocity, including free-surface effects that cannot be neglected for $z/H > 0.6$. To determine the Π value, eq. 2.70 must be extended until $z/H = 1$ to obtain its difference. Only in this case (for $z/H = 1$), the wake function is equal to $wake(z/H) = 2\Pi/\kappa \Rightarrow U^+_{sup} - U^+ = 2\Pi/\kappa$, where $U^+_{sup} = U_{sup}/U_*$ is the non-dimensional time-averaged velocity in the free-surface and $U^+ = U/U_*$ is the non-dimensional time-averaged velocity for $z/H = 1$, calculated through eq. 2.70.

Figure 2.12 shows the behavior of the Π value for different Reynolds numbers $\mathrm{Re}_* = HU_*/\nu$ and $\mathrm{Re}_h = 4HU_{CS}/\nu$ (U_{CS} is the cross-section averaged velocity), which presents a steep increase at small values of Re_*, until reaching a constant value equal to 0.2 for $\mathrm{Re}_* > 2000$, approximately.

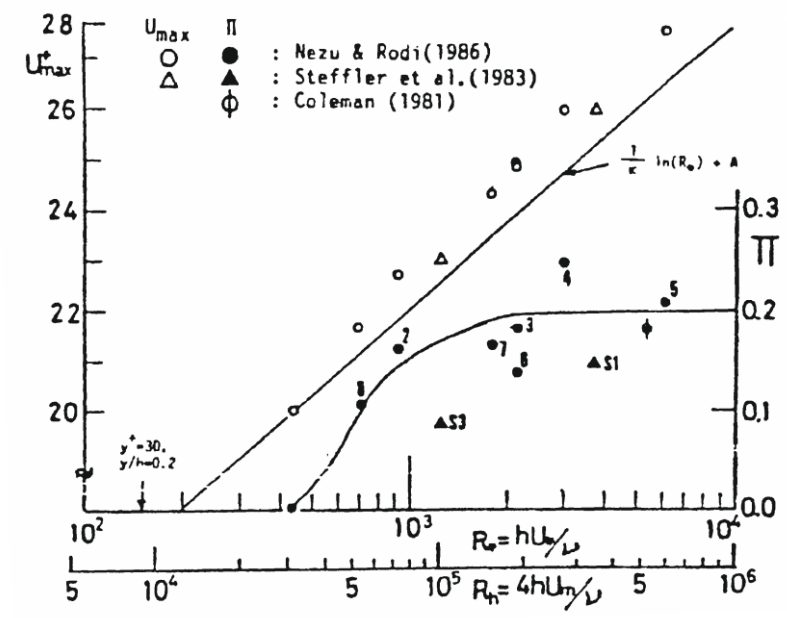

Figure 2.12 Wake strength parameter Π and maximum velocity $U^+_{\max}$ as functions of Reynolds number Re_* and Re_h. Nezu and Nakagawa (1993)

Moreover, in the region closest to the wall of the channel, the behavior of the time-averaged velocity does not follow the eq. 2.70. These regions are known as the viscous sublayer and the buffer sublayer. The viscous sublayer presents a linear behavior of the velocity U^+ according to the vertical distance $z^+ = {zU_*}/{\nu}$, as shown in eq. 2.73, and it is valid for $z^+ < 5$.

$$U^+ = z^+ \tag{2.73}$$

The region known as buffer sublayer is located at $5 < z^+ < 30$ and makes the transition between eqs. 2.73 and 2.70. In this region, the velocity behavior follows the expression for the dimensionless velocity gradient, given by:

$$\frac{dU^+}{dz^+} = \frac{2\left(1 - {z}/{H}\right)}{1 + \sqrt{1 + 4l^{+2}\left(1 - {z}/{H}\right)}} \tag{2.74}$$

where $l^+ = \kappa z^+\left[1 - \exp\left(-{z^+}/{B}\right)\right] = {lU_*}/{\nu}$ represents the dimensionless mixing length and $B = 26$ was obtained empirically for boundary layers by Van Driest (1956) and by Nezu and Rodi (1986).

Synthesizing, in an open channel flow, under conditions of fully developed 2D flow and smooth bed, the cross-section of a statistically developed flow can be divided into three regions according to the water depth, as shown in fig. 2.13.

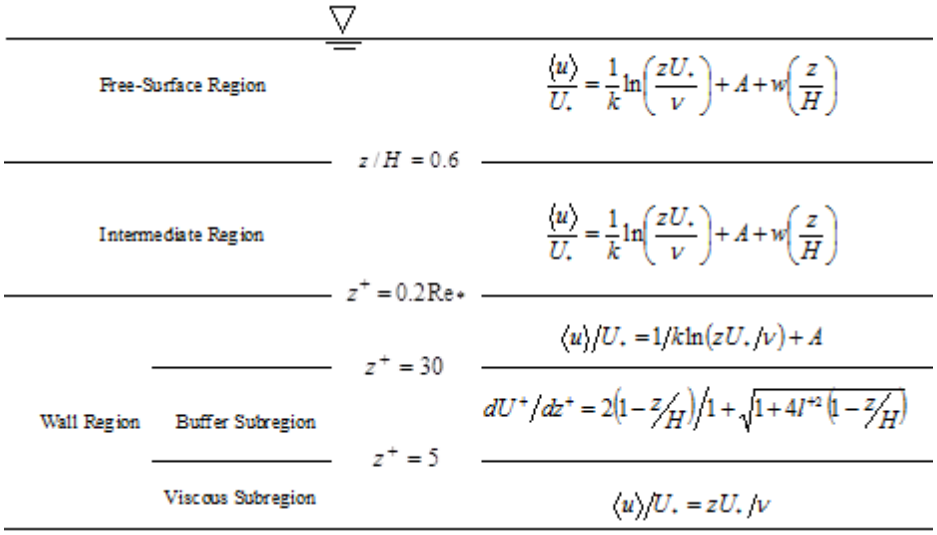

Figure 2.13 Sub-division of the flow field in open channels (*cf.* Nezu and Nakagawa 1993).

2.3.2 *Turbulence Intensity*

According to Nezu and Nakagawa (1993), the expressions that better fit the behavior of the turbulence intensities *U'*, *V'* and *W'*are the following:

$$\frac{U'}{U_*} = D_u \exp\left(-C_k \frac{z}{H}\right) \tag{2.75}$$

$$\frac{V'}{U_*} = D_v \exp\left(-C_k \frac{z}{H}\right) \tag{2.76}$$

$$\frac{W'}{U_*} = D_w \exp\left(-C_k \frac{z}{H}\right) \tag{2.77}$$

where $C_k \approx 1$, $D_u \approx 2.30$, $D_v \approx 1.63$ and $D_w \approx 1.27$.

The equations presented above are semi-theoretical expressions, which arise adopting the $k-\varepsilon$ turbulent model and neglecting the viscous diffusion term of the turbulent kinetic energy equation. However, this term can be neglected only in the region of the flow away from the wall and at high Reynolds number. In consequence, for the viscous sublayer, eqs. 2.75 to 2.77 are not valid.

Furthermore, within the viscous sublayer, U'/U_* was correlated using experimental data carried out by Van Driest (1956) and it is given by the following expression:

$$\frac{U'}{U_*} = D_u \exp\left(-\frac{z^+}{\mathrm{Re}_*}\right)\cdot\Gamma\left(z^+\right)+Cz^+\cdot\left(1-\Gamma\left(z^+\right)\right) \tag{2.78}$$

where,

$$\Gamma\left(z^+\right)=1-\exp\left(-\frac{z^+}{B}\right) \tag{2.79}$$

The value of B is approximately 10, C is approximately 0.3 and the behavior of U'/U_* presents a maximun for $z^+ = 10-20$, indicating that the viscous effects begin to lose importance.

2.3.3 *Effect of rough beds*

To determine the effect of the roughness of channel bottom on the flow behavior, it is necessary to calculate the average size of its elements. For homogeneous roughness, *i.e.*, spheres with same diameter, the size of the roughness k_s is given by the diameter of the spheres, as can be seen in fig. 2.14.

However, in most cases, to determine the size of the roughness is not a simple task. To do this, Te Chow (1959), Massey and Ward-Smith (1998), Sturm and Tuzson (2001), developed three expressions which allow estimating the average bottom roughness as a function of the geometrical characteristics of the channel and the flow field, under uniform flow condition, as presented in eqs. 2.80-82.

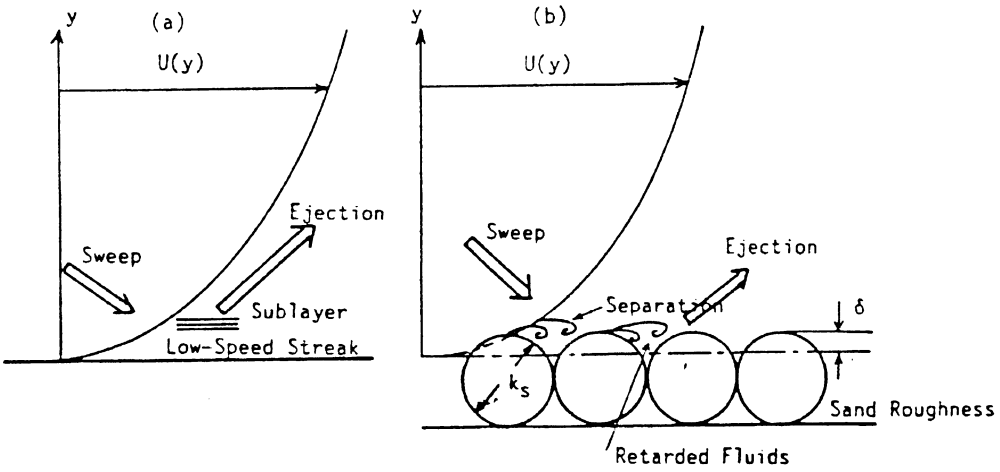

Figure 2.14 Turbulent flow over smooth and rough beds. a) Smooth bed. b) Rough bed. Nezu and Nakagawa (1993)

$$\text{Chow: } k_s = \frac{12.2R_h}{10^{\left(\frac{0.0457\,R_h^{1/6}}{n}\right)}} \tag{2.80}$$

$$\text{Massey: } k_s = \frac{14.85R_h}{10^{\left(\frac{0.0564\,R_h^{1/6}}{n}\right)}} \tag{2.81}$$

$$\text{Sturm: } k_s = \left(\frac{n}{0.0391}\right)^6 \tag{2.82}$$

where n is the Manning number $n = R_h^{2/3} S_o^{1/2} A/Q$, being R_h the hydraulic radius, S_o the channel slope, A the cross-section flow and Q the discharge.

In this case, the flow behavior can be classified depending of the dimensionless bottom roughness $k_s^+ = k_s U_* / \nu$, as:

- Hydraulically smooth bed ($k_s^+ < 5$).
- Incompletely rough bed ($5 \le k_s^+ \le 70$).
- Completely rough bed ($k_s^+ > 70$).

For completely rough bed, the flow viscous effects near to the wall disappear, since roughness elements disrupt the viscous sublayer and penetrate the logarithmic layer. On the other hand, for hydraulically smooth bed the viscous sublayer is dominant over the roughness effects. In this last case, the time-averaged velocity behavior is defined by equations (2.68 -

2.74). However, in presence of rough effects, the behavior of the time-averaged velocity is given by:

$$U^+ = \frac{1}{\kappa}\ln\left(\frac{z}{k_s}\right) + A_r + wake\left(\frac{z}{H}\right) \tag{2.83}$$

where, $A_r = {}^{1}\!/_{\kappa}\ln(k_s) + A$ can be assumed constant for completely rough bed and equal to 8.5. The wake function can be neglected for $z/H \leq 0.2$.

If $k_s^+ > 70$, eq. 2.83 fits the logarithmic behavior of the velocity for $0 < \delta < k_s$, due to the destruction of the viscous sublayer caused by the roughness penetration. According to Grass (1971), Blinco and Partheniades (1971) and Nakagawa et al. (1975), δ value is between 0.15 - 0.3 (see Nezu and Nakagawa, 1993, for more information)

The turbulent intensity in the streamwise direction is given by the following expression:

$$\frac{U'}{U_*} = K^{-1/3}\left(1 - {}^{z}\!/_{H}\right)^{1/3}\left(\kappa\, {}^{z}\!/_{H}\right)^{-1/3}\left(\frac{L_x}{H}\right)^{1/3} \tag{2.84}$$

considering that $\left(1 - {}^{z}\!/_{H}\right)^{1/3}\left(k\, {}^{z}\!/_{H}\right)^{-1/3} = {}^{\varepsilon H}\!/_{U_*^3}$ in the energy equilibrium region, $50 < z^+ < 0.6\mathrm{Re}_*$. Moreover, the value of K is an expression that relates the integral length scale L_x with its respective wave number k_0, as shown in eq. 2.85. The expression of K is simply the combination of the -5/3 power law of Kolmogorov, eq. 2.59, with the spectral function based on an extension of the Heisenberg formula in the viscous subrange, resulting in the eq. 2.85. However, in 1972 Rotta adjusted the value of K for values of $R_L = {}^{U' L_x}\!/_{\nu} \geq 200$ and assuming a value of $C = 0.5$, through the eq. 2.86.

$$K = \left(\frac{2}{\pi C}\right)^{3/2}\left(L_x k_0\right)^{5/2} \tag{2.85}$$

$$K = 0.691 + \frac{3.98}{\sqrt{R_L}} \tag{2.86}$$

Figure 2.15 shows the behavior of K for differnt values of R_L and C.

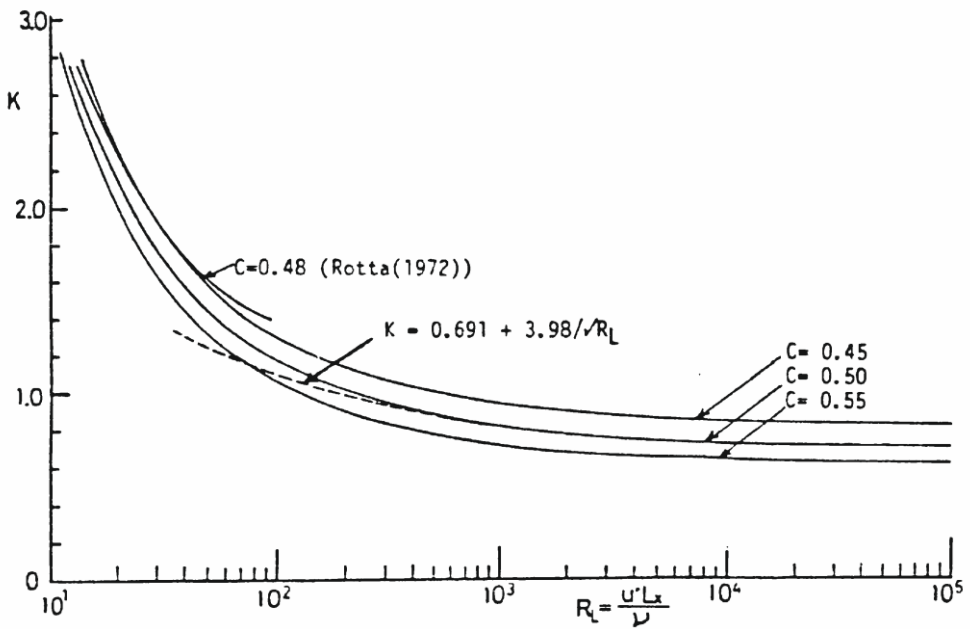

Figure 2.15 Variation of coefficient K against the Reynolds number R_L. Nezu and Nakagawa (1993)

2.3.4 *Integral length scale of eddies*

By definition, the integral length scale value L_x (or alternatively the integral time scale L_τ) is given as the integral of the autocorrelation function (eq. 2.21) or by spectral analysis (eq. 2.26). However, in this particular case, being the measurements records of the instantaneous velocity *vs*. time, the Taylor's hypothesis was adopted to transform the temporal record into a space record, so as to obtain an estimate of the streamwise and transversal turbulent terms distribution. Moreover, adopting a convection velocity, it assumes the alteration of the spectral signal distribution, especially for lower frequencies. In this sense, Nezu (1977) proposed a correlation to correct the integral length scale values from the -5/3 law of Kolmogorov, as shown in eq. 2.87.

$$\widehat{L}_x = L_x \left(\frac{\gamma_t}{\gamma_m} \right)^{3/2} \tag{2.87}$$

where, $\widehat{L}_x$ is the corrected value. The γ_t and γ_m values are obtained through the follow expression, respectively:

$$\gamma_t = C \cdot K^{2/3} \tag{2.88}$$

$$\gamma_m = \frac{S(k_w)}{L_x}(L_x k_w)^{5/3} \tag{2.89}$$

where $S(k_w) = E(k_w)/\overline{u'^2}$. Once the L_x values are corrected, they present a $^1/_2$ power behavior in the wall layer, as well as, in the intermediate layer, reaching values that appear to remain constant in the free-surface layer. Equations 2.90 and 2.91, describe such behavior.

$$\frac{\hat{L}_x}{H} = B_1\left(\frac{z}{H}\right)^{1/2} \qquad \text{for} \qquad {}^{z}/_{H} < 0.6 \tag{2.90}$$

$$\frac{\hat{L}_x}{H} = 0.77B_1 \qquad \text{for} \qquad {}^{z}/_{H} \geq 0.6 \tag{2.91}$$

where B_1 = 1 for $\mathrm{Re}_* = 1600$. According to Nezu (1977) the B_1 value increases slightly as the Reynolds number based on the friction velocity Re_* decreases, *i.e.*, B_1 = 1.1 for $\mathrm{Re}_* = 600$.

Moreover, and returning to the origin of the eq. 2.85, which comes from the combination of the spectral function based on the Heisenberg extention and eq. 2.59, it is possible to obtain an expression that relates the turbulent dissipation rate with the integral length scale, as:

$$\varepsilon = K\frac{U'^3}{L_x} \tag{2.92}$$

The importance of eq. 2.92, is that it allows us to obtain new expressions that relate the turbulent integral length scale with the Taylor's and Kolmogorov's microscales, through the following equations:

$$\frac{L_x}{\lambda} = \left(\frac{K}{15}\right)^{1/2} R_L^{1/2} \approx 0.21(R_L)^{1/2} \tag{2.93}$$

$$\frac{L_x}{\eta} = K^{1/4} R_L^{3/4} \approx 0.91(R_L)^{3/4} \tag{2.94}$$

2.3.5 *Microscale of eddies*

Combining eqs. 2.75, 2.90, 2.92, 2.93 and 2.94, semi-theoretical distributions of Taylor's and Kolmogorov's microscales are obtained as:

$$\frac{\lambda}{H} = \left(\frac{15B_1^2}{2.3K\,\mathrm{Re}_*}\right)^{1/2}\left(\frac{z}{H}\right)^{1/4}\exp\left(\frac{z}{2H}\right) \tag{2.95}$$

$$\frac{\eta}{H} = \frac{B_1}{\left(2.3K^{1/3}\,\mathrm{Re}_*\right)^{3/4}}\left(\frac{z}{H}\right)^{1/4}\exp\left(\frac{3z}{4H}\right) \tag{2.96}$$

where B_1 = 1.0 for Re_* = 1600.

Figure 2.16 shows the experimental values of the Taylor's microscale distribution, taken by Raichlen (1967) and Nezu (1977), in an open channel for high Reynolds numbers and different Froude numbers, according to eq. 2.95. Nezu and Nakagawa (1993) argueed that the deviation between experimental data and curve 2.95 is mainly due to the lower acquisition frequencies that does not allow to obtain a suitable spectral analysis for the viscous sublayer.

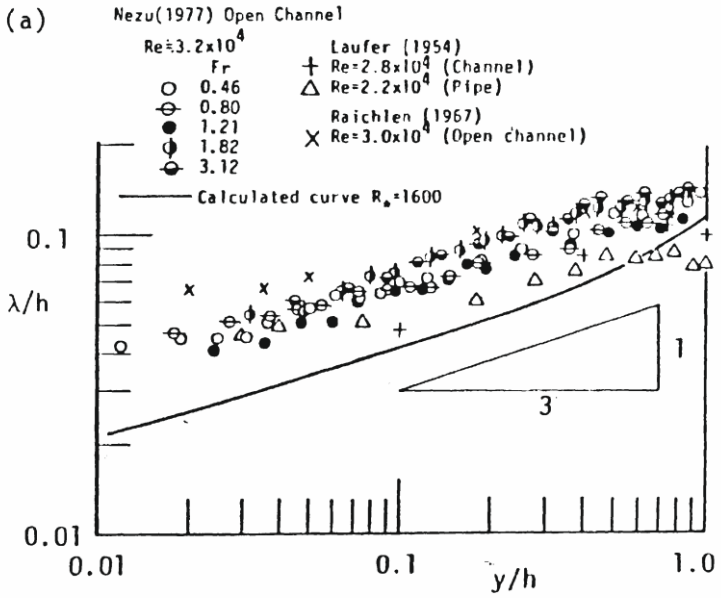

Figure 2.16 Distributions of Taylor's micro-scale λ/H varying Reynolds and Froude numbers. Nezu and Nakagawa (1993)

2.3.6 *Dissipation rate of turbulent energy*

With regard to the turbulent energy dissipation rate, a semi-theoretical expression is obtained from equations 2.75, 2.90 and 2.92, expressed as:

$$\frac{\varepsilon H}{U_*^3} = \left(\frac{12.2K}{B_1}\right)\cdot\left(\frac{z}{H}\right)^{-1/2}\exp\left(\frac{-3z}{H}\right) \tag{2.97}$$

For Reynolds numbers between 10^4 - 10^5, the first coefficient of equation 2.97 is equal to $\frac{12.2K}{B_1} = 9.8$, approximately.

The expressions presented to fit the integral lenth scale, Taylor's and Kolmogorov's microscales and the turbulent energy dissipation rate behavior, are expressions that have been developed through experimental settings for fully developed 2D flows. In this sense, it is important to note that, these expressions will be taken in this research as a reference to compare the turbulent structure observed in a compound channel under different flow conditions, as well as, to determine to which extent these expressions can be used to describe the behavior of different turbulent parameters in compound channel flows.

2.3.7 *Shear or Friction Velocity*

The friction velocity is one of the most important parameters to describe the velocity field and turbulent field of the flow. By definition, the shear velocity is given by the square root of the fluid shear stress in the wall over fluid density, *i.e.*, $U_* = \left(\tau_b / \rho\right)^{1/2}$. However, to obtain a value of the friction velocity, different methods can be used, depending on the required accuracy and the measurement equipment available.

The most popular method used to calculate the shear velocity is the geometrical method. This method can be used only if the flow is statistically uniform and developed, *i.e.*, the ascendant/descendant flows and the streamwise variation of the flow can be neglected. In this case, the friction velocity is given by the following expression:

$$U_* = \sqrt{gR_h S_o} \tag{2.98}$$

The second method is based on the calculation of the friction velocity directly from eq. 2.70 and using the measurements of time-averaged velocity profiles. For this purpose, a linear fit of the velocity measurements in the range $30^+ < z^+ < 0.2\mathrm{Re}_*$ is performed, obtaining the integration constant A value and the U_* value.

A third method requires to calculate U_* from the Reynolds stresses distribution $\overline{u'w'}$, where u' represents the streamwise velocity fluctuations and w' the velocity fluctuations normal to the channel bottom.

On the other hand, if the flow has a viscous sub-layer, the friction velocity can be determined taking measurements of the velocity field in this area and using eq. 2.73. However, in most cases, the thickness of the viscous sub-layer is not sufficiently large to be measured with some current available instruments or measurement techniques or to take a sufficient number of measurements to allow us to obtain an acceptable fit. Finally, the U_* can also be measured directly through a Preston tube.

As mentioned above, each of these methods present an accuracy that will depend on the assumed simplifications or on the measurement technique used to acquire the associated data.

The first method, eq. 2.98, allows us to obtain a total value of U_* in a fairly simple way. However, sometimes, this value is not the most appropriate to characterize some of the turbulent terms.

Moreover, and according to Nezu and Nakagawa (1993), measurements taken by Nezu (1977) with a hot-film showed that the U_* value calculated by the first three methods differ in up to 30% among themselves. Whereas, measurements taken by Nezu and Rodi (1986) showed that these same methods differ in up to 5% among themselves using LDA measurements.

3

Chapter 3

Experimental Setup and Measuring

3.1 Experimental Setup

The experiments were carried out in an asymmetric compound flume channel located at the Hydraulic Laboratory of University of Beira Interior, Portugal, built over a concrete structure. The flume channel water feeding was made through a centrifugal pump Pentax model CM65-125B with a nominal power of 7.5 hp. Since the hydraulic system was limited by the size of the reservoir, 3.5 m^3 with a water depth of 0.7 m, the pump suction was connected through a manifold to diminish the likelihood of cavitation, as shown in fig. 3.1. The flume channel has an in-built set of glass windows distributed longitudinally and located on the side wall, through which the LDV measurements were performed.

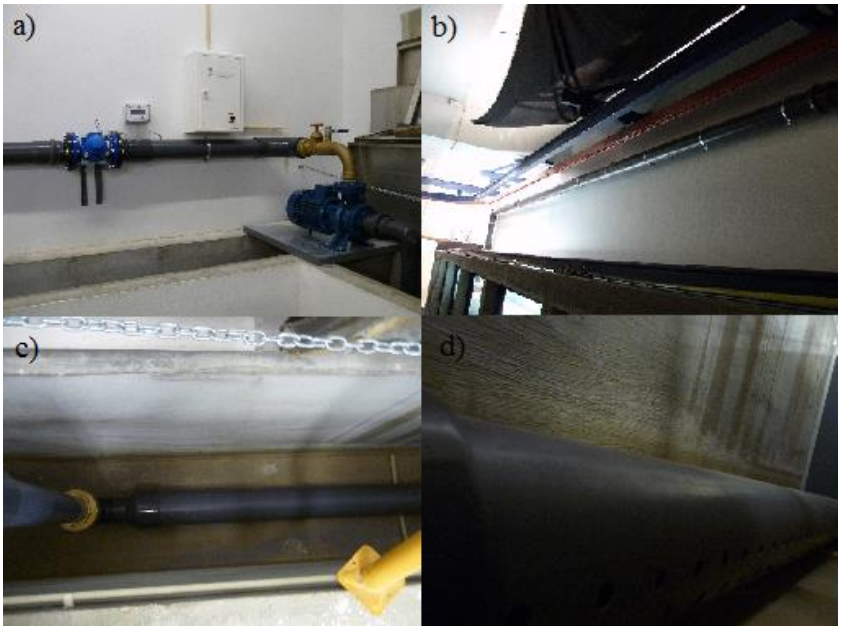

Figure 3.1 Hydraulic system. a) Pump and electromagnetic flowmeter. b) Location of the pumping system.c) Pump suction. d) Manifold.

To determine the flow discharge, an electromagnetic flowmeter was installed at the pump outlet. To reduce the lateral transference of momentum at the inlet of the flume channel between the main channel and the floodplain, a set of 1"-diameter tubes was located in this section with 0.3 m length, as well as a plate dividing both sub-regions (main channel and floodplain), as shown fig. 3.2. Thus, the uniform flow is attained in a smaller streamwise distance from the entrance (Bousmar et al., 2005; Bousmar and Zech, 1999; Uijttewaal, 2005). Further, to promote a fully developed flow, gravel with $d_{50} \approx 0.5$ cm was placed along the first 0.5 m of the main channel inlet, as shown in fig. 3.2. The entrance of the floodplain sub-channel was left without artificial roughness since its low water depth required a smaller distance to promote a fully developed flow. On the other hand, to control the water depth, a single gate, located in the final section of the flume, was used. To establish the uniform flow, measurements of the water

depth with a point gauge were made each 0.5 m length in inflow-outflow direction on the middle of the main channel and on the middle of the floodplain.

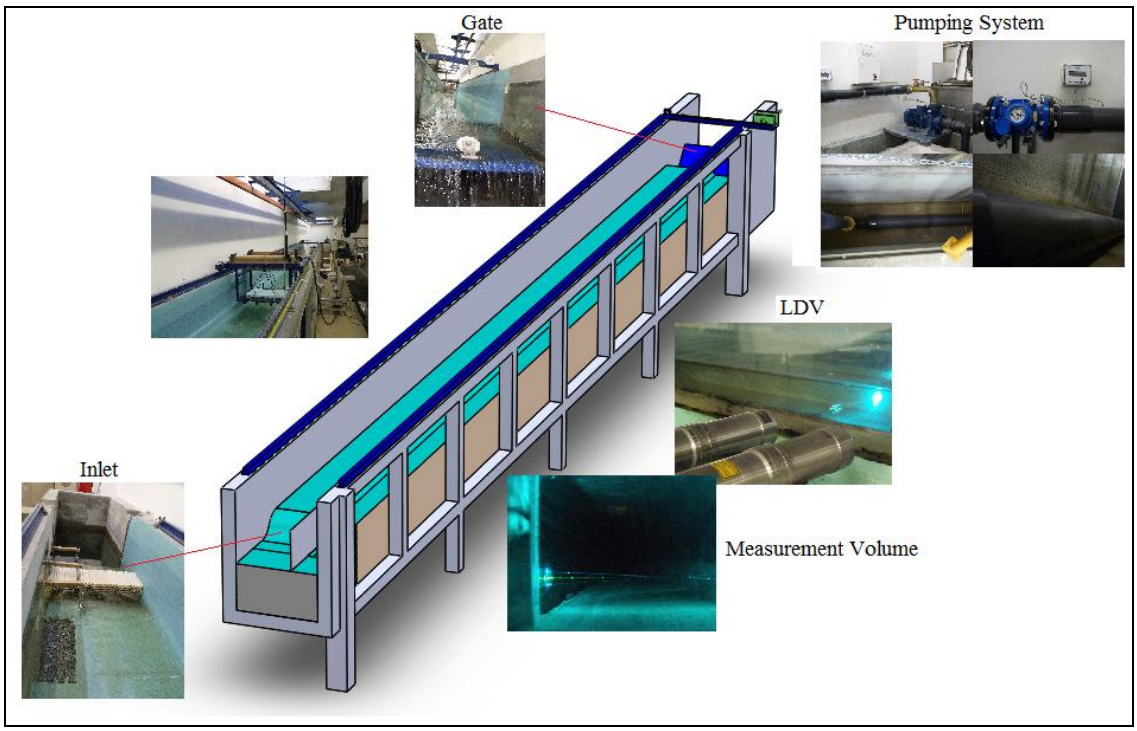

Figure 3.2 Components of the Experimental Rig.

The flume channel is 11.60 ± 0.001 m long and 0.79 ± 0.002 m wide. To determine the total width of the channel measurements were taken each 0.5 m, for both main channel and floodplain. In the case of the flume slope, it was determined through a topographic laser level device. For that, 14 transversal measurement points (11 points on the floodplain and 5 points on the main channel) were used each 0.5 m. Table 3.1 presents the mean geometrical characteristics of the flume and fig. 3.3 shows a sketch of the asymmetric compound flume.

3.1.1 *Roughness Coefficient*

In compound channel flows, the *Manning/Strickler* equation, eq. 3.1, can be used in two different manners to determine the characteristic roughness coefficient of the channel k_s, where $k_s = 1/n$ and n is the Manning coefficient. The first avenue is the so called Single Channel Method (SCM) which consists in considering the hydraulic radius and area of the total cross-section in order to obtain the characteristic roughness coefficient of the channel. The second way, known as Divide Channel Method (DCM), consist in calculating the hydraulic radius and area of each sub-division of the cross-section, *i.e.*, the main channel and the floodplain,

separately, obtaining one roughness coefficient for each sub-division. However, the discharge through each sub-division must be known.

Table 3.1 Main geometry of the channel.

Channel Length L (m)	11.600 ± 0.001
Channel Width B (m)	0.790 ± 0.002
Main Channel Width B_{MC} (m)	0.205 ± 0.002
Floodplain Width B_{FP} (m)	0.531 ± 0.001
Interface Width B_I (m)	0.054 ± 0.002
Interface/bankfull Depth h (m)	0.051 ± 0.001
Main Channel Slope S_{MC} (%)	-0.099 ± 0.004
Floodplain Slope S_{FP} (%)	-0.091 ± 0.003
Channel Slope S_o (%)	-0.095 ± 0.003

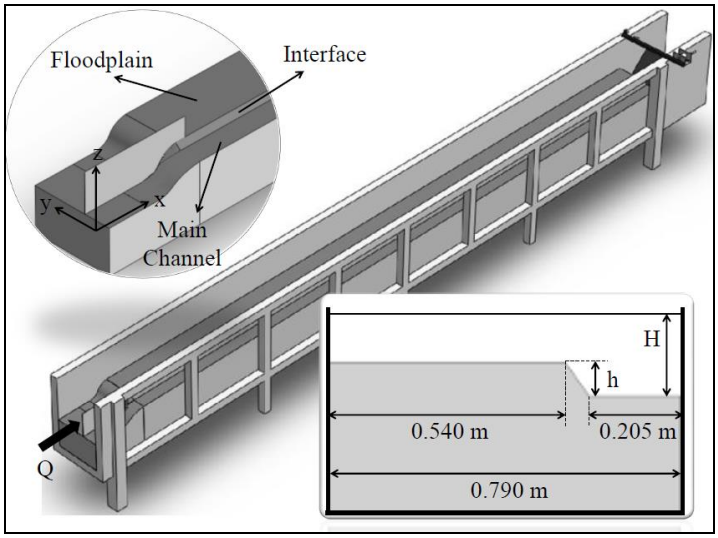

Figure 3.3 Channel geometry.

$$Q = k_s R_h^{2/3} S_o^{1/2} A \tag{3.1}$$

In this case, since the channel flow is established through a single pump and no devices were installed to obtain the discharge of each sub-division, the roughness evaluation was made in a single cross-section configuration (i.e. using just the main channel). Therefore, the water depth cannot exceed the interface/bankfull depth h. The maximum flow discharge was set to 2.5 L/s, obtaining a water depth of 0.0391 m. Table 3.2 shows the experimental conditions in quasi-uniform flow conditions settled to determine the roughness of the channel, where Q is the inlet

flow, H_{MC} the water depth in the middle of the main channel, A the area of the flow cross-section, R_h the hydraulic radius, S_o the free-surface slope and Re the Reynolds number. Table 3.3 shows the k_s and the Manning coefficient n values, as well the mean roughness of the channel calculated from Chow, Massey and Sturm equations, eq. 2.79, 2.80 and 2.81, respectively.

Table 3.2 Experimental conditions to determine the channel roughness.

Q (m^3/s)	1.2×10^{-3}	1.4×10^{-3}	1.8×10^{-3}	2.4×10^{-3}
H_{MC} (m)	0.0235	0.0285	0.0318	0.0391
A (m^2)	0.0051	0.0062	0.0070	0.0087
R_h (m)	0.0195	0.0228	0.0249	0.0292
S_o	1.035×10^{-3}	0.968×10^{-3}	0.982×10^{-3}	0.968×10^{-3}
Re	5.44×10^{3}	6.50×10^{3}	8.29×10^{3}	10.83×10^{3}

Table 3.3 Channel roughness.

k_s	95.83
n	0.0104
Chow (mm)	1.33
Massey (mm)	0.46
Sturm (mm)	0.37

The values presented in Table 3.3, correspond to the roughness of the walls measured only in the main channel. However, and limited by experimental resources, these values will be assumed similarly as the roughness of the bottom of the floodplain. On the other hand, and considering the physical bottom roughness of the channel, Chow's equation shows a higher value, not corresponding to the reality, while Massey's and Sturm's equations, present more credible values.

3.2 Measuring Technique: Laser Doppler Velocimeter

Laser Doppler Velocimeter is a technique based on the Doppler effect which measures the instantaneous velocity of a fluid in a given control volume during a period of time long enough to capture statistically valid mean values of the velocity field and its corresponding

fluctuating components. In this particular case, this technique is being used by a Coherent Laser Doppler Velocimeter of the Innova 70C Argon series with a maximum output power of 2W, which allows us to obtain 2D measurements of the velocity field through one probe.

The process to obtain the instantaneous fluid velocity field with a LDV system, involves measuring the velocity of small particles passing through a control volume formed for two light beams emitted by the system (so small that it can be assumed that the velocity of the particle is equal to the fluid velocity). This control volume is established for bright fringes and fringes not so bright, separated by a known distance δ_f, as shown in fig. 3.4. When a particle passes through the control volume, it gives rise to a succession of pulses or light reflections, which are captured by a photomultiplier tube. The sequence of pulses is known as Doppler frequency f_D. To calculate the particle velocity, eq. 3.2 is used:

$$u = \delta_f \cdot f_D \tag{3.2}$$

However, the fringe spacing depends of the wavelength of light (λ) and the angle formed between both light beams (ϕ), as shown by eq. 3.3. If the input beams from the probe do not undergo a refraction, due to traveling through medium changes, *e.g.*, air-glass-water or another combination of continuous matter, the control volume will not capture changes from the theoretical values (fringe spacing, number of fringes, control volume dimensions, etc.). However, if the input beams travel through different media, as in this investigation, the new values of the geometric control volume must be calculated.

$$\delta_f = \frac{\lambda}{2\sin(\phi)} \tag{3.3}$$

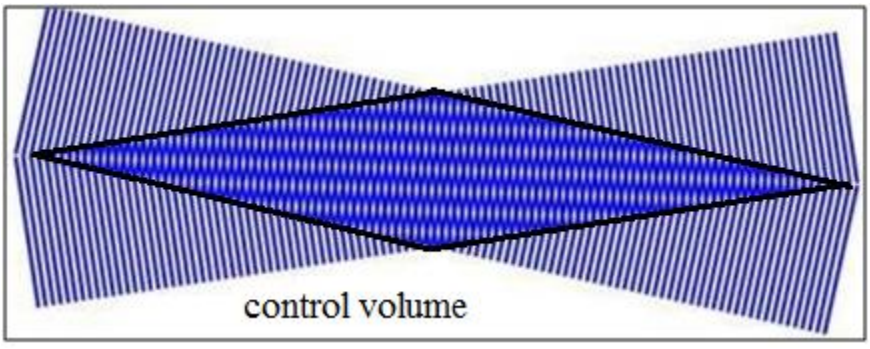

Figure 3.4 Control volume of measurement.

Assuming that both beams have the same frequency, the bright fringes remain stationary. In this case, the frequency emitted by a particle traveling immersed in the flow stream at a velocity V_1, is f_1. Now, if we visualize a particle traveling at the same velocity V_1 but in the opposite direction to the main flow, the particle also emits a frequency f_1. Obviously, the

software is able to calculate the velocity of the particle, however, it cannot predict the direction of the particle.

To solve this problem, the system adds an additional frequency to one of the beams. With this, the beams observed in fig. 3.4 does not remain static, but instead moves from the beam which was added with an additional frequency towards the beam that has not been modified, known as unshifted beam. This phenomenon is achieved through a Bragg Cell, also known as Acoustic-Optic Modulator, AOM.

Thus, when the particle moves from the unshifted to the shifted beam, the "relative" frequency of the particle will be the frequency added in the shifted beam (which in this case is 40 MHz) over the Doppler frequency, *i.e.* equal to the particle velocity divided by the distance between the fringes generated in the control volume. Otherwise, when the particle travels from the shifted beam towards the unshifted beam, the "relative" frequency of the particle is 40 MHz minus the Doppler frequency, therefore resulting evident what is the particle direction.

The measurements from the probe are sent to the Photodetector Module (PDM), which through a high pass filter, allows removing the pedestal and low frequency signal. Once this procedure is performed, the signal follows to the flow size analyzer (FSA) where its frequency is mixed with another frequency between 0-40 MHz, and filtered by a band-pass filter to eliminate the noise and other unwanted frequencies. Finally, the signal is processed by the FSA and sent to the computer for further analysis. Figure 3.5 shows a diagram of each of the LDV system components.

Table 3.4 shows the relevant optics characteristics of the Laser Doppler Velocimeter used in this investigation, where d_m and l_m represent the measurement control volume diameter and length, respectively.

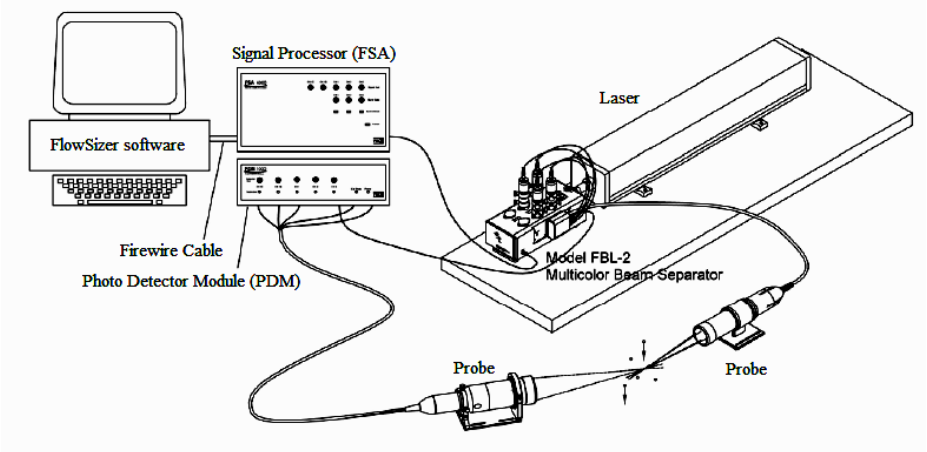

Figure 3.5 Components of the LDV system.

Table 3.4 Main characteristics of the LDV system.

	Channel 1	Channel 2
Wavelength (nm)	514.5	488
Focal Length (mm)	363	363
Beam Separation (mm)	50	50
Brag Cell Freq. (MHz)	40	40
Theo. Fringe Spacing (μm)	3.7441	3.5513
Theo. Nº of Fringes	24	24
Theo. Angle ϕ (rad)	3.94	3.94
Theo. d_m (mm)	0.0899	0.0853
Theo. l_m (mm)	1.3060	1.2388
Exp. Fringe Spacing (μm)	4.9422	4.6877
Exp. Nº of Fringes	18	18
Exp. Angle ϕ (rad)	2.98	2.98
Exp. d_m (mm)	0.0898	0.0852
Exp. l_m (mm)	1.7239	1.6352

3.2.1 *Probe Calibration*

This kind of measuring technique does not need to be calibrated to obtain the correct particle velocity crossing the control volume, contrary to other techniques such as the constant temperature anemometer technique (CTA). However, in order to obtain a greater number of captured particles by the Photodetector Module, the intensity of the flashes reflected from the particles must reach a minimum intensity to be processed. Thus, the higher the intensity of the output beams of the probes, the greater the intensity of the flashes reflected from the particles. To increase the intensity of the output beams of the probes, the power supplied to the laser must be increased accordingly. However, to ensure that the laser beam, that enters to the Multi Beam Separator, is transmitted correctly to the sensors through the optical fiber, the coupler should be aligned to maximize the output power. Figure 3.6 shows a schematic of the mirrors located within the coupler, and their role in the alignment process.

Considering that the alignment of the couplers is a methodological process that has great influence on the quality of the measurements, and being this a step whose description is not easily found in the literature, the procedure used in this research to align the couplers is explained in the following lines:

1. Start by turning the focus knob or screw all the way down (clockwise), and adjust both sets of *x-y* translation knobs so that they are near the center of their range of motion.
2. Open the shutter on the bottom of the corresponding working coupler unit. Close all others.
3. Begin adjusting the focus upward (counter clockwise) until some light is seen out of the probe.
4. If no light is seen, return the focus-adjust knob to the bottom of its range (clockwise). Turn the coarse *x-y* adjustment knobs 1 or 2 turns in either direction, and repeat the process.
5. When even a small amount of light is seen out of the probe, this is a good signal. From now on, use an iterative technique adjusting the *x-y* and focus until the intensity of the output spot is maximized.
6. Adjust the focus knob $^1/_2$ turn counter-clockwise (the spot may initially become weaker with a focus adjustment).
7. Adjust the *x*-translation (fine and coarse) until the output is at its brightest point.
8. Adjust the *y*-translation (fine and coarse) until the output is at its brightest point.
9. Repeat steps 6, 7 and 8 until the output is no longer getting brighter.

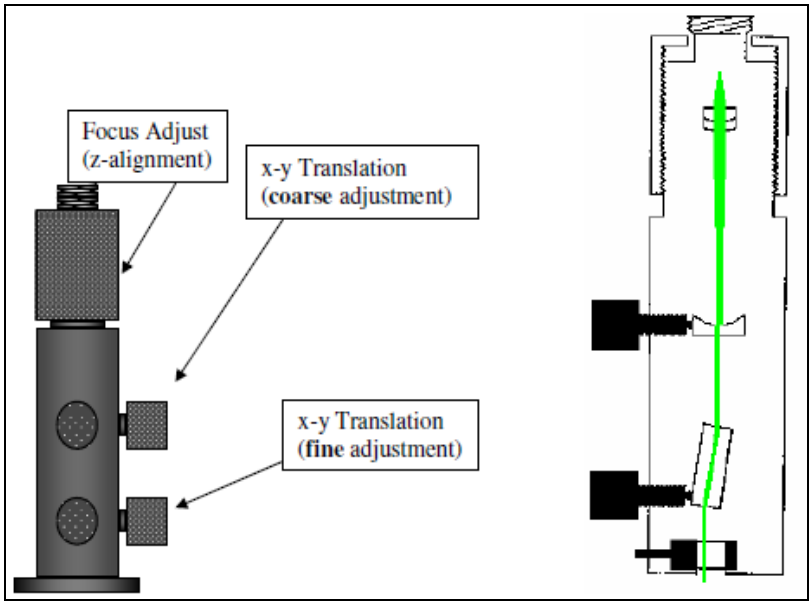

Figure 3.6 Scheme of Couplers

3.2.2 *FlowSizerTM Software*

The use of the Laser Doppler Velocimeter measurement technique requires the adjustment of some parameters to perform measurements with high quality. All these parameters, involved in this investigation, are controlled through the *FlowSizer*^{TM} software, such as the different frequency filters (photodetector module - PDM, downmixing, band-pass filters and SNR), burst threshold, measurement time, etc. Each of these elements is explained as follows:

PMT Voltage: the photodetector module (PDM) is the equipment responsible to convert the reflected light from particles seeding in the flow into electrical signals. This reflected light is detected from a photomultiplier tube, PMT, which presents a voltage between 0-1000 V, allowing an amplification of the signal, *i.e*. increasing the voltage and, consequently, increasing the number of particles detected through the measurement control volume. However, all the electrical signals and noise increase as well. In most applications, the optimum voltage is between 350 and 600 V. Voltages higher than 600 V do not necessarily imply an increase of the number of particles detected, but imply an increase of the noise signal, *i.e*. it is necessary to adjust the PMT Voltage until the system shows a higher quantity of particles detected. The values used in this investigation were between 450 and 600 V.

High-pass Filter: once the light intensity distribution emitted from the beams presents a Gaussian behavior, the light scattering from the particles crossing the control volume will result

in a light scattering pattern similar to the one shown in fig. 3.7. However, the lower frequencies generated due to the Gaussian behavior, also called pedestal, can be removed using one of two default pedestal frequencies: 5 MHz is used when a high velocity reversing flow exists, or a 20 MHz filter is used for most applications and for very short transit time signals. The reader should remember that the frequencies for reversing flows will be lower than 40 MHz, while the frequencies for normal or streamwise flows will be higher than 40 MHz. In this case, a 20 MHz frequency filter was used.

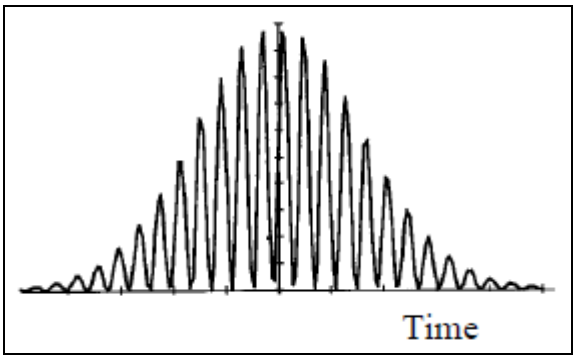

Figure 3.7 Light scattering pattern - Gaussian distribution.

Downmixing: once the pedestal frequency is removed, the signal is sent to the flow size analyzer (FSA), where the signal is captured by the PDM and afterwards processed and transmitted to the computer. The first process developed by the FSA is the analysis of the existing recirculating flows or the velocities close to zero. For this, the downmixing process subtracts the downmix frequency from the input signal. Downmix frequency varies between 0 – 40 MHz. If a downmix frequency of 40MHz, is selected, all the Bragg Cell Shift will be eliminated, so only the Doppler frequency is left. On the other hand, entering 39 MHz means that 1 MHz is still added onto the Doppler frequency (39 MHz – 40 MHz, this last is the Bragg Cell Shift frequency), allowing 1 MHz of reversal flows. In terms of velocity, if the fringe spacing δ_f is 3.74 µm, the velocity of the allowed reversal flows is 3.74 m/s. In this case, the experimental fringe spacing of both channels are 4.94 µm and 4.69 µm, and the downmix frequency of 39.5 MHz and 39.2 MHz, respectively, allowing reversal velocities until 2.47 m/s and 3.75 m/s, respectively. If 0MHz is entered, then the downmixing process is ignored.

Band Pass Filter: the main goal of the band pass filter is to eliminate the noise and the higher frequencies left in the downmixing process. For this purpose, the band pass filter has 20 default band filters choices. Knowing the frequency range of the flow in study (given by the particle velocity divided by the fringe spacing), we need to choose the band pass filter that best fits. However, the downmixing frequency left in the previous step must be added to the flow frequency, *i.e.*, if the expected flow velocity is between -0.1 m/s and 0.8 m/s, which represents -

0.02 MHz and 0.16 MHz (using 4.69 µm as fringe spacing), and the downmixing frequency left was 0.8 MHz, the expected frequencies are between 0.78 MHz and 0.96 MHz, which represents the frequencies for -0.1 m/s and 0.8 m/s, respectively. In this case, the band pass filter that best fits is 0.1 - 1 MHz. Figure 3.8 shows a cut-off frequency histogram for a bad choice of the band pass filter (fig. 3.8a) and a good frequency histogram (fig. 3.8b).

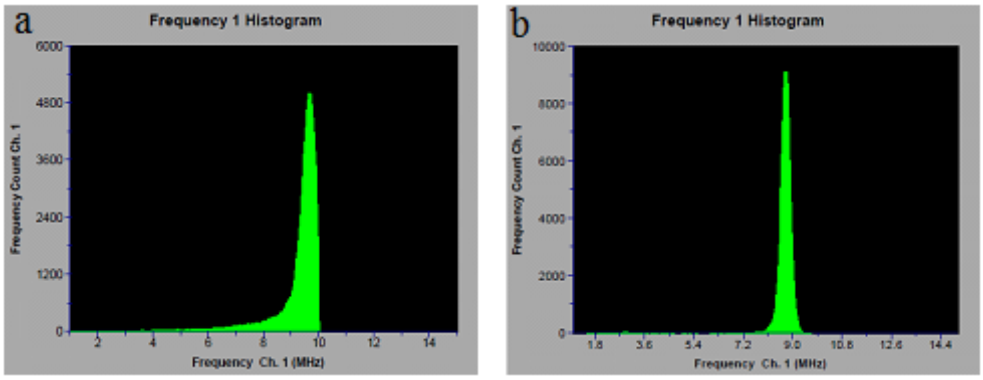

Figure 3.8 Frequency histogram a) Bad choice of the band pass filter b) Good choice of the band pass filter.

Burst Threshold: it is another very important variable to obtain good quality LDV data. When the particles cross the measurement control volume, they scatter some amount of light with a given electrical signal amplitude. Larger particles scatter more light and thus, they will have higher signal amplitude. Typical *Burst Threshold* values will range from 30 mV to 300 mV. For applications with small particles (< 10 µm) the optimum voltage will probably be 30 mV. On the other hand, with larger particles an optimized value might be 100 mV or 200 mV. In situations with high levels of background light, such as near-wall measurements, Burst Threshold over 500 mV may be needed to achieve the best data rate. In this investigation the particles seeded into the water were aluminum oxide powder with a diameter of less than 10 µm, so the Burst Threshold value used was 30 mV.

SNR: the signal-to-noise ratio is the second requirement necessary to process a particle (the first requirement is the Burst Threshold). Through the SNR box, the operator can define the quality of the signal to be processed. Entering "High" means that the best signal quality will be processed, while entering "Very Low" means that the signals processed will have a wide noise levels. However, choosing "Very Low" increases the number of processed particles. In this investigation, the signal-to-noise ratio was selected as "Medium", since it ensured a good quality of signals without compromising too much the amount of particles to be detected.

Table 3.5 shows the most important parameters used in this investigation for both channels.

Table 3.5 Adjustment of the main parameters of the LDV system.

	Channel 1	Channel 2
PMT Voltage	600 V	600 V
High-Pass Filter	20 MHz	20 MHz
Downmixing	39.5 MHz	39.2 MHz
Band-Pass Filter	0.1 - 1 MHz	0.1 - 1 MHz
Burst Threshold	30 mV	30 mV
SNR	Medium	Medium
Measuring Time	210 s	210 s

3.3 Seeding Particles Characteristics used for LDV System

When a LDV system is used to characterize the velocity field, particles must be seeded into the flow. The quality of the measurements not only depends on the adjustment of the above parameters, but also on the characteristics of the particles seeded into the flow. Particles with a high reflection capacity can be detected easily by the LDV, increasing the frequency of measured particles. Statistically, frequencies of 30 Hz are suitable to investigate the behavior of the mean properties or mean velocities of the flow. However, when a detailed analysis is required, as for example a spectrum analysis, higher frequencies are required.

Four kind of seeding particles were studied: pepper powder, talcum powder, titanium dioxide powder and aluminum oxide powder. In a first phase, the pepper powder and talcum powder were compared in order to determine which one presented better results. Figure 3.9 shows the distribution for both kind of seeding particles. In the case of the pepper powder, the mean particle diameter is 46.85 μm, while the mean particle diameter of the talcum powder is 14.16 μm.

Once the mean particle diameter of both particles was determined, the PMT voltage and the Burst Threshold parameters were adjusted in order to increase the data acquisition rate. The talcum powder presented better results than the pepper powder. fig. 3.10 shows the behavior of the Data Rate *vs*. PMT voltage and the Data Rate *vs*. Burst Threshold for three different water depth conditions. The higher values of Data Rate as a function of the PMT voltage are obtained for 575 V and 625 V, for channel 1 and 2, respectively. Only for z/H = 0.90, the higher values

of Data Rate are achieved for 675 V in both channels. However, this voltage increases the electrical noise of the signal, as mentioned above, and is not recommended.

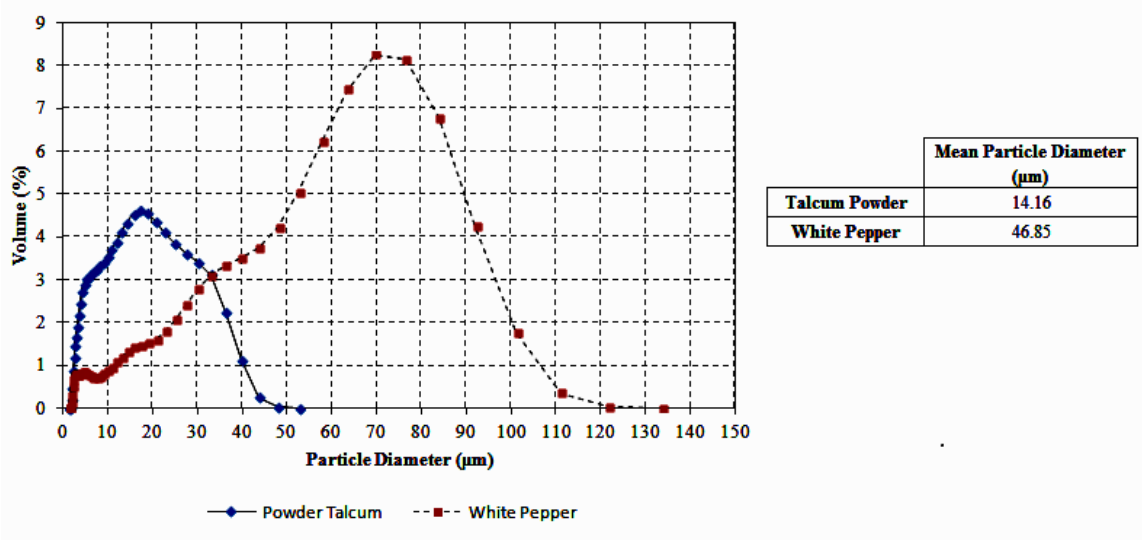

	Mean Particle Diameter (µm)
Talcum Powder	14.16
White Pepper	46.85

Figure 3.9 Distribution of the particles diameter.

In the case of the Burst Threshold, fig. 3.10 shows that the LDV system detects more talcum powder particles if the threshold is adjusted between 30 - 35 mV for all cases. This values correspond very well with the information found in the technical manual of the LDV, which recommends that for applications with small particles (< 10 µm) the optimum voltage would likely be 30 mV.

Although talcum powder presents better results than white pepper, the attained data rate was not sufficient to estimate the turbulent parameters correctly. Therefore, other types of particles were tested as titanium dioxide (particle size < 40 µm) and aluminum oxide (particle size < 10 µm) and afterwards, a similar study of the behavior of the particles was performed. The results showed that titanium oxide powder has a similar behavior than talcum powder. However, aluminum oxide powder presents data rates 5 times higher, approximately.

Figure 3.11 shows a cross-section of the flume-channel where data rate distribution can be observed using aluminum oxide powder as seeding particles. One of the most difficult issues associated to the use of the LDV technique is to ensure a statistically homogeneous particles distribution into the flow over time. In order to prevent the decantation process of particles, the measurements were stopped every 3-4 hours and the bottom of the flume-channel was swept to remove all particles before continuing the experiments. When using aluminum oxide, it was noticed that some particles remained attached to the pipe system, accounting for 50 gr. approximately. Therefore, that amount of extra aluminum oxide particles was added during all

the experimental campaign. The initial dosage of particles placed in the water was 250 gr. On the other hand, due the low velocities obtained close to the side walls, the data rate acquisition decreased in these regions.

The higher data rates obtained using aluminum oxide powder demonstrated that it is the best quality of seeding particles when compared to the other three types of particles studied. Additionally, it was also considered glass spheres as seeding particles since it was expected to obtain even higher acquisition data rates than for aluminum oxide, however, it resulted to be very expensive and not economically feasible, since it would have required to install a very expensive system to recover the particles after each measurement run. The variables used in the *FlowSizer*^{TM} software were presented in tab. 3.5.

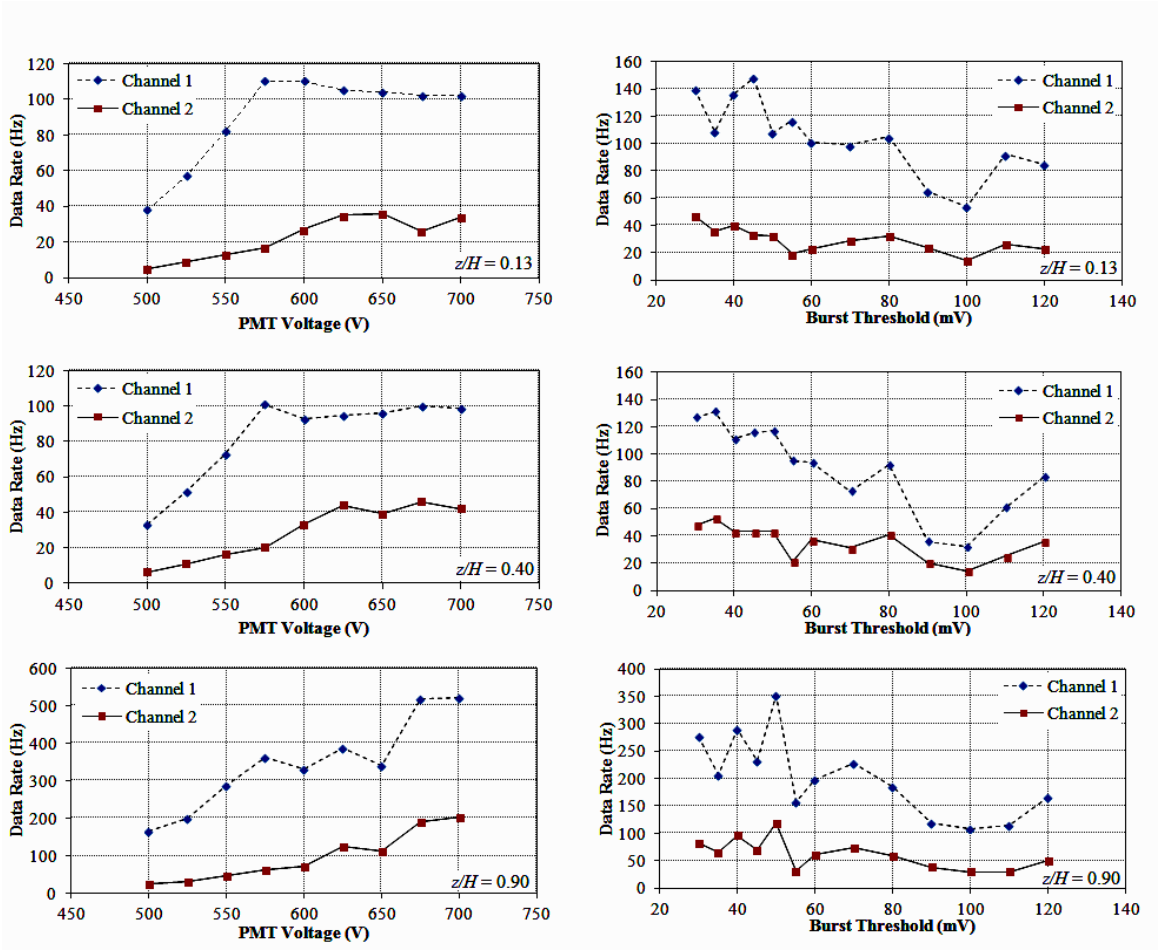

Figure 3.10 Adjustment of the PMT Voltage and Burst Threshold.

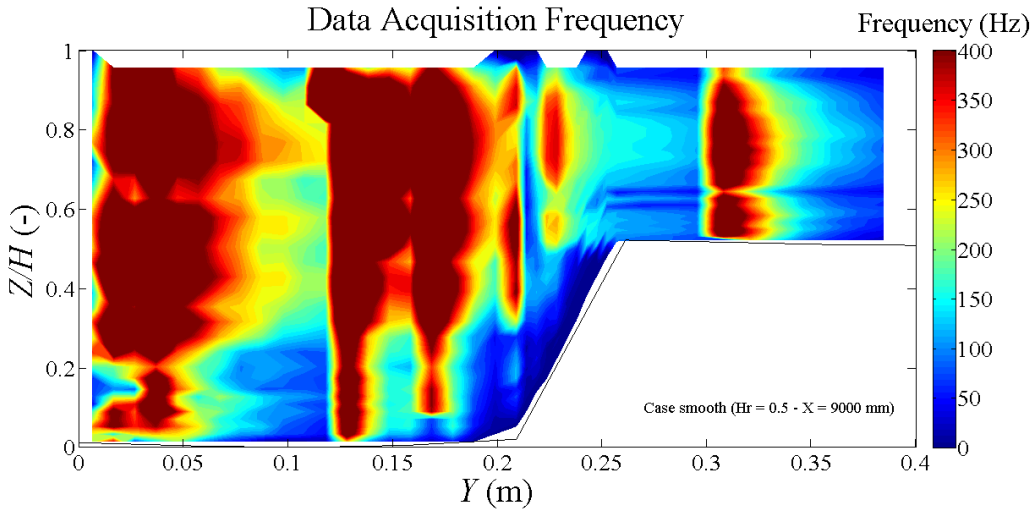

Figure 3.11 Distribution of the frequency data on the cross-section at 9.0 m.

3.4 Experimental Campaign

In this investigation, the main goal is to characterize the turbulent structures in compound channel flows under two very special conditions: (a) without roughness or smooth; and (b) with roughness. Additionally, it was also a major objective to analyze how the turbulent structures are affected when operating under different inlet water depths. On this regards, three different relative water depths for the smooth case were tested: (a) Hr = 0.50; (b) Hr = 0.31; and (c) Hr = 0.23, where $Hr = (H - h)/H$ is the relative water depth, H is the water depth and h is the interface/bankfull depth. The roughness effect was evaluated by using vertical cylinders placed at the interface with three different spacing between roughness elements: (a), S_{d1} = 1 m; (b) S_{d2} = 0.2 m; and (c) S_{d3} = 0.04 m, and two relative water depth for each spacing:,(a) Hr = 0.51 and Hr = 0.31 for S_{d1} = 1 m; (b) Hr = 0.45 and Hr = 0.28 for S_{d2} = 0.2 m; and (c) Hr = 0.34 and Hr = 0.25 for S_{d3} = 0.04 m.

The most common spacing between trees in the environment is in the range of 4 < S/D < 20 (Esfahani and Keshavarzi, 2010; Notes, 1998; Shiono, Ishigaki, et al., 2009; Terrier, 2010), being S the spacing between trees and D the mean diameter of the tree. In order to evaluated the effect of the spacing between trees on the turbulence structures, the rough elements consist of aluminum cylindrical rods with 10.0 mm of diameter and 100.0 mm length placed in vertical position. In this case, the S/D values to study are S/D = 100, S/D = 20 and S/D = 4.

As mentioned in the previous paragraph, all measurements were performed under quasi-uniform flow condition. For smooth bottom conditions, the quasi-uniform flow was established measuring the water depth in the middle of the main channel and in the middle of the floodplain each 0.5 m, starting at 1.0 m from the inlet until 10.0 m from the entrance. To determine the

free-surface slope, each measure of the water depth was added to the bottom elevation corresponding at this exact measurement point. The bottom elevation or the bottom slope was determined through a topographic laser level device as mentioned at the beginning of this section. The uniform flow was established when the difference between the free-surface slope on each region (middle of the main channel and middle of the floodplain) and the bottom slope was less than ±0.1 mm/m, as shown in fig.3.12. The water depth was controlled with a gate located in the final section of the flume. Table 3.6 shows the mean characteristics for each flow discharge.

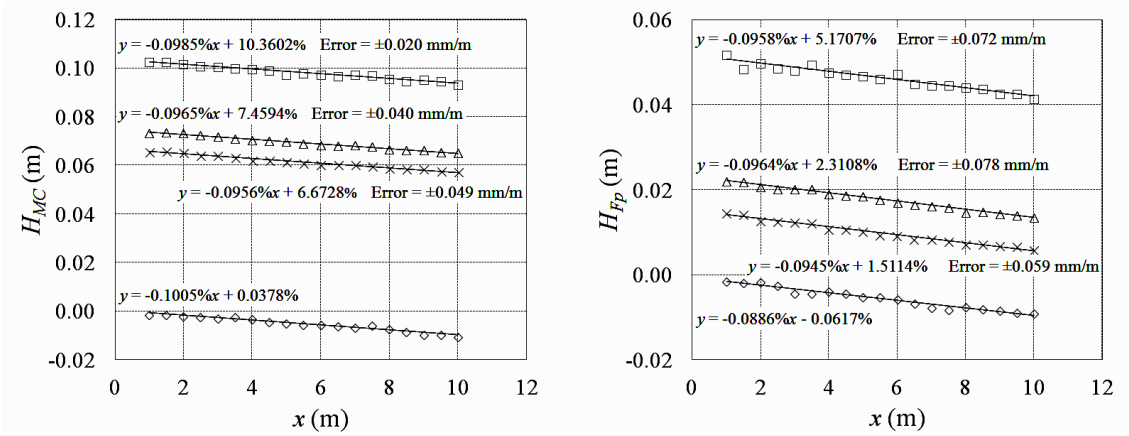

Figure 3.12 Free-surface slope for the smooth case with *Hr* = 0.50, *Hr* = 0.31 and *Hr* = 0.23 a) Free-surface slope in the Main Channel b) Free-surface slope in the Floodplain.

Moreover, the mean water depth measured in the middle of the main channel was compared with the Single Channel Method (SCM) and with the Divided Channel Method (DCM) in order to verify that this value lied between the estimations from both methods (Bousmar et al., 2005). For low inlet flow rates, the Single Channel Method over-estimates the water depth expected to be attained for the quasi-uniform flow, while the Divided Channel Method under-estimates it. However, increasing the inlet flow rate the difference between both methods decreases, becoming more accurate the calculation by either method. Figure 3.13 shows the mean water depth for the three conditions considered above. For *Hr* = 0.31 and *Hr* = 0.23, the experimental mean water depth lies between both methods, as expected. Nevertheless, for *Hr* = 0.50 the experimental mean water depth is 0.90% less than the value calculated from the Divided Channel Method. However, considering the error obtained, ±0.0006 m, the value of the mean water depth in fact lies between both the estimation by both methods, SCM and DCM, respectively.

Table 3.6 Mean experimental conditions for smooth case.

	Hr = 0.50		*Hr* = 0.31		*Hr* = 0.23	
	Main Channel	Floodplain	Main Channel	Floodplain	Main Channel	Floodplain
Discharge (m^3/h)	83.38 ± 0.29		35.50 ± 0.09		24.59 ± 0.07	
Mean water depth (m)	0.1033 ± 0.0006	0.0519 ± 0.0007	0.0744 ± 0.0005	0.0233 ± 0.0006	0.0666 ± 0.0007	0.0154 ± 0.0006
Bottom slope (%)	-0.1005	-0.0886	-0.1005	-0.0886	-0.1005	-0.0886
Free-surface slope (%)	-0.0985	-0.0958	-0.0965	-0.0964	-0.0956	-0.0945
Slopes difference (mm/m)	0.020	0.072	0.040	0.078	0.049	0.059

Additionally, vertical profiles in the middle of the main channel, lower interface, upper interface and in the middle of the floodplain, along the whole channel, were measured in order to verify the development of the boundary layer. These measurements were performed for the three relative water depths at distances 4.5 m, 6.0 m, 7.5 m and 9.0 m from the inlet of the channel. In all cases, the difference of the streamwise depth-averaged velocity between 7.5 m and 9.0 m is less than 5%. Moreover, the cross-section selected to take the measurements and characterize the behavior of the flow was the cross-section at 9.0 m from the inlet of the channel. Figure 3.14 shows the vertical profiles for *Hr* = 0.50 at that streamwise position.

For the rough bottom case, the water depth measurements were carried out each 0.5 m starting at 5.0 m from the inlet up to 10.0 m downstream. The rough elements were placed between 4.75 m and 10.75 m from inlet and were located at the interface between the main channel and floodplain, as shown in fig. 3.15. In order to determine the evolution of the velocity field along the channel, measurements were carried out in three cross sections located relative to the rods: (a) downstream; (b) middle; and (c) upstream of them. All these cross sections were taken at around 9.0 m length from the inlet.

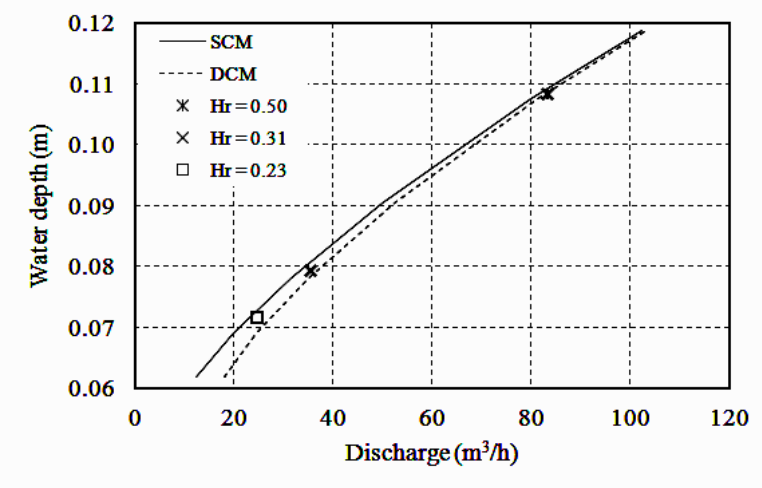

Figure 3.13 Mean water depth. Comparison between measurements and estimations from Divided Channel Method and Single Channel Method.

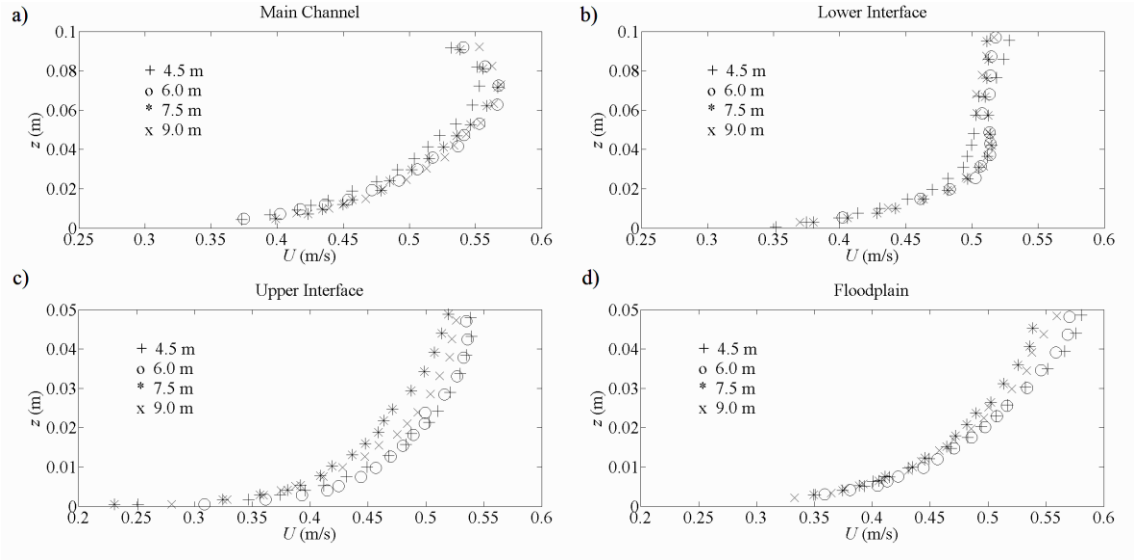

Figure 3.14 Verticals velocity profile at different cross-section.

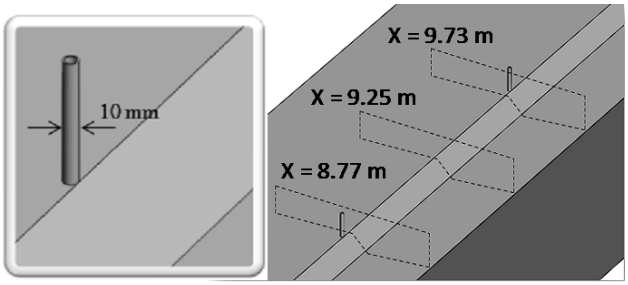

Figure 3.15 Channel geometry for roughness cases. x = 8.77 m, downstream of the rod; x = 9.27 m, in the middle of the rods; x = 9.73 m, upstream of the rod.

As mentioned above, three different spacing between rods were used, S_{d1} = 1 m, S_{d2} = 0.2 m and S_{d3} = 0.04 m, and two different relative water depth for each spacing. In order to establish the quasi-uniform flow for each spacing condition, the gate was fixed and the discharge was adjusted until free-surface slope was parallel with the bottom slope, as shown in fig. 3.16. To do that, and knowing the location of the gate for each relative water depth set in the smooth conditions, the gate was placed in the position for *Hr* = 0.50 in the smooth condition and then, the discharge was adjusted for each spacing condition. The same procedure was performed but placing now the gate for *Hr* = 0.31 in smooth conditions. It was not an easy task to set a uniform flow due to the free-surface perturbation caused by the rods, obtaining in some cases differences between the bottom slope and the free-surface slope of up to 0.4 mm/m. However, the uniform flow was established, in this investigation, when the free-surface slope matched the bottom slope in the main channel and when similar conditions occurred between the free-surface and bottom slope in the floodplain. Table 3.7 shows, the experimental conditions for roughness cases.

In total, 9 inlet conditions were studied, 3 inlet conditions for the smooth case and 6 for the roughness case, and 21 cross sections were measured. In each cross section, 775 points were measured during 210 s each one to obtain statistically mean steady values, resulting in 45 hours of measuring by cross section. These 775 measured points, corresponded to 31 vertical profiles with 25 measurement points each one, for which 11 vertical profiles were located in the main channel, 11 vertical profiles in the interface (region between main channel and floodplain) and 9 in the floodplain. Each vertical profile contains 25 measured points, 10 points were concentrated in the wall region (20% below from the wall), 10 points in the intermediate region (between 20% and 60% of the water depth) and 5 points in the free-surface region.

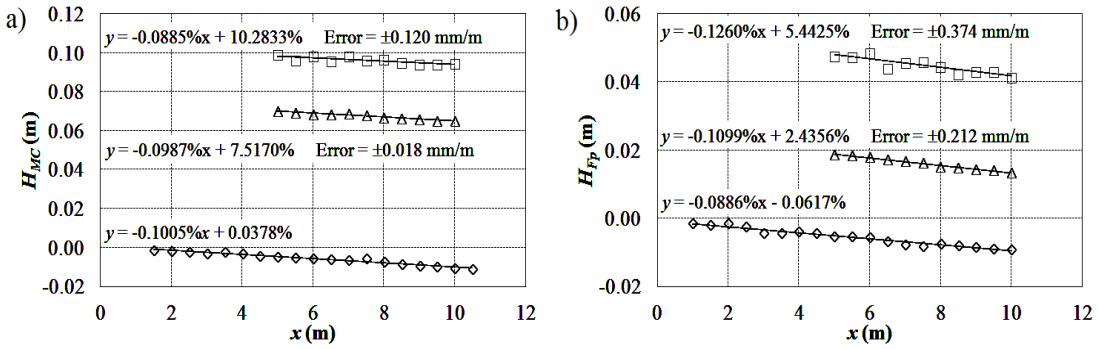

Figure 3.16 Free-surface slope for roughness case for *Hr* = 0.50 and *Hr* = 0.31 and S_{d1} = 1.00 m a) Free-surface slope in the Main Channel b) Free-surface slope in the Floodplain.

Table 3.7 Mean experimental conditions for roughness case.

	S_{d1} = 1.00 m				S_{d2} = 0.20 m				S_{d3} = 0.04 m			
	Hr = 0.51		*Hr* = 0.31		*Hr* = 0.45		*Hr* = 0.28		*Hr* = 0.34		*Hr* = 0.25	
	Main Channel	Floodplain	Main Channel	Floodplain	Main Channel	Floodplain	Main Channel	Floodplain	Main Channel	Floodplain	Main Channel	Floodplain
Discharge (m^3/h)	82.99 ± 0.26		35.50 ± 0.08		62.72 ± 0.15		31.31 ± 0.09		36.36 ± 0.13		26.41 ± 0.07	
Mean water depth (m)	0.1033 ± 0.0009	0.0523 ± 0.0011	0.0749 ± 0.0005	0.0234 ± 0.0006	0.0941 ± 0.0005	0.0422 ± 0.0008	0.0718 ± 0.0005	0.0204 ± 0.0006	0.0784 ± 0.0004	0.0270 ± 0.0005	0.0683 ± 0.0005	0.0170 ± 0.0005
Bottom slope (%)	-0.1005	-0.0886	-0.1005	-0.0886	-0.1005	-0.0886	-0.1005	-0.0886	-0.1005	-0.0886	-0.1005	-0.0886
Free-surface slope (%)	-0.0885	-0.1260	-0.0987	-0.1099	-0.1176	-0.1008	-0.0954	-0.1028	-0.0987	-0.0982	-0.0998	-0.0980
Slopes difference (mm/m)	0.120	0.374	0.018	0.212	0.171	0.121	0.051	0.141	0.018	0.096	0.008	0.094
Cross Section Measured (m)	8.770		8.770		8.965		8.965		9.005		9.005	
	9.250		9.250		9.050		9.050		9.010		9.010	
	9.730		9.730		9.135		9.135		9.015		9.015	

3.5 Data Acquisition and Pre-processing

The *u* and *w* instantaneous velocities were obtained from FlowSizerTM software, measured at a given cross section. However, before calculating any turbulence parameters, the instantaneous velocity must be filtered to remove some signal perturbations associated to noise. On this regards, a filtering method was used to detect the noise spikes, namely *Phase-Space Thresholding Method*.

The *Phase-Space Thresholding Method* uses the Poincaré map concept which relates a variable and its derivatives, concentrating the points in an ellipsoid defined through the so called Universal criterion and considering the points outside of the ellipsoid as spikes. The Universal criterion results from the normal probability distribution theory which for a normal random variable, whose standard deviation is estimated by $\hat{\sigma}$ and the mean is zero, has an expected absolute maximum given by:

$$\lambda_{U\hat{\sigma}} = \sqrt{2\ln n}\hat{\sigma} \tag{3.4}$$

The *Phase-Space Thresholding Method* proves to be useful detecting spikes, as noted by Goring and Nikora (2002), for measurement points located very near to the walls, where the instantaneous velocity of a large number of particles captured by LDV system presents values well defined in two ranges. However, when the first range of values corresponds to the real velocity of the measurement point and a second range corresponds to spikes caused by light reflection from the wall, the method fails, since there exists a dichotomy on which of these two ranges of values is the real instantaneous velocity (see fig. 3.17). To correct this issue, a pre-filtering was developed in order to eliminate the values obtained by reflections. In this case, a threshold was defined for the values that exceed $U \pm \Delta u \cdot U$, where Δu is between 0.5 - 0.8.

Completed the pre-filtering process, the *Phase-Space Thresholding Method* was executed. For this purpose, the following steps were developed:

1. Calculate the instantaneous fluctuations from instantaneous velocity.
2. Calculate the acceleration coefficient for the first and second derivatives from:

$$\Delta u'_i = \left(u'_{i+1} - u'_{i-1}\right)/2 \tag{3.5}$$

$$\Delta^2 u'_i = \left(\Delta u'_{i+1} - \Delta u'_{i-1}\right)/2 \tag{3.6}$$

3. Calculate the standard deviation of all three variables, $\sigma_{u'}$, $\sigma_{\Delta u'}$ and $\sigma_{\Delta^2 u'}$. To calculate the standard deviation, eq. 3.7 was used:

$$\sigma_x = \left(\frac{1}{n-1} \sum_{i=1}^{n} \left(x_i - \bar{x} \right)^2 \right)^{1/2} \tag{3.7}$$

4. Calculate the rotation angle θ of the principal axis of $\Delta^2 u'_i$ *vs.* u'_i, $\theta = \tan^{-1}\left(\sum u'_i \, \Delta^2 u'_i \Big/ \sum u'^2_i \right)$. Note that for $\Delta u'_i$ *vs.* u'_i, and $\Delta^2 u'_i$ *vs.* $\Delta u'_i$ $\theta \equiv 0$ because of symmetry.
5. Calculate the major and minor axes of the ellipse for each pair of variables. On this regard, for $\Delta u'_i$ *vs.* u'_i, the major axis is $\lambda_u \sigma_u$ and the minor axis is $\lambda_u \sigma_{\Delta u}$; for $\Delta^2 u'_i$ *vs.* $\Delta u'_i$, the major axis is $\lambda_u \sigma_{\Delta u}$ and the minor axis is $\lambda_u \sigma_{\Delta^2 u}$; and for $\Delta^2 u'_i$ *vs.* u'_i, the major and minor axes are given by *a* and *b*, respectively, being *a* and *b* the solution of:

$$\left(\lambda_x \sigma_x \right)^2 = a^2 \cos^2 \theta + b^2 \sin^2 \theta \tag{3.8}$$

$$\left(\lambda_x \sigma_{\Delta^2 x} \right)^2 = a^2 \sin^2 \theta + b^2 \cos^2 \theta \tag{3.9}$$

6. Identify the points outside of each ellipse and replace them. Once the outlier points for each spike (outside points of the ellipse) are replaced, all steps must be repeated until further spikes replacements have no effect in the size of the ellipsoid. This is an iterative process.

3.5.1 *Spike Replacement*

To replace the spikes, a third-order polynomial was used. In this case, the following steps were executed:

1. Identify a spike and replace it momentarily by the time-averaged record.
2. Use 12 points on either side of the spike to fit a third-order polynomial.
3. Replace the spike by the value obtained from the third-order polynomial.
4. Follow step 1, 2 and 3 for each spike.

Figure 3.17 shows an example of the data obtained after using the Phase-Space Thresholding Method.

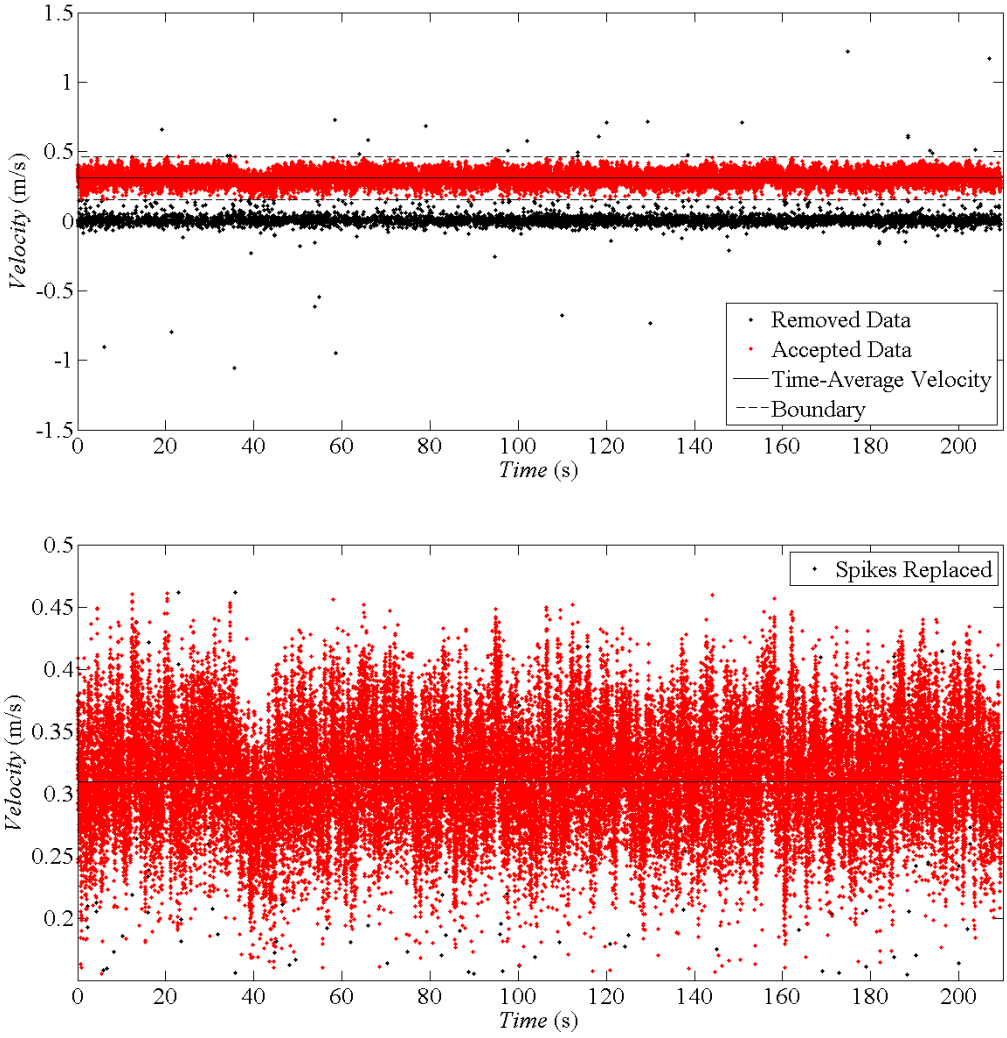

Figure 3. 17 Pre-processing of the data a) Pre-filtering b) Spike replacement after applying the *Phase-Space Thresholding Method.*

4

Chapter 4

Results

4.1 Influence of the sidewall effect on asymmetric compound channel flows

Azevedo, R., et al. (2011). Influencia del efecto pared-lateral en flujos en canales asimétricos compuestos (Influence of the sidewall effect on asymetric compound channel flows). IX Congreso Anual de Ingenieria ASME USB 2011. U. S. Bolívar. Caracas - Venezuela.

Abstract: Depending on the relationship between the main channel width and the flow depth, the influence of the sidewall can have an important role in the development of Prandtl's second kind secondary currents. These can have a major effect on the mean flow and on turbulence structures developed at the mixing layer between the floodplain and main channel. To check the influence of the sidewall effect, the velocity field was measured with a Laser Doppler Velocimeter (LDV). The discharge values used for the measurements were of 23.0 L/s and 9.8 L/s which correspond to relative depths (floodplain depth/flow depth) of 0.50 and 0.31, respectively. The results show that as a consequence of sidewall effect the maximum velocity presented by the flow in the streamwise direction occurs quite below the free surface. This effect, named "velocity-dip" phenomenon, has been investigated by several researchers. Furthermore, the secondary currents located between the main channel and the floodplain, generate a downstream flow on the interface (region between main channel-floodplain), which stimulates further the momentum and energy transfer between the sidewall and the center of the main channel, promoting the dip phenomenon. These effects were observed for both discharges, however, as the main channel width-depth aspect ratio increases, the influence of the sidewall effect decreases.

Key words: Compound open-channel, secondary currents, sidewall effect.

Resumen: Dependiendo de la relación entre el ancho del canal principal y el tirante del flujo, la influencia de la pared lateral puede jugar un papel importante en el desenvolvimiento de las corrientes secundarias de segundo orden de Prandtl. Esto puede tener un mayor impacto sobre el flujo medio y dependiendo de la estructura turbulenta en la capa de mezcla, entre la planicie de inundación y el canal principal, las corrientes secundarias de segundo orden de Prandtl pueden ser intensificadas. Para verificar la influencia que tiene el efecto de la pared lateral, el campo de velocidad fue medido con un Laser Doppler Velocimeter (LDV). Los caudales empleados fueron de 23.0 L/s. y 9.8 L/s. correspondientes a alturas relativas (altura en la planicie de inundación/tirante del flujo) de 0.50 y 0.31, respectivamente. Los resultados señalan, que uno de los efectos que tiene la pared lateral sobre el comportamiento del flujo en el canal principal, y que ya ha sido evidenciado por otros investigadores, es que la velocidad máxima que presenta el flujo en el sentido longitudinal, se encuentra por debajo de la superficie libre. Dicho fenómeno

es conocido como el fenómeno dip. Asimismo, las corrientes secundarias formadas entre el canal principal y la planicie de inundación, generan un flujo descendente en la interfaz (zona entre canal principal-planicie de inundación) que estimula aún más la transferencia de momento y energía entre la pared lateral y el centro del canal principal, promoviendo el fenómeno dip. Estos efectos fueron observados para ambos caudales, sin embargo, a medida que la relación entre el ancho del canal principal y el tirante del flujo aumenta, la influencia que tiene la pared disminuye, siendo la transferencia de flujo desde la pared hacia el centro del canal principal menos intenso y ubicándose la velocidad máxima, en sentido longitudinal, más próxima a la superficie libre.

Palabras claves: Canal compuesto, corrientes secundarias, efecto pared-lateral.

4.1.1 *Introduction*

To determine the behavior of rivers it is essential to formulate mathematical models in order to predict the new currents caused when the level of rivers go beyond its natural course and flood surrounding areas, which are characterized as areas of recreation, agriculture or even inhabited. To study the impact that this natural phenomenon can cause, several investigations have been conducted on different types of experimental open channels. The first aspect that has been studied is the distribution of shear stress across the width of a rectangular channel. Keulegan (1938), proposed a method in which the cross sectional area of the flow is divided into three areas using the bisector of the angle formed between the side wall and the bottom of the channel. Einstein (1942) proposed a method in which the cross section of the flow is divided into two areas and then relates the weight of both areas with the resistance of the bottom and walls of the channel. Both methods have been used by several researchers and have undergone certain modifications to be adjusted to the velocity profiles measured near the sidewall.

One phenomenon commonly observed in open channels is that the maximum flow velocity is below the free surface. This phenomenon, called "velocity dip", has been observed not only in rectangular channels (Kang and Choi, 2006; Yang et al., 2004) but also in asymmetric compound channels (Shiono and Komatsu, 2000). The "dip" phenomenon has been attributed by many researchers to secondary currents originated near the side walls of the channel. Nezu and Rodi (1985) found that the "dip" phenomenon occurs when the relationship between the width of the rectangular channel and the water depth is less than or equal to 5. Yang et al. (2004) presented a modification of the "log-law" which shows a traditional good fit with the velocity distribution, including the inertial region.

In the case of compound open channels, the “dip” phenomenon remains a research topic. The behavior of secondary currents observed by Shiono and Knight (1991) is described in

Figure 4.1. Moreover, measurements taken by Stocchino et al. (2011) of flow velocities at the free surface, using "Particle Image Velocimetry" (PIV) in a symmetrical compound channel, show macrovortices of vertical axis (normal to the channel bottom) near the side wall of the floodplain when the relation of the water depth between main channel and floodplain is less than 2. They indicate that these macro vortices were observed only in the side wall region and not in the interface region. This shows the complex formation of secondary currents close to the side wall as the water depth increases.

In this study measurements made in an asymmetric compound channel will be presented where the "dip" phenomenon is again observed. The first objective will be to present the time-averaged velocity fields *U* and *W*, in order to observe how the side wall of the main channel and secondary currents, generated by the interaction of flows between the main channel and floodplain, influence on the emergence of the "dip" phenomenon. Further, the turbulent intensities *U'* and *W'* will be presented. All results will be compared with results reported in rectangular and compound channels by other researchers.

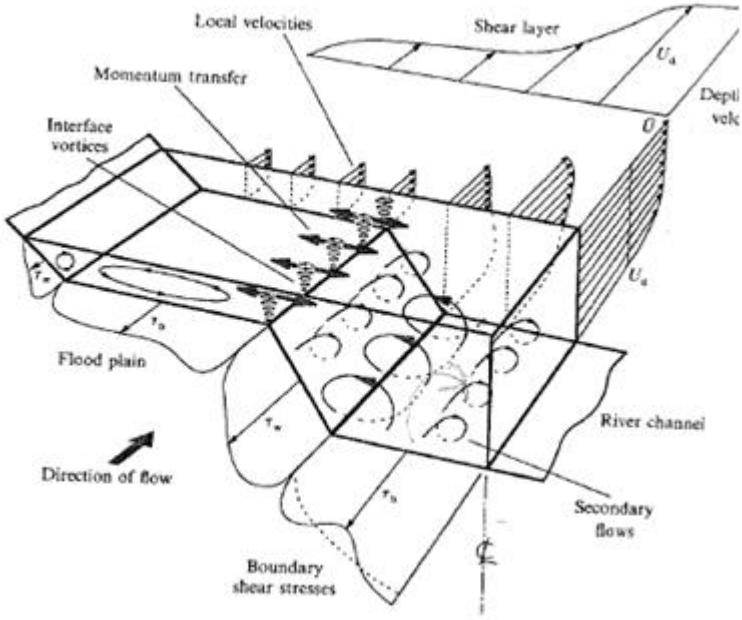

Figure 4.1 Secondary Currents observed by Shiono and Knight (1991) in a straight compound channel.

4.1.2 *Experimental Setup*

The measurements were performed in an asymmetric compound open channel built on a concrete structure. To make the bottom of the channel smoother, a layer of mastic was added. Figure 4.2 shows the side wall of the flume, which presents a set of glass windows that allow taking measurements with Doppler Velocimeter Laser (LDV). However, to avoid the effects of

the windows edges on the flow, a 0.01 m thick acrylic sheet was placed between the sidewall and the channel.

The feeding system of the channel was carried out by a single pump and the water level is adjusted through a gate located in the final section of the channel. The total flow rate is determined for an electromagnetic flowmeter located in the supply pipe and the water level is obtained with a water gauge level.

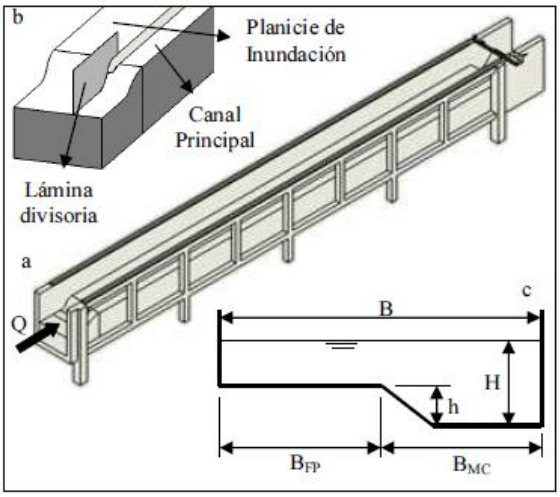

Figure 4.2 Asymmetric Compound Channel Description a) Set of windows through measurements are made b) Inlet of the channel. c) Cross-section of the channel.

Figure 4.2b shows the initial section of the channel, where the floodplain and main channel are separated by a plate in order to decrease the mass transfer between them. Thus, the entry conditions are improved to establish uniform flow conditions (Bousmar et al., 2005)

The flume is 11.60 m. long and 0.790 ± 0.002 m. wide. The main channel has a width of 0.259 ± 0.002 m. and an average slope of 0.0985%, while the floodplain has a width of 0.531 ± 0.001 m. and an average slope of 0.0910%. Table 4.1 shows the most important parameters of the compound channel.

Velocity measurements were made using a LDV Innova 70C Argon-ion with a maximum power of 2W. In this system, two light beams crossing at the focal length of the fiber probe (measurement volume) are needed in order to measure one component of velocity. For measuring two velocity components, the system displays two pairs of beams. This measurement technique is a non-invasive technique based on the Doppler effect. When a particle crosses the measurement volume, it emits a sequence of light reflections that are captured by the system and stored as a measurement frequency. To determine the direction of the particle, the wave frequency of one of the two light beams is modified (shifted beam). In this case, the frequency

of the shifted beam is 40 MHz, causing a displacement of fringes formed in the measuring volume, from the shifted beam to the unshifted beam. Therefore, when a particle crosses the measuring volume from the unshifted beam to the shifted beam direction, the measurement frequency will be the aggregate frequency (40MHz) plus the Doppler frequency (the frequency emmitted by a particle when crossing the measuring volume without altering the wave frequency of the shifted beam, *i.e*. the fringes remain static in the measurement volume). Otherwise, if the particle crosses the measurement volume from the shifted beam to the unshifted beam, the measurement frequency will be the aggregate frequency (40 MHz) minus the Doppler frequency (TSI, 2006).

Table 4.1 Main Geometrical Characteristics of the Channel.

Channel Length L (m)	11.60
Channel Wide B (m)	0.790 ± 0.002
Number of Floodplains	1
Floodplain Width B_{FP} (m)	0.531 ± 0.001
Floodplain Slope	0.0910 %
Main Channel Width B_{MC} (m)	0.259 ± 0.002
Main Channel Slope	0.0985 %
Interface Depth h (m)	0.051 ± 0.001
Manning Coefficient n (s/m1/3)	0.01044

Once the beams travel through different refraction materials, the focal length and size of the measurement volume change. Table 4.2 shows the main features of LDV. To perform measurements, particles of talcum powder with an average diameter of D_{50}=14.16 μm were used. However, recent studies show that the use of aluminum oxide particles as seeding increases the acquisition rate. The measurement time at each point was 210 s. which allows data rates between 5 Hz - 150 Hz. The velocity measurements were performed at a cross-section located 7.5 m from the channel entrance, where mass transfer between the floodplain and main channel, due to overfeeding of the floodplain region, is almost balanced (Bousmar et al., 2005). Discharges of 23 L/s. and 9.8 L/s were used, corresponding to a relative water depth of 0.50 and 0.31, respectively. The number of measurement points for a relative height of 0.50 were 1748, corresponding to 70 verticals distributed along the cross section of the channel, and the number of measurement points for a relative water depth of 0.31 were 1050, corresponding to 42 verticals. The measurements were performed from the main channel lateral wall until 0.40 m from that wall due to the configuration used with LDV. Moreover, due to some interference

between LDV beams and the channel bottom, measurements below 0.05 m and 0.02 m could not be developed in the main channel and floodplain regions, respectively.

Table 4.2 Main Characteristics of LDV.

	Beam 1 (u)	Beam 2 (w)
Beam Color	Green	Blue
Wavelength (nm)	514.5	488.0
Focal Length (mm)	363	363
Beam Separation (mm)	50	50
Laser Beam Diameter (mm)	2.65	2.65
Theoretical Measurement Beam Waist (μm)	89.95	85.31
Experimental Measurement Beam Waist (μm)	99.29	94.18
Theoretical Measurement Beam Length (mm)	1.31	1.24
Experimental Measurement Beam Length (mm)	1.91	1.81
Theoretical Fringe Spacing (mm)	0.0037	0.0036
Experimental Fringe Spacing (mm)	0.0049	0.0047
Theoretical Number of Fringes	24	24
Experimental Number of Fringes	20	20

Table 4.3 shows the flow conditions used for both relative water depths. The relative water depth is calculated as the ratio of the water depth in the floodplain and the water depth in the main channel ($Hr = (H–h) / H$). The friction velocity was calculated by the geometric characteristics of the channel ($U_* = (gR_hS)^{0.5}$) and the cross-section averaged velocity was calculated with the rate between the flow discharge and the section area.

Table 4.3 Experimental Flow Conditions.

Q (m^3/s)	H (m)	Hr	Area (m^2)	U_{CS} (m/s)	U_* (m/s)	Re ($x10^3$)	Fr
0.0098	0.0745	0.31	0.0302	0.324	0.0179	10.02	0.567
0.0230	0.1022	0.50	0.0521	0.441	0.0229	22.73	0.606

4.1.3 *Results and Analysis of Results*

This section describes the velocity fields and turbulent intensities measured at the asymmetric compound open channel.

Figure 4.3 shows the distribution of velocities *U* and *W*. For both flow discharges, it can be verified that the maximum velocity of the *U* is below the free surface in the main channel region ("dip" phenomenon). In the case of fig. 4.3a (*Hr* = 0.31), the maximum velocity is located at 80% of the water depth, whereas in fig. 4.3b (*Hr* = 0.50), the maximum velocity is reached at 70% of the water depth. However, in the floodplain region the maximum velocity is attained at the free surface. A similar behavior was observed by Shiono and Komatsu (2000) in an asymmetric compound channel. A bulge of the isolines in the upper interface is also observed in fig. 4.3b, due to an ascendant flow located in this region. Isolines of the velocity *W* (fig. 4.3c and 4.3d) show that in the main channel, close to the interface, there is a descendant flow, while in the upper interface an ascendant flow is observed. The behavior of the movement of the secondary currents between the main channel and floodplain are consistent with observations made by Shiono and Knight (1991). Due to the loss of the measurement field of the *W* component for *Hr* = 0.31, the ascendant flow in the upper interface is not clearly observed.

According to Nezu and Nakagawa (1993), for rectangular channels, there is a vortex of high intensity originated near the free surface and called "free-surface vortex", rotating in clockwise direction, which generates a downward flow of great intensity, causing a momentum transfer from the side wall towards the center of the main channel and from the free surface towards the bottom of the channel. The descendant flow in the main channel causes an immersion of the vortex located near the free surface, resulting in the aforementioned "dip" phenomenon. In this case, the existence of a descendant flow of high intensity is clearly observed in the area of the main channel near the interface, resulting from the interaction between the flows of the main channel and floodplain, which generates such momentum transfer between side-wall / center of the main channel, and free surface / half depth in the main channel.

As for *Hr* = 0.50, the descendant flow has greater intensity than for *Hr* = 0.31, the maximum velocity presented in fig. 4.3b is attained deeper than the one presented in fig. 4.3a. Moreover, it is also expected that as more intense the secondary currents originated in the interface region are, a greater momentum transfer exists from the side wall and from the free surface, causing the "dip" phenomenon. However, increasing the width of the main channel, the effect of momentum transfer between the sidewall and the center of the main channel decreases.

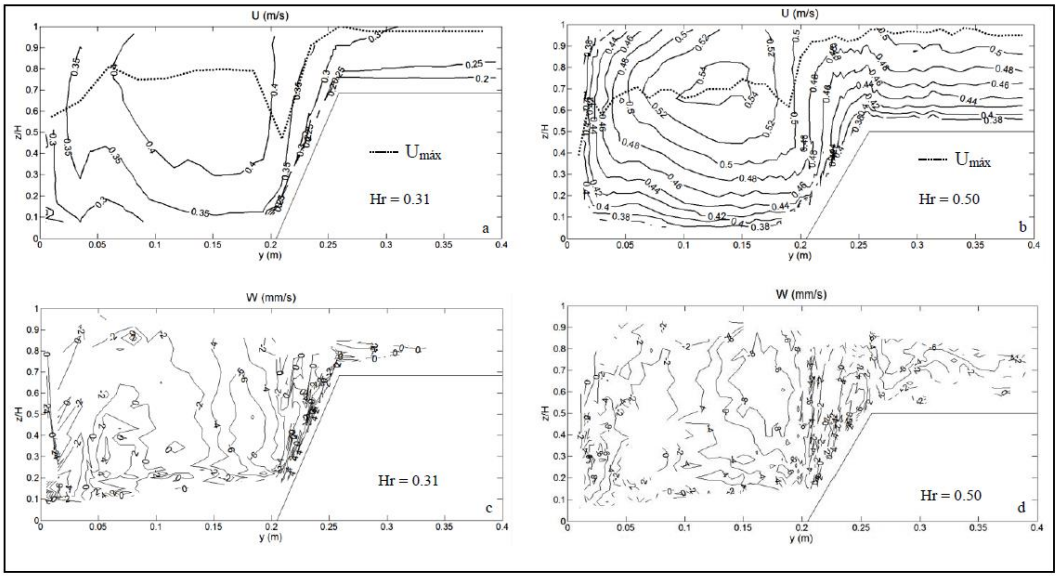

Figure 4.3 Isolineas of Velocities *U* and *W*.

According to Nezu and Nakagawa (1993), the velocity distribution in rectangular channels fits nicely to the "log-law", except for the vicinity of the side walls, where there is turbulence anisotropy. For those regions, where the flow behavior is 3D, it is necessary to know a priori the von Kármán constant and the constant of integration. For 2D flows, the values recommended by Nezu and Nakagawa (1993) for those constants are 0.41 and 5.3, respectively.

Figure 4.4 shows the behavior of the velocity profiles in the main channel. For the velocity profile near to the side wall, the profile does not have a good fit with the "log-law". For Hr = 0.50, the velocity profile near to the side wall has a larger deviation than the one presented for Hr = 0.31. This is due to a greater intensity of the turbulence anisotropy. However, as the profiles move away from the side wall, they begin to progressively resemble the traditional "log-law".

The velocity profiles closest to the interface region ($Y \approx 0.20$) do not have a good fit with the traditional “log-law”. However, for both cases Hr = 0.31 and Hr = 0.50, the velocity profiles show a similarity between them. Moreover, these profiles have a logarithmic behavior in the bottom section, except for the velocity profile taken in the main channel at the lower interface. Probably, adjusting the values of the von Kármán constant and the integration constant of the traditional "log-law", an expression that fits better the velocity profile could be obtained.

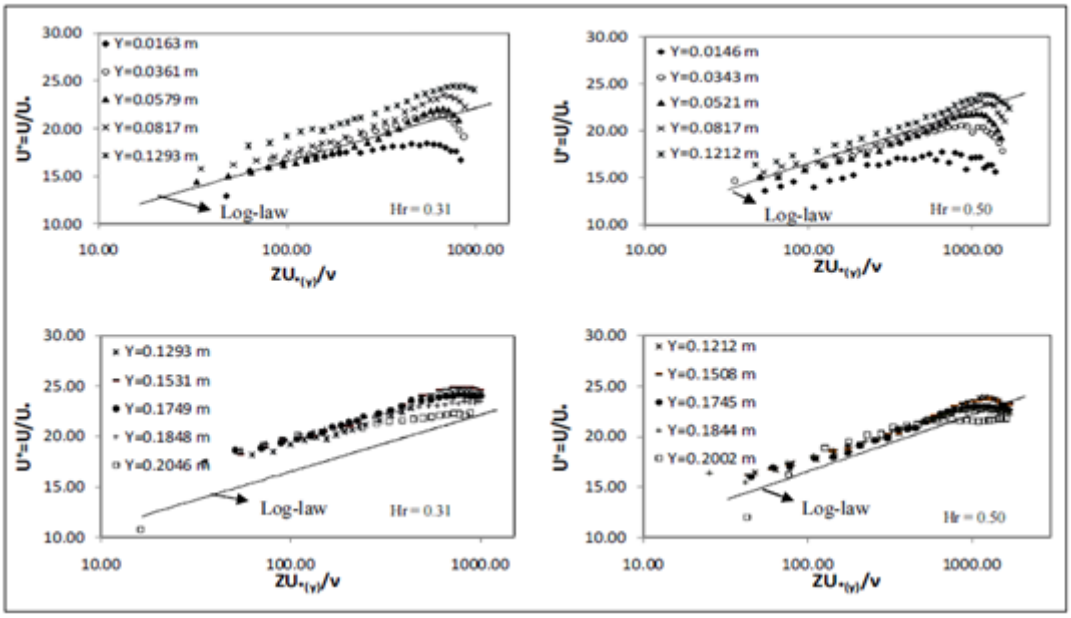

Figure 4.4 Vertical Velocity Profiles of U/U_* in the main channel.

Yang et al. (2004) proposed a modification of the traditional "log-law" in order to describe the behavior of the velocity distribution across the width of a rectangular channel, considering the “dip” phenomenon. They consider two logarithmic distances, one from the bottom of the channel and the other from the free surface, and a correction factor of the distance where the maximum velocity U occurs. A similar analysis can be made in compound channels where secondary flows are more complex. However, in this section we will only consider the influence of the side wall and the secondary currents formed between the main channel and floodplain, on the “dip” phenomenon.

Figure 4.5 shows the distribution of turbulent intensities U' and W' normalized by friction velocity U_*. In the case of isolines of turbulent intensity U', fig. 4.5a and 4.5b show a resemblance with the isolines of velocity U. The turbulent intensity is greater near to the bottom and side wall of the channel, while the lower turbulent intensity is below the free surface due to the “dip” phenomenon. On the other hand, fig. 4.5c and 4.5d show how the higher turbulent intensity W' is located near to the bottom and the side wall of the channel and decreases towards the free surface. These observations were also reported by Kang and Choi (2006) and Nezu and Rodi (1985) in rectangular channels.

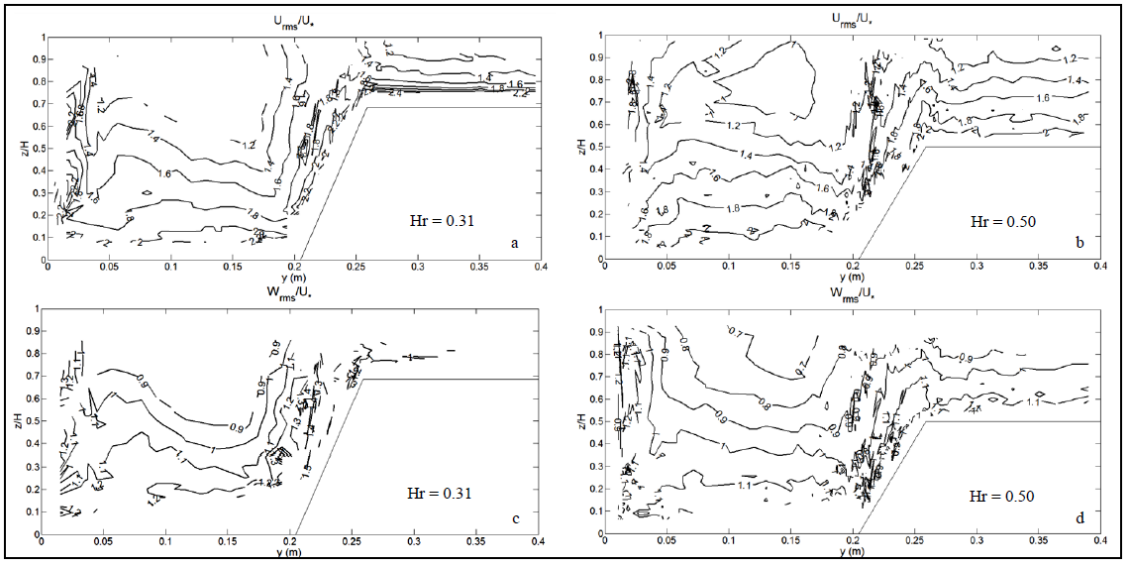

Figure 4.5 Normalized Isolineas of Turbulent Intensity *U'* and *W'*.

4.1.4 *Conclusions*

According to the results shown in this work it can be concluded that the "dip" phenomenon occurs not only in rectangular channels, product of the lateral wall of the channel, but also in compound channels where additional secondary currents are formed by the interaction between the main channel and floodplain flows.

The existence of a descendant flow of high intensity in the main channel region close to the interface due to the interaction between the main channel and floodplain flows was observed. This flow generates a momentum transfer between the side wall and the center of the main channel, and between the free surface and the half depth area, rendering the maximum velocity below the free surface. This allows concluding that, as higher are the secondary currents in the interface region, more intense will be the "dip" phenomenon.

Velocity profiles measured in the main channel do not fit the traditional "log-law", corroborating the existence of a 3D flow. However, the velocity profiles have a logarithmic trend near the bottom of the channel (wall region).

In the case of the turbulent intensity U', it has a similarity with the isolines of velocity U. However, the greater turbulent intensity is in the vicinity of the side wall and the bottom of the channel. Also, lower turbulent intensity is just below the free surface due the dip phenomenon. In the case of the turbulent intensity W', the highest intensity is located near the side wall and the bottom of the channel and decreases in the direction of the free surface.

4.2 Experimental Characterization of Straight Compound-Channel Turbulent Field

Azevedo, R., Rojas-Solórzano, L., & Leal, J. (2012). Experimental characterization of straight compound-channel turbulent field. In *in 2nd European IAHR Congress 2012 Munich*.

Abstract: Straight compound-channel flows have been studied by many authors, mainly concerned with mean flow variables. Detailed information on the complex turbulent field of these flows is still scarce. In the present paper, high data rate measurements were obtained for the streamwise and vertical velocity components, using a 2D Laser Doppler Velocimeter in an experimental compound flume. The filtered velocities time series allowed the computation of relevant turbulence statistics: autocorrelation functions, dissipation spectra, turbulence scales and dissipation rate. The results are analyzed by comparison with universal laws drawn for isotropic turbulent 2D fully developed open-channel flow. The presence of strong secondary currents does not affect the universal law in the floodplain, as long as the constants are changed. In the main channel the 3D behavior of the flow is more pronounced and the universal laws fail to reproduce accurately the experimental results.

4.2.1 *Introduction*

Straight compound-channel flows have been studied by many authors due to their practical importance related to floods in rivers. In terms of physical interpretation and numerical modeling they constitute a challenge, since they present a complex 3D structure that can include large scale horizontal vortices and helicoidal longitudinal vortices, also known as secondary currents (Shiono and Knight, 1991). Despite the presence of these structures, most studies are focused only in the mean flow variables. The studies of Knight and Shiono (1990), Shiono and Knight (1991), Tominaga and Nezu (1991), Nezu et al. (1999),Van Prooijen et al. (2005), Stocchino and Brocchini (2010) and Stocchino et al. (2011) are among the few studies where the turbulent field in straight compound-channel was addressed. Nevertheless, the influence of the vortex structure in the turbulent scales and in the dissipation rate was not assessed.

In the present study, high data rate measurements were obtained for the streamwise and vertical velocity components, using a 2D Laser Doppler Velocimeter in an experimental compound flume with a deep flow, where secondary currents are dominant (Nezu et al., 1999). The analysis of the effect of secondary currents in the turbulent scales and in the dissipation rate is made by comparison with universal laws drawn for isotropic turbulent 2D fully developed open-channel flow (Nezu and Nakagawa, 1993).

4.2.2 *Experimental Setup*

The experiments were conducted in an asymmetric compound flume built in cement at University of Beira Interior. The flume is 11.60 m long and 0.790 m wide. The main channel width is 0.205 m, while the floodplain width is 0.540 m. The width of the region between the main channel and floodplain, called interface, is 0.054 m and the bank full depth is 0.051 m, as shown in fig. 4.6.

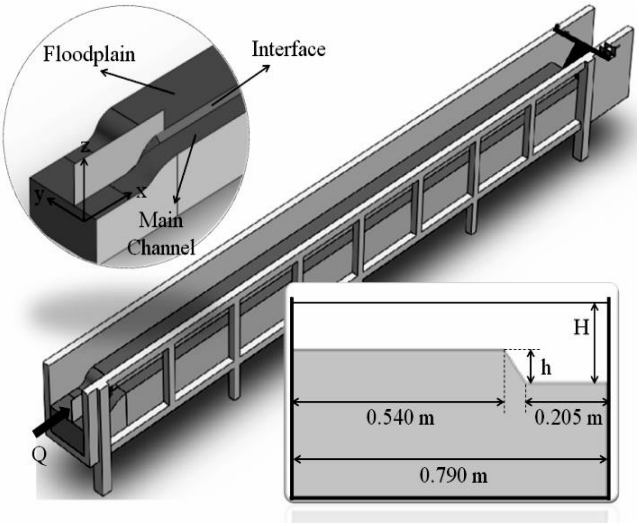

Figure 4.6 Description of the asymmetric compound flume.

The average longitudinal bottom slope of the main channel and floodplain is 0.986 and 0.911 mm/m, respectively. To set the quasi-uniform flow it was necessary to measure the water depth in the middle of the main channel and also in the floodplain to verify that the value of the free-surface slope, in both sub-regions, was between the value of the main channel and the floodplain longitudinal bottom slope.

The measurements of the velocity field were made with a 2D Laser Doppler Velocimeter (LDV) in a cross-section located 9.0 m from the inlet of the channel, where the downstream gate does not influence the flow. Measurements in backscattering mode were performed through a glass window located on the main channel lateral wall of the channel next to the main channel. The total number of points measured to characterize the cross-section was 1,148. The measurement time was 210 s per point and aluminum oxide powder was used as seeding.

The discharge used during the experiments was 23.16 l/s and the quasi-uniform flow water depth was 0.1033 m. The relative water depth, H_r, calculated through eq. 4.1 was 0.50. In that equation H_{fp} and H_{mc} are the floodplain and main channel water depths, respectively.

$$H_r = H_{fp} / H_{mc} \tag{4.1}$$

4.2.3 *Results and Discussion*

The terms used to describe the velocity field are *u* and *w* for the instantaneous velocity; *u*' and *w*' for the velocity fluctuations; *U* and *W* for the time-averaged velocity; and *U*' and *W*' for the root mean square or turbulence intensity in the longitudinal direction, *X*, and vertical direction, *Z*, respectively (see fig. 4.6).

Table 4.4 shows the experimental conditions where measurements were made. The cross-section mean velocity, U_{cs}, was calculated by the relation between the inlet discharge and the area of the cross section. The geometrical method ($U_* = \sqrt{gR_hS_0}$, where $g = 9.8\,\text{m/s}^2$ is the gravitational acceleration and R_h is the hydraulic radius) was used to compute the friction velocity of the section. Further, the Reynolds number and Froude number were calculated by the expression $Re = 4U_{cs}R_h/\nu$ (ν = 7.96x10^{-7} m^2/s is the kinematic viscosity of water at 30º C) and $Fr = U_{cs}/\sqrt{gH_{mc}}$ respectively.

Table 4.4 Experimental Conditions.

Q (l/s)	H_{mc} (m)	H_r	U_{cs} (m/s)	U_* (m/s)	Re (x10^{-4})	Fr
23.16	0.1033	0.50	0.4301	0.0227	11.78	0.425

4.2.3.1 Velocity Distribution

Figure 4.7 shows the time-averaged velocity distribution *U* and *W* measured in the cross section at 9.0 m from the inlet of the cannel, as well as turbulent intensity distribution U'/U_* and W'/U_*. The interaction between the main channel flow (with higher velocity and inertia) and floodplain flow (with lower velocity and inertia) generates a momentum transfer causing the formation of different types of turbulent structures as vertical axis vortex, due to the shear layer between the main channel and floodplain flows, or longitudinal axis vortex, called secondary currents, due to the anisotropy of turbulence (Nezu et al., 1999; Shiono and Knight, 1991).

In fig. 4.7a, an ascendant flow in the interface region near the upper interface is evident, as well as the descendant flow in the floodplain region near the interface (0.26 m ≤ *Y* ≤ 0.29 m) and in the main channel region near the lower interface. The generation of the ascendant/descendant flow (secondary currents) is caused by the strong anisotropy between the floodplain and main channel flows, resulting in a vortex on the interface/floodplain region,

called “floodplain vortex”, and a vortex in the main channel/interface region called “main channel vortex” (Tominaga and Nezu, 1991).

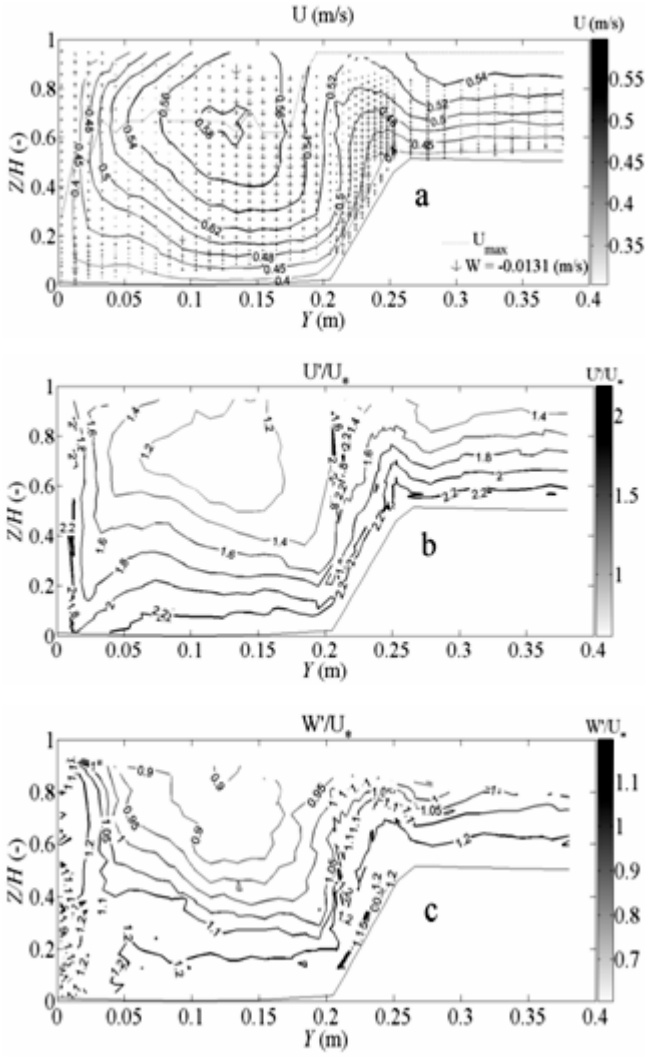

Figure 4.7 Isovels of mean velocity U and vectors of mean velocity W; (b) Isovels of turbulent intensity U’; (c) Isovels of turbulent intensity W’.

The magnitude of *W* velocity in the main channel and interface region is similar, around 30% of U_*. In the floodplain region near the interface, the magnitude of the *W* velocity decreases until approximately 10% of U_*. The strong descendant flow in the main channel region is due to the meeting of two vortexes, the “main channel vortex” and the “free-surface vortex”, that is caused by the anisotropy of lateral wall and free-surface turbulence (Nezu and Nakagawa, 1993). On the other hand, fig. 4.7a shows how the isovels are affected by the momentum transport of the secondary currents. Since there is an ascendant flow in the interface region, the *U* isovels are displaced upwards by influence of the *W* velocity. The same effect

occurs with the descendant flows. Further, due to effects of the "free-surface vortex", the maximum *U* velocity is in the middle of the main channel at 65% of the water depth.

For the *U*' turbulent intensity (fig. 4.7b) a similarity with the isovels of *U* is observed. However, the bulging of the isovels *U*' is more intense and corresponds with the ascendant/descendant flows of the cross section. On the other hand, the lower turbulent intensity *U*' is observed in the middle of the main channel below the free-surface due to the dip-velocity phenomenon. In the case of the turbulent intensity *W*' (fig. 4.7c), a bulging of the isovels in the upper interface is again observed. The main difference between *U*' and *W*' is that, while the lower turbulent intensity *U*' is below the free-surface, the *W*' turbulent intensity decreases towards the free-surface. Further, the magnitude of *W*' is slightly smaller than the magnitude of *U*'.

Figure 4.8 shows the vertical distribution of U^+ for Y = 0.104 m, 0.205 m, 0.253 m and 0.380 m, with U^+ and Z^+ defined as:

$$U^+ = U/U_{*(Y)} \tag{4.2}$$

$$Z^+ = ZU_{*(Y)}/\nu \tag{4.3}$$

where the term $U_{*(Y)}$ is the local friction velocity. The local friction velocity was determined using the log-law, considering that the vertical location of the measured point could have some uncertainties. Therefore, a displacement ΔZ was considered in the vertical location. The ΔZ was adjusted so that the integral constant of the log-law (eq. 4.4, where $\kappa = 0.41$ is the von Kármán constant) was equal to $A = 5.3$, valid for 2D open-channel flow (Nezu and Nakagawa, 1993). The log-law is presented in fig. 4.8 by a line.

$$U^+ = \frac{1}{\kappa}\ln\left[\frac{(Z+\Delta Z)U_{*(Y)}}{\nu}\right] + A \tag{4.4}$$

The velocity profiles in the upper interface and floodplain present a trend similar to 2D open-channel flows, *i.e.* they follow the log-law in the inner layer and as they approach the free-surface they depart from the log-law to a log-wake law (Nezu and Nakagawa, 1993). In the main channel and lower interface the velocity profiles also follow the log-law, but they decrease abruptly near the free-surface, which is due to the presence of strong secondary currents.

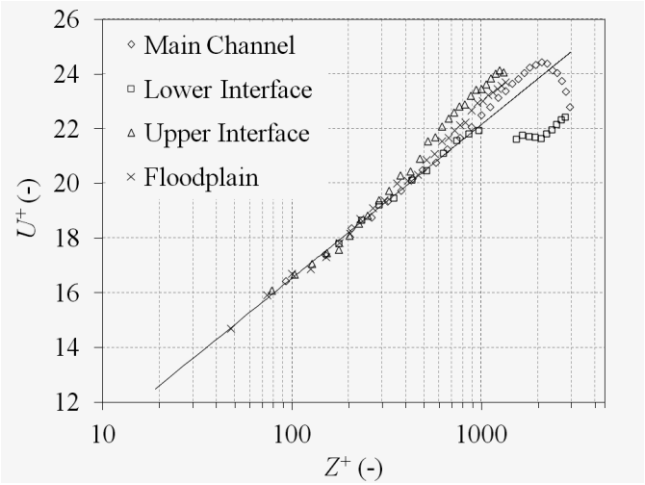

Figure 4.8 Vertical distribution of time-averaged velocity U.

Figure 4.9 shows the distribution of turbulent intensity $U^{'}$ against Z/H. In the figure is also included the universal eq. 4.5 valid for the intermediate region ($0.1< Z/H <0.6$) of 2D fully developed flows (Nezu and Nakagawa, 1993).

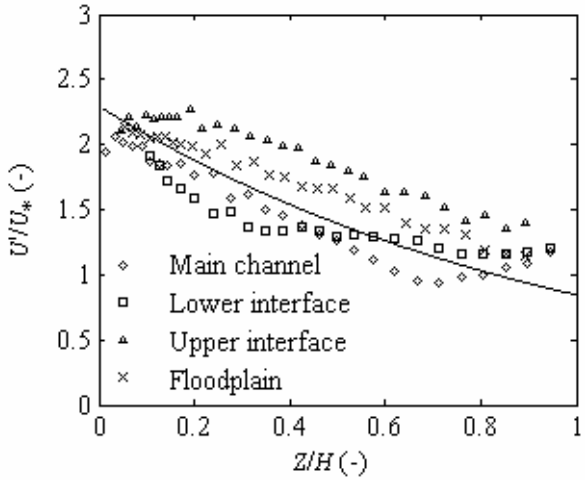

Figure 4.9 Vertical distribution of turbulent intensity U'.

$$U'/U_* = 2.30\exp\left(-Z/H\right) \tag{4.5}$$

The experimental results for the upper interface and floodplain seem to follow a similar trend to eq. 4.5, although with higher turbulent intensities. This means that the flow at those two verticals behaves like a 2D flow but with higher turbulence intensity. In the main channel the experimental data follows the universal equation until Z/H around 0.6. As the flow approaches

the free surface the turbulent intensity starts to increase, which is due to the presence of strong secondary currents. For the lower interface, until *Z*/*H* around 0.3, the turbulent intensity decreases and stays below the universal equation. For *Z*/*H* >0.3 the turbulent intensity reaches a plateau. The discrepancies between the experimental results and the universal eq. 4.5 clearly highlight the 3D character of the flow.

4.2.3.2 Turbulent longitudinal scales and dissipation

The velocities time series can be transformed into an equally spaced temporal record by taking an averaged time step, τ:

$$\tau = t_{\max} / n \tag{4.6}$$

being $t_{\max}$ the maximum time in the record and n the number of measurements in the record. The instantaneous velocity values for each time can be obtained from the original record through linear regression. Adopting Taylor's frozen-field hypothesis, the time record can be transformed into a space record, using a convection velocity, U_c, with a space interval

$$r = U_c \tau \tag{4.7}$$

In the present study, for each record, U_c was considered constant and equal to the time-averaged velocity *U*. Although this criterion implies that the convection velocity is the same for all flow scales, which is not true for most cases, it holds for large and intermediate scales if turbulent intensity is less than 20% (Tropea et al., 2007). The space record allows the computation of the longitudinal autocorrelation function (Pope, 2000)

$$\rho(r) = \frac{\overline{u'(r)u'(x+r)}}{\overline{u'^2}} \tag{4.8}$$

One example of autocorrelation function is presented in fig. 4.10 for the point *Z*/*H* = 0.46 in the main channel vertical. In the figure, the integral length scale obtained by eq. 4.9 (Pope, 2000) is also presented

$$L_x = \int_0^\infty \rho(r)\,\mathrm{d}r \tag{4.9}$$

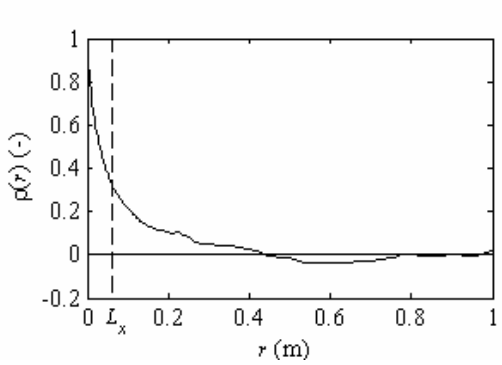

Figure 4.10 Longitudinal autocorrelation function.

Figure 4.11 shows the vertical distribution of the longitudinal integral scales obtained from the autocorrelation function for all points. In the figure, eq. 4.10 is also plotted with B_1 = 1.0, 1.5, 2.5 and 3.5. This equation was proposed by (Nezu and Nakagawa, 1993) for 2D fully developed open-channel flow, with B_1 approximately equal to 1.0.

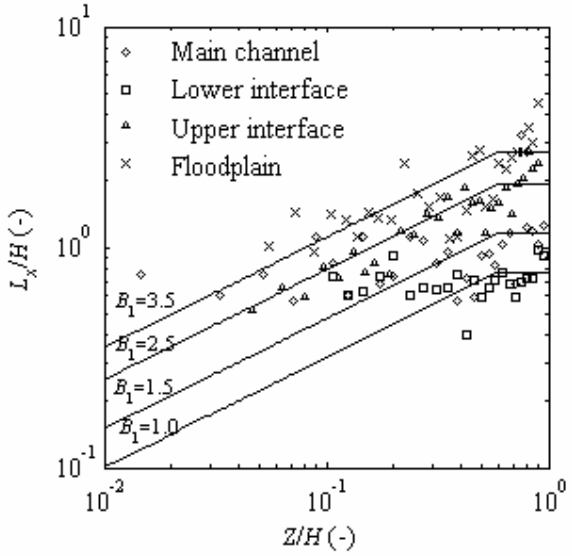

Figure 4.11 Vertical distribution of the longitudinal integral length scale, Lx.

$$\frac{L_x}{H} = \begin{cases} B_1 (Z/H)^{1/2} & \text{for } Z/H < 0.6 \\ 0.77 B_1 & \text{for } Z/H > 0.6 \end{cases} \tag{4.10}$$

The upper interface and the floodplain results fairly follow eq. 4.10, but with higher coefficient B_1. Near the free surface, contrary to eq. 4.10, the experimental data do not present a plateau, instead the integral length scale continue to increase towards the free-surface. For the main channel vertical the integral length scale is almost constant through the depth, with a value

close to the flow depth. This indicates that the secondary current in the main channel dictates the characteristic size of the large turbulent structures. The lower interface present a similar pattern of the one observed for the main channel, but with smaller integral scale.

In fig. 4.12 the longitudinal dissipation spectrum is presented for point Z/H = 0.8 in the lower interface. The spectrum was obtained using a Yule-Walker spectral estimator which is extremely smooth (Stoica and Moses, 2005), but allows an easy identification of the inertial subrange. The dissipation spectrum can be computed from the velocity power spectrum, E_{11}, using the Kolmogorov $-5/3$ law for the inertial subrange (Pope, 2000).

$$E_{11} = C_1 k_w^{-5/3} \varepsilon^{2/3} \Rightarrow \varepsilon = \left(E_{11} \Big/ \left(C_1 k_w^{-5/3} \right) \right)^{3/2} \tag{4.11}$$

where ε is the turbulent dissipation rate, k_w is the wave number and C_1 is a universal constant equal to ≈0.53. In the figure the dissipation rate, ε, was taken from the plateau and the integral scale, L_x, and the microscale, λ_x, are also presented.

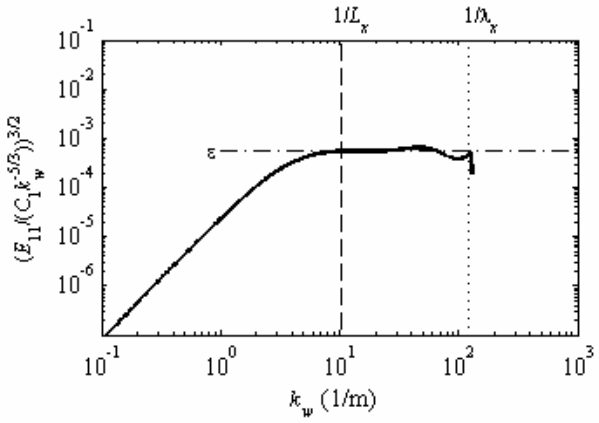

Figure 4. 12 Longitudinal dissipation spectrum for point Z/H = 0.8 in the lower interface.

The microscale was obtained from the dissipation rate by assuming isotropic turbulence (Tropea et al., 2007)

$$\lambda_x = \sqrt{\frac{30 \nu U'^2}{\varepsilon}} \tag{4.12}$$

Figure 4.13 shows the vertical distribution of the longitudinal microscale for all points. In the figure is also plotted the semi-theoretical relation proposed by Nezu and Nakagawa (1993) for 2D fully developed open-channel flow

$$\frac{\lambda_x}{H} = \sqrt{\frac{15B_1}{2.3KRe_*}}\left(\frac{Z}{H}\right)^{1/4} \exp\left(\frac{Z}{2H}\right) \tag{4.13}$$

where

$$Re_* = U_* H/\nu \tag{4.14}$$

$$K = 0.691 + 3.98/\sqrt{Re_L} \tag{4.15}$$

$$Re_L = U' L_x/\nu \tag{4.16}$$

In eq. 4.13 to 4.16 L_x is computed using eq. 4.10 and U' using eq. 4.5.

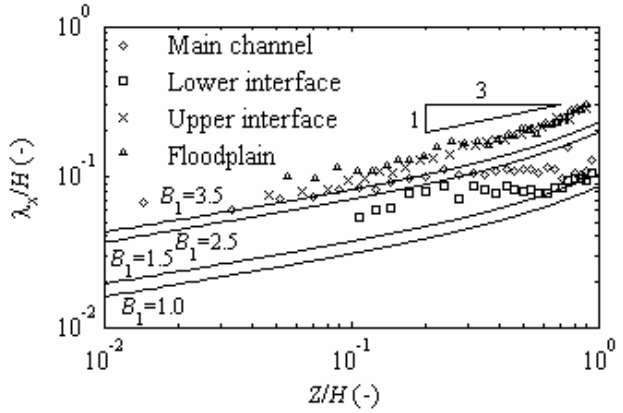

Figure 4.13 Vertical distribution of the longitudinal microscale, λ_x.

The results of the microscale for the floodplain and the upper interface are almost coincident and present a similar trend to the theoretical curves. The experimental values are higher than the theoretical ones, which can be attributed to the underestimation of U' values given by eq. 4.5 (see fig. 4.9). For the main channel and lower interface the experimental results depart from the theoretical curves, mostly due to the wrong estimation of U' caused by the influence of strong secondary currents.

Figure 4.14 shows the vertical distribution of the dissipation rate for all points, computed through the dissipation spectra as mentioned before (see fig. 4.12). In the figure, the equation proposed by Nezu and Nakagawa (1993) for 2D fully developed open-channel flows is included

$$\frac{\varepsilon H}{U_*^3} = \frac{12.2K}{B_1}\left(\frac{Z}{H}\right)^{-1/2} \exp\left(-\frac{3Z}{H}\right) \tag{4.17}$$

The experimental results show good agreement with the theoretical curves, except for the lower interface where the dissipation is substantially higher for the free-surface region. The extra dissipation must be linked to the strong secondary currents observed.

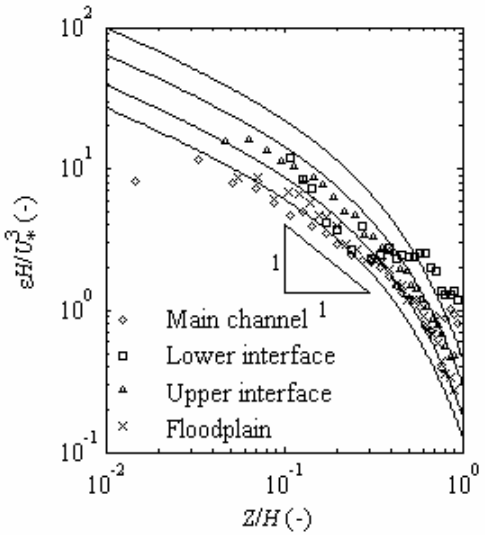

Figure 4.14 Vertical distribution of the dissipation rate, ε.

4.2.4 *Conclusions*

For deep water flow in straight compound channel the results presented above allow to extract the following conclusions:

- The universal laws for 2D fully developed open-channel flows are valid in the upper interface and floodplain, although the coefficients have to be increase, mostly due to the increase of turbulent intensity. This should be a consequence of the shallowness of the flow which contributes to maintain boundary turbulence as the dominant process.
- For the lower interface and main channel, the presence of strong secondary currents contributes to the non validity of the universal laws, even if their coefficients are changed. This means that the 3D character of the flow is "printed" in the turbulent field and boundary turbulence should not be dominant.

4.3 Influence of Vegetation on Compound-channel Turbulent Field

Azevedo, R., Leal, J. B., & Rojas-Solórzano, L. (2012). Influence of vegetation on compound-channel turbulent field. *River Flow* 2012, Murillo, R. ed, Taylor & Francis, 209-216 (ISBN 978-0-415-62129-8).

Abstract: During floods, rivers generally present a compound section configuration, constituted by a faster flow in the main channel and a slower one in the floodplains. The interaction of these flows has a complex turbulent 3D field composed by large-scale horizontal structures and secondary cells. These turbulent structures are responsible for significant lateral momentum transfer. Most rivers present also vegetation, namely trees along the floodplains edges. The wakes formed in front of the vegetation elements alter the classical compound channel turbulent field. In this paper, rods were placed at the edge of the floodplain of an experimental flume, simulating trees. A 2D LDV was used to measure the velocity field. The velocity distribution is modified by the rods due the formation of wakes. In particular, the 2D flow equations are not applicable and the turbulent scales and dissipation rate acquire a longitudinal variation due to longitudinal vortex propagation.

4.3.1 Introduction

During floods, rivers generally present a compound section configuration, constituted by a faster flow in the main channel and a slower one in the floodplains. The interaction of these flows has been studied by several authors (Bousmar and Zech, 1999; Knight and Shiono, 1990; Proust et al., 2010; Shiono and Knight, 1991; Tominaga and Nezu, 1991; Van Prooijen et al., 2005) that observed a complex turbulent 3D field composed by large-scale horizontal structures and secondary cells. These turbulent structures are responsible for significant lateral momentum transfer, increasing flow resistance and diminishing the total conveyance.

Most rivers present also vegetation, namely trees along the floodplains edges. The presence of these vegetation elements originates another source of flow resistance caused by drag force on the elements. The wakes formed in front of the vegetation elements also alter the classical compound-channel turbulent field. There have also been many studies focused on the effect of vegetation in compound channel flows, usually considering a vegetated floodplain (Naot et al., 1996; Nezu and Onitsuka, 2001; Rameshwaran and Shiono, 2007). From these studies it can be inferred that the drag force due to rigid vegetation is mainly dictated by stem geometry, stem displacement, stem density and flow conditions. The turbulence length scale is of the order of the stem diameter and turbulence intensities increase with the introduction of sparse vegetation due to the wake.

Although vegetation exists in most river floodplains, vegetation such as trees and shrubs are also common along the edges of the floodplains. Therefore, recently, several authors investigated the effect of rigid elements placed along the floodplain edge (Sanjou and Nezu, 2010; Sun and Shiono, 2009). Those authors associated their results with lateral momentum transfer. Analyzing the differences on turbulent field behind the natural vegetation and rigid stem is important since the secondary currents are strongly affected by the turbulence as well as the mean flow structure (Sun and Shiono, 2009)

In this paper, rods were placed at the edge of the floodplain of an experimental flume, simulating trees. Large rod spacing was tested to study its influence on the turbulent field, taking as reference the measurements made in the same flume without vegetation (Azevedo et al., 2012). A 2D Laser Doppler Velocimeter was used to measure the streamwise and vertical velocity components at different stations. The velocity distribution without vegetation is completely altered by the rods due the formation of wakes. In particular, the secondary currents become weaker, and the mixing layer horizontal vortices are replaced by two weaker horizontal vortices travelling in parallel on both sides of the bank region (Sun and Shiono, 2009).

4.3.2 Experimental Setup

The experiments were carried out in the asymmetric compound flume located at the Hydraulics Laboratory of University of Beira Interior, Portugal. The flume has a length of 11.60 m, a width of 0.79 m and was built over a cement structure. The floodplain has a width of 0.531 m and a mean longitudinal slope of 0.0911% while the main channel has a width of 0.205 m and a mean slope of 0.0986%. The region that separates the main channel and the floodplain is called interface and has a width of 0.054 m and a bankfull depth of 0.051 m. Figure 4.15 shows a scheme of the geometry of the asymmetric compound channel.

The water height was controlled using a gate at the final section of the channel and measured with a point gauge both in the main channel and in the floodplain. In order to reduce the lateral transfer between the floodplain and the main channel, a stainless steel sheet was placed at the channel entrance between the two sub-regions.

The flow velocity field was measured with a laser Dopler Velocimeter Innova 70C Argon series with a maximum power of 2W. Particles placed into the fluid were aluminum oxide powder with a diameter of 10μm, approximately.

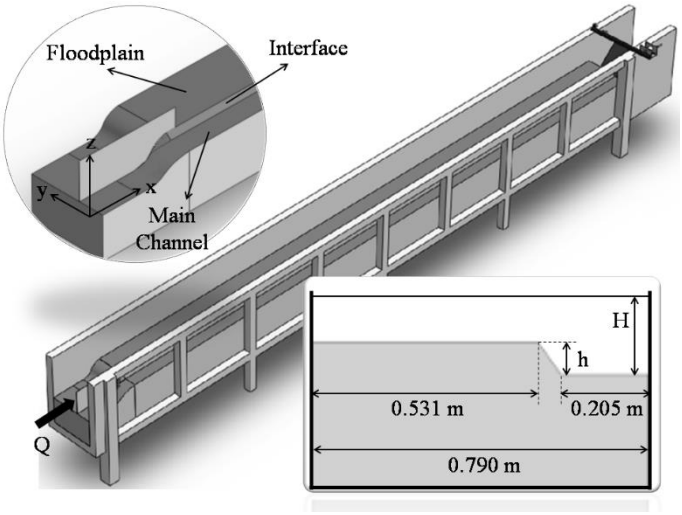

Figure 4.15 Description of the asymmetric compound open-channel flow.

To observe the influence of vegetation on the turbulent structure of the flow, several tubes were placed along the top of the interface, named upper interface. The tubes are of aluminum with 10 mm diameter. The separation distance between the tubes was of 1 m and the placement of the tubes started at 4.75 m from the inlet channel to 10.75 m. In order to determine the evolution of the velocity field along the channel, measurements took place in three cross sections, which were at 8.77 m, 9.25 m and 9.73 m from the inlet channel, as shown in fig. 4.16.

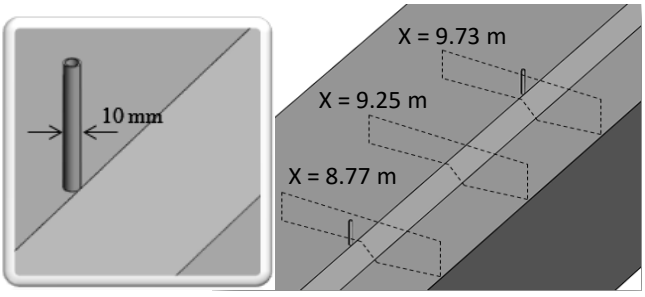

Figure 4. 16 Description of the measuring cross-sections

4.3.3 Results and Discussion

4.3.3.1 Test characterization

The terms used to describe the velocity field are *u* and *w* for the components of the instant velocity; *u'* and *w'* for the velocity fluctuations; *U* and *W* for the mean average velocity; and *U'* and *W'* for the turbulent intensity or r.m.s. values in the longitudinal direction, *X*, and vertical direction, *Z*.

Table 4.5 indicates the conditions at which the tests were performed. The discharges used were of 83.38 m^3/h, for the case without rods, and 82.99 m^3/h, for the case with rods, corresponding to an average water depth of 0.1033 and 0.1034 m, respectively. Determining the uniform depth with rods is not a simple process due to the disturbance of the free surface. In this case, the disturbance can be up to 3 mm. Figure 4.17 shows this disturbance.

Table 4.5 Experimental Conditions.

$Q\ (m^3/h)$	$H_{mc}\ (m)$	Hr	$U_{cs}\ (m/s)^*$	$U_*\ (m/s)^*$	$Re\ (x\ 10^4)^*$	Fr^*
83.38	0.1033	0.5	0.430	0.023	11.78	0.43
82.99	0.1034	0.5	0.435	0.023	11.07	0.43

* Calculated with the water depth of the cross-section.
0.1044 m tests without rods.
0.1035 m tests with rods.

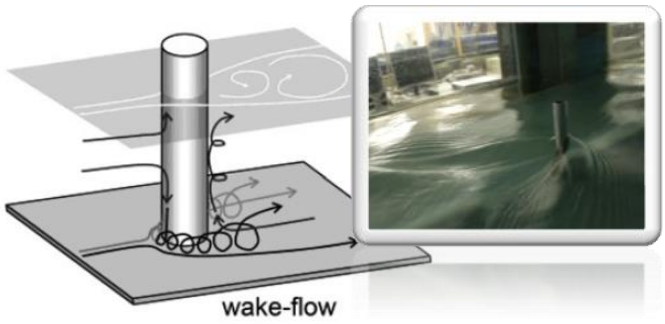

Figure 4.17 Schematic view of 3D turbulent structures around rigid stem (Schnauder and Moggridge, 2009) (Photograph of the experiments).

4.3.3.2 Velocity and turbulent intensity distribution

Figure 4.18 shows the *U* isovels distribution for the cases without rods measured at 9.0 m from the inlet of the channel (fig. 4.18a) and with rods measured at 8.77 m, 9.25 m and 9.73 m from the inlet of the channel (fig. 4.18b-4.18d), as well as *W* velocity distribution for each case.

In Figure 4a, the behavior of *U* isovels is governed by the momentum transfer due to the interaction between the main channel and floodplain flows, causing the formation of two strong longitudinal axis vortex (secondary currents) caused by the anisotropy of turbulence. Further, the main channel side-wall plays an important role in the formation of those two vortices, called "bottom vortex" and "free-surface vortex". The latter vortex is responsible for the maximum velocity *U* being achieved below the free-surface (Shiono and Knight, 1991).

The turbulent structure known to smooth channels is abruptly modified when rods are placed on the upper interface. New turbulent structures are generated due the interaction between rods and flow. Figure 4.18b shows the U isovels at approximately 2 cm after the rod, where new bulging is observed around the rod. Schnauder and Moggridge (2009) comment that for impermeable rod a recirculation of the flow exists behind the obstacle which explains the U velocity bulging in this region. Therefore, the approaching flow is slowed and part of the flow is deflected downward until the rod base, causing a horseshoes-vortex system as presented in fig. 4.17. This horseshoes-vortex system is the responsible for the U isovels bulging at both side of the rod in fig. 4.18b.

Further, the U velocity is accelerate in the middle of the main channel in the experiments with rods for water depths higher than $Z/H = 0.4$. However, for depths minor than $Z/H = 0.4$ the flow do not present significant disturbance compared with the measurements without rods. For the case with rods the maximum U velocity is in the middle of the main channel at a water depth of $Z/H \approx 0.85$, while for case without rods that value is located at $Z/H \approx 0.65$

In the case of W velocity for the section located between rods in the zone close to the interface, it can be seen the existence of an ascendant flow with higher intensity in the direction of the free surface (fig. 4.18c). This ascendant flow is not observed in sections located before and after the rods (figs. 4.18d, 4.18b, respectively). The presence of this ascendant flow is probably due to the decreasing of the wake intensity and the increasing of the interaction of the floodplain flow and the main channel flow, as seen in compound channel flows with rods. The magnitude of this ascendant flow as well as the magnitude of the descendant flow, observed in the vicinity of the upper interface, are of approximately $0.40U_*$. These magnitudes are slightly higher than the ascendant/descendant flows observed in the main channel and the interface for the case without rods ($\approx 0.30U_*$). Additionally, the magnitude of the velocity W upstream of the roughness is $0.40U_*$, showing a maximum value of $0.55U_*$ at Z/H between 0.60 and 0.75 (see fig. 4.18d). It should be noted that the descendant flow is responsible for the generation of horseshoes-vortex explained by Schnauder and Moggridge (2009). In the case of the velocity W downstream of the rod, the value is much higher, around $4.45U_*$ (fig. 4.18b).

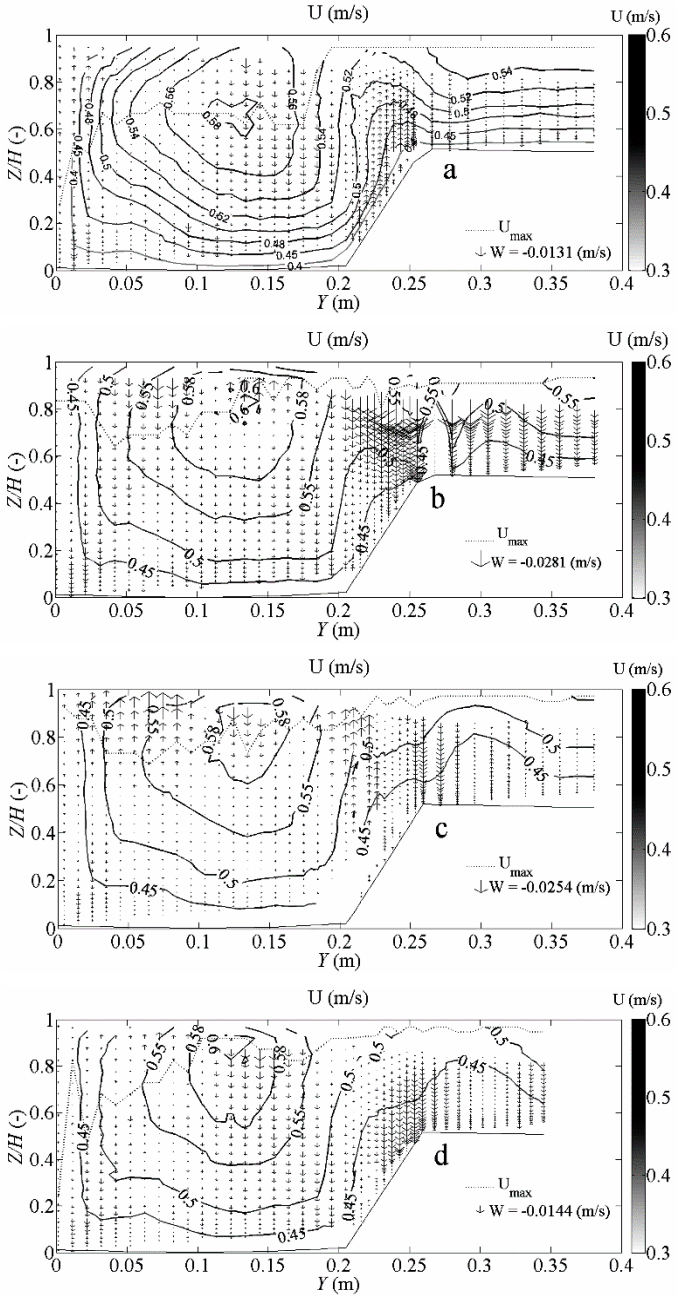

Figure 4.18 Isovels of mean velocity *U* and vectors of mean velocity *W*: a) without rods, *X* = 9.00 m; b) with rods, *X* = 8.77 m; c) with rods, *X* = 9.25 m; d) with rods, *X* = 9.73 m.

The turbulence intensities distribution *U'* and *W'* are presented in figs. 4.19 and 4.20, respectively, which corresponds to the cross section downstream of the rod. For the turbulent intensity *U'*, it is observed again a bulging of the isolines in the region near the rods due to the secondary currents generated by the interaction between the rods and the flow. Also, the minimum turbulent interaction *U'* is at the center of the main channel below the free surface and then starts to increase in the direction of the free surface due to the interaction of diverging flow from the rods and the boundary layer of the main channel side wall as seen in fig. 4.19. This same behavior is observed for the turbulent intensity *W*', fig. 4.20.

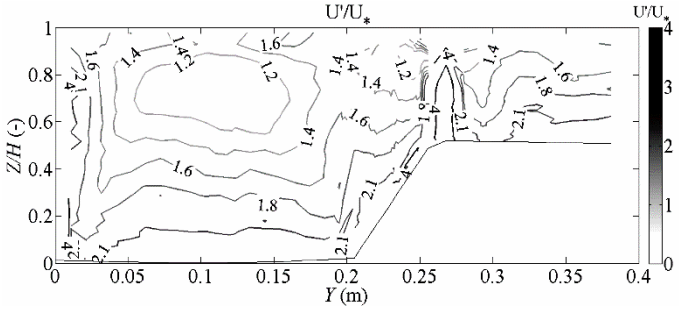

Figure 4.19 Isovels of turbulent intensity *U*' in the lee of the rod.

In the section near the free surface with rods, fig. 4.19, it can be seen that turbulent intensity *U'* increases in the direction of the free surface. It should be noted that in this zone the free surface suffers a concavity caused by the rod, as seen in fig. 4.17. Moreover, fig. 4.19 and fig. 4.20 show how the maximum turbulent intensity *U'* and *W'* are located behind the roughness, due to the existing recirculation.

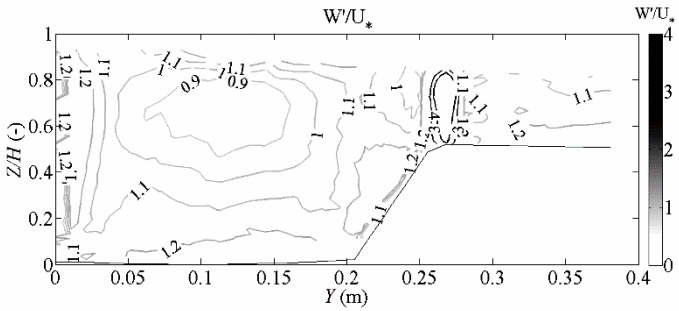

Figure 4.20 Isovels of turbulent intensity *W*' in the lee of the rod.

Figure 4.21 shows the *U* velocity distribution at the center of the main channel, at the lower interface, at the upper interface and at the floodplain for the three measuring cross-sections as well as for the case without rods.

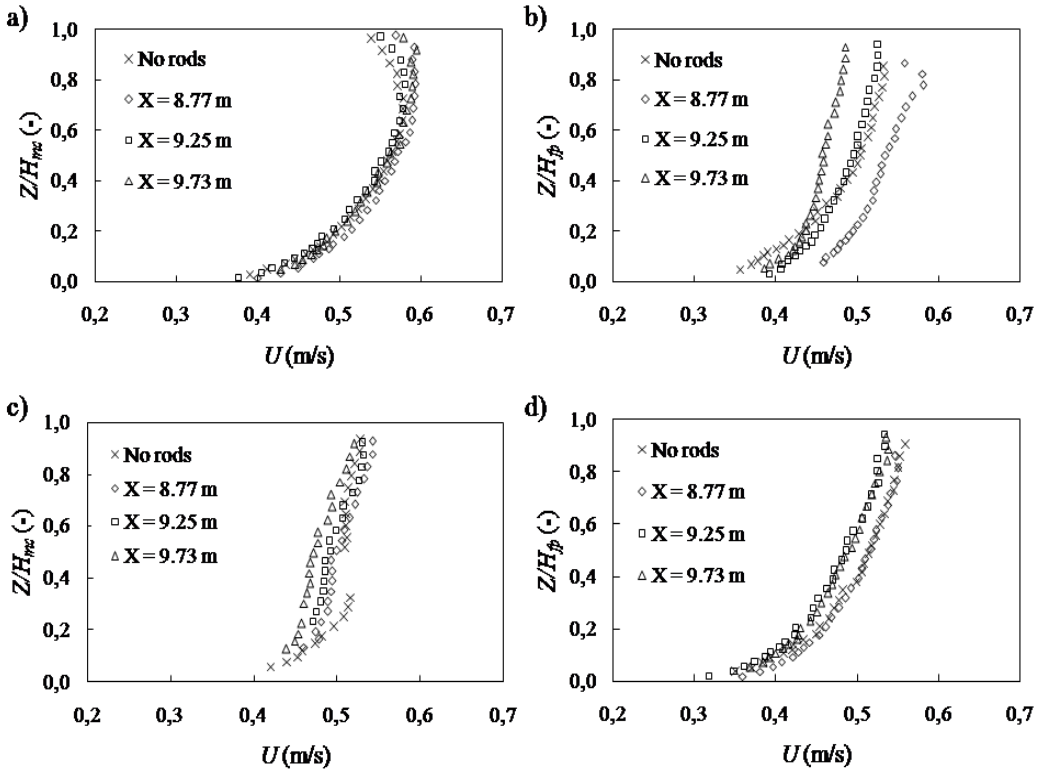

Figure 4.21 Vertical distribution of time-averaged velocity *U*: a) Main channel; b) Upper Interface; c) Lower Interface; d) Floodplain.

The velocity profiles measured at the center of the main channel are very similar to each other, except for the area near the free surface $Z/H \approx 0.85$, where the profiles measured before and after the rod (X = 9.73 m and X = 8.77 m, respectively) have their maximum value due to the secondary currents originated by the rods.

In the case of the velocity profile taken in the main channel at X = 9.25 m, it can be seen that it is very similar to the profile taken without rods; this is due to the decrease of the influence caused by the secondary currents. In the case of the profiles taken at the lower interface, fig. 4.21c shows that the maximum velocity is reached in the area near the free surface, except for the profile measured without rods, showing a large increase in speed for $Z/H \approx 0.3$ due to the mass transfer generated by the particular secondary currents for compound channels without rods. Figure 4.21b shows the distribution of the velocity U in the region of the upper interface. For X = 8.77m it can be observed that the maximum velocity is reached at approximately $Z/H \approx 0.8$ due to the deformation caused in the free surface which can be seen in fig. 4.17. It is also showed a deep slowdown of the flow from X = 8.77 m (area downstream of the rod) to X = 9.73 m (area upstream of the rod). Again, this deceleration/acceleration of the flow before and after the rod is due to the secondary currents existing in that area. As expected, the velocity profile that most closely matches the measured profile without rods is that measured at X = 9.25 m, where the influence of the secondary currents generated by the rods is lower. In the case of the floodplain region, fig. 4.21d shows how the velocity U for X = 9.25 m

and 9.73 m is slightly lower than the one for the profile measured without rods except for the profile measured at X = 8.77 m which is very similar to the velocity U without rods.

Figure 4.22 shows the distribution of turbulent intensity U' against Z/H for tests without and with rods. In the figure is also included the universal eq. 4.18 valid for the intermediate region ($0.1< Z/H <0.6$) of 2D fully developed flows (Nezu and Nakagawa, 1993)

$$U'/U_* = 2.30\exp\left(-Z/H\right) \tag{4.18}$$

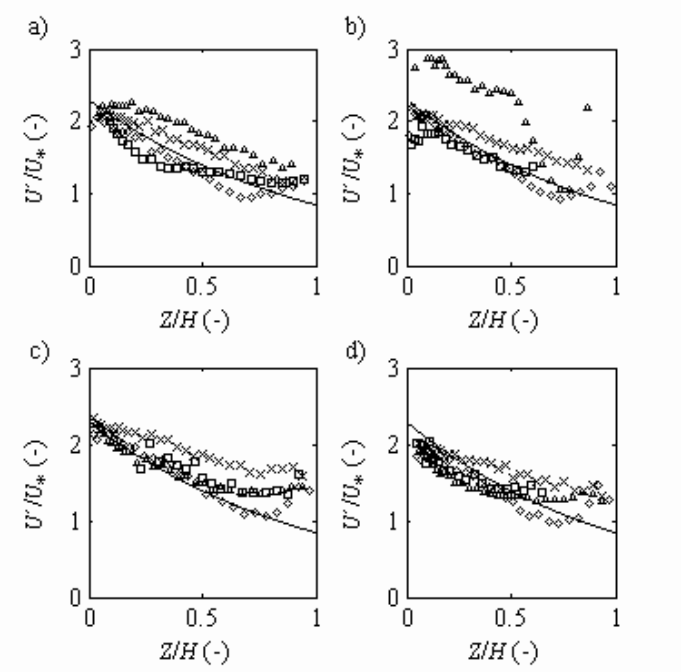

Figure 4.22 Vertical distribution of turbulent intensity U': a) without rods, X = 9.00 m; b) with rods, X = 8.77 m; c) with rods, X = 9.25 m; d) with rods, X = 9.73 m. (◊) Main channel, (□) Lower interface, (Δ) Upper interface, (×) Floodplain, (—) equation (4.18).

For the situation with rods, the main channel and lower interface turbulent intensities follow the universal eq. 4.18 bellow the bankfull depth (i.e., $Z/H \approx 0.5$). Above that level U' increases due to the vortex structure generated by the rods. In the upper interface, the behavior of U' is highly influence by the rods. In the section near the rod, U' presents high values (fig. 4.22b) that decrease downstream (figs. 4.22c, 4.22d). In the floodplain, U' is always higher than the values given by eq. 4.18, and is similar for all sections with and without rods.

The discrepancies between the experimental results and the universal eq. 4.18 clearly highlight the 3D character of the flow, while the differences between the tests without rods (fig. 4.22a) and with rods (figs. 4.22b-4.22c) show the influence of the rods in the increase of U', specially for elevation above the bankfull depth.

4.3.3.3 Turbulent longitudinal scales and dissipation

The velocities time series can be transformed into an equally spaced temporal record by taking an averaged time step, τ:

$$\tau = t_{\max} / n \tag{4.19}$$

where t_{max} = maximum time in the record; and n = number of measurements in the record. The instantaneous velocity values for each time can be obtained from the original record through linear regression. Adopting Taylor's frozen-field hypothesis the time record can be transformed into a space record, using a convection velocity, U_c, with a space interval

$$r = U_c \tau \tag{4.20}$$

In the present study, for each record, U_c was considered constant and equal to the time-averaged velocity U. Although this criterion implies that the convection velocity is the same for flow scales, which is not true for most cases, it holds for large and intermediate scales if turbulent intensity is less than 20% (Tropea et al., 2007). The space record allows the computation of the longitudinal autocorrelation function (Pope, 2000)

$$\rho(r) = \frac{\overline{u'(r)u'(x+r)}}{\overline{u'^2}} \tag{4.21}$$

The integral length scale can be obtained by (Pope, 2000)

$$L_x = \int_0^\infty \rho(r)\,\mathrm{d}r \tag{4.22}$$

Figure 4.23 shows the vertical distribution of the longitudinal integral scales obtained from the autocorrelation function for all points. In the figure is also plotted eq. 4.23 proposed by (Nezu and Nakagawa, 1993) for 2D fully developed open-channel flow, where B_1 is approximately equal to 1.0.

$$\frac{L_x}{H} = \begin{cases} B_1 (Z/H)^{1/2} & \text{for } Z/H < 0.6 \\ 0.77 B_1 & \text{for } Z/H > 0.6 \end{cases} \tag{4.23}$$

The presence of the rods increases the integral scales in the lower interface and in the floodplain due to the vortex structure. In the upper interface, near the rods (fig. 4.23b), the integral scales are smaller and then increase downstream (figs. 4.23c, 4.23d). The experimental results are always higher than the 2D flow results (eq. 4.23). Moreover, the integral scale for each vertical appears to reach a constant value for the inner layer (*i.e.*, $Z/H < 0.2$), indicating that bottom turbulence limits the integral scale but does not decrease it like in 2D flows.

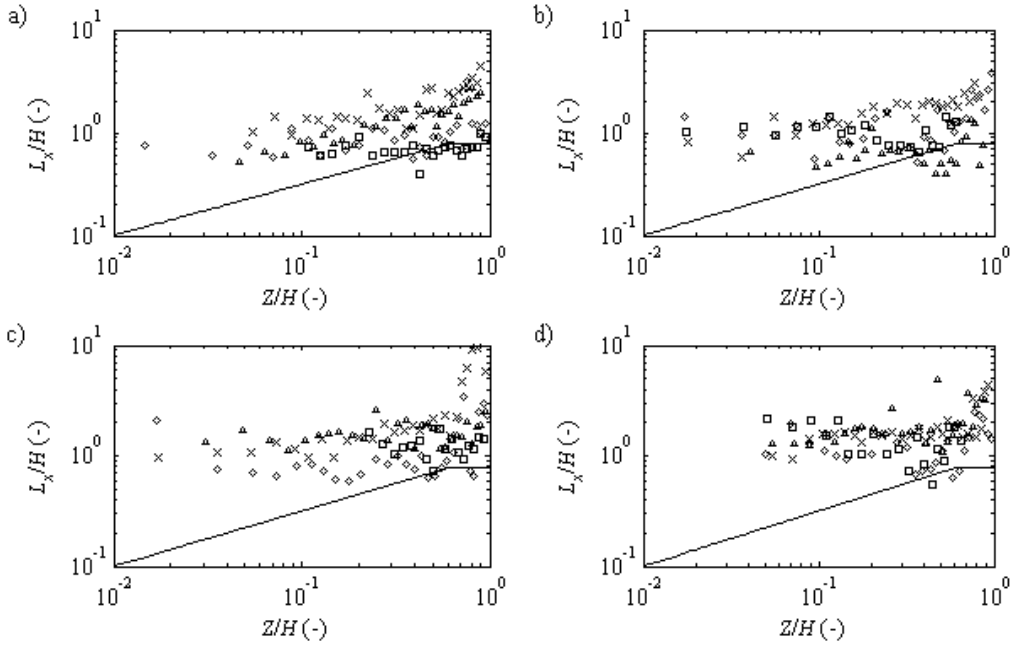

Figure 4.23 Vertical distribution of the longitudinal integral length scale, L_x: a) without rods, X = 9.00 m; b) with rods, X = 8.77 m; c) with rods, X = 9.25 m; d) with rods, X = 9.73 m. (◊) Main channel, (□) Lower interface, (Δ) Upper interface, (×) Floodplain, (-) equation (4.23)

In fig. 4.24, the longitudinal dissipation spectrum is presented for point Z/H = 0.8 for the upper interface of all tests. The spectrum was obtained using a Yule-Walker spectral estimator which is extremely smooth (Stoica and Moses, 2005), but allows an easy identification of the inertial subrange. The dissipation spectrum can be computed from the velocity power spectrum, E_{11}, using the Kolmogorov $-5/3$ law for the inertial subrange (Pope, 2000)

$$E_{11} = C_1 \kappa^{-5/3} \varepsilon \Rightarrow \varepsilon = E_{11} \Big/ \left(C_1 k_w^{-5/3} \right) \tag{4.24}$$

The microscale was obtained from the dissipation rate by assuming isotropic turbulence (Tropea et al., 2007)

$$\lambda_x = \sqrt{\frac{30\nu U'^2}{\varepsilon}} \tag{4.25}$$

The dissipation spectra (fig. 4.24) shows some differences between tests without rods and with rods, and in this last one also presents different behavior depending on the longitudinal coordinate. The intermediate region, between the integral and the microscale, shrinks from case without rods to case with rods just after the rod. For sections downstream of the rod the intermediate region seems to maintain its dimensions, enlarging for the section located further downstream. The procedure to compute the dissipation from the inertial subrange appears to be valid, since a plateau exists. For the section near the rod the procedure can give worst predictions, since the plateau is almost inexistent.

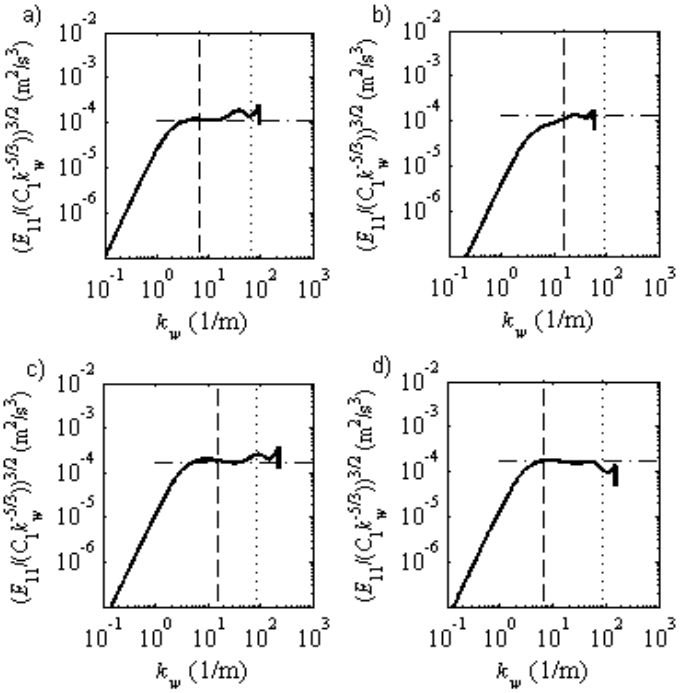

Figure 4.24 Longitudinal dissipation spectrum for point Z/H = 0.8 in the upper interface: a) without rods, X=9.00 m; b) with rods, X = 8.77 m; c) with rods, X = 9.25 m; d) with rods, X = 9.73 m.

Figure 4.25 shows the vertical distribution of the longitudinal microscale for all points. In the figure is also plotted the semi-theoretical relation proposed by Nezu and Nakagawa (1993) for 2D fully developed open-channel flow

$$\frac{\lambda_x}{H} = \sqrt{\frac{15B_1}{2.3KRe_*}}\left(\frac{Z}{H}\right)^{1/4} \exp\left(\frac{Z}{2H}\right) \tag{4.26}$$

where

$$Re_* = U_* H / \nu \tag{4.27}$$

$$K = 0.691 + 3.98 / \sqrt{Re_L} \tag{4.28}$$

$$Re_L = U' L_x / \nu \tag{4.29}$$

where L_x is computed using eq. 4.23 and U' using eq. 4.18.

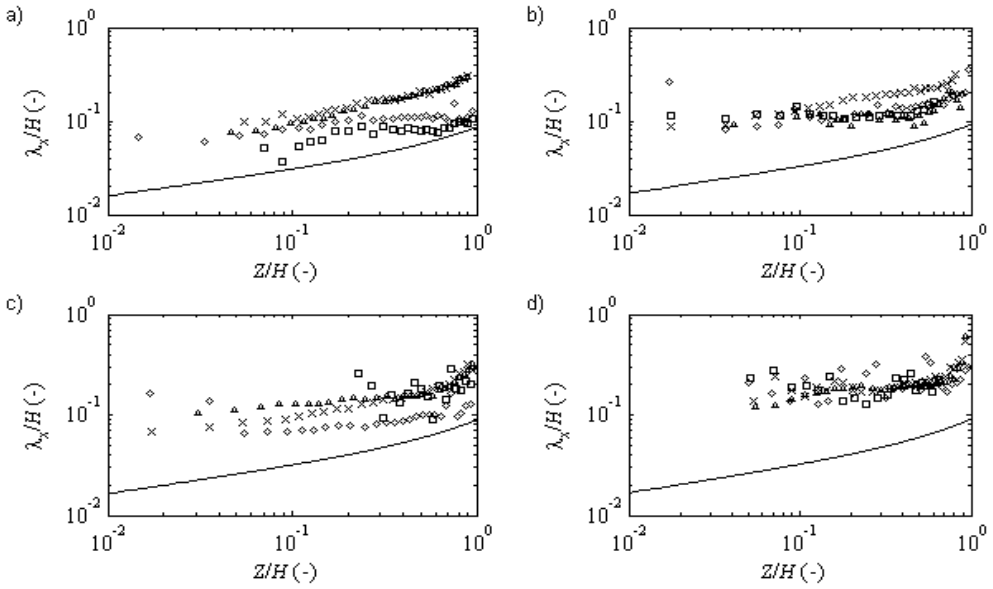

Figure 4.25 Vertical distribution of the longitudinal microscale, λ_x: a) without rods, X = 9.00 m; b) with rods, X = 8.77 m; c) with rods, X = 9.25 m; d) with rods, X = 9.73 m. (◊) Main channel, (□) Lower interface, (Δ) Upper interface, (×) Floodplain, (—) equation (4.26).

The microscales for all tests are higher than the 2D flow values given by eq. 4.26. The trend of the experimental results follows approximately that equation in the outer region (i.e., Z/H), but is different for the inner layer, where a plateau exists. The values for the rods case increase from the section near the rod (fig. 4.25b) to the section located immediately downstream (fig. 4.25c). As the flow develops downstream the microscales increase again (fig. 4.25d) and have similar values for all verticals.

Figure 4.26 shows the vertical distribution of the dissipation rate for all points, computed through the dissipation spectra as mentioned before (see fig. 4.24). In the figure, the equation proposed by Nezu and Nakagawa (1993) for 2D fully developed open-channel flows is included

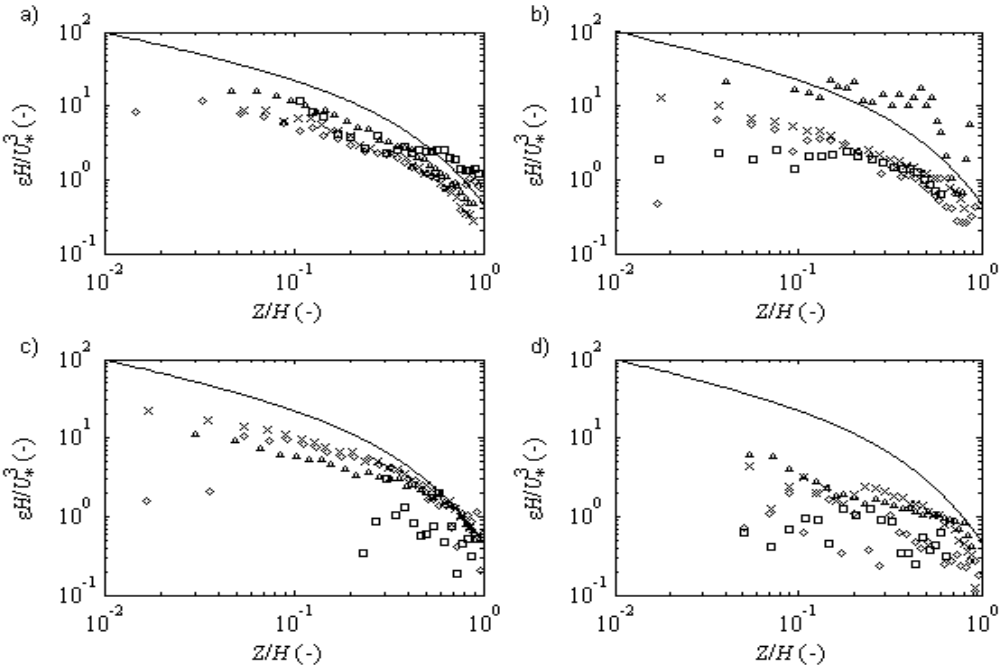

Figure 4.26 Vertical distribution of the dissipation rate, ε: a) without rods, X = 9.00 m; b) with rods, X = 8.77 m; c) with rods, X = 9.25 m; d) with rods, X = 9.73 m. (◊) Main channel, (□) Lower interface, (Δ) Upper interface, (×) Floodplain, (—) equation (4.30).

$$\frac{\varepsilon H}{U_*^3} = \frac{12.2K}{B_1}\left(\frac{Z}{H}\right)^{-1/2} \exp\left(-\frac{3Z}{H}\right) \tag{4.30}$$

All experimental results present smaller dissipation than the one for 2D flows given by eq. 4.30, excepting the vertical in front of the rod (fig. 4.26b). Therefore vortex structure originated at the rods seems to block the usual interaction between main channel and floodplain flows. For the mean channel, lower interface and floodplain verticals the dissipation is smaller for the section near the rod (fig. 4.26b) and increases immediately downstream (fig. 4.26c). Further downstream (Figure 4.26d) the dissipation decreases again. These results indicate that the vortex structure created by the rods influences dissipation for all verticals and produces a longitudinal variability.

4.3.4 Conclusions

For deep water flow in straight compound channel with rigid elements along the floodplains edges the results presented above allow to extract the following conclusions:

- The universal laws for 2D fully developed open-channel flows are not valid for the case with rods, due to the dominant influence of the wakes generated by the rods that govern the turbulent field instead of the boundary layer.
- The integral length scale seems to have an almost constant value in the studied verticals, which indicates that the wakes exert their influence not only near the free-surface but also in regions close to the bottom.
- The turbulent microscale and dissipation rate acquire a longitudinal variation due to the vortex propagation in the downstream direction. Excluding the vertical at the upper interface, the microscale scale is higher and the dissipation is lower in the section nearest to the rod. Further downstream the microscale decreases and the dissipation increases. After, the behavior is inverse and the microscale increases whereas the dissipation decreases.
- At the upper interface vertical near the rod the microscale is minimum, but still above the 2D flow values, and the dissipation is maximum exceeding the 2D flow values.

4.4 Turbulent Structures, Integral Length Scale and Dissipation Rate in Compound Channel Flow

Azevedo, R., Leal, J. B., & Rojas-Solórzano, L. (2016). "submitted to Flow Measurements and Instrumentation"

Abstract: In the present study, high data rate measurements were obtained for the streamwise and vertical velocity components using 2D Laser Doppler Velocimeter, allowing the characterization of the turbulent field in a straight compound-channel flow for three different uniform flow water depths, corresponding to "deep flows", "intermediate flows" and "shallow flows" conditions. Several methodologies were studied to process the data and to obtain autocorrelation functions, integral length scale and dissipation rate. The Sample and Hold method was adopted to interpolate the unevenly spaced record and calculate the autocorrelation function; the integral-stop-value 1/e was used to estimate the integral length scale; and the dissipation rate was estimated through the velocity energy spectrum. A double shear layer composed of two counter-rotating vertical oriented vortices, interacting with the secondary currents, is observed in the interface region for deep flow conditions. By decreasing the water depth, the interface region becomes dominated by a strong mixing layer of vertical oriented vortices with high dissipation rate and large integral length scale, acting as a vertical wall to the weak secondary currents that develop at the main channel. The determination of the integral length scale permits to confirm the existence and the strength of these turbulence structures, unveiling the strong mixing layer as the origin of the highest integral length scales, even higher than the flow depth, and as the most efficient mechanism to redistribute turbulence generated at the bottom towards upper flow regions. Despite the high complexity of turbulence structures present in the flow, for all water depths, a linear dependence is depicted between integral length scale, dissipation rate, and streamwise turbulent intensity.

4.4.1 *Introduction*

The most natural water streams and artificial channels located in the environment are classified as compound channel due the shape of their cross-section in flood condition. Over the past decades, a great effort has been made to understand the physical laws that define the behavior of the mean flow variables in straight compound-channel flows (Knight and Shiono, 1990; Shiono and Knight, 1991; Tominaga and Nezu, 1991). However, few studies have been focused in the distribution of scales and dissipation rate of turbulence due to the difficult task of characterizing the turbulent field.

In the present study, several methodologies were used to characterize the turbulent field and estimate the streamwise integral length scale and the dissipation rate. For that purpose, high data rate measurements in uniform flow conditions were obtained using 2D Laser Doppler Velocimeter in an experimental compound flume. Special attention was given to alternative methodologies for data processing. In order to estimate the integral length scale and dissipation rate of turbulence structures, a time-step and interpolation method were defined to resample the instantaneous velocity record. Moreover, several methodologies were studied to estimate the integral length scale and dissipation rate. Throughout the data processing, Taylor's frozen-field approximation was adopted (Tropea et al., 2007).

Three different discharge rates were used, corresponding to the relative water depth Hr = 0.50, Hr = 0.31 and Hr = 0.23 (Hr is defined as the ratio between floodplain and main channel water depths), in order to compare the results between "deep flows", "intermediate flows" and "shallow flows". For "deep flows", the existence of a local minimum of the depth-averaged streamwise velocity U_d at the interface due the ascendant flow, originates two counter-rotating vertical oriented vortices that interact with the secondary currents. However, for lower water depth, the two counter-rotating vertical vortices are replaced by one strong vertical oriented vortex that acts as a "vertical wall" in the interface region, diminishing the secondary currents that develop at the main channel (Stocchino and Brocchini, 2010).

The different restructuration of the flow for deeper and shallower flows has also impact on the turbulent intensity. For deeper flows, the turbulent intensity distribution follows the behavior of the secondary currents throughout the cross-section, presenting similar turbulent intensity distribution and normalized isolines of mean velocity, while for shallower flow the turbulent intensity distribution is dictated by the mixing layer present at the interface region (Nezu et al., 1999; Stocchino and Brocchini, 2010). However, few information is known about how the restructuration of the flow between "deep flows", "intermediate flows" and "shallow flows" affect the integral length scale and dissipation rate distribution.

In this paper, a methodology to process high data rate measurements as well as an estimation of the turbulent field, the integral length scale distribution and the dissipation rate distribution throughout the cross-section will be presented, which never has been referred before for compound channel flows.

4.4.2 *Experimental Setup*

Experimental tests comprising three different water depths were conducted in an asymmetric compound flume channel, located at the Hydraulic Laboratory of University of Beira Interior - Portugal. Figure 4.27 presents the main geometrical characteristics of the experimental flume.

The channel was fed through a pump with an electromagnetic flowmeter installed at the outlet to control the flow discharge. A single gate weir located in the final section of the flume was used to control the water depth. In order to reduce the entrance lateral momentum transfer between the main channel and the floodplain, at the inlet of the flume channel a separating plate and a set of 1"-diameter/ 0.3m-long tubes were installed. Additionally, 6 mm-diameter stones were placed along the first 0.5 m at the inlet main channel to promote the development of the turbulent boundary layer in a short streamwise distance (Bousmar and Zech, 1999; Van Prooijen et al., 2005).

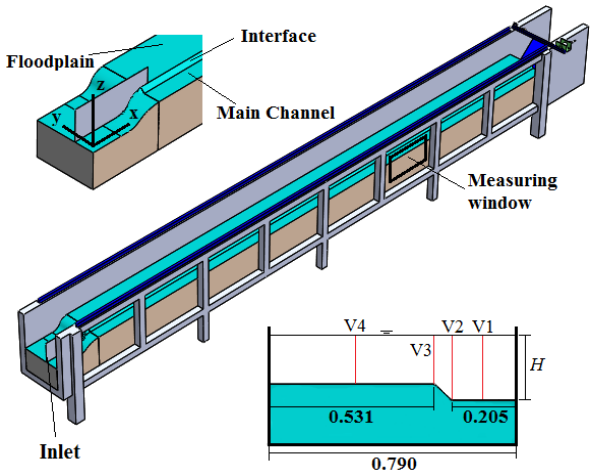

Channel Length L (m)	11.600 ± 0.001
Channel Wide B (m)	0.790 ± 0.002
Main Channel Width B_{MC} (m)	0.205 ± 0.002
Floodplain Width B_{FP} (m)	0.531 ± 0.001
Interface Width B_I (m)	0.054 ± 0.002
Interface Depth h (m)	0.051 ± 0.001
Main Channel Slope S_{MC} (%)	0.099 ± 0.004
Floodplain Slope S_{FP} (%)	0.091 ± 0.003
Channel Slope S_0 (%)	0.095 ± 0.003

V1: Vertical Profile in Main Channel
V2: Vertical Profile in Lower Interface
V3: Vertical Profile in Upper Interface
V4: Vertical Profile in Floodplain

Figure 4.27 Main geometrical characteristics of the flume

Velocity field measurements were made using a 2D Laser Doppler Velocimeter (LDV) in backscattering mode through a glass window located on the main channel lateral wall. Once the uniform flow conditions were established, measurements were made in a cross-section located at 9.0 m from the inlet, as explained in details in next paragraphs. The measurement time was 210 s per point and aluminum oxide powder with diameter less than 10 µm was used as seeding. The maximum data sampling acquisition frequency measured was around 1000 Hz. However, the acquisition frequency decreased for measurement points close to the walls, sampling at frequencies around 30 Hz, since flow velocity in those regions is smaller and uniform spreading of the seeding in the cross-section is not typically possible to ensure.

Table 4.6 indicates the conditions at which the tests were performed. In that table $Hr = H_{fp}/H_{MC}$ is the relative water depth, $U_{CS} = Q/A_{CS}$ is the cross-section averaged

velocity, A_{CS} is the cross-section area, $U_* = \sqrt{gR_h S_o}$ is the friction velocity, where g = 9.8 m/s2, Rh is the hydraulic radius, So is the bottom slope, $Re = 4R_h U_{CS}/\nu$ is the Reynolds number, where ν is the kinematic viscosity of water, and $Fr = U_{CS}/\sqrt{gH_{MC}}$ is the Froude number.

Table 4.6 Flow properties for the three experimental tests.

Q (l/s)	H_{MC} (m)	Hr	T (ºC)	U_{CS} (m/s)	U_* (m/s)	Re $\times 10^4$	Fr
23.16	0.1033	0.50	30.0	0.4301	0.0226	11.78	0.43
9.86	0.0744	0.31	26.0	0.3170	0.0176	4.88	0.37
6.83	0.0666	0.23	26.5	0.2713	0.0159	3.47	0.33

To establish the uniform flow, measurements of the water depth along the middle of the main channel and in the middle of the floodplain were taken allowing the comparison between the free-surface and bottom slopes. The water depth obtained for each flow condition was compared with the predicted value by Divide Channel Method and Single Channel Method, to ensure that its value was bounded by both methods (Bousmar et al., 2005). To verify the development of boundary and mixing layers, four velocity vertical profiles (see fig. 4.28) at cross-sections 4.5, 6.0, 7.5 and 9.0 m from the inlet were measured. For *Hr* = 0.50, the difference of the depth-averaged velocity (U_d) between vertical profiles taken at 7.5 and 9.0 m was 0.47%, 0.59%, 2.62% and 1.13% for main channel, lower interface, upper interface and floodplain, respectively. These small differences confirm the establishment of a quasi-uniform flow. The same procedure was also followed for the other relative water depths.

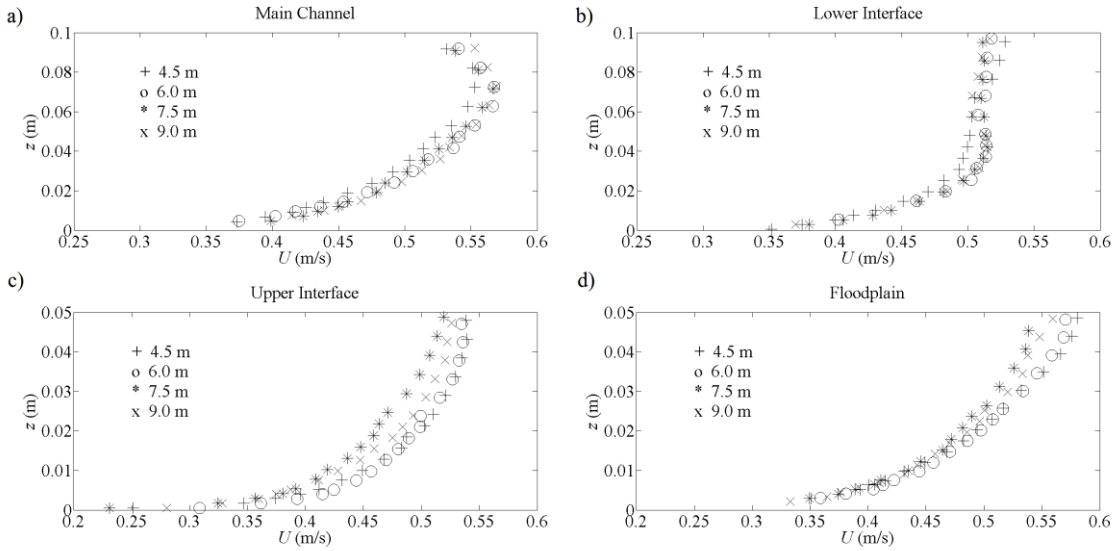

Figure 4.28 Vertical profiles of streamwise velocity at different cross-sections (*Hr* = 0.5). a) Middle of main channel; b) Lower interface; c) Upper interface; d) Middle of floodplain

To characterize the cross-section at 9.0 m from the inlet, 1148, 1050 and 766 points were measured for *Hr* = 0.50, 0.31 and 0.23, respectively, concentrating more points near the bottom and at the interface (see fig. 4.29b). Due to the lateral set-up of the LDV, it was not possible to measure the *w* component near the free-surface and bottom of the channel (see fig. 4.29a), since the laser beams interfered with those boundaries.

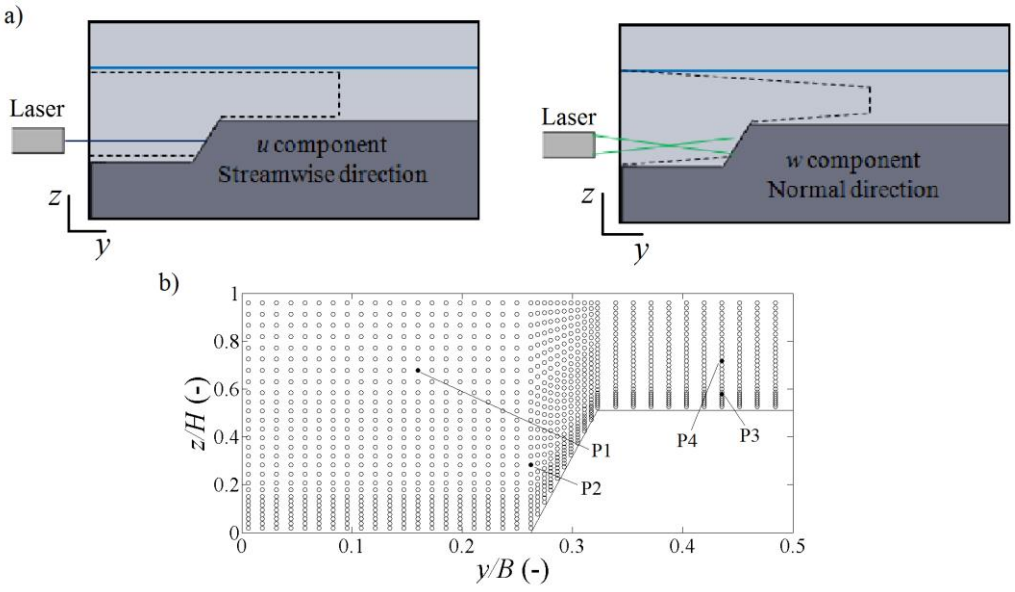

Figure 4.29 Description of the measurement points in a cross-section with LDV equipment in the compound channel flow. a) Measurement field visualization for *u* component velocity and *w* component velocity. b) Measurement mesh to characterize the turbulent structures for *Hr* = 0.50 (1148 points) and location of points P1, P2, P3 and P4.

4.4.3 *Methodology*

4.4.3.1 Resampling

The raw data was filtered defining a maximum turbulent intensity which was well over the expected natural random fluctuation of the velocity (0.8 times the mean average velocity for u component and 0.3 for w component). This procedure was useful to clean outliers mainly in points near the walls that presented obvious erroneous behavior. Finally, the measurements were filtered with the Phase-Space Thresholding Method developed by Goring and Nikora (2002).

In all the analysis presented through this section, four measurement points will be used (see fig. 4.29b). These points were chosen as representatives of different flow regions: free-surface (point P1), interaction between vortices (point P2), near wall (point P3), and 2D flow (point P4).

Throughout the analysis, Taylor's frozen-field approximation was adopted to transform the time record to a space record using a convection velocity U_c. The convection velocity is influenced by the turbulent intensity of the flow (Tropea et al., 2007). That influence can be incorporated as suggested by L'vov et al. (1999):

$$U_c = \sqrt{(U)^2 + \frac{1}{N-1}\sum_{i=1}^{N}\left(u'_i{}^2\right)} \tag{4.31}$$

where U is the streamwise time-averaged velocity and u'_i is the velocity turbulent fluctuation in direction i.

To characterize the turbulent field, different methods were used in order to estimate the integral length scale and the dissipation rate, involving the FFT computation in the determination of the autocorrelation function, energy spectrum and structure functions. For that purpose the unevenly spaced record had to be transformed into an equally spaced record. This requires the definition of a time-step (*i.e.* of a resampling frequency) and an interpolation method. The average sampling rate was chosen as resampling frequency of the record (Biron et al., 1995).

The choice of interpolation method to resample the instantaneous velocity record was made based on the comparison of results from the linear, cubic and nearest neighbor interpolation, and sample and hold (S-H) methods. The nearest neighbor interpolation method selects the value of the nearest point to rebuild the new record, while the S-H method selects the immediately previous value (Benedict et al., 2000). Figure 4.30a shows the autocorrelation function, ρ, for each interpolation method, calculated through:

$$\rho(r_x) = \frac{\overline{u'(x)u'(x+r_x)}}{\overline{u'^2}} \tag{4.32}$$

where r_x is the space lag in the streamwise direction. From fig. 4.30a it can be observed that all methods present similar results.

Figure 4.30b presents the streamwise integral length scale value of the autocorrelation function until the first zero found. For the four points studied, the linear and cubic methods present the highest values of the integral length scale due to the highest values of the autocorrelation function. However, nearest neighbor and S-H methods present closer values. Considering the results obtained in this investigation and the results obtained by Benedict et al. (2000), the S-H method will be used to resample the unevenly spaced record.

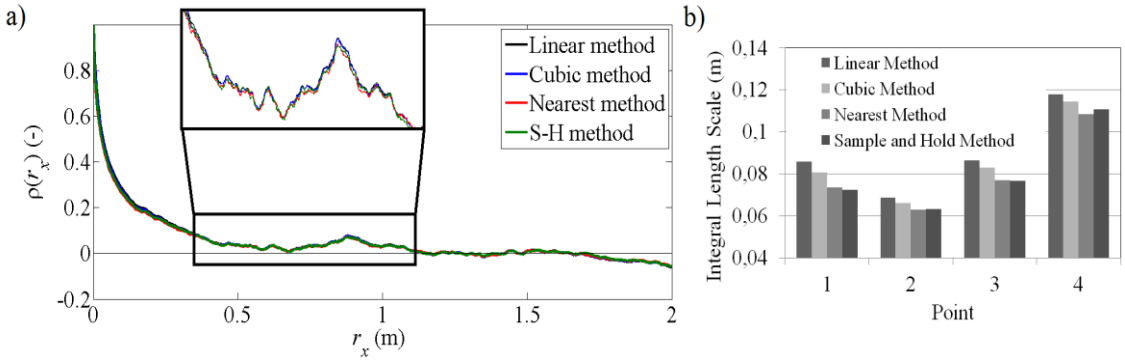

Figure 4.30 a) Streamwise autocorrelation function using different interpolation methods to rebuild the instantaneous velocity for P4, and b) Streamwise integral length scale for four different measurement points (P1 to P4, see fig. 4.29b).

4.4.3.2 Velocity and turbulent intensity estimation

The notation used to describe the velocity field in the compound channel flow are *u* and *w* for the components of the instant velocity in the streamwise direction, *X*, and vertical direction, *Z*, respectively; *u'* and *w'* for the velocity fluctuations; *U* and *W* for the time-averaged velocity; and *U'* and *W'* for the turbulent intensity or r.m.s. values in their corresponding directions. Table 4.7 shows the equations used to calculate velocities and turbulent intensities. The time-averaged velocity *U* was calculated using the equation in tab. 4.7. Since the LDV system captures a greater number of particles associated to higher velocities than for lower velocities, McLaughlin and Tiederman (1973) proposed the equation used for the time-averaged velocity *U* to reduce the velocity bias impact due this imbalance on the particle concentration. For the mean average velocity *W*, the former equation cannot be applied since the instantaneous velocity *w* presents values around zero. For this velocity component, a standard mean average equation was used (see tab. 4.7).

Table 4.7 Description of equations of turbulence terms.

Description	Equation	Comments
Streamwise mean average velocity U	$U = \left(\frac{1}{N} \sum_{i=1}^{N} 1/u_i \right)^{-1}$	N is the number of measurements
Vertical mean average velocity W	$W = \frac{1}{N} \sum_{i=1}^{N} w_i$	
Streamwise velocity fluctuation u'	$u'_i = u_i - \frac{1}{N} \sum_{i=1}^{N} u_i$	To ensure that $\overline{u'_i} \equiv 0$
Vertical velocity fluctuation w'	$w'_i = w_i - \frac{1}{N} \sum_{i=1}^{N} w_i$	To ensure that $\overline{w'_i} \equiv 0$
Streamwise turbulent intensity U'	$U' = \sqrt{\frac{1}{N} \sum_{i=1}^{N} \left(u'^{2}_{i} \right)}$	
Vertical turbulent intensity W'	$W' = \sqrt{\frac{1}{N} \sum_{i=1}^{N} \left(w'^{2}_{i} \right)}$	

4.4.3.3 Integral length scale estimation

By definition, the streamwise integral length scale, L_x, is obtained through.

$$L_x \equiv \int_0^{\infty} \rho(r_x) dr_x \tag{4.33}$$

However, in practical terms, the integral of the autocorrelation function must be defined until a finite value. In this study, three integral-stop-values were used in order to analyze their influence on the results under different conditions, namely: the second zero found on the autocorrelation function; the first minimum found on the autocorrelation function; and the integral length-scale defined as the wavenumber value when the autocorrelation function reaches 1/*e*, *i.e*. the value expected if an exponential decay of the autocorrelation function is assumed (Tropea et al., 2007).

Figure 4.31a shows the behavior of the autocorrelation function as well as, the three integral-stop-values and the evolution of the integral length scale. For the first minimum integral-stop-value the evolution of the integral length scale is still developing, while for the second zero integral-stop-value the evolution of the integral length scale is completely developed. However, integral length scale values obtained using the first minimum or the second zero exhibit an unsystematic behavior, presenting high differences between neighboring

measurement points (results are not shown here, but this conclusion was achieved by comparing all measuring points results for all methods using similar figures to fig. 4.36). This is a result of the randomness of the autocorrelation function for higher space lags, r_x, which makes that the location of the second zero is not always found when the evolution of the integral length scale is completely developed. Therefore, the estimator using 1/*e* is chosen to compute the integral length scale in the entire cross-section measuring mesh (see fig. 4.36), since it is the most consistent method to understand the behavior of L_x, even knowing that the values will certainly be underestimated (Bewley et al., 2012; Tritton, 1988).

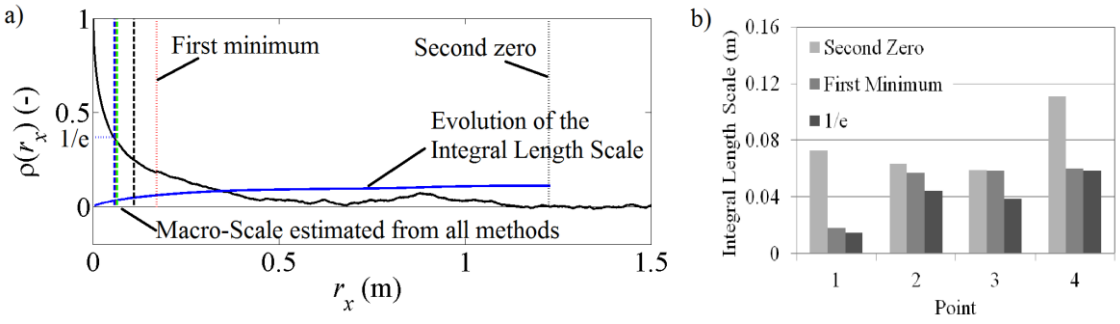

Figure 4.31 a) Streamwise autocorrelation function and evaluation of three integral-stop-values for P4, and b) Streamwise integral length scale for four different measurement points (P1 to P4, see fig. 4.29b).

4.4.3.4 Dissipation rate estimation

For estimating the dissipation rate, three methods were used, being the first one a derivation from the third-order structure function; the second one a derivation from the second-order structure function and the last one from the energy spectrum of the velocity (Frisch, 1995).

Assuming a local isotropic flow and that an inertial sub-range exists, the third-order structure function is equal to:

$$S^{(3)}(r_x,t) = -\frac{4}{5}\varepsilon r_x \tag{4.34}$$

The dissipation rate will be the value when the normalized third-order structure function reaches a plateau (see fig. 4.32a). To find a plateau the algorithm obtains the maximum value in the third-order structure function distribution and calculates the mean value taking data points before and after the maximum until the difference between them is less than 1%, as shown fig. 4.32a. However, for points with low acquisition frequencies, the third-order structure function starts to exhibit less correlation for low space steps r_x, being more difficult to find a plateau

(results are not shown here, but this conclusion was achieved by comparing all measuring points results using similar figures to fig. 4.32a). On the other hand, the assumption of a local isotropic turbulent flow can be debated and the presence of a large inertial sub-range should not be so obvious.

The second method to estimate the dissipation rate is derived from the second-order structure function, eq. 4.35, where C_2 is a universal constant equal to 2 and it does not depends on the Reynolds number (Pope, 2000). Figure 4.32b shows the distribution of the normalized second-order structure function where the plateau was found using the same algorithm used in the third-order method. However, for points with high acquisition frequency, the correlation of the velocity fluctuations does not present a plateau (results are not shown here, but this conclusion was achieved by comparing all measuring points results using similar figures to fig. 4.32b). This should be a consequence of noise increase for low space steps which is not cancelled out by opposite sign peaks for the second-order structure function as it is in the case of the third-order structure function.

$$S^{(2)}(r_x,t) = C_2(\varepsilon r_x)^{2/3} \tag{4.35}$$

Finally, the dissipation rate is also estimated from the spectrum of the streamwise velocity. In this case, the Yule-Walker spectral estimation algorithm was used, which is highly smoothed but allows identifying a clear plateau in the inertial sub-range. This plateau occurs at around 1.5 times the wavenumber of integral length scale, $k_{w\varepsilon} = 1.5/L_x$, as shown in fig. 4.32c, where the distribution of the dissipation rate is given by

$$\varepsilon \approx \left(\frac{E_{xx}(k_w)}{C k_w^{-5/3}} \right)^{3/2} \tag{4.36}$$

being E_{xx} the streamwise velocity energy spectrum, k_w the wave number and C the universal constant of Kolmogorov equal to 0.53 (Pope, 2000).

Figure 4.32d shows a comparison between dissipation rate values obtained using the three methods. As mentioned before, the third and second order structure function methods are much more sensitive to acquisition frequencies, exhibiting a poor trend between neighboring points. On the other hand, the method based on the energy spectrum is much more robust and less sensitive to the acquisition frequency and for that reason is the one chosen for estimating the dissipation rate in the entire cross-section measuring mesh (see fig. 4.37).

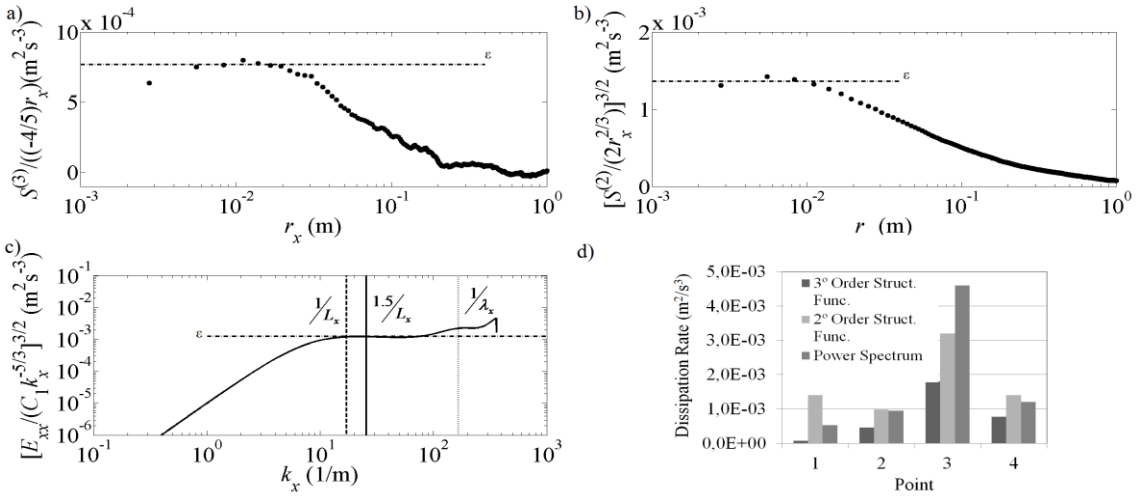

Figure 4.32 Estimation of the dissipation rate from three methods: a) third-order structure function for point P4; b) Second-order structure function for point P4; c) Spectrum of the velocity for point P4. d) Dissipation rate from the three methods for four different measurement points (P1 to P4, see fig. 4.29b).

4.4.4 *Results*

4.4.4.1 Velocity and Turbulent Intensity

Figures 4.33a, 4.33c and 4.33e show the distribution of the time-averaged velocity U/U_* and vectors of W/U_{max}, while fig. 4.33b, 4.33d and 4.33f, show the depth-averaged streamwise velocity U_d. For the cases Hr = 0.23 and 0.31, the high difference between the depth-averaged streamwise velocity in the main channel and the floodplain (fig. 4.33d and 4.33f) originates vertical axis vortices at the interface, which can also be depicted by the inflection of the velocity isolines near the free-surface from the interface to the main channel (fig. 4.33c and 4.33e). These turbulent structures constitute a mixing layer with a strong momentum transfer between main channel and floodplain flows (Shiono and Knight, 1991). However, for Hr = 0.50 it is clear, from the inflection of the velocity isolines at the interface region (see fig. 4.33a), that the 2D shear layer is replaced by a 3D turbulent field, where streamwise orientated vortices interact, known as secondary currents due to the anisotropy of turbulence (Azevedo et al., 2012; Nezu et al., 1999; Shiono and Knight, 1991). The difference between the depth-averaged streamwise velocity U_d is in this case small and a local minimum exist at the interface (fig. 4.33b), which can be originated by two counter-rotating vertical oriented vortices that interact with the secondary currents resulting in a complex 3D turbulence field, as mentioned by Nezu et al. (1999) for deep flows.

In all cases, the maximum velocity U in the middle of the main channel is located at around 65% of the flow depth (see dotted line in fig. 4.33a, 4.33c and 4.33e). The location of the maximum velocity U under the free-surface is generated by effects of the descendant flow

which are caused by the encounter of the "main channel vortex" and the "free-surface vortex" Nezu and Nakagawa (1993), for *Hr* = 0.50, and by the interaction between the side-wall effect and the shear layer effect (interface region) with the main channel flow, for *Hr* = 0.31 and 0.23. In other words, the shear layer effect on the secondary currents is similar to a vertical wall, which is corroborated by the resemblance of the secondary currents observed for *Hr* = 0.23 (fig. 4.33e) and the ones observed in narrow rectangular channels (Nezu and Nakagawa, 1993).

The strong descendant flow located in the main channel reaches 30% of the friction velocity U_* for all cases (fig. 4.33a, 4.33c and 4.33e). However, it is displaced towards the main channel lateral wall) as the relative water depth decreases (from *y/B* = 0.19 for *Hr* = 0.50 to *y/B* = 0.14 for *Hr* = 0.23). This transverse displacement of the descendant flow is due to the differences in the turbulent field. Namely, for the deeper flow the mixing layer is weak (eventually composed of two counter rotating vertical oriented vortices) and the secondary currents are strong extending their influence towards the interface. By opposition, for shallower flows the mixing layer is strong (composed of single vertical orientated vortices) acting as a vertical wall to the weak secondary currents that develop at the main channel, as mentioned before.

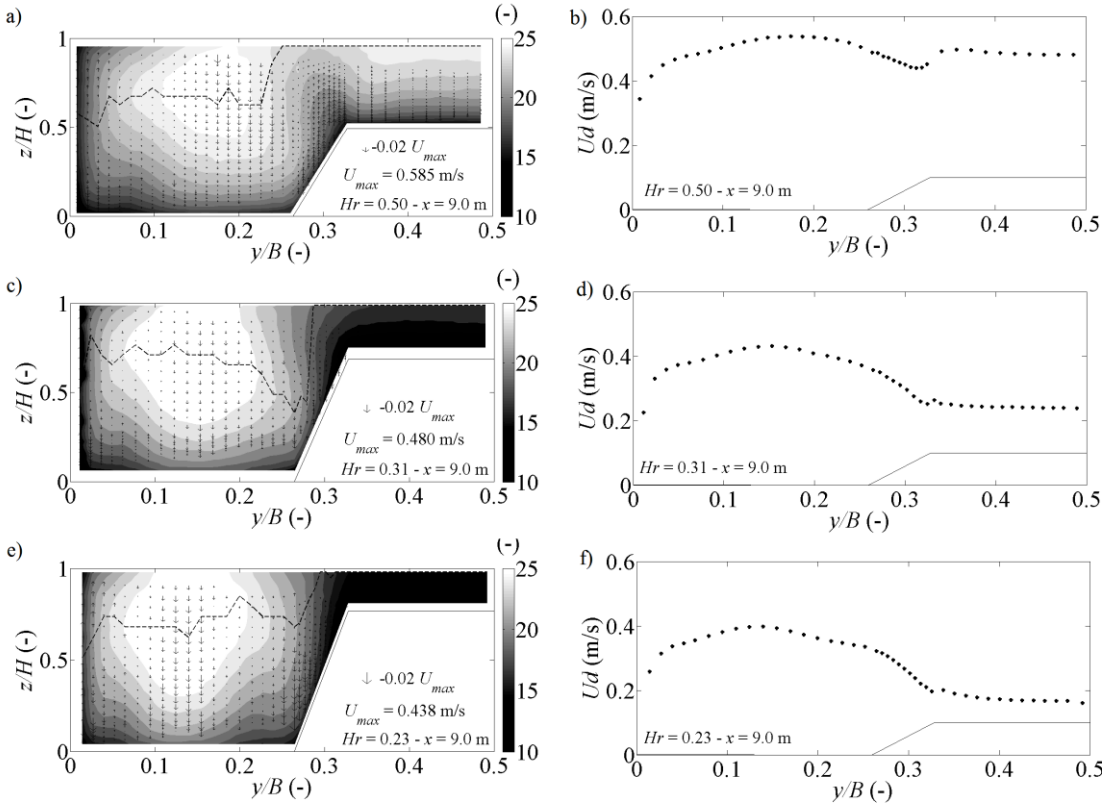

Figure 4.33 a), c) and e) Cross-section distribution of the normalized mean velocity U/U_* and vectors of mean velocity W/U_{max}. b), d) and f) Lateral distribution of the depth-averaged streamwise

velocity *Ud* for *Hr* = 0.50, *Hr* = 0.31 and *Hr* = 0.23. The dotted line in a), c) and e) Corresponds to the maximum streamwise velocity in each vertical.

Figure 4.34 presents the turbulent intensity distribution U'/U_* on the left side and W'/U_* on the right side. Turbulent intensity U'/U_* follows the trends of U/U_*, but with inverse values, *i.e*. with highest values near the walls and lowest values deep below the free-surface in the middle of the main channel and close to the free-surface in the floodplain region. For the deeper flow (fig. 4.34a and 4.34b) it is clear that the strong secondary currents dictate the turbulence distribution throughout the cross-section. Namely, they convey higher turbulent flow from near the walls up into the free-surface in ascending flow regions (like the interface) and convey less turbulent flow from the free-surface region into the near wall region in descending flow regions (like the main channel corners). For the shallower flow (fig. 4.34e and 4.34f) one can observe that the vertical oriented vortices in the mixing layer convey high turbulent flow from the interface bottom into the main channel direction. It is interesting to note that the high turbulence intensity region occupies the interface region, while for the deeper flow it is located in the upper corner of the interface (fig. 4.34a and 4.34b). This indicates that the vertical orientated vortices seem to be a more efficient mechanism to redistribute the turbulence generated at the bottom than the secondary currents. For the intermediate flow depth *Hr* = 0.31 (fig. 4.34c and 4.34d), a mixed behavior of the ones referred for deeper and for shallower flows exists, *i.e*. the mixing layer vortices influence the interface region but not up to the free-surface, while in the upper interface corner a bulging of the isolines is still observed due to weak secondary currents.

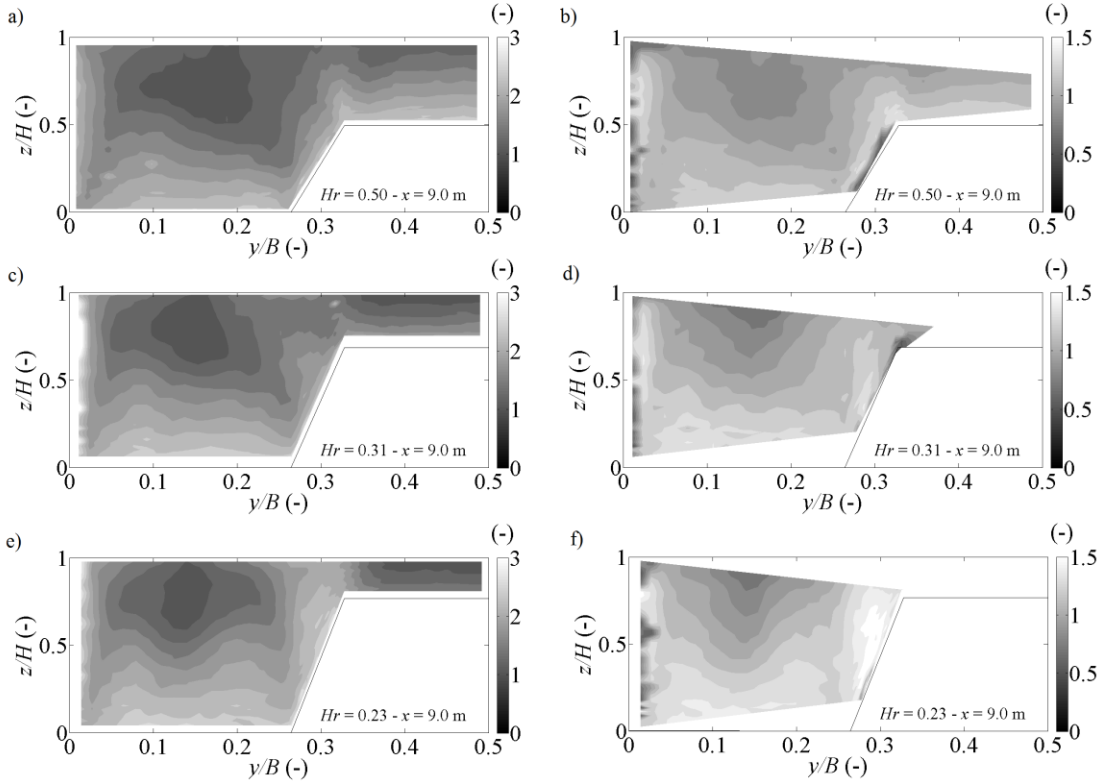

Figure 4.34 Cross-section distribution of the normalized streamwise and vertical turbulent intensities (U'/U_* in left side and W'/U_* in right side, respectively). For *Hr* = 0.50, *Hr* = 0.31 and *Hr* = 0.23.

4.4.4.2 Reynolds Stress $-\overline{u'w'}/U_*^2$ Distribution

Figure 9 shows isolines of the normalized Reynolds stresses $-\overline{u'w'}/U_*^2$.

For all cases, maximum values are observed near the bottom of the main channel diminishing towards the free-surface. Also, a negative Reynolds stress is observed in the corner between the side-wall and free-surface, where an ascendant flow exists. This region of negative Reynolds stress is originated on the momentum transfer from the side-wall towards the middle of the main channel (Kara et al., 2012).

For *Hr* = 0.50 (fig. 4.35a), a strong positive Reynolds stress occurs in the interface between main channel and floodplain due to secondary currents, confirming the high values of the streamwise and vertical turbulent intensities (fig. 4.34a and 4.34b). For shallower flows (fig. 4.35b and 4.35c) the Reynolds stress at the interface region is small and can even be negative. This seems contrary to the results of the streamwise and vertical turbulent intensities that show an increase of both values in the interface region (fig. 4.34c, 4.34d, 4.34e and 4.34f). The explanation for high values of U'/U_* and W'/U_* and low values of $-\overline{u'w'}/U_*^2$ can be explained based on the conceptualization of the topographical forcing proposed by Van Prooijen et al.

(2005). In fact, the mixing layer at the interface will have vortices with flow going from the main channel to the floodplain at their front (accelerating upwards) and flow going in the opposite direction at their back (decelerating downwards). The time-averaging of successive vortices can render a null or small $-\overline{u'w'}/U_*^2$ contribution.

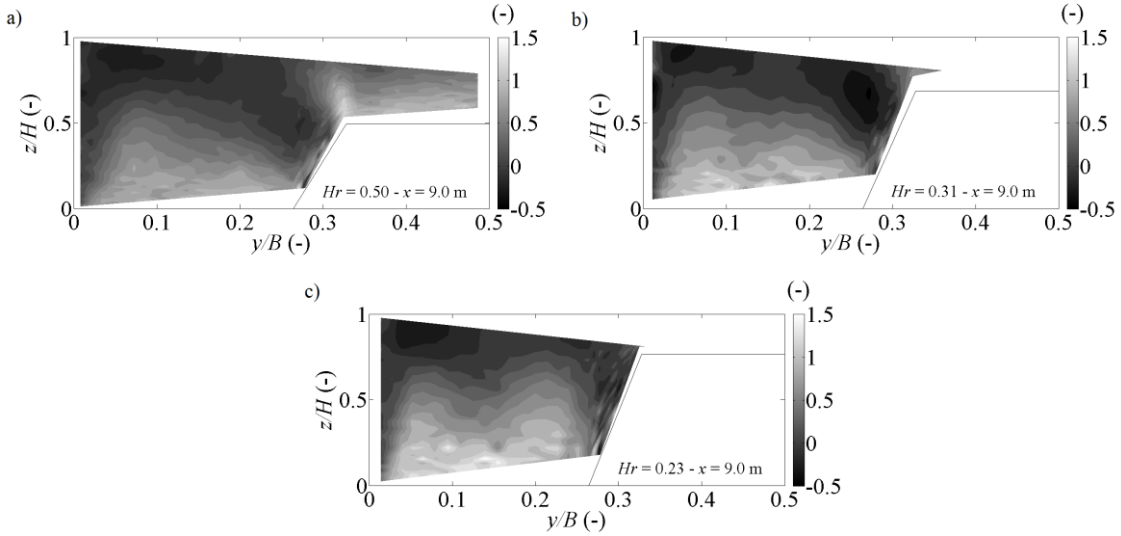

Figure 4.35 Cross-section distribution of the Reynolds stress $-\overline{\boldsymbol{u'w'}}$ normalized by U_*^2 for a) *Hr* = 0.50, b) *Hr* = 0.31 and c) *Hr* = 0.23

4.4.4.3 Integral length scale and dissipation rate distribution

Figure 4.36 shows the integral length scale distribution (normalized by the water depth H_{MC}) estimated according to third method presented in section 4.4.3.3 (*i.e.*, L_x is defined as the wavenumber value for which the autocorrelation function reaches 1/*e*). For all cases, the streamwise integral length scale increases close to the bottom in the main channel, due to the interaction between the descendant flow in the middle of the main channel and the side walls.

For the deeper flow *Hr* = 0.50, a large value of the integral length scale is observed near the free-surface in the interface region. As mentioned before, according to Nezu et al. (1999) and Stocchino and Brocchini (2010), the surface velocity is characterized by weak double shear layers, which are caused by an ascendant flow (secondary currents), as shown in fig. 4.33a and 4.33b. The integral length scale results in fig. 4.36a confirm this double shear layer, corresponding to macro vortices (*i.e.* high integral length scale values) located between the interface and the main channel, around *y/B* = 0.25, and between the interface and the floodplain, around *y/B* = 0.32. These macro vortices are bigger near the free-surface. For the shallower flow *Hr* = 0.23, the interface region, where a strong mixing layer exists, presents high values of the integral length scale, even higher than the flow depth H_{MC}, confirming the results for shallow mixing layers (Uijttewaal, 2014).

Although the method used to estimate the integral length scale is based in premises that can be debated, the results showed in fig. 4.36 help to understand the turbulent field and confirm the observations of other researchers.

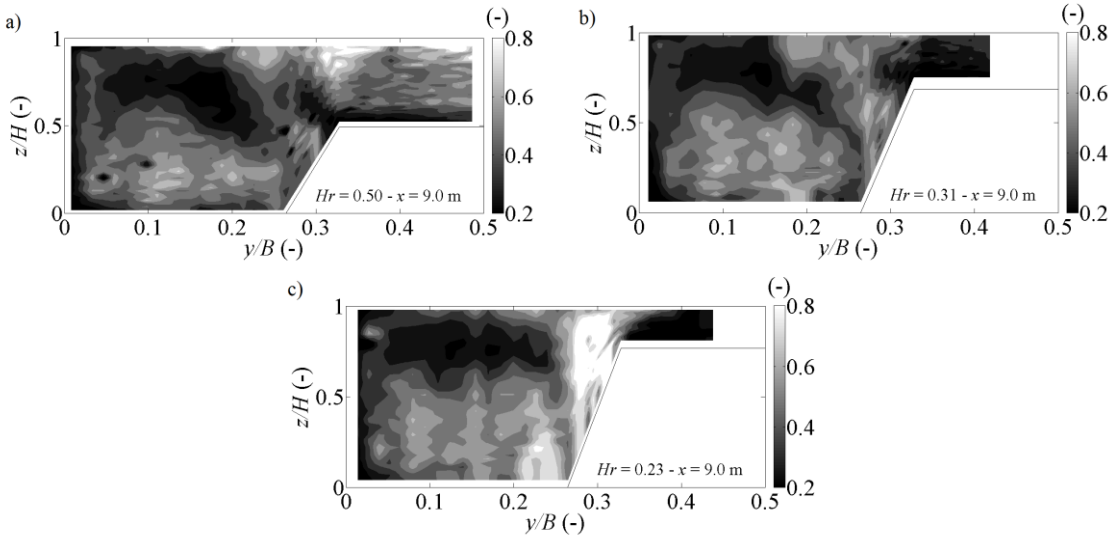

Figure 4.36 Cross-section distribution of the streamwise integral length scale normalized by H_{MC} for a) Hr = 0.50, b) Hr = 0.31 and c) Hr = 0.23.

Figure 4.37 shows the dissipation rate obtained by the energy spectrum method (see section 4.4.3.4). The figure shows that the highest dissipation rate occur near the side wall and the bottom of the channel, decreasing towards the free-surface. This behavior is independent of the relative water depth. Three differences exist between each case, the first one is that the lower dissipation rate is well below the free-surface for Hr = 0.50, but it moves towards the free-surface as the relative water depth decreases. The second one is that the dissipation rate increase for Hr = 0.31 and Hr = 0.23 in the interface region. It may be due effects of the vertical axis vortex caused by the shear layer. The last difference is that high values of the dissipation rate in the floodplain extend to the free-surface for Hr = 0.31 and Hr = 0.23.

Results in fig. 4.37 and 4.34 show no correspondence suggesting that the dissipation rate is independent of the anisotropy. Bewley et al. (2012) carried out measurements of the velocity field of air jets pointed towards the center of a spherical chamber, concluding also that the normalized dissipation rate is independent of the anisotropy. Likewise, they suggest that the ratio between two integral length scales (for example L_z/L_x) depended on the anisotropy in the fluctuations W'/U'. In our case, due the poor results obtained of the integral length scale for the Z direction, this dependence could not be verified. However, a clear relation between the streamwise integral length scale, L_x, the dissipation rate, ε, and the streamwise turbulent intensity U', can be observed as shown in fig. 4.38.

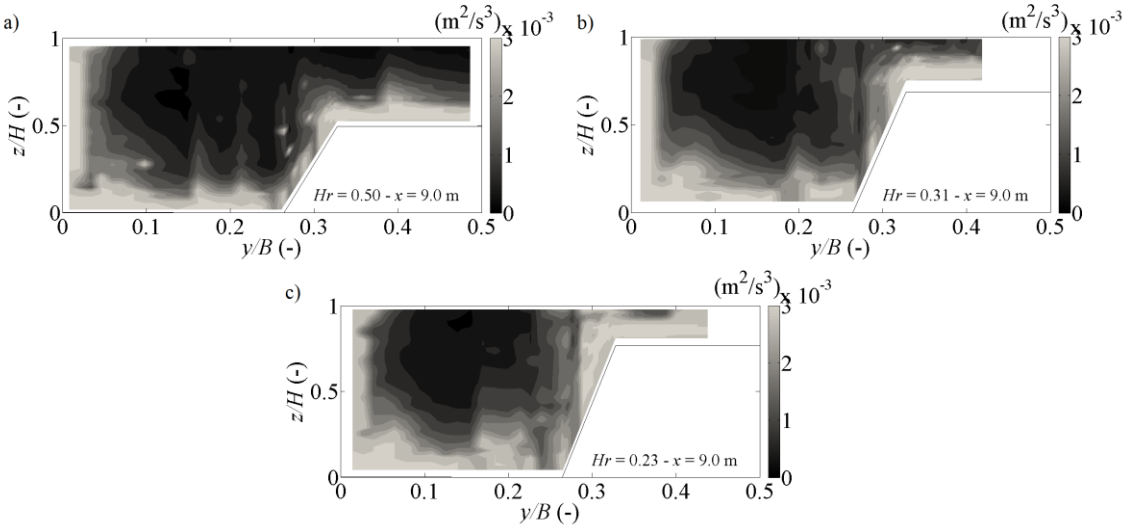

Figure 4.37 Cross-section distribution of the dissipation rate for a) *Hr* = 0.50, b) *Hr* = 0.31 and c) *Hr* = 0.23.

As reference, fig. 4.38 also shows the semi-theoretical equation $L_x\varepsilon^{1/3}$ for 2D fully developed open-channel flow (Nezu and Nakagawa, 1993), where

$$\frac{L_x}{H} = \begin{cases} B_1\left(Z/H\right)^{1/2} \rightarrow Z/H < 0.6 \\ 0.77B_1 \rightarrow Z/H > 0.6 \end{cases} \tag{4.37}$$

$$\frac{\varepsilon H}{U_*^3} = \frac{12.2K}{B_1}\left(\frac{Z}{H}\right)^{-1/2}\exp\left(-\frac{3Z}{H}\right) \tag{4.38}$$

$$K = 0.691 + 3.98/\sqrt{\mathrm{Re}_L} \tag{4.39}$$

$$\mathrm{Re}_L = U'\left(L_x/\nu\right) \tag{4.40}$$

$$U'/U_* = 2.30\exp\left(-Z/H\right) \tag{4.41}$$

with B_1 = 1.0. The data plotted in fig. 4.38 was divided in four groups, "+" for verticals near to the side wall ($y/B < 0.075$), "○" for verticals in the main channel ($0.075 < y/B < 0.260$), "×" for verticals in the interface region ($0.260 < y/B < 0.330$), and "□" for verticals in the floodplain ($0.330 < y/B$).

The behavior of the turbulent intensity *U'* appears to have a strong dependence with the interaction between the streamwise integral length scale and the dissipation rate, where the behavior of the trend can be assumed as 1:1 (see dashed line in fig. 4.38), except the verticals located near to the side wall for *Hr* = 0.50. On the other hand, decreasing the water depth the

verticals located in the interface region and floodplain begins to departure from the trend 1:1, but maintain a linear relationship. This is caused by the high dissipation rate presented in those regions.

Contrary to 2D fully developed open-channel flow equations, the linear relation appear to be constant for all the water depths and no apparent change occurs for Z/H = 0.60, as predicted by eq. 4.37.

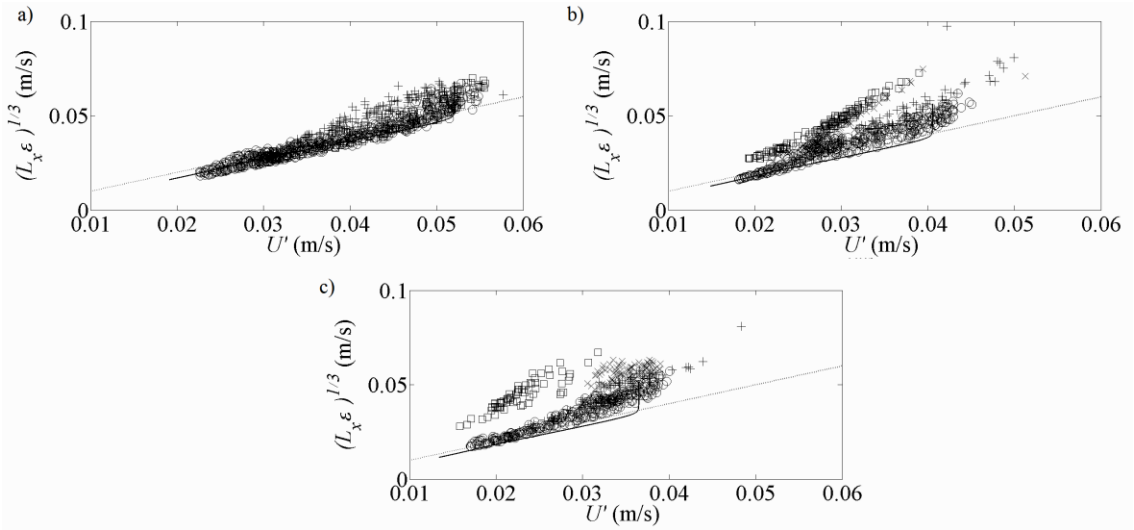

Figure 4.38 $L_x\varepsilon^{1/3}$ vs. U' for each vertical profile where "+", "o", "x" and "□" represent verticals near the side-wall, in the main channel, in the interface region and in the floodplain, respectively. Continuous line "-" represents the semi-theoretical equation $L_x\varepsilon^{1/3}$ for 2D fully developed open-channel flow. Dashed line ".." represents a line with slope 1:1.

4.4.5 *Conclusions*

The characterization of turbulence structures in compound channel flows under shallow, intermediate and deep flows conditions, using LDV high data rate measurements and several methodologies to determine its fundamental features were presented. After analyzing the results obtained using four interpolation methods to resample the instantaneous velocity record, three integral-stop-values of the autocorrelation function to obtain an estimation of the integral length scale and three methods to estimate the dissipation rate, the following conclusions can be extracted:

- The resampling data from the linear and cubic interpolation methods present the highest values of the streamwise integral length scale while the nearest neighbor and S-H methods present closer values. The latter was consider the best interpolation method to rebuild the unevenly spaced record.

- The integral-stop-value 1/*e* is the most consistent method to estimate the integral length scale of the methods studied in this investigation, presenting similar results between neighboring measurement points. An opposite behavior was found using the first minimum and the second zero as integral-stop-value due to the randomness of the autocorrelation function for higher space lags.
- The comparison between dissipation rate values obtained through the three methods studied show that the third and second order structure function methods are much more sensitive to acquisition frequencies, exhibiting a poor trend between neighboring measurement points, while the method based on the energy spectrum, using the Yule-Walker spectral estimation algorithm, is much more robust and less sensitive to acquisition frequencies.

According with the results obtained for deep water flow, intermediate water flow and shallow water flow, the conclusions are:

- The mixing layer observed for deeper flow is weak and a local minimum of the depth-averaged streamwise velocity U_d exists at the interface, which is originated by two counter-rotating vertical oriented vortices that interact with the secondary currents. For shallower flows the mixing layer strongly acts as a vertical wall to the weak secondary currents that develop at the main channel.
- For deeper flow, the turbulent intensity distribution is clearly dictated by the secondary currents throughout the cross-section. However, for shallower flow the vertical oriented vortices in the mixing layer represent the mechanism who defines the turbulent intensity behavior, conveying high turbulent flow from the interface bottom into the main channel direction. For intermediate flow, a mixed behavior exists between deeper and shallower flows.
- The normalized Reynolds stresses $-\overline{u'w'}/U_*^2$ distribution can be explained with the streamwise and vertical turbulent intensities for deeper flow. However, for intermediate and shallower flows the Reynolds stress distribution is dictated by the topographical forcing.
- A double shear layer can be observed in the integral length scale distribution for Hr = 0.50, where macro vortices are located between the interface/main channel and interface/floodplain interacting with the secondary currents. Decreasing the water depth, the interface region transforms into a strong mixing layer composed of single vertical orientated vortices, presenting high values of the integral length scale, even higher than the flow depth.
- For all relative depths, the dissipation rate is highest near the sidewall and the bottom of the channel, decreasing towards the free-surface. However, by effect of the vertical

orientated vortices caused by the shear layer in the interface region, the dissipation rate is larger for $Hr = 0.31$ and $Hr = 0.23$.

- A clear linear relation exists between the streamwise integral length scale, L_x, the dissipation rate, ε, and the streamwise turbulent intensity U'. Contrary to 2D fully developed open-channel flow equations, that relation appears to be constant for all water depths.

5

Chapter 5

Conclusions and Future Research

The results presented in chapter 4 allowed to characterize the turbulent structures originated in compound channels flows under different inlet conditions, namely, deep flows and shallow flows, and also, considering the placement of rods on the upper bank between main channel and floodplain.

Regarding the first experimental campaign of this investigation (objective 1 in p. 5), the following conclusions can be listed:

- A strong descendant flow in the middle of the main channel was observed for all relatives water depths studied. For Hr = 0.23 and Hr = 0.31, which correspond to shallow flows, this descendant flow is caused by a momentum transfer from the lateral side-wall to main channel and from the floodplain to main channel. This last caused by the gradient velocity between both sub-regions. For Hr = 0.50, the momentum transfer observed from floodplain to main channel is due to the strong ascendant flow located in the upper interface.
- The maximum longitudinal average velocity U is located below free-surface for all relative water depth. This phenomenon, known as "dip" phenomenon, is a consequence of the descendant flow explained before.
- For Hr = 0.50, the universal laws for 2D fully developed open-channel flows are valid in the upper interface and floodplain, although the coefficients have to be increase, mostly due to the increase of turbulent intensity. This should be a consequence of the shallowness of the flow which contributes to maintain boundary turbulence as the dominant process.
- The turbulent intensity distribution U'/U_* follows the same tendency of isovels U/U_*, where the higher turbulent intensity is located close to the walls and the lower turbulent intensity is below free-surface in the middle of main channel, due to the dip-velocity phenomenon. The secondary currents have an important role in the turbulent intensity distribution U'/U_* in the interface region, causing a bulging of isovels U'/U_*.
- In the case of turbulent intensity W'/U_*, it presents the higher values close to the walls and decrease towards the free-surface. As turbulent intensity U'/U_*, W'/U_* presents also a bulging of the isovels in the interface region due secondary currents.
- The negative Reynolds shear stresses $-\overline{u'w'}/U_*^2$ are located close to the free-surface and they increase towards the bottom of the channel. The "dip" phenomenon causes a negative shear stress in the corner between side-wall and free-surface. Decreasing the relative water depth, the Reynolds shear stresses decrease in the interface region but increase close of the bottom in the main channel.
- In the case of the integral length scale distribution, the double shear layer caused by an ascendant flow in the interface region, originates vortices rotating clockwise with

vertical axis between main channel and interface, while vortices rotating anticlockwise are observed between interface and floodplain, for Hr = 0.50. High values of the integral length scale are not observed in the upper interface, y/B = 0.3, which corresponds with the ascendant flow location. For Hr = 0.31 and Hr = 0.23, high values of the integral length scale are confined in the interface region with vortices rotating in clockwise direction. For all cases, the integral length scale increases close to the bottom in the main channel.

- The turbulence dissipation rate increases close to the walls and decreases towards the free-surface. For Hr = 0.31 and Hr = 0.23, high values of the dissipation rate are pulled until the free-surface in the interface region, due to vertical axis vortexes originated by the shear layer.
- For Hr = 0.5, the maximum integral length scale is close to the free-surface in the middle of the main channel, between $0.5 < z/H < 1$, and in the floodplain for Hr = 0.31 and 0.23, decreasing towards the walls of the flume. Decreasing the relative water depth increases Taylor's micro scale.

On the other hand, for the case where rods were placed on the upper bank (objective 2 in p. 5), the following conclusions can be listed:

- For Hr = 0.50, the universal laws for 2D fully developed open-channel flows are not valid for the case with rods, due to the dominant influence of the wakes generated by the rods that govern the turbulent field instead of the boundary layer.
- The integral length scale presents almost constant values in the vertical direction, which indicates that the wakes generated by the rods influence the entire water column.
- The turbulent microscale and dissipation rate acquire a streamwise variation due to the vortex propagation in the downstream direction.
- At the upper interface near the rod the microscale is minimum, but still above the 2D flow values, and the dissipation is maximum exceeding the 2D flow values.

Finnally, the conclusions about the different approaches to estimate the integral length scale, dissipation rate and micro scale (objective 3 in p. 5) are:

- The most consistent method to estimate the integral length scale is when the autocorrelation function reaches the value 1/e.
- The estimation of the integral length scale through the autocorrelation function with integral-stop-values second zero and first minimum, presents a random behavior.

- The third order structure function can be used to get good estimation of the dissipation rate. However, a high acquisition frequency is necessary (> 100 Hz).
- The second order structure function does not allow getting good estimation of the dissipation rate since a plateau was not found. Possible, a higher acquisition frequency is necessary (>100Hz).
- The most consistent way of estimating the dissipation rate is from the energy spectrum of the velocity, where the plateau occurs at 1.5 times the wavenumber of the integral length scale.
- The Taylor's microscale was estimated from incompressible homogeneous isotropic turbulent flow equation and considering the dissipation rate from the third order structure function.

Future Research

In this investigation, several inlet discharges have been studied taking into account the placement or not of roughness, in a straight asymmetric compound channel and under the quasi-uniform flow condition. Also, the measurements were made through a 2D Laser Doppler Velocimeter. On this regards, some progress can be developed as follow:

- Improve the LDV system in order to take the third velocity component. With this improvement, the tree velocity components can be measured at the same time, allowing the evaluation of the shear stress $\overline{v'v'}$; $\overline{u'v'}$ and $\overline{u'w'}$, as well the turbulence kinetic energy k.
- Placement of new configuration of rods should be evaluated, *e.g*. vegetated regions over floodplain using rods with different spacing configuration; placement of flexible vegetation, shrubbery, etc. The study of different kinds of vegetation will allow to understand the behavior of mass and momentum transfer between main channel and floodplain under different roughness conditions, as well the turbulent structures originated.
- Different approaches should be evaluated in order to characterize the turbulent field.

References

Azevedo, R., Rojas-Solórzano, L., and Leal, J. (2012). *Experimental characterization of straight compound-channel turbulent field.* Paper presented at the in 2nd European IAHR Congress 2012 Munich.

Benedict, L., Nobach, H., and Tropea, C. (2000). Estimation of turbulent velocity spectra from laser Doppler data. *Measurement Science and Technology, 11*(8), 1089.

Bewley, G. P., Chang, K., and Bodenschatz, E. (2012). On integral length scales in anisotropic turbulence. *Physics of Fluids (1994-present), 24*(6), 061702.

Biron, P., Roy, A. G., and Best, J. L. (1995). A scheme for resampling, filtering, and subsampling unevenly spaced laser Doppler anemometer data. *Mathematical geology, 27*(6), 731-748.

Blinco, P. H., and Partheniades, E. (1971). Turbulence characteristics in free surface flows over smooth and rough boundaries. *Journal of Hydraulic Research, 9*(1), 43-71.

Bousmar, D., Riviere, N., Proust, S., Paquier, A., Morel, R., and Zech, Y. (2005). Upstream discharge distribution in compound-channel flumes. *Journal of Hydraulic Engineering, 131*(5), 408-412.

Bousmar, D., and Zech, Y. (1999). Momentum transfer for practical flow computation in compound channels. *Journal of Hydraulic Engineering, 125*(7), 696-706.

Coles, D. (1956). The law of the wake in the turbulent boundary layer. *Journal of Fluid Mechanics, 1*(02), 191-226.

Einstein, H. A. (1942). Formulas for the transportation of bed load. *Trans. ASCE Paper, 2140*, 561-597.

Esfahani, F. S., and Keshavarzi, A. R. (2010). How far must trees be cultivated from the edge of the flood plain to provide best river bank protection? *International Journal of River Basin Management, 8*(1), 109-116. doi: 10.1080/15715121003714894

Frisch, U. (1995). *Turbulence: the legacy of AN Kolmogorov*: Cambridge university press.

Goring, D. G., and Nikora, V. I. (2002). Despiking acoustic Doppler velocimeter data. *Journal of Hydraulic Engineering, 128*(1), 117-126.

Grass, A. (1971). Structural features of turbulent flow over smooth and rough boundaries. *Journal of Fluid Mechanics, 50*(02), 233-255.

Kang, H., and Choi, S. U. (2006). Reynolds stress modelling of rectangular open-channel flow. *International journal for numerical methods in fluids, 51*(11), 1319-1334.

Kara, S., Stoesser, T., and Sturm, T. W. (2012). Turbulence statistics in compound channels with deep and shallow overbank flows. *Journal of Hydraulic Research, 50*(5), 482-493.

Keulegan, G. H. (1938). *Laws of turbulent flow in open channels* (Vol. 21): National Bureau of Standards US.

Knight, D., and Shiono, K. (1990). Turbulence measurements in a shear layer region of a compound channel. *Journal of Hydraulic Research, 28*(2), 175-196.

L'vov, V. S., Pomyalov, A., and Procaccia, I. (1999). Temporal surrogates of spatial turbulent statistics: The Taylor hypothesis revisited. *Physical Review E, 60*(4), 4175.

Lorenz, E. N. (1963). Deterministic nonperiodic flow. *Journal of the atmospheric sciences, 20*(2), 130-141.

Massey, B. S., and Ward-Smith, J. (1998). *Mechanics of fluids* (Vol. 1): CRC Press.

McLaughlin, D., and Tiederman, W. (1973). Biasing correction for individual realization of laser anemometer measurements in turbulent flows. *Physics of Fluids (1958-1988), 16*(12), 2082-2088.

McLaughlin, J. B., and Martin, P. C. (1975). Transition to turbulence in a statically stressed fluid system. *Physical Review A, 12*(1), 186.

Millikan, C. B. (1937). The Physicist Gets Air Minded. *Journal of Applied Physics, 8*(2), 107-116.

Myers, W. (1978). Momentum transfer in a compound channel. *Journal of Hydraulic Research, 16*(2), 139-150.

Nakagawa, H., Nezu, I., and Ueda, H. (1975). Turbulence of open channel flow over smooth and rough beds. *Proceedings of the Japan Society of Civil Engineers, 1975*(241), 155-168.

Naot, D., Nezu, I., and Nakagawa, H. (1996). Hydrodynamic behavior of partly vegetated open channels. *Journal of Hydraulic Engineering, 122*(11), 625-633.

Nezu, I. (1977). Turbulent structure in open-channel flows: Kyoto University.

Nezu, I., Kadota, A., and Nakagawa, H. (1997). Turbulent structure in unsteady depth-varying open-channel flows. *Journal of Hydraulic Engineering, 123*(9), 752-763.

Nezu, I., and Nakagawa, H. (1993). Turbulence in open-channel flows. *IAHR Monograph Series*.

Nezu, I., and Nakayama, T. (1997). Space-time correlation structures of horizontal coherent vortices in compound open-channel flows by using particle-tracking velocimetry. *Journal of Hydraulic Research, 35*(2), 191-208. doi: 10.1080/00221689709498426

Nezu, I., and Onitsuka, K. (2001). Turbulent structures in partly vegetated open-channel flows with LDA and PI V measurements. *Journal of Hydraulic Research, 39*(6), 629-642.

Nezu, I., Onitsuka, K., and Iketani, K. (1999). Coherent horizontal vortices in compound open-channel flows. *Hydraulic Modeling (ed. VP Singh, IW Seo & JH Sonu)*, 17-32.

Nezu, I., and Rodi, W. (1985). *Experimental study on secondary currents in open channel flow*. Paper presented at the Proceedings of 21st IAHR Congress.

Nezu, I., and Rodi, W. (1986). Open-channel flow measurements with a laser Doppler anemometer. *Journal of Hydraulic Engineering, 112*(5), 335-355.

Nikora, V., and Roy, A. G. (2012). Secondary flows in rivers: Theoretical framework, recent advances, and current challenges. *Gravel-bed rivers: Processes, tools, environments*, 3-22.

Notes, L. (1998). Watercourse re-vegetation using indigenous plants. *Não consultado*.

Pope, S. B. (2000). *Turbulent flows*: Cambridge university press.

Proust, S., Bousmar, D., Rivière, N., Paquier, A., and Zech, Y. (2010). Energy losses in compound open channels. *Advances in water Resources, 33*(1), 1-16.

Raichlen, F. (1967). Some turbulence measurements in water. *Journal of the Engineering Mechanics Division, 93*(2), 73-98.

Rameshwaran, P., and Shiono, K. (2007). Quasi two-dimensional model for straight overbank flows through emergent. *Journal of Hydraulic Research, 45*(3), 302-315.

Reynolds, O. (1894). On the Dynamical Theory of Incompressible Viscous Fluids and the Determination of the Criterion. *Proceedings of the Royal Society of London, 56*(336-339), 40-45.

Rotta, v. J. (1972). Turbulence stromungen. *BG Teubner, Stuttgart*.

Sanjou, M., and Nezu, I. (2010). *Large eddy simulation of compound open-channel flows with emergent vegetation near the floodplain edge*. Paper presented at the 9th International Conference on Hydrodinamics, Shangai, China.

Schnauder, I., and Moggridge, H. L. (2009). Vegetation and hydraulic-morphological interactions at the individual plant, patch and channel scale. *Aquatic Sciences, 71*(3), 318-330.

Sellin, R. (1964). A laboratory investigation into the interaction between the flow in the channel of a river and that over its flood plain. *La Houille Blanche*(7), 793-802.

Sellin, R. H., Bryant, T. B., and Loveless, J. H. (2003). An improved method for roughening floodplains on physical river models. *Journal of Hydraulic Research, 41*(1), 3-14.

Shiono, K., Chan, T. L., Spooner, J., Rameshwaran, P., and Chandler, J. H. (2009a). The effect of floodplain roughness on flow structures, bedforms and sediment transport rates in meandering channels with overbank flows: Part I. *Journal of Hydraulic Research, 47*(1), 5-19.

Shiono, K., Chan, T. L., Spooner, J., Rameshwaran, P., and Chandler, J. H. (2009b). The effect of floodplain roughness on flow structures, bedforms and sediment transport rates in meandering channels with overbank flows: Part II. *Journal of Hydraulic Research, 47*(1), 5-19.

Shiono, K., Ishigaki, T., Kawanaka, R., and Heatlie, F. (2009). *Influence of one line vegetation on stage-discharge rating curves in compound channel.* Paper presented at the Proc. 33 rd IAHR Congress.

Shiono, K., and Knight, D. W. (1991). Turbulent open-channel flows with variable depth across the channel. *Journal of Fluid Mechanics, 222*, 617-646.

Shiono, K., and Komatsu, T. (2000). Simple Analytical Solution for Advection Equation in Rectangular and Compound Channels. *Annual J. Hydr. Engrg, JSCE, 44*, 557-562.

Stocchino, A., Besio, G., Angiolani, S., and Brocchini, M. (2011). Lagrangian mixing in straight compound channels. *Journal of Fluid Mechanics, 675*, 168-198.

Stocchino, A., and Brocchini, M. (2010). Horizontal mixing of quasi-uniform straight compound channel flows. *Journal of Fluid Mechanics, 643*, 425-435.

Stoica, P., and Moses, R. L. (2005). *Spectral analysis of signals*: Pearson/Prentice Hall Upper Saddle River, NJ.

Sturm, T., and Tuzson, J. (2001). Open channel hydraulics. *Applied Mechanics Reviews, 54*, 107.

Sun, X., and Shiono, K. (2009). Flow resistance of one-line emergent vegetation along the floodplain edge of a compound open channel. *Advances in Water Resources, 32*(3), 430-438.

Te Chow, V. (1959). *Open channel hydraulics* (I. N. Y. McGraw-Hill Book Company Ed.).

Terrier, B. (2010). *Flow characteristics in straight compound channels with vegetation along the main channel.* © Benoit Terrier.

Tominaga, A., and Nezu, I. (1991). Turbulent structure in compound open-channel flows. *Journal of Hydraulic Engineering, 117*(1), 21-41.

Tritton, D. (1988). Physical fluid mechanics. *Clarendon, Oxford*.

Tropea, C., Yarin, A. L., and Foss, J. F. (2007). *Springer handbook of experimental fluid mechanics* (Vol. 1): Springer Science & Business Media.

TSI. (2006). Phase Doppler Particle Analyzer/Laser Doppler Velocimeter Operations Manual. 2.1-2.3, A.4-A.5.

Uijttewaal, W. S. (2005). Effects of groyne layout on the flow in groyne fields: Laboratory experiments. *Journal of Hydraulic Engineering, 131*(9), 782-791.

Uijttewaal, W. S. (2014). Hydrodynamics of shallow flows: application to rivers. *Journal of Hydraulic Research, 52*(2), 157-172.

Van Driest, E. (1956). The problem of aerodynamic heating. *Aeronautical Engineering Review, 15*(10), 26-41.

Van Prooijen, B. C., Battjes, J. A., and Uijttewaal, W. S. (2005). Momentum exchange in straight uniform compound channel flow. *Journal of Hydraulic Engineering*.

White, F. M. (2011). Fluid mechanics.(7thedn): McGraw Hill, New York.

Yang, S.-Q., Tan, S.-K., and Lim, S.-Y. (2004). Velocity distribution and dip-phenomenon in smooth uniform open channel flows. *Journal of Hydraulic Engineering, 130*(12), 1179-1186.

Yen, B. C. (2002). Open channel flow resistance. *Journal of Hydraulic Engineering, 128*(1), 20-39.

Appendix A

Codes to Data Processing

- Filter based on Phase-Space Thresholding Method, Goring and Nikora 2002

In this section, the codes used to filter the raw data from LDV will be presented for *u* component. The codes were developed in Matlab and must be processed in this software. To run the code, a previous folders distribution must be made in order to the code find the raw data from LDV and create a new folder with the filter data. The code below presents the *u* component case. However, in the case of *w* component, the main structure of the filter used was similar.

- Filter code for *u* component

```
% This code performs a simple filter that removes negative velocities and velocities
that exceed 50% of turbulent intensity. Basically this is needed in the closest to the
main channel side wall and for verticals in the transition.


% Written by Joao Leal and Ricardo Azevedo, February 2012.


      clc
      clear all
      close all


      %DATA THAT NEEDS TO BE CHANGED
      root_path='G:\'; % needs to be changed according to the computer
      folder_tests='Ensaios'; % should be keept constant
      rough_type='smooth'; % smooth or rough
      if strcmp(rough_type,'smooth')
          relative_water_depth='Hr_02'; % Choices: Hr_05; Hr_03; Hr_02
          relative_depth=relative_water_depth;
      elseif strcmp(rough_type,'rough')
          rod_diameter='D_10'; % Choices: D_10; D_6
          rod_spacing='S_1000'; % Choices: S_1000; S_200; S_40
          relative_water_depth='Hr_05'; % Choices: Hr_05; Hr_03; Hr_02
          relative_depth=strcat(rod_diameter,'\',rod_spacing,'\',relative_water_depth);
      end
      section='X8750'; % cross section (X7500, X8000, X9000,...)
      vel_component='U'; % velocity component (U, W or U_W)
      data_path='raw_data'; % should be keept constant
      files=dir(strcat(root_path,'\',folder_tests,'\',rough_type,'\',relative_depth,'\',
section,'\',vel_component,'\',data_path,'\*.csv'));
      number_points=length(files); % number of files in the raw data directory (number
of points in each section)
      data_file_name='STR18105'; % begining of name of the file
      % creates the directory of filtered data
```

```
      filtered_path=strcat(root_path,'\',folder_tests,'\',rough_type,'\',relative_depth,
'\',section,'\',vel_component,'\','filtered_data');

      mkdir(filtered_path);  % creates the directory of results

      count=0;

      j=0;

      for k=1:number_points

          disp(['Treating    file:    ',    num2str(k),'                still    missing
',num2str(number_points-k),' files']);

          % reads the data from the raw files

      file_name=strcat(root_path,'\',folder_tests,'\',rough_type,'\',relative_depth,'\',
section,'\',vel_component,'\',data_path,'\',data_file_name,'_',num2str(k),'.csv');

          data_matrix=csvread(file_name,1,0);

          original_T=data_matrix(1:end,1);

          U_Tseries=data_matrix(1:end,2);

          XXXX=data_matrix(1,3);

          YYYY=data_matrix(1,4);

          ZZZZ=data_matrix(1,5);

          if length(U_Tseries)>100 % files with few samples are not considered

              U_filtered=U_Tseries;

              T_filtered=original_T;

              % filter to remove values equal or below zero (U<=0.1)

              i=1;

              while i<=length(U_filtered)

                  if U_filtered(i)<=0.1

                      U_filtered=[U_filtered(1:i-1);U_filtered(i+1:length(U_filtered))];

                      T_filtered=[T_filtered(1:i-1);T_filtered(i+1:length(T_filtered))];

                      i=i;

                  else

                      i=i+1;

                  end

              end

              n_zeros=length(U_Tseries)-length(U_filtered);

              percent_zeros=n_zeros/length(U_Tseries)*100;

              disp(['Number   of   zeros   in   the   series:   ',   num2str(n_zeros),'
Percentage: ',num2str(percent_zeros),'%']);

              if length(U_filtered)>100

                  mean_U  =  ((1/length(U_filtered))*sum(U_filtered.^(-1)))^(-1);  %Mean-
average Velocity --> Correction of the Velocity Bias

                  median_U=median(U_filtered);

                  u_filtered=U_filtered-mean_U;

                  TI=(mean(u_filtered.^2))^0.5;

                  if strcmp(rough_type,'smooth')

                      max_TI=0.5; % limit of turbence intensity

                  elseif strcmp(rough_type,'rough')

                      max_TI=0.8; % limit of turbence intensity

                  end

                  max_u=max_TI*mean_U;
```

```
            % filter for the cases where the median is well bellow the mean
                if median_U<0.8*mean_U
                    i=1;
                    while i<=length(U_filtered)
                        if (U_filtered(i)>=median_U-
*max_u)&&(U_filtered(i)<=median_U+2*max_u)
                            U_filtered=[U_filtered(1:i-
1);U_filtered(i+1:length(U_filtered))];
                            T_filtered=[T_filtered(1:i-
1);T_filtered(i+1:length(T_filtered))];
                            i=i;
                        else
                            i=i+1;
                        end
                    end
                end
                mean_U  =  ((1/length(U_filtered))*sum(U_filtered.^(-1)))^(-1);  %Mean-
average Velocity --> Correction of the Velocity Bias
                median_U=median(U_filtered);
                u_filtered=U_filtered-mean_U;
                TI=(mean(u_filtered.^2))^0.5;
                max_u=max_TI*mean_U;
            % filter to remove values that exceeds 50% of turbulence intensity
                i=1;
                while i<=length(U_filtered)
                    if (U_filtered(i)<mean_U-max_u)||(U_filtered(i)>mean_U+max_u)
                        U_filtered=[U_filtered(1:i-
1);U_filtered(i+1:length(U_filtered))];
                        T_filtered=[T_filtered(1:i-
1);T_filtered(i+1:length(T_filtered))];
                        i=i;
                    else
                        i=i+1;
                    end
                end
                mean_U  =  ((1/length(U_filtered))*sum(U_filtered.^(-1)))^(-1);  %Mean-
average Velocity --> Correction of the Velocity Bias
                n_TI=length(U_Tseries)-length(U_filtered);
                percent_TI=n_TI/length(U_Tseries)*100;
                disp(['Total number of removed samples: ', num2str(n_TI),'
Percentage: ',num2str(percent_TI),'%']);
                fLDA=length(U_filtered)/T_filtered(end);
                disp(['Mean frequency of the series: ', num2str(fLDA)]);
                figure(1)
                plot(original_T,U_Tseries,'k.',T_filtered,U_filtered,'r.'),hold
                plot([0            original_T(end)],[mean_U            mean_U],'k-',[0
original_T(end)],[mean_U-max_u   mean_U-max_u],'k--',[0   original_T(end)],[mean_U+max_u
mean_U+max_u],'k--'), hold
                %save figure with raw and filtered data
```

```
fig_path=strcat(root_path,'\',folder_tests,'\',rough_type,'\',relative_depth,'\',section
,'\',vel_component,'\raw_and_filtered_velocity_',num2str(k-count));

                    saveas(gcf, fig_path, 'fig');

                    %Goring_filter(T_filtered,U_filtered)

                    [T_filtered1,U_filtered1]=Goring_filter_U(T_filtered,U_filtered);
%calls function Goring_filter

                    mean_U1     =     ((1/length(U_filtered1))*sum(U_filtered1.^(-1)))^(-1);
%Mean-average Velocity --> Correction of the Velocity Bias

                    figure(2)

                    plot(T_filtered,U_filtered,'k.',T_filtered1,U_filtered1,'r.'),hold

                    plot([0             T_filtered(end)],[mean_U            mean_U],'k-',[0
T_filtered1(end)],[mean_U1 mean_U1],'k--'), hold

                    %save figure with filtered and GORING filtered data

fig_path=strcat(root_path,'\',folder_tests,'\',rough_type,'\',relative_depth,'\',section
,'\',vel_component,'\filtered_and_Goring_filtered_velocity_',num2str(k-count));

                    saveas(gcf, fig_path, 'fig');

                    %saves the filtered values in a csv flie

                    filtered_name=strcat(filtered_path,'\',data_file_name,'_',num2str(k-
count),'.csv');

                    % saves the header to the file

                    fid = fopen(filtered_name,'w');

                    fprintf(fid,'Time Ch. 1 (sec),Velocity Ch. 1 (m/sec),X Axis Position,Y
Axis Position,Z Axis Position\n');

                    fclose(fid);

                    % saves the first line of values with 5 colums

                    dlmwrite(filtered_name,[T_filtered1(1)    U_filtered1(1)    XXXX    YYYY
ZZZZ],'-append')

                    % saves the values after the first line

                    dlmwrite(filtered_name,[T_filtered1(2:end)
U_filtered1(2:end)],'precision', '%.9f','-append')

                else

                    j=j+1;

                    elim=k;

                    count=count+1;

                    name_elim{j}=[strcat(data_file_name,'_',num2str(elim),'.csv')];

                end

            else

                j=j+1;

                elim=k;

                count=count+1;

                name_elim{j}=[strcat(data_file_name,'_',num2str(elim),'.csv')];

            end

            save var_filtro;

        end

        if j==0

            disp('No files were eliminated by the filter');

        else

            disp(['Number of files eliminated by the filter: ', num2str(count)]);

            disp('Name of eliminated files by the filter: ');
```

```
        disp(name_elim);
    end
```

To run the code above, the function "Goring_Filer_U" will be called. In this regards, the function is described following:

- Goring Filer Function

```
%This function performs a filter that removes peaks contained in a sample.
%This filter is based on the paper of Goring and Nikora 2002.
%This filter does not remove the peaks founds in the sample. The filter
%relocated the peaks using a polynomial curve of 3° order taken 12 points
%before and after of the peak.

%Written by Ricardo Azevedo, May 2012

function [T_filtered1,U_filtered1]=Goring_filter_U(T_filtered,U_filtered)
clear T_filtered1 U_filtered1

mean_U = ((1/length(U_filtered))*sum(U_filtered.^(-1)))^(-1); %Mean-average %Velocity --
> Correction of the Velocity Bias
u(:,1) = U_filtered - mean_U; %Velocity fluctuations

n_picos=11;
iteracoes=0;
warning('off');   %Remove the warnings -> The polyfit funtion produced some warnings

    while n_picos > 0   %First stop condition (All peaks were relocated)
        picos1=0;
        picos2=0;
        picos3=0;
        n_picos=0;
        iteracoes=iteracoes+1;
     %____Delta_ui
        Delta_u(1,1) = (U_filtered(2,1)-U_filtered(1,1))/2;
%First line of Delta_u
        Delta_u(length(U_filtered),1) = (U_filtered(length(U_filtered),1)-
U_filtered(length(U_filtered)-1,1))/2;    %last line of Delta_u
        i=2;
        while i<length(U_filtered)
           Delta_u(i,1)=(U_filtered(i+1,1)-U_filtered(i-1,1))/2;%Calculation of Delta_u
           i=i+1;
        end

     %____Delta2_ui
        i=2;
        while i<length(U_filtered)
           Delta2_u(i,1)=(Delta_u(i+1,1)-Delta_u(i-1,1))/2;%Calculation of Delta^2_u
           i=i+1;
        end

        Delta2_u(1,1) = (Delta_u(2,1)-Delta_u(1,1))/2;
%First line of Delta2_u
        Delta2_u(length(U_filtered),1) = (Delta_u(length(U_filtered),1)-
Delta_u(length(U_filtered)-1,1))/2;    %Last line of Delta2_u

     %____Original Data
        if iteracoes==1
            original_data(:,1)=u;
            original_data(:,2)=Delta_u;
            original_data(:,3)=Delta2_u;
        end
```

```
     %____Program Control -> Second stop condition
        p_picos=1;
        if iteracoes>10 %The second stop condition start on the iteration %10 (If during
5 iterations the number of peaks is same, the program stop)
            if picos(iteracoes-1)==picos(iteracoes-6)||(picos_1(iteracoes-
1)==picos_1(iteracoes-6))||...
                (picos_2(iteracoes-1)==picos_2(iteracoes-6))||(picos_3(iteracoes-
1)==picos_3(iteracoes-6))
                p_picos=0;
            else
                p_picos=1;
            end
        end

        if p_picos==1
          %____Calculation of variables for replacement of peaks
          %____Standard desviation (u; Delta_u; Delta^2_u)
          %____Step 2 Goring paper (2002): Phase_space Thresholding Method
            Stand_dev(1)=std(u);
            Stand_dev(2)=std(Delta_u);
            Stand_dev(3)=std(Delta2_u);

          %____Delta_ui vs ui
            Major_axis1 = sqrt(2*log(length(U_filtered)))*Stand_dev(1);%Eq.2
            Minor_axis1 = sqrt(2*log(length(U_filtered)))*Stand_dev(2);

          %____Delta_ui2 vs delta_ui
            Major_axis2 = sqrt(2*log(length(U_filtered)))*Stand_dev(2);%Eq.2
            Minor_axis2 = sqrt(2*log(length(U_filtered)))*Stand_dev(3);

          %____Delta_ui2 vs ui
            theta=atan(sum(u.*Delta2_u)/sum(u.^2)); %Results in radians - %Eq. 9
            eq10 = Major_axis1^2; %Eq. 10
            eq11 = Minor_axis2^2; %Eq. 11
            A = [eq10 ; eq11];
            B = [(cos(theta)).^2 (sin(theta)).^2 ; (sin(theta)).^2 (cos(theta)).^2];
            El = B^(-1)*A; %Solve the equations system
            Major_axis3 = sqrt(El(1,1)); %Value of a of the eq. 10 and 11
            Minor_axis3 = sqrt(El(2,1)); %Value of b of the eq. 10 and 11

          %____Focal Points of the ellipses
            c1=sqrt((Major_axis1)^2-(Minor_axis1)^2); %Delta_ui vs ui
            c2=sqrt((Major_axis2)^2-(Minor_axis2)^2); %Delta_ui2 vs %delta_ui
            c3=sqrt((Major_axis3)^2-(Minor_axis3)^2); %Delta_ui2 vs ui;
            c3x=c3*cos(theta);
            c3y=c3*sin(theta);

          %____Max. distance of each ellipse to the focal points
            dmax1=2*sqrt(c1^2+Minor_axis1^2);
            dmax2=2*sqrt(c2^2+Minor_axis2^2);
            dmax3=2*sqrt(c3^2+Minor_axis3^2);

          %____Distance of each point to the focal points
            %____Delta_ui vs ui
            dist1 = sqrt((u-c1).^2+(Delta_u).^2)+sqrt((u+c1).^2+(Delta_u).^2);
            %____Delta_ui2 vs delta_ui
            dist2 = sqrt((Delta_u-
c2).^2+(Delta2_u).^2)+sqrt((Delta_u+c2).^2+(Delta2_u).^2);
            %____Delta_ui2 vs ui
            dist3 = sqrt((u-c3x).^2+(Delta2_u-
c3y).^2)+sqrt((u+c3x).^2+(Delta2_u+c3y).^2); %Confirmar eixos

           %____Count and relocation of peaks
            %__Mat_dados_c will be use to relocate the peaks
            Mat_dados_c(:,1) = T_filtered;
            Mat_dados_c(:,2) = u;
            Mat_dados_c(:,3) = Delta_u;
            Mat_dados_c(:,4) = Delta2_u;

            i=1;
            while i < length(U_filtered)
                j=0;
                if dist1(i,1)>dmax1
                    j=1;
```

```
                    picos1=picos1+1;
                end
                if dist2(i,1)>dmax2
                    j=1;
                    picos2=picos2+1;
                end
                if dist3(i,1)>dmax3
                    j=1;
                    picos3=picos3+1;
                end

                if j>0
                    %__The peak is replaced at the moment by the mean
                    %__average velocity
                    Mat_dados_c(i,2)= ((1/length(u))*sum(u.^(-1)))^(-1);

               %___Analysis of Delta_ui vs ui
                    if dist1(i,1)>dmax1
                        if i+12>length(U_filtered)
                            Coef=polyfit(Mat_dados_c(i-12:i-1,1),Mat_dados_c(i-12:i-
1,2),3);
                            u(i,1) =
Mat_dados_c(i,1)^3*Coef(1)+Mat_dados_c(i,1)^2*Coef(2)+Mat_dados_c(i,1)*Coef(3)+Coef(4);
                        elseif i-12<1
Coef=polyfit(Mat_dados_c(1:i+12,1),Mat_dados_c(1:i+12,2),3);
                            u(i,1) =
Mat_dados_c(i,1)^3*Coef(1)+Mat_dados_c(i,1)^2*Coef(2)+Mat_dados_c(i,1)*Coef(3)+Coef(4);
                        else
                            M1 = vertcat(Mat_dados_c(i-12:i-
1,1),Mat_dados_c(i+1:i+12,1));
                            M2 = vertcat(Mat_dados_c(i-12:i-
1,2),Mat_dados_c(i+1:i+12,2));
                            Coef=polyfit(M1,M2,3);
                            u(i,1) =
Mat_dados_c(i,1)^3*Coef(1)+Mat_dados_c(i,1)^2*Coef(2)+Mat_dados_c(i,1)*Coef(3)+Coef(4);
                        end
                    end

               %___Analysis of Delta_ui2 vs delta_ui
                    if dist2(i,1)>dmax2
                        if i+12>length(U_filtered)
                            Coef=polyfit(Mat_dados_c(i-12:i-1,1),Mat_dados_c(i-12:i-
1,2),3);
                            u(i,1) =
Mat_dados_c(i,1)^3*Coef(1)+Mat_dados_c(i,1)^2*Coef(2)+Mat_dados_c(i,1)*Coef(3)+Coef(4);
                        elseif i-12<1
Coef=polyfit(Mat_dados_c(1:i+12,1),Mat_dados_c(1:i+12,2),3);
                            u(i,1) =
Mat_dados_c(i,1)^3*Coef(1)+Mat_dados_c(i,1)^2*Coef(2)+Mat_dados_c(i,1)*Coef(3)+Coef(4);
                        else
                            M1 = vertcat(Mat_dados_c(i-12:i-
1,1),Mat_dados_c(i+1:i+12,1));
                            M2 = vertcat(Mat_dados_c(i-12:i-
1,2),Mat_dados_c(i+1:i+12,2));
                            Coef=polyfit(M1,M2,3);
                            u(i,1) =
Mat_dados_c(i,1)^3*Coef(1)+Mat_dados_c(i,1)^2*Coef(2)+Mat_dados_c(i,1)*Coef(3)+Coef(4);
                        end
                    end

               %___Analysis of Delta_ui2 vs ui
                    if dist3(i,1)>dmax3
                        if i+12>length(U_filtered)
                            Coef=polyfit(Mat_dados_c(i-12:i-1,1),Mat_dados_c(i-12:i-
1,2),3);
                            u(i,1) =
Mat_dados_c(i,1)^3*Coef(1)+Mat_dados_c(i,1)^2*Coef(2)+Mat_dados_c(i,1)*Coef(3)+Coef(4);
                        elseif i-12<1
Coef=polyfit(Mat_dados_c(1:i+12,1),Mat_dados_c(1:i+12,2),3);
                            u(i,1) =
Mat_dados_c(i,1)^3*Coef(1)+Mat_dados_c(i,1)^2*Coef(2)+Mat_dados_c(i,1)*Coef(3)+Coef(4);
                        else
                            M1 = vertcat(Mat_dados_c(i-12:i-
1,1),Mat_dados_c(i+1:i+12,1));
```

```
                            M2 = vertcat(Mat_dados_c(i-12:i-
1,2),Mat_dados_c(i+1:i+12,2));
                            Coef=polyfit(M1,M2,3);
                            u(i,1) =
Mat_dados_c(i,1)^3*Coef(1)+Mat_dados_c(i,1)^2*Coef(2)+Mat_dados_c(i,1)*Coef(3)+Coef(4);
                        end
                    end
                end
                i=i+1;
            end

        %___n_picos count the number of peaks in each iteration
            n_picos=picos1+picos2+picos3;
            picos(iteracoes)=n_picos;
            picos_1(iteracoes) = picos1;
            picos_2(iteracoes) = picos2;
            picos_3(iteracoes) = picos3;
            number_picos = n_picos;
            percent_picos_u = (picos1/length(U_filtered))*100;
            percent_picos_deltau = (picos2/length(U_filtered))*100;
            percent_picos_delta2u = (picos3/length(U_filtered))*100;
            disp(['Iteration: ',num2str(iteracoes),'     Relocated samples by Goring
filter: ', num2str(number_picos)]);
            disp(['                 u Vs Delta_u: ',num2str(picos1),'
Percentage: ',num2str(percent_picos_u),'%']);
            disp(['                 Delta_u Vs Delta^2_u: ',num2str(picos2),'
Percentage: ',num2str(percent_picos_deltau),'%']);
            disp(['                 Delta^2_u Vs u: ',num2str(picos3),'
Percentage: ',num2str(percent_picos_delta2u),'%']);
        elseif p_picos==0
            n_picos=0;
        end
    end

    T_filtered1 = T_filtered;
    U_filtered1 = u+mean_U;

%___This variables are cleaning because the size of this variables change
%___in each file
    clear T_filtered U_filtered Mat_dados_c picos picos_1 picos_2 picos_3 u Delta_u
Delta2_u
end
```

Filtered the data, the “Data Processing” code is runned. In this code, .xls file is created where the experimental conditions are saved. Likewise, the information of each measurement points are organized and saved for vertical profiles. This organization of the information is essential to run the “Turbulence” code.

- **Data Processing**

```
% This function transforms the raw data into a directory/file structure and creates the
xls input file that can be used by the program turbulence.m.


% Written by Joao Leal and Ricardo Azevedo, February 2012

clc

clear all

close all


      %_____________________DATA THAT NEEDS TO BE CHANGED_____________________%

      %--------------------------------------------------------------------------
```

```
filter=1; % 0 - no filter; 1 - filter
discharge=26.41; % flow discharge in m3/h
discharge=discharge/3600;
mean_water_depth=0.0683; % water depth in the midle of the main channel
slope=0.000948216621; % mean longitudinal slope (should be keept constant)
Temperature=27.0; % water temperature in °C
Y_reference=5.56; % location of the window in the "y" direction
Z_reference=0.13795; % location of the bottom in the "z" direction in meters
Y_lower_int=156.00; % location of the lower interface
Y_upper_int=197.68; % location of the upper interface
root_path='G:\'; % needs to be changed according to the computer
folder_tests='Ensaios'; % should be keept constant

rough_type='rough'; % smooth or rough

if strcmp(rough_type,'smooth')
    relative_water_depth='Hr_02'; % Choices: Hr_05; Hr_03; Hr_02
    relative_depth=relative_water_depth;
elseif strcmp(rough_type,'rough')
    rod_diameter='D_10'; % Choices: D_10; D_6
    rod_spacing='S_40'; % Choices: S_1000; S_200; S_40
    relative_water_depth='Hr_03'; % Choices: Hr_05; Hr_03; Hr_02
    relative_depth=strcat(rod_diameter,'\',rod_spacing,'\',relative_water_depth);
end

section='X9015'; % cross section (X7500, X8000, X9000,...)
vel_component='W'; % velocity component (U, W or U_W)
if filter==0
    data_path='raw_data'; % should be keept constant
else
    data_path='filtered_data'; % should be keept constant
end

files=dir(strcat(root_path,'\',folder_tests,'\',rough_type,'\',relative_depth,'\',
section,'\',vel_component,'\',data_path,'\*.csv'));
number_points=length(files); % number of files in the raw data directory (number
of points in each section)
data_file_name='R901503'; % begining of name of the file
%--------------------------------------------------------------------------

% Finds and interpolates the bottom of the cross-section where the
% measurement was made
x_section=strread(section,'%d','delimiter','X');
x_section=x_section(2);
[y_flume,z_flume]=Channel_geometry(x_section);
```

```
      n_vertical=1;
      cont=0;
      k=1;
      % reads the data from the raw files or from the filtered data files
      file_name=strcat(root_path,'\',folder_tests,'\',rough_type,'\',relative_depth,'\',
section,'\',vel_component,'\',data_path,'\',data_file_name,'_',num2str(k),'.csv');
      data_matrix=csvread(file_name,1,0);
      t{n_vertical}{k-cont}=data_matrix(1:end,1);
      U{n_vertical}{k-cont}=data_matrix(1:end,2);
      Y{n_vertical}(k-cont)=data_matrix(1,4);
      Z{n_vertical}(k-cont)=data_matrix(1,5);
      t1=t;
      U1=U;
      Y1=Y;
      Z1=Z;


      for k=2:number_points
          % reads the data from the raw files or from the filtered data files

file_name=strcat(root_path,'\',folder_tests,'\',rough_type,'\',relative_depth,'\',sectio
n,'\',vel_component,'\',data_path,'\',data_file_name,'_',num2str(k),'.csv');
          data_matrix=csvread(file_name,1,0);
          t1{n_vertical}{k-cont}=data_matrix(1:end,1);
          U1{n_vertical}{k-cont}=data_matrix(1:end,2);
          Y1{n_vertical}(k-cont)=data_matrix(1,4);
          Z1{n_vertical}(k-cont)=data_matrix(1,5);
          if Y1{n_vertical}(k-cont)==Y1{n_vertical}(k-cont-1)
              t{n_vertical}{k-cont}=data_matrix(1:end,1);
              U{n_vertical}{k-cont}=data_matrix(1:end,2);
              Y{n_vertical}(k-cont)=data_matrix(1,4);
              Z{n_vertical}(k-cont)=data_matrix(1,5);
          else
              cont=k-1; %Count the number of points per vertical
              if n_vertical==1
                  n_point(n_vertical)=cont; %The number of points of each vertical are
save in n_point
              else
                  n_point(n_vertical)=cont-sum(n_point(1:n_vertical-1));
              end
              n_vertical=n_vertical+1;  %When the coordinate "Y" change, n_vertical
change too
              t{n_vertical}{k-cont}=data_matrix(1:end,1);
              U{n_vertical}{k-cont}=data_matrix(1:end,2);
              Y{n_vertical}(k-cont)=data_matrix(1,4);
              Z{n_vertical}(k-cont)=data_matrix(1,5);
              t1=t;
              U1=U;
```

```
            Y1=Y;
            Z1=Z;
        end
    end
    n_point(n_vertical)=number_points-cont; %Save the number of points in the last vertical

    for i=1:n_vertical
        Yexp{1,i}=((Y{1,i}-Y_reference)*1.331081081)/1000;    %coordinate y (El Coeficiente fue corregido por los valores Teóricos de los Ángulos de Refracción)
        Zexp{1,i}=Z{1,i}/1000; %coordinate z related to the bottom (used in the vertical profiles)
    end

    % Look the Lower Interface and Upper Interface
    Y_lowerinterface = ((Y_lower_int-Y_reference)*1.331081081)/1000;
    Y_upperinterface = ((Y_upper_int-Y_reference)*1.331081081)/1000;
    % Look the window reference
    ref_window = abs((y_flume(5,1))-Y_lowerinterface);

    if (Y_lowerinterface>(y_flume(5,1)))
        for i=1:n_vertical
            Yexp{1,i} = Yexp{1,i}-ref_window; % Adjust the Y distance
        end
    elseif(Y_lowerinterface<(y_flume(5,1)))
        for i=1:n_vertical
            Yexp{1,i} = Yexp{1,i}+ref_window; % Adjust the Y distance
        end
    end

    for i=1:n_vertical
        Y_vert(i,1) = Yexp{1,i}(1);
        if Y_vert(1)<0
            Y_vert(1)=0;
        end
        Z_vert(i,1) = interp1(y_flume,z_flume,Y_vert(i));
    end

    Z_vert = Z_vert+abs(z_flume(3,1)); % Middle of the Main Channel
    width_mc = 0.205;
    width_fp = 0.531;
    width_i = 0.054;
    depth_i = 0.051;

    % Cross-Section parameters; Friction Velocity
    area_cross_section = (((width_mc*2)+width_i)*depth_i/2)+((mean_water_depth-depth_i)*(width_mc+width_i+width_fp));
```

```
      wetted_perimeter      =      mean_water_depth+width_mc+width_fp+(mean_water_depth-
depth_i)+(((width_i^2)+(depth_i^2))^(1/2));
      hydraulic_radius = area_cross_section/wetted_perimeter;
      U_friction = (9.81*hydraulic_radius*slope)^(1/2);


      % Adjust de Z reference
      for i=1:n_vertical
          Z_contour{1,i} = Z_reference-Zexp{1,i};
      end
      % Look the bottom reference
      for i=1:n_vertical
          dz_bot(1,i) = Z_vert(i,1)-(min(Z_contour{1,i}));
      end
      dz_bottom = max(dz_bot);


      disp('start creating files')
      for i=1:n_vertical
          water_depth(i) = mean_water_depth-Z_vert(i,1); %Water depth for each velocity
profile
          u_atri(i) = U_friction; % Friction velocity determined by gravity method
          Z_contour{1,i} = Z_contour{1,i}+dz_bottom; %coordinate Z related a reference
level (used in the isolines)
          Zexp{1,i}  =  Z_contour{1,i}-Z_vert(i,1);  %coordinate  Z  related  with  each
velocity profile


file_path{i}=strcat(root_path,'\',folder_tests,'\',rough_type,'\',relative_depth,'\',sec
tion,'\',vel_component,'\','V',num2str(i));
          mkdir(file_path{i});


          for j=1:n_point(i)
              P(:,1) = t{1,i}{j};
              P(:,2) = U{1,i}{j};
              Point = ['P',num2str(j),'.txt'];
dlmwrite(strcat(file_path{i},'\',Point),P,'delimiter','\t','newline','pc','precision',
'%.6f');
              clear P
          end
      end
      rough_name=char(rough_type);
      rd_name=char(relative_water_depth);
      section_name=char(section);


      %creates the xls file to be used in turbulence.m
      if strcmp(rough_type,'smooth')

xls_file_name=strcat('input_',rough_name(1),'_',rd_name(4:5),'_',section_name(2:5),'_',v
el_component,'.xls');
      elseif strcmp(rough_type,'rough')
```

```
            rod_d=char(rod_diameter);
            rod_s=char(rod_spacing);

xls_file_name=strcat('input_',rough_name(1),'_',rod_d(3:end),'_',rod_s(3:end),'_',rd_nam
e(4:5),'_',section_name(2:5),'_',vel_component,'.xls');
      end


      %creates the data spreadsheet
      %--------------------------------------------------------------------------%
      %Run this code to opens the activex server. We need to run xlswrite11
      Excel = actxserver ('Excel.Application');
      File=strcat('C:\Users\Ricardo\Documents\MATLAB\',xls_file_name);
      if ~exist(File,'file')
          ExcelWorkbook = Excel.workbooks.Add;
          ExcelWorkbook.SaveAs(File,1);
          ExcelWorkbook.Close(false);
      end
      invoke(Excel.Workbooks,'Open',File)
      %--------------------------------------------------------------------------%
      line1={'Root directory',root_path,'(place the path until the folder tests it will
depend on the computer)'};
      xlswrite1(xls_file_name,line1,'Data','A1');
      line2={'Folder of tests',folder_tests,'(should not change)'};
      xlswrite1(xls_file_name,line2,'Data','A2');
      line3={'Roughness type',rough_type,'(smooth or rough)'};
      xlswrite1(xls_file_name,line3,'Data','A3');
      line4={'Relative depth',relative_depth,'(Hr_03, Hr_02 or Hr_05, depending on the
relative depth)'};
      xlswrite1(xls_file_name,line4,'Data','A4');
      line5={'Section',section,'(X7500, X8000 or X9000, depending on the longitudinal
location of the section)'};
      xlswrite1(xls_file_name,line5,'Data','A5');
      line6={'Velocity',vel_component,'(U, W or U_W, depending on the measured
component)'};
      xlswrite1(xls_file_name,line6,'Data','A6');
      line8={'Flow discharge',discharge,'(in m3/s, depends on the relative depth and
roughness type)'};
      xlswrite1(xls_file_name,line8,'Data','A8');
      line9={'Channel slope',slope,'(equal to the mean slope, should not change)'};
      xlswrite1(xls_file_name,line9,'Data','A9');
      line10={'Temperature',Temperature};
      xlswrite1(xls_file_name,line10,'Data','A10');
      line11={'Number of veticals',n_vertical,'(number of verticals in the section)'};
      xlswrite1(xls_file_name,line11,'Data','A11');


      %creates the verticals spreadsheets
      header1={'Vertical','Y transversal coordinate','H water depth','U* friction
velocity','Number of points for each vertical'};
```

```
      xlswrite1(xls_file_name,header1,'Verticals','A1');
      for i=1:n_vertical

lines1={strcat('V',num2str(i)),Yexp{i}(1),water_depth(i),u_atri(i),n_point(i)};
          xlswrite1(xls_file_name,lines1,'Verticals',strcat('A',num2str(i+1)));   %writes
the lines in spreadsheet 'Verticals'


          header2={'Point','Z  elevation  for  vertical  profiles','Z  elevation  for
isolines'};
          xlswrite1(xls_file_name,header2,strcat('V',num2str(i)),'A1');
          for j=1:n_point(i)
              lines2={strcat('P',num2str(j)),Zexp{i}(j),Z_contour{i}(j)};

xlswrite1(xls_file_name,lines2,strcat('V',num2str(i)),strcat('A',num2str(j+1)));  %writes
the lines in spreadsheet of each vertical
          end
      end
      %-------------------------------------------------------------------------%
      %Run this code to close the activex server
      invoke(Excel.ActiveWorkbook,'Save');
      Excel.Quit
      Excel.delete
      clear Excel
      %-------------------------------------------------------------------------%
      close all
      disp('end')
```

The “Turbulence” code is the most complex code developed in this investigation where the main variables of turbulence are calculated.

Turbulence U

```
      % This function calculates the main turbulent characteristics of the 2 component
LDV signal. Includes:
      % - time averaged u and w velocity
      % - Reynolds stresses (u'2)
      %  -  Autocorrelation  functions  (of  u  and  w  along  x,  using  corrected  Taylor
hypothesis)
      % - Taylor u and w macroscales from the autocorrelation functions
      % - Taylor microscale, lamda, from the osculating parabola; dissipation rate from
lamda
      % - dissipation rate from the derivative of the signal (requires isotropy)
      % - Second order structure functions for u and w (dissipation rate from the second
order u function)
      %  -  Third  order  structure  function  (dissipation  rate  from  the  third  order  u
function)
```

```
% - Taylor microscale and Kolmogorov microscale from the dissipation rate
% - Spectra for u
% - dissipation spectra and dissipation rate
% - quadrant decomposition

% Adaptado por Ricardo Azevedo a partir de Rui Ferreira (2009)

clc
clear all
close all
nome_fich_dados='input_s_05_9000_U';

 [~, root_path] = xlsread(nome_fich_dados, 'Data', 'B1');    % root directory
root_path=strcat(root_path,'\');
[~, folder_tests] = xlsread(nome_fich_dados, 'Data', 'B2');   % main folder of
tests
[~, rough_type] = xlsread(nome_fich_dados, 'Data', 'B3');      % folder of the
roughness type
[~, relative_depth] = xlsread(nome_fich_dados, 'Data', 'B4');     % folder of the
relative depth
[~, section] = xlsread(nome_fich_dados, 'Data', 'B5');          % folder of the
cross-section
[~, vel_component] = xlsread(nome_fich_dados, 'Data', 'B6');      % folder of the
velocity component
discharge = xlsread(nome_fich_dados, 'Data', 'B8');     % discharge m^3/s
slope = xlsread(nome_fich_dados, 'Data', 'B9'); % channel slope
Temperature = xlsread(nome_fich_dados, 'Data', 'B10'); % temperature
kvisc=kinetic_viscosity(Temperature);
N_verticals = xlsread(nome_fich_dados, 'Data', 'B11'); % number of verticals in
the cross-section

% creates the directory of results
results_path=strcat(root_path,folder_tests,'\',rough_type,'\',relative_depth,'\',s
ection,'\',vel_component,'\','results');
mkdir(results_path{1});  % creates the directory of results

% MAIN CYCLE - runs through all verticals in the section
vert_initial=1;
vert_final=N_verticals;



for n=vert_initial:vert_final
    cell=strcat('E',mat2str(n+1));
    N_points(n)=xlsread(nome_fich_dados, 'Verticals', cell); % reads the number of
points in each vertical
end

t{1,vert_final} = [];
```

```
x{1,vert_final} = [];
% longitudinal
U_Tseries_all{1,vert_final}     = [];
u_Tseries_all{1,vert_final}     = [];
uref_all{1,vert_final}          = [];
AC11adim_all{1,vert_final}      = [];
S11_all{1,vert_final}           = [];
S311_all{1,vert_final}          = [];
kw_all{1,vert_final}            = [];
spectra_uWK_all{1,vert_final}   = [];
spectra_uWHmm_all{1,vert_final} = [];
spectra_uPer_all{1,vert_final}  = [];
spectra_uY_all{1,vert_final}    = [];
spectra_uPer1_all{1,vert_final} = [];
freq_uWK_all{1,vert_final}      = [];
freq_uWHmm_all{1,vert_final}    = [];
freq_uPer_all{1,vert_final}     = [];
freq_uY_all{1,vert_final}       = [];
freq_uPer1_all{1,vert_final}    = [];

Z_all                 = zeros(max(N_points),vert_final);
fLDA_all              = zeros(max(N_points),vert_final);
mean_u_all            = zeros(max(N_points),vert_final);
sample_variance_u_all = zeros(max(N_points),vert_final);
m3111_all             = zeros(max(N_points),vert_final);
skewU_all             = zeros(max(N_points),vert_final);
m41111_all            = zeros(max(N_points),vert_final);
kurtU_all             = zeros(max(N_points),vert_final);
MacroTu_all           = zeros(max(N_points),vert_final);
MacroTu1_all          = zeros(max(N_points),vert_final);
MacroTu2_all          = zeros(max(N_points),vert_final);
MacroTu3_all          = zeros(max(N_points),vert_final);
MacroTut_all          = zeros(max(N_points),vert_final);
MacroTut1_all         = zeros(max(N_points),vert_final);
MacroTut2_all         = zeros(max(N_points),vert_final);
MacroTut3_all         = zeros(max(N_points),vert_final);
epsilonNIL_all        = zeros(max(N_points),vert_final);
epsilonNIL1_all       = zeros(max(N_points),vert_final);
epsilonNIL2_all       = zeros(max(N_points),vert_final);
epsilonNIL3_all       = zeros(max(N_points),vert_final);
epsilonA_all          = zeros(max(N_points),vert_final);
microTuA_all          = zeros(max(N_points),vert_final);
microTwA_all          = zeros(max(N_points),vert_final);
KolmLA_all            = zeros(max(N_points),vert_final);
KolmVA_all            = zeros(max(N_points),vert_final);
```

```
microTuB_all          = zeros(max(N_points),vert_final);
epsilonB1_all         = zeros(max(N_points),vert_final);
KolmLB1_all           = zeros(max(N_points),vert_final);
KolmVB1_all           = zeros(max(N_points),vert_final);
epsilonCa_all         = zeros(max(N_points),vert_final);
epsilonCb_all         = zeros(max(N_points),vert_final);
epsilonC_all          = zeros(max(N_points),vert_final);
microTuC_all          = zeros(max(N_points),vert_final);
microTwC_all          = zeros(max(N_points),vert_final);
KolmLC_all            = zeros(max(N_points),vert_final);
KolmVC_all            = zeros(max(N_points),vert_final);
epsilonD_all          = zeros(max(N_points),vert_final);
microTuD_all          = zeros(max(N_points),vert_final);
microTwD_all          = zeros(max(N_points),vert_final);
KolmLD_all            = zeros(max(N_points),vert_final);
KolmVD_all            = zeros(max(N_points),vert_final);
epsilonE_all          = zeros(max(N_points),vert_final);
microTuE_all          = zeros(max(N_points),vert_final);
microTwE_all          = zeros(max(N_points),vert_final);
KolmLE_all            = zeros(max(N_points),vert_final);
KolmVE_all            = zeros(max(N_points),vert_final);
C2uC_all              = zeros(max(N_points),vert_final);
C2uE_all              = zeros(max(N_points),vert_final);
C1uC_all              = zeros(max(N_points),vert_final);
C1uE_all              = zeros(max(N_points),vert_final);


for n=vert_initial:vert_final
    % read verticals data in the input file
    cell=strcat('A',mat2str(n+1));
    [~, vertical(n)] = xlsread(nome_fich_dados, 'Verticals', cell);     % reads the
name of each vertical
    cell=strcat('B',mat2str(n+1));
    Y(n)  =  xlsread(nome_fich_dados,  'Verticals',  cell);        %  reads  the  Y
coordinate of each vertical
    cell=strcat('C',mat2str(n+1));
    water_depth(n)  = xlsread(nome_fich_dados, 'Verticals', cell);     % reads the
water depth in each vertical
    cell=strcat('D',mat2str(n+1));
    u_atri(n)  =  xlsread(nome_fich_dados,  'Verticals',  cell);        %  reads  the
friction velocity in each vertical
    %cell=strcat('E',mat2str(n+1));
    %N_points(n)=  xlsread(nome_fich_dados,  'Verticals',  cell);       %  reads  the
number of points in each vertical


    %%OPEN_FIGURES ----------------------------------------------------------
    f11 = figure('outerposition',[20 20 800 600],'color',[1 1 1]);
    f111 = figure('outerposition',[20 20 800 600],'color',[1 1 1]);
```

```
f12 = figure('outerposition',[20 20 800 600],'color',[1 1 1]);
f13 = figure('outerposition',[20 20 800 600],'color',[1 1 1]);
f14 = figure('outerposition',[20 20 800 900],'color',[1 1 1]);
f15 = figure('outerposition',[20 20 800 600],'color',[1 1 1]);
f16 = figure('outerposition',[20 20 800 600],'color',[1 1 1]);
f17 = figure('outerposition',[20 20 800 600],'color',[1 1 1]);
% creates the directory of results for each vertical
vertical_path{n} = strcat(results_path{1},'\V',num2str(n));
mkdir(vertical_path{n});  % creates the directory of results

point_final=N_points(n);
point_initial=1;

% Pre-allocating the main variables.
t{n}{1,point_final} = [];
x{n}{1,point_final} = [];
% longitudinal
U_Tseries_all{n}{1,point_final}     = [];
u_Tseries_all{n}{1,point_final}     = [];
uref_all{n}{1,point_final}          = [];
AC11adim_all{n}{1,point_final}      = [];
S11_all{n}{1,point_final}           = [];
S311_all{n}{1,point_final}          = [];
kw_all{n}{1,point_final}            = [];
spectra_uWK_all{n}{1,point_final}   = [];
spectra_uWHmm_all{n}{1,point_final} = [];
spectra_uPer_all{n}{1,point_final}  = [];
spectra_uY_all{n}{1,point_final}    = [];
spectra_uPer1_all{n}{1,point_final} = [];
freq_uWK_all{n}{1,point_final}      = [];
freq_uWHmm_all{n}{1,point_final}    = [];
freq_uPer_all{n}{1,point_final}     = [];
freq_uY_all{n}{1,point_final}       = [];
freq_uPer1_all{n}{1,point_final}    = [];

for j = point_initial:point_final

    % read points data in the input file
    cell=strcat('A',mat2str(j+1));
    [ndata, point] = xlsread(nome_fich_dados, vertical{n}, cell);     % reads
the name of each vertical
    clear ndata
    cell=strcat('B',mat2str(j+1));
    elevation = xlsread(nome_fich_dados, vertical{n}, cell);      % reads the
elevation of each point
```

```
            % creates a directory for the results of each elevation
            point_path = strcat(vertical_path{n},'\P',num2str(j));
            mkdir(point_path);

            % opens the data file of each point
nome_fich=(strcat(root_path,folder_tests,'\',rough_type,'\',relative_depth,'\',section,'
\',vel_component,'\',vertical{n},'\',point,'.txt'));
            [original_T,U_Tseries] = textread(nome_fich{1},'%f %f');

            % basic manipulation of the data
            if (length(U_Tseries)/2-round(length(U_Tseries)/2))==0 % procedure to turn
even the number of time values
            else
                U_Tseries=U_Tseries(1:length(U_Tseries)-1);
                original_T=original_T(1:length(original_T)-1); %real time vector
            end
            dt = ( original_T(length(original_T)) - original_T(1) ) ...
                / ( length(original_T) - 1 ); % average dt
            fLDA = round(1/dt);

            disp(['Vertical: ', num2str(n)])
            disp(['Ponto: ', num2str(j)])
            disp(['Frequencia: ', num2str(fLDA),' Hz'])

            if fLDA > 30 % condição para excluir os pontos com frequência inferior a
30 Hz

            % builds the vector of equispaced time
            T_equi = 0:1:length(original_T)-1; % NOTE: vector must be even
            time = T_equi*dt; % NEW equispaced time series

      %---------------------------- Metodo S + H --------------------------------
            disp('Start S-H Method Calculation')
            % Pre-allocating variables.
            dist = zeros(1,length(time));
            u_Tint = zeros(1,length(time));
            %u_Tint1 = zeros(1,length(time));

            for it = 1:length(time)
                [d p] = min(abs(original_T-time(it)));
                if time(it) >= original_T(p)
                    u_Tint(it) = U_Tseries(p);
                elseif (time(it) <= original_T(p)) && (p>1)
                    u_Tint(it) = U_Tseries(p-1);
                else
                    u_Tint(it) = U_Tseries(1);
```

```
            end
        end

        clear it
        disp('End S-H Method Calculation')
    %-------------------------------------------------------------------------
        if sum(isnan(u_Tint))~=0 % if there are NaN
            [ii,jj]=find(isnan(u_Tint)==1); % finds the matrix index of NaN
            jj=max(jj); % maximum index of cells with NaN
            u_Tint = u_Tint(jj+1:length(u_Tint)); % cut the NaN at the beggining
            for i=1:jj
                u_Tint = [u_Tint, u_Tint(i)]; % completes the series introducing
at the end the first values
            end
        end
        U_Tseries = u_Tint;
    %*************************************************************************
        % basic statistics for this run (1st, 2nd, 3rd and 4th moments)
        % vectors of fluctuations of velocity, mean, variance and other statistics
        % longitudinal
        mean_u  =  ((1/length(U_Tseries))*sum(U_Tseries.^(-1)))^(-1);  %Mean-average
Velocity --> Correction of the Velocity Bias
        u_Tseries  =  U_Tseries  -  mean(U_Tseries);   % longitudinal velocity series
is now a fluctuation of velocity
        sample_variance_u = var(u_Tseries); % porque quero o estimador enviesado

        % higher order moments
        % 3rd order
        m3111 = mean(u_Tseries.^3);
        skewU = mean(u_Tseries.^3)/sample_variance_u^(3/2);

        % 4th order
        m41111 = mean(u_Tseries.^4);
        kurtU = mean(u_Tseries.^4)/sample_variance_u^2;
    %*************************************************************************
        %   MAIN TURBULENT FUNCTIONS: autocorrelation x of u (AC11) and w (AC31),
        %      second order structure functions, in x, of u (S11) and w (S31),
        %      third order longitudinal structure function (S311) and
        %      u and w spectra



        % Longitudinal autocorrelation function
        AC11 = xcorr(u_Tseries);     % this will return a vector with 2*length - 1
entries (length is the size of the velocity series, MUST be EVEN);
        % only the entries (length (AC11)+1)/2 to length(AC11) will be retrieved
        % (the series will be length (u_Tseries) long)
```

```
            AC11 = AC11((length(AC11)+1)/2:length(AC11));
            AC11adim = AC11/max(AC11); % igual a AC11adim = AC11/AC11(1);
            AC11 = AC11adim*sample_variance_u; % to retrive the physical meaning! the xcorr function does not preserve the right variance (there is sort of a signal amplification)
            % Second order structure function (longitudinal) FOR HOMOGENEOUS
            %   TURBULENCE
            S11 = 2*(AC11(1)-AC11);
            %  calculations necessary for the third order structure function (longitudinal) and the estimate 1
            %   of the dissipation rate
            if j>1
                clear S311
                S311(1:length(u_Tseries)) = 0;
            end

            % Pre-allocating variables.
            derU = zeros(1,length(u_Tseries)-1);
            for k = 0:length(u_Tseries)-1

                % auxiliary calculations for the THIRD order structure function
                %  only the longitudinal component is relevant (see Frisch "Turbulence", p. 76)
                aux3a_u                                                                 = (u_Tseries(1+k:length(u_Tseries)).^2).*u_Tseries(1:length(u_Tseries)-k);
                aux3b_u                                                                 = u_Tseries(1+k:length(u_Tseries)).*(u_Tseries(1:length(u_Tseries)-k).^2);
                aux3c_u = u_Tseries(1+k:length(u_Tseries)).^3;
                aux3d_u = u_Tseries(1:length(u_Tseries)-k).^3;

                zero_pad = zeros(1,k);
                aux3a_u  =  [zero_pad,  aux3a_u];  %this  is  the  correct  way  for periodogram-based  spectra  and  structure  functions  (follows  the  definition)  (it  is biased)
                aux3b_u = [aux3b_u, zero_pad];
                aux3c_u  =  [zero_pad,  aux3c_u];  %this  is  the  correct  way  for periodogram-based  spectra  and  structure  functions  (follows  the  definition)  (it  is biased)
                aux3d_u = [aux3d_u, zero_pad];

                aux3ma_u(k+1) = mean(aux3a_u);
                aux3mb_u(k+1) = mean(aux3b_u);
                aux3mc_u(k+1) = mean(aux3c_u);
                aux3md_u(k+1) = mean(aux3d_u);
                %   The longitudinal third order structure function FOR HOMOGENEOUS TURBULENCE
                %  The longitudinal third order structure function FOR NON-HOMOGENEOUS TURBULENCE
                S311(k+1)    =    aux3md_u(k+1)+3*(aux3ma_u(k+1)    -    aux3mb_u(k+1))-aux3mc_u(k+1);
```

```
                % calculation of the derivative of the time series for the
                % calculation of the dissipation rate
                % NOTE that this is valid for homogeneous turbulence (see Chassaing p.
158)
                % and also for isotropic turbulence (isotropy is a strong restriction
in this definition)
                % the definition is equation 4-63, Chassaing
                % will be using first order differences
                if ( (k >= 1) && (k <= length(u_Tseries) - 1) )
                    derU(k+1) = u_Tseries(k+1) - u_Tseries(k);
                end
            end
    %************************************************************************
            % CALCULATION OF THE SPECTRA
            %  Longitudinal and vertical spectra are calculated in the original time
            %  domain. They are plotted however against wavenumbers

            % calculation of the spectra with a Kaiser window (because it can
approximate a Rectangular window (beta = 0) or a Hamming window beta > 5)

            % Create a Welch spectral estimator with Kaiser window. beta = 2
            % approximates a rectangular window
            % 2^7 = 128 points per segment and a overlapping of 25%
            % longitudinal
            h_uWK = spectrum.welch({'Kaiser',1},2^7,25);
            % this is the default:    h_uWH = spectrum.welch('Hamming',2^6,50);
            h_uWHmm = spectrum.welch('Hamming',2^7,50);      % Create a ? spectral
estimator.

            % Create a Yulear spectral estimator which is extremely smooth - it
            % will be used to calculate the dissipation rate from the
            % dissipation spectra
            h_uY = spectrum.yulear;

            % Create periodogram
            h_uPer = spectrum.periodogram({'Hamming'});

            uref = sqrt(mean_u^2+sample_variance_u); % correction for medium urms
(according to l'vov et al. 1999)
            space = time*uref;  % space coordinate
            dl = dt*uref;        % space increment

            kw=fLDA/uref;  % definiçao do numero de ondas

            Hpsd_uWK = psd(h_uWK,u_Tseries,'Fs',kw);     % Calculate the PSD
            Hpsd_uWHmm = psd(h_uWHmm,u_Tseries,'Fs',kw); % Calculate the PSD
```

```
            Hpsd_uPer = psd(h_uPer,u_Tseries,'Fs',kw);    % Calculate the PSD
            Hpsd_uY = psd(h_uY,u_Tseries,'Fs',kw);        % Calculate the PSD


            % other estimates for ther periodogram
            nfft = round(round(length(u_Tseries)/2 + 1)/3);
            [Per_u.data,Per_u.freq] = periodogram(u_Tseries,[],nfft,fLDA);
      %**************************************************************************
            % Cálculo das grandezas dependentes (Macroescalas e microescalas de
Taylor,
            %     microscalas de Kolmogorov e estimativas de taxas de dissipação e
constantes
            %   das funções de estrutura e dos espectros)

            % ------- TAYLOR MACROSCALE ---------------------------------------------
            % Procedure: compute the integral of the autocorrelation function.
            %   Note that it is a very long series and, if considered fully,
            %   would inevitably render very small
            %    integral scales (the integral of the first points will have a small
importance
            %    in the overall integral; do not forget the AC series has, for large
scales,
            %     zero mean). Hence, the first step is the calculation of the
integration
            %   limit: it is considered that the limt should correspond to the second
            %   local maximum of the cumulative integral of the AC series. This is
            %   equivalent to finding the second point where the series plunge into
            %   negative values.
            %   Note: it assumes that the cumulative integral is positive in the first
            %   two segments (quivalently, it needs that the third point is positive).
            %   This is true in general for time series acquired with high frequencies
            %   (more than 50 hz should be sufficient).
            %   Note also that the integral is that of the non-dimensional AC function
            %   and that it is performed in the space domain (not time). Hence the
            %   integral scale is directly Taylor's macroscale

            %   LONGITUDINAL
            MacroTaylor_u(1:length(space)) = NaN;


            i = 3; %needs sufficient discretization so that the 2nd segment is still
of positive slope
            found = 0;  % found counts the number of local maxima (number of plunges
into negative values)


            while ( (found < 2) && (i <= length(space)) ) % searches the AC series
until the second maximum (or the end of the series)
                MacroTaylor_u(i)  =  trapz(space(1:i),AC11adim(1:i));     % cumulative
integral (integral of AC from the beginning until entry i)
```

```
                if ( (MacroTaylor_u(i) < MacroTaylor_u(i-1)) && (MacroTaylor_u(i-1) >=
MacroTaylor_u(i-2)))  % this represents a local peak
                    found = found + 1;   % found one local maximum (the AC series
plunges to negative values)
                end
                i = i+1;
            end
            % at this point it has found 2 local maxima; goes back two steps to
            % retain the actual local maximum
            MacroTu = max(MacroTaylor_u(max(i,3)-2),1e-8); % integral scale in m
            if found<2
                save problemas j elevation(j)
            end
            % this is a 2nd estimate of the integral length scale based on
            % the 1st minimum (Tropea et al. 2007, p. 787)
            k = 2; %needs sufficient discretization so that the 2nd segment is still
of positive slope
            found = 0;  % found counts the number of local maxima (number of plunges
into negative values)
            while ( (found < 1) && (k <= length(space)-1) ) % searches the AC series
until the 1st minimum (or the end of the series)
                if ( (AC11adim(k) > AC11adim(k-1)) && (AC11adim(k+1) > AC11adim(k)))
% this represents a local peak
                    found = found + 1;   % found one local maximum (the AC series
plunges to negative values)
                end
                k = k+1;
            end
            MacroTu1 = trapz(space(1:k-1),AC11adim(1:k-1));     % cumulative integral
(integral of AC from the beginning until entry i)
            % this is a 3rd estimate of the integral length scale based on
            % the value 1/e (Tropea et al. 2007, p. 787)
            nn = 2; %needs sufficient discretization so that the 2nd segment is still
of positive slope
            found = 0;  % found counts the number of local maxima (number of plunges
into negative values)
            while ( (found < 1) && (nn <= length(space)) ) % searches the AC series
until the 1st minimum (or the end of the series)
                if ( (AC11adim(nn) <= 1/exp(1)) && (AC11adim(nn-1) >= 1/exp(1)))   %
this represents a local peak
                    found = found + 1;   % found one local maximum (the AC series
plunges to negative values)
                end
                nn = nn+1;
            end
            MacroTu2 = space(nn-1);    % cumulative integral (integral of AC from the
beginning until entry i)

            % este é 4 método de estimação do comprimento de escala
            % Lx = pi/2*S(0) sendo S(0)=E(0)/u'^2 (Nezu and Nakagawa, 1993)
            S = Hpsd_uY.data./sample_variance_u;
```

```
                S0 = max(S);
                MacroTu3 = S0/2;
                numero_ondas = Hpsd_uY.frequencies;

                figure(f17)
                plot(numero_ondas,S,'b',[0 200],[S0 S0],'k--');
                xlabel('\itk_w\rm (1/m) ','Fontsize',11,'Fontname','Times'),
                ylabel('S (m)','Fontsize',11,'Fontname','Times'),
                set(gca,'Fontsize',11,'Fontname','Times');
                file_and_path_fig=strcat(point_path,'\Espectro do numero de ondas ,
elevation ',num2str(j));
                saveas(gcf, file_and_path_fig, 'fig');

                figure(f15)
                plot([0              max(space)],[0              0],'k',space,AC11adim,'k-
',space,MacroTaylor_u(1:length(space)),'b-',[MacroTu   MacroTu],[0   1],'k--',[space(i-2)
space(i-2)],[0   1],'k:',[MacroTu1   MacroTu1],[0   1],'r--',[space(k-1)   space(k-1)],[0
1],'r:',[MacroTu2       MacroTu2],[0       1],'b--',[space(1)       space(nn-1)],[1/exp(1)
1/exp(1)],'b:',[MacroTu3 MacroTu3],[0 1],'g--');
                axis([0 2 -0.2 1]); %escalas dos eixos
                xlabel('\itr_x\rm (m) ','Fontsize',11,'Fontname','Times'),
                ylabel('\rho\rm(\itr_x\rm) (-)','Fontsize',11,'Fontname','Times'),
                set(gca,'Fontsize',11,'Fontname','Times');
                if ( MacroTu == 1e-8)
                    MacroTu = ERR;
                    disp(['X Macroscale wrong, elevation ', num2str(j)])
                end
                MacroTut = MacroTu/uref;    % integral scale in s
                MacroTut1 = MacroTu1/uref;    % integral scale in s
                MacroTut2 = MacroTu2/uref;    % integral scale in s
                MacroTut3 = MacroTu3/uref;    % integral scale in s

                l_end_u = min( space(max(i-1,1)), 10*water_depth(n)) ;           % second
point post plunge (in m)
                if ( l_end_u == (10*water_depth(n)))
                    disp(['X Macroscale unreliable, elevation ', num2str(j)])
                end
                t_end_u = l_end_u/uref; % second point post plunge (in s)
                file_and_path_fig=strcat(point_path,'\Auto-correlation,           elevation
',num2str(j));
                saveas(gcf, file_and_path_fig, 'fig');

                %   AT THIS POINT THE INTEGRAL MACROSCALES u and w ARE COMPUTED
                % ------- Isotropic turbulence estimates of the dissipation rate  --------
------
                % note that the dimensions of the dissipation rate are V^3/L
                % estimate Zero, Chassaing, p. 285, equation 8-15 - energy contained in
large
                % ISOTROPIC scales (that is not the case of rough boundary layers,
```

```
% this should be very wrong)
epsilonNIL = sample_variance_u^(3/2)/MacroTu;
epsilonNIL1 = sample_variance_u^(3/2)/MacroTu1;
epsilonNIL2 = sample_variance_u^(3/2)/MacroTu2;
epsilonNIL3 = sample_variance_u^(3/2)/MacroTu3;
% estimate A
derU2 = (derU/(1*dl)).^2; % square of the vector of space derivatives
% esta definição de \epsilon é válida para turbulência isotrópica,
%   equation 4-63, Chassaing, p. 159 (not a good estimate)
epsilonA = 15*kvisc*mean(derU2); % atenção, a estimativa da viscosidade
pode ter que ser refinada
microTuA = sqrt( 30*kvisc*sample_variance_u/epsilonA ); % not a very good
estimate
microTwA = sqrt( 15*kvisc*sample_variance_u/epsilonA ); % not a very good
estimate
KolmLA = ( kvisc^3/epsilonA )^(1/4);        % Kolmogorov length scale,
Chassaing, p. 8-25 and may others
KolmVA = ( kvisc*epsilonA )^(1/4);        % Kolmogorov velocity scale,
Chassaing, p. 8-25 and may others


% estimate B - microT from the osculating parabola (not very good either)
% Chassaing, p. 144, p. 159
% the LESS bad is epsilonB2
microTuB = (sqrt(2)/2)*dl/(1-AC11adim(2))^0.5;
epsilonB1 = 30*kvisc*sample_variance_u/microTuB^2; % atenção, a estimativa
da viscosidade pode ter que ser refinada
KolmLB1 = ( kvisc^3/epsilonB1 )^(1/4);       % Kolmogorov length scale,
Chassaing, p. 8-25 and may others
KolmVB1 = ( kvisc*epsilonB1 )^(1/4);        % Kolmogorov length scale,
Chassaing, p. 8-25 and may others


%-------------------------------------------------------------------------
-
%   ESTIMATE OF THE DISSIPATION RATE FROM THE THIRD ORDER STRUCTURE
FUNCTION
%   this is a very good estimate but only if the data is noise free and
the
%  adquisition frequency is high!
%   Rationale: Frisch, p. 76 and following, the 4/5ths law. At small
scales,
%   the (longitudinal) third order structure function should be linear in
the
%   distance with slope equal to -4/5*epsilon (this is valid for TIH but
it
%   is generally a good assumption that there is isotropy at small scales
-
%   it should be confirmed in the spectra if the u and w spectra colapse
at
%  small scales)
%  Procedure: first step is calculate S311/(-(4/5) x ) - there should be a
plateau after the
```

```
%    first few points (corresponding to noise) and until a larger scale
where
%    isotropy is lost. The plateau is the dissipation range epsilonC =
S311/(-(4/5) x )
%   for l_noise < x < l_non_iso.
%   Second step is finding the maximum which should occur somewhere in the
%   plateau.
%    Third step is performing a mean of the values around the maximum
(first to
%   the left and then to the right) while evaluating the rate of change of
the gradient.
%    Step three stops when the average of the points changes above a
certain
%   threshold.

Nss = 75;   % number of points in the subseries where the plateau will be
searched
eMl = 1;    % maximum error in percentage , left
eMr = 1;    % maximum error in percentage , right
NDS311 = S311./( (-4/5)*space ); % first step
% the first point is eliminated; it is ASSUMED that the plateau occurs
% in the first N points (it is dangerous to use a too long series because
% other maxima might occour at larger scales) (a small series is dangerous
too)
subVec = NDS311(1:Nss); subVec(1) = 0; %(otherwise it would be nan)

[eps, max_plat, ~, ~, ~] = plateau(subVec, eMl, eMr);
epsilonCa = eps;  % THIS IS THE BEST ESTIMATE FOR THE DISSIPATION RATE
                  % NOT ALL THE DATA SETS ARE GOOD ENOUGH TO ALLOW FOR
THIS CALCULATION
                  % BE WEARY OF LOW FREQUENCY DATA AND NOISY DATA (check
the longitudinal spectra
                  % and the plot of the 3rd order function)
                  % RA: I DO NOT SEE ANY INFLUENCE OF THE WALL IN
                  % THE BEHAVIOR OF THE NDS311. HOWEVER, FOR LOW
                  % FREQUENCY DATA THE BEHAVIOR IS WEARY
if ( 100*abs( (eps-max_plat)/max_plat ) > (eMl+eMr+8) )
    disp(['Calculation of the dissipation rate from the 3rd order
structure function is unreliable. See figure elevation ',num2str(j)])
%     faulty3rd = 1;
% else
%     faulty3rd = 0;
end

% ------------------------------------------------------------------------
%   Construct to derive epsilon from the third order structure function
%
TOPLOT = S311./( (-4/5)*space );
figure(f11)
```

```
            plot(space,TOPLOT,'ok','MarkerSize',6), hold on,
            plot( [ 0 0.4 ],  [ epsilonCa epsilonCa ],'k-.','LineWidth',1.0);
            hold off

            axis([0 2 -1e-4 5e-4])
            xlabel('\itr_x\rm (m)','Fontsize',11,'Fontname','Times'),
            ylabel('\itS\rm^(^3^)\it_x_x\rm/((-4/5)\itr_x\rm)(m^2s^-
^3)','Fontsize',11,'Fontname','Times'),

            set(gca,'Fontsize',11,'Fontname','Times');
            file_and_path_fig=strcat(point_path,'\Plateau,  dissipation  3rd  order
structure function, elevation ',num2str(j));
            saveas(gcf, file_and_path_fig, 'fig');

            %-------------------------------------------------------------------------
-
            %  ANOTHER ESTIMATE OF THE DISSIPATION RATE FROM THE THIRD ORDER STRUCTURE
FUNCTION
            %   this is a very good estimate but only if the data is noise free and
the
            %   adquisition frequency is high!
            %   Rationale: Frisch, p. 76 and following, the 4/5ths law. At small
scales,
            %   the (longitudinal) third order structure function should be linear in
the
            %   distance with slope equal to -4/5*epsilon (this is valid for TIH but
it
            %   is generally a good assumption that there is isotropy at small scales
-
            %   it should be confirmed in the spectra if the u and w spectra colapse
at
            %   small scales)
            %  Procedure: first step is calculate the reach where S311 is linear; the
            %   first few points (corresponding to noise) should not obey a linear
law.
            %   Second step is finding the slope of this reach.
            %   Third step is evaluating the correlation coefficient.
            %   Step three stops when the correlation drops below a certain threshold.

            Nss = 75;   % number of points in the subseries where the plateau will be
searched
            eMl = 0.9;    % minimum coef correl, left
            eMr = 0.95;    % minimum coef correl, right
            NDS311 = S311; % first step
            NDS311H = S311./( (-4/5)*space );
            % the first point is eliminated; it is ASSUMED that the linear reach
            % in the first N points (it is dangerous to use a too long series because
            % other maxima might occour at larger scales) (a small series is dangerous
too)
            subVec = NDS311(1:Nss);      % subseries
```

```
            subVecH = NDS311H(1:Nss);  subVecH(1) = 0; % first entry would be nan
            subspace = space(1:Nss);


            [eps, beps, r_coef, locusM, ~, mright ] = linear_reach(subVec, subVecH,
subspace, eMl, eMr);


            epsilonCb = eps;  % THIS IS THE BEST ESTIMATE FOR THE DISSIPATION RATE
                              % NOT ALL THE DATA SETS ARE GOOD ENOUGH TO ALLOW FOR
THIS CALCULATION
                              % BE WEARY OF LOW FREQUENCY DATA AND NOISY DATA (check
the longitudinal spectra
                              % and the plot of the 3rd order function)
            if ( r_coef < eMr )
                disp('Calculation of the dissipation rate from the 3rd order structure
function is unreliable. See figure')
            end
            % I will consider that the dissipation rate is the mean of thos
            % computed by the two methods
            epsilonC = 0.5*( epsilonCa + epsilonCb );
            microTuC = sqrt( 30*kvisc*sample_variance_u/epsilonC ); % not a very good
estimate
            microTwC = sqrt( 15*kvisc*sample_variance_u/epsilonC ); % not a very good
estimate
            KolmLC = ( kvisc^3/epsilonC )^(1/4);        % Kolmogorov length scale,
Chassaing, p. 8-25 and may others
            KolmVC = ( kvisc*epsilonC )^(1/4);         % Kolmogorov length scale,
Chassaing, p. 8-25 and may others


            % ------------------------------------------------------------------------
            %   Construct to derive epsilon from the third order structure function
            TOPLOT = S311(1:Nss);
            XtoPlot = space(1:Nss);
            figure(f111)
            plot(XtoPlot,TOPLOT,'ok','MarkerSize',6), hold on,
            plot(  [  space(1)  space(locusM  +  mright  +  5)  ],     [  beps+(-
4/5)*space(1)*epsilonCb    beps+(-4/5)*space(locusM    +    mright    +    5)*epsilonCb
],'b','LineWidth',1.0);
            plot(  [  space(1)  space(locusM  +  mright  +  5)  ],     [  (-
4/5)*space(1)*epsilonCa     (-4/5)*space(locusM     +     mright     +     5)*epsilonCa
],'r','LineWidth',1.0);
            plot( [ space(1) space(locusM + mright + 5) ],  [ (-4/5)*space(1)*epsilonC
(-4/5)*space(locusM + mright + 5)*epsilonC ],'k','LineWidth',1.0);
            hold off
            axis([0 2 -1e-4 2e-5])
            xlabel('\itr_x\rm (m)','Fontsize',11,'Fontname','Times'),
            ylabel('\itS\rm^(^3^)\it_x_x\rm                                        (m^3s^-
^3)','Fontsize',11,'Fontname','Times'),
            set(gca,'Fontsize',11,'Fontname','Times');
            file_and_path_fig=strcat(point_path,'\3rd  order  structure  function,
elevation ',num2str(j));
            saveas(gcf, file_and_path_fig, 'fig');
```

```
            %-------------------------------------------------------------------------
-
            %   ESTIMATE OF THE DISSIPATION RATE FROM THE SECOND ORDER STRUCTURE
FUNCTION
            %    Note that it is only a good estimate if there is a large range of
scales
            %    where isotropy holds.
            %   Rationale: If the Kolmogorov constant C2 is universal and C2 = 2.0,
            %    and if there is an inertial range where isotropy holds, then there
            %    should be a plateau in the function S11./( 2*space.^(2/3) ).
            %    Power (3/2) of this plateau is the dissipation rate.
            %     Note that the universality of the constant C2 is disputed (Landau
remark,
            %      Frisch, pp. 93-99). The constant will be computed later assuming
other
            %    estimates of epsilon


            Nss = 75;    % number of points in the subseries where the plateau will be
searched
            eMl = 1;     % maximum error in percentage , left
            eMr = 1;     % maximum error in percentage , right
            KC2 = 2.0;   % Kolmogorov constant (ATTENTION might not be universal but
only scale independent!)
            NDS11 = ( S11./( KC2*space.^(2/3) ) ).^(3/2);
            subVec = NDS11(1:Nss); subVec(1) = 0;
            [eps, max_plat, locusM, mleft, mright] = plateau(subVec, eMl, eMr);
            epsilonD = eps;   % BE WEARY OF LOW FREQUENCY DATA AND NOISY DATA (check
the longitudinal spectra
                              % and the plot of the 2nd order longitudinal
                              % function)
            if ( 100*abs( (eps-max_plat)/max_plat ) > (eMl+eMr+8) )
                disp(['Calculation of the dissipation rate from the 2nd order
longitudinal structure function is unreliable. See figure elevation',num2str(j,n)])
            end
            microTuD = sqrt( 30*kvisc*sample_variance_u/epsilonD ); % not a very good
estimate
            microTwD = sqrt( 15*kvisc*sample_variance_u/epsilonD ); % not a very good
estimate
            KolmLD  =  (  kvisc^3/epsilonD  )^(1/4);      %  Kolmogorov  length  scale,
Chassaing, p. 8-25 and may others
            KolmVD  =  (  kvisc*epsilonD  )^(1/4);         %  Kolmogorov  length  scale,
Chassaing, p. 8-25 and may others
            % -------------------------------------------------------------------------
            %   Construct to derive epsilon from the second order structure function
            %
            TOPLOT = ( S11./( KC2*space.^(2/3) ) ).^(3/2);
            figure(f12)
            plot(space,TOPLOT,'ok','MarkerSize',6), hold on,
            plot( [ 0 0.04 ],  [ epsilonD epsilonD ],'k-.','LineWidth',1.0);
```

```
            hold off
            axis([0 space(Nss) 0 5e-4])
            xlabel('\itr_x\rm (m)','Fontsize',11,'Fontname','Times'),
            ylabel('[\itS\rm^(^2^)\it_x_x\rm/(2\itr_x\rm^2^/^3)]^3^/^2          (m^2s^-
^3)','Fontsize',11,'Fontname','Times'),
            set(gca,'Fontsize',11,'Fontname','Times'),
            file_and_path_fig=strcat(point_path,'\Plateau,   dissipation   2nd   order
structure function, elevation ',num2str(j));
            saveas(gcf, file_and_path_fig, 'fig');
            %-------------------------------------------------------------------------
-
            %  ESTIMATE OF THE DISSIPATION RATE FROM THE SPECTRUM OF THE LONGITUDINAL
            %       VELOCITY
            %   Note that this estimate should be very similar to that obtained with
            %    the second order structure function because they are conjugates.
            %   Rationale: In the inertial range the spectra should obey
            %       E11 = C1*epsilon^(2/3)*k^(-5/3)
            %      The  constant  should  be  C1  =  0.53  (Chassaing,  p.  300)  if  it  is
universal
            %      (this is disputed the constant will be calculated later).
            %   Procedure: as before, a plateau should exist in the function
            %       e = ( E11/( C1*k^(-5/3) ) )^(3/2)
            %     the plateau is epsilonE
            %   The Yulear estimate of the spectrum is highly smoohted but presents a
            %     clear plateau in the inertial range that is approximately the
            %     moving average of the periodogram. Tests carried out 26-30 dec 2009
            %      showed that at 1.5 times the Macroscale the corresponding scale is
at the
            %     plateau(!). Thus, the value of plateau is taken as e(1.5*MacroTu).

            KC1 = 0.53; % universal? should not be...
            %    first step - find the entry in the frequncy array that corresponds to
            %    the frequency of the longitudinal integral scale
            [ minimo ponto ] = min(abs(Hpsd_uY.frequencies - 1.5*1/MacroTut2)); %RA:
the better integral length scale is through 1/e
            %    step two -
            epsilonE          =          (          Hpsd_uY.data(ponto)/(KC1*uref^(5/3)
*(Hpsd_uY.frequencies(ponto)^(-5/3))) ).^(3/2);
            % Verify  the  quality  of  the  estimate  in  the  figure  of  the  disspation
spectra
            microTuE = sqrt( 30*kvisc*sample_variance_u/epsilonE ); % not a very good
estimate
            microTwE = sqrt( 15*kvisc*sample_variance_u/epsilonE ); % not a very good
estimate
            KolmLE  =  (  kvisc^3/epsilonE  )^(1/4);        %  Kolmogorov  length  scale,
Chassaing, p. 8-25 and may others
            KolmVE  =  (  kvisc*epsilonE  )^(1/4);         %  Kolmogorov  length  scale,
Chassaing, p. 8-25 and may others
            % ------------------------------------------------------------------------
            %   Construct to derive epsilon from the longitudinal dissipation spectra
```

```
%

wavenum = Hpsd_uY.frequencies/uref;

spectrumU  =  (  Hpsd_uY.data./(KC1*  uref^(5/3)  *(Hpsd_uY.frequencies.^(-
5/3))) ).^(3/2);

wavenum1 = Hpsd_uPer.frequencies/uref;

spectrumU1        =        (        Hpsd_uPer.data./(KC1*        uref^(5/3)
*(Hpsd_uPer.frequencies.^(-5/3))) ).^(3/2);

wavenum2 = Hpsd_uWHmm.frequencies/uref;

spectrumU2        =        (        Hpsd_uWHmm.data./(KC1*        uref^(5/3)
*(Hpsd_uWHmm.frequencies.^(-5/3))) ).^(3/2);

wavenum3 = Hpsd_uWK.frequencies/uref;

spectrumU3  =  ( Hpsd_uWK.data./(KC1* uref^(5/3)  *(Hpsd_uWK.frequencies.^(-
5/3))) ).^(3/2);


figure(f13)

loglog(wavenum,spectrumU,'k-'), hold on

loglog(wavenum1,spectrumU1,'r-'),

loglog(wavenum2,spectrumU2,'b-'),

loglog(wavenum3,spectrumU3,'g-'),

if ( ~isnan(epsilonE) )

    loglog( [ 1 1000 ],  [ epsilonE epsilonE ],'-.k','LineWidth',1.0),

end

if ( ~isnan(1/MacroTu2) ) %RA: the better integral length scale is through
1/e

    loglog(   [   1/MacroTu2   1/MacroTu2   ],      [   1e-7   10   ],'--
k','LineWidth',0.5), %RA: the better integral length scale is through 1/e

    loglog(   [   1.5*1/MacroTu2   1.5*1/MacroTu2   ],     [   1e-7   10   ],'-
k','LineWidth',0.5), %RA: the better integral length scale is through 1/e

end

if ( ~isnan(1/microTuE) )

    loglog( [ 1/microTuE 1/microTuE ],  [ 1e-7 10 ],':k','LineWidth',0.5),

end

hold off

if isnan(epsilonE)

    yuplim = 10;

else

    yuplim = max(10*epsilonE,10);

end

axis([1e-1 1e3 1e-7 yuplim]);     % the plot scale is fixed for the first
run

xlabel('\itk_x\rm (1/m)','Fontsize',11,'Fontname','Times'),

ylabel('[\itE_x_x\rm/(\itC\rm_1\itk_x\rm^-^5^/^3]^3^/^2             (m^2s^-
^3)','Fontsize',11,'Fontname','Times'),

set(gca,'xtick',[0.1 1 10 100 1000],'Fontsize',11,'Fontname','Times'),

set(gca,'ytick',[1e-6     1e-5     1e-4     1e-3     1e-2     1e-1     1     10
100],'Fontsize',11,'Fontname','Times'),

set(gca,'Fontsize',11,'Fontname','Times'),

file_and_path_fig=strcat(point_path,'\Dissipation   spectra   u,   elevation
',num2str(j));
```

```
            saveas(gcf, file_and_path_fig, 'fig');


            %     AT THIS POINT ALL THE ESTIMATES FOR THE DISSPATION RATE HAVE BEEN
            %     COMPUTED

%**************************************************************************
            % ESTIMATES OF THE CONSTANTS OF THE SECOND ORDER STRUCTURE FUNCTIONS AND
OF
            % THE LONGITUDINAL SPECTRUM
            %-------------------------------------------------------------------------
-
            % CONSTANT OF THE SECOND ORDER LONGITUDINAL STRUCTURE FUNCTION
            % The constant will be calculated from the dissipation rate calculated
            % from the third order structure function,  from the estimate from the
            % osculating parabola and from the estimate from the dissipation spectra

            epsilonX = [ epsilonC epsilonE ] ;
            Nss = 75;    % number of points in the subseries where the plateau will be
searched
            eMl = 1;     % maximum error in percentage , left
            eMr = 1;     % maximum error in percentage , right

            % Pre-allocating variables.
            C2uX = zeros(1,2);

            for xi = 1:2
                NDS11 = S11./( (epsilonX(xi)^(2/3)).*(space.^(2/3)) ) ;
                subVec = NDS11(1:Nss); subVec(1) = 0;
                [eps, max_plat, locusM, mleft, mright] = plateau(subVec, eMl, eMr);
                C2uX(xi) = eps;   % BE WEARY OF LOW FREQUENCY DATA AND NOISY DATA
(check the longitudinal spectra
                                  % and the plot of the 2nd order longitudinal
                                  % function)
                if ( 100*abs( (eps-max_plat)/max_plat ) > (eMl+eMr+8) )
                    disp(['Estimate ',num2str(xi),' of the constant of the 2nd order
l. s. f. is unreliable. See figure elevation ',num2str(j,n)])
                end
                if (isnan(C2uX(xi)))
                    C2uX(xi) = 0;
                end
            end
            C2uC = C2uX(1); C2uE = C2uX(2);


            % ------------------------------------------------------------------------
            %   construct to derive the constant of the longitudinal second order
```

```
%   structure function
clear TOPLOT;


for xi = 1:2
    TOPLOT(Sun and Shiono) = S11./( space*epsilonX(xi) ).^(2/3);
end
figure(f14)
subplot(2,1,1)
plot(space,TOPLOT{1},'ok','MarkerSize',6), hold on,
plot( [ 0 0.04 ],  [ C2uC C2uC ],'k-.','LineWidth',1.0);
hold off
axis([0 0.2 0 5.0])
xlabel('\itr_x\rm (m)','Fontsize',11,'Fontname','Times'),
ylabel('\itS\rm^(^2^)\it_x_x\rm/(\itr_x\rm\epsilon_1)^2^/^3              (-
)','Fontsize',11,'Fontname','Times'),
set(gca,'Fontsize',11,'Fontname','Times'),
subplot(2,1,2)
plot(space,TOPLOT{2},'ok','MarkerSize',6), hold on,
plot( [ 0 0.04 ],  [ C2uE C2uE ],'k-.','LineWidth',1.0);
hold off
axis([0 0.2 0 5.0])
xlabel('\itr_x\rm (m)','Fontsize',11,'Fontname','Times'),
ylabel('\itS\rm^(^2^)\it_x_x\rm/(\itr_x\rm\epsilon_2)^2^/^3              (-
)','Fontsize',11,'Fontname','Times'),
 set(gca,'Fontsize',11,'Fontname','Times'),
file_and_path_fig=strcat(point_path,'\Plateau,  non-dimensional  2nd  order
structure function, elevation ',num2str(j));
saveas(gcf, file_and_path_fig, 'fig');



%-------------------------------------------------------------------------
-
% CONSTANT OF THE LONGITUDINAL SPECTRUM
%   The constant of the u-spectrum will be calculated from the dissipation
rate calculated
% from the third order structure function,  from the estimate from the
% osculating parabola and from the estimate from the dissipation spectra


clear epsilonX
epsilonX = [ epsilonC epsilonE ];
Nss = 75;    % number of points in the subseries where the plateau will be
searched
eMl = 1;     % maximum error in percentage , left
eMr = 1;     % maximum error in percentage , right


% Pre-allocating variables.
C1uX = zeros(1,2);
```

```
            for xi = 1:2
                % variable ponto was computed above (it is the frequency for 1.5 the
macroscale)
                C1uX(xi)        =        Hpsd_uY.data(ponto)/(        uref^(5/3)        *
(epsilonX(xi)^(2/3))*(Hpsd_uY.frequencies(ponto)^(-5/3)));
                if (isnan(C1uX(xi)))
                    C1uX(xi) = 0;
                end
            end
            C1uC = C1uX(1); C1uE = C1uX(2);

            % ------------------------------------------------------------------------
            %     Construct to derive the constant of the longitudinal dissipatin
spectra
            figure(f16)
            subplot(2,1,1)
            wavenum = Hpsd_uY.frequencies/uref;
            spectrumU        =        Hpsd_uY.data./(epsilonX(1)^(2/3)*        uref^(5/3)
*(Hpsd_uY.frequencies.^(-5/3))) ;
            wavenum1 = Hpsd_uPer.frequencies/uref;
            spectrumU1       =       Hpsd_uPer.data./(epsilonX(1)^(2/3)*       uref^(5/3)
*(Hpsd_uPer.frequencies.^(-5/3))) ;
            wavenum2 = Hpsd_uWHmm.frequencies/uref;
            spectrumU2       =      Hpsd_uWHmm.data./(epsilonX(1)^(2/3)*      uref^(5/3)
*(Hpsd_uWHmm.frequencies.^(-5/3))) ;
            wavenum3 = Hpsd_uWK.frequencies/uref;
            spectrumU3       =       Hpsd_uWK.data./(epsilonX(1)^(2/3)*       uref^(5/3)
*(Hpsd_uWK.frequencies.^(-5/3))) ;

            semilogx(wavenum,spectrumU,'k-'), hold on
            semilogx(wavenum1,spectrumU1,'r-'),
            semilogx(wavenum2,spectrumU2,'b-'),
            semilogx(wavenum3,spectrumU3,'g-'),

            if ( ~isnan(C1uC) )
                semilogx( [ 1 1000 ],  [ C1uC C1uC ],'-.k','LineWidth',1.0),
            end
            if ( ~isnan(1/MacroTut) )
                semilogx(    [    1/MacroTu    1/MacroTu    ],       [    1e-7    10    ],'--
k','LineWidth',0.5),
            end
            if ( ~isnan(1/microTuC) )
                semilogx(    [    1/microTuC    1/microTuC    ],        [    1e-7    10
],':k','LineWidth',0.5),
            end
            hold off
            axis([1e-1 1e3 0 1]);    % the plot scale is fixed for the first run
            xlabel('\itk_x\rm (1/m)','Fontsize',11,'Fontname','Times'),
```

```
            ylabel('[\itE_x_x\rm/(\epsilon_1^2^/^3\itk_x\rm^-^5^/^3]^3^/^2          (-
)','Fontsize',11,'Fontname','Times'),

            set(gca,'xtick',[0.1 1 10 100 1000],'Fontsize',11,'Fontname','Times'),



            subplot(2,1,2)

            wavenum = Hpsd_uY.frequencies/uref;

            spectrumU       =       Hpsd_uY.data./(epsilonX(2)^(2/3)*       uref^(5/3)
*(Hpsd_uY.frequencies.^(-5/3))) ;

            wavenum1 = Hpsd_uPer.frequencies/uref;

            spectrumU1      =      Hpsd_uPer.data./(epsilonX(2)^(2/3)*      uref^(5/3)
*(Hpsd_uPer.frequencies.^(-5/3))) ;

            wavenum2 = Hpsd_uWHmm.frequencies/uref;

            spectrumU2      =      Hpsd_uWHmm.data./(epsilonX(2)^(2/3)*      uref^(5/3)
*(Hpsd_uWHmm.frequencies.^(-5/3))) ;

            wavenum3 = Hpsd_uWK.frequencies/uref;

            spectrumU3      =      Hpsd_uWK.data./(epsilonX(2)^(2/3)*       uref^(5/3)
*(Hpsd_uWK.frequencies.^(-5/3))) ;


            semilogx(wavenum,spectrumU,'k-'), hold on

            semilogx(wavenum1,spectrumU1,'r-'),

            semilogx(wavenum2,spectrumU2,'b-'),

            semilogx(wavenum3,spectrumU3,'g-'),

            if ( ~isnan(C1uE) )

                semilogx( [ 1 1000 ],  [ C1uE C1uE ],'-.k','LineWidth',1.0),

            end

            if ( ~isnan(1/MacroTu) )

                semilogx(   [   1/MacroTu   1/MacroTu   ],      [   1e-7   10   ],'--
k','LineWidth',0.5),

            end

            if ( ~isnan(1/microTuE) )

                semilogx(    [    1/microTuE    1/microTuE    ],        [    1e-7    10
],':k','LineWidth',0.5),

            end

            hold off

            axis([1e-1 1e3 0 1]);    % the plot scale is fixed for the first run

            xlabel('\itk_x\rm (1/m)','Fontsize',11,'Fontname','Times'),

            ylabel('[\itE_x_x\rm/(\epsilon_2^2^/^3\itk_x\rm^-^5^/^3]^3^/^2          (-
)','Fontsize',11,'Fontname','Times'),

            set(gca,'xtick',[0.1 1 10 100 1000],'Fontsize',11,'Fontname','Times'),

            set(gca,'Fontsize',11,'Fontname','Times'),

            file_and_path_fig=strcat(point_path,'\Normalised  dissipation  spectra  u,
elevation ',num2str(j));

            saveas(gcf, file_and_path_fig, 'fig');


%************************************************************************

            %   keep all the functions of this point in arrays of cells

            t{n}{j} = time;
```

```
x{n}{j} = space;
% longitudinal
U_Tseries_all{n}{j} = U_Tseries;
u_Tseries_all{n}{j} = u_Tseries;
uref_all{n}{j}=uref;
AC11adim_all{n}{j} = AC11adim;
S11_all{n}{j} = S11;
S311_all{n}{j} = S311;
kw_all{n}{j} = kw;
spectra_uWK_all{n}{j} = Hpsd_uWK.data;
spectra_uWHmm_all{n}{j} = Hpsd_uWHmm.data;
spectra_uPer_all{n}{j} = Hpsd_uPer.data;
spectra_uY_all{n}{j} = Hpsd_uY.data;
spectra_uPer1_all{n}{j} = Per_u.data;
freq_uWK_all{n}{j} = Hpsd_uWK.frequencies;
freq_uWHmm_all{n}{j} = Hpsd_uWHmm.frequencies;
freq_uPer_all{n}{j} = Hpsd_uPer.frequencies;
freq_uY_all{n}{j} = Hpsd_uY.frequencies;
freq_uPer1_all{n}{j} = Per_u.freq;
Z_all(j,n)=elevation;
fLDA_all(j,n)=fLDA;
mean_u_all(j,n)=mean_u;
sample_variance_u_all(j,n)=sample_variance_u;
m3111_all(j,n)=m3111;
skewU_all(j,n)=skewU;
m41111_all(j,n)=m41111;
kurtU_all(j,n)=kurtU;
MacroTu_all(j,n)=MacroTu;
MacroTu1_all(j,n)=MacroTu1;
MacroTu2_all(j,n)=MacroTu2;
MacroTu3_all(j,n)=MacroTu3;
MacroTut_all(j,n)=MacroTut;
MacroTut1_all(j,n)=MacroTut1;
MacroTut2_all(j,n)=MacroTut2;
MacroTut3_all(j,n)=MacroTut3;
epsilonNIL_all(j,n)=epsilonNIL;
epsilonNIL1_all(j,n)=epsilonNIL1;
epsilonNIL2_all(j,n)=epsilonNIL2;
epsilonNIL3_all(j,n)=epsilonNIL3;
epsilonA_all(j,n)=epsilonA;
microTuA_all(j,n)=microTuA;
microTwA_all(j,n)=microTwA;
KolmLA_all(j,n)=KolmLA;
KolmVA_all(j,n)=KolmVA;
microTuB_all(j,n)=microTuB;
```

```
            epsilonB1_all(j,n)=epsilonB1;
            KolmLB1_all(j,n)=KolmLB1;
            KolmVB1_all(j,n)=KolmVB1;
            epsilonCa_all(j,n)=epsilonCa;
            epsilonCb_all(j,n)=epsilonCb;
            epsilonC_all(j,n)=epsilonC;
            microTuC_all(j,n)=microTuC;
            microTwC_all(j,n)=microTwC;
            KolmLC_all(j,n)=KolmLC;
            KolmVC_all(j,n)=KolmVC;
            epsilonD_all(j,n)=epsilonD;
            microTuD_all(j,n)=microTuD;
            microTwD_all(j,n)=microTwD;
            KolmLD_all(j,n)=KolmLD;
            KolmVD_all(j,n)=KolmVD;
            epsilonE_all(j,n)=epsilonE;
            microTuE_all(j,n)=microTuE;
            microTwE_all(j,n)=microTwE;
            KolmLE_all(j,n)=KolmLE;
            KolmVE_all(j,n)=KolmVE;
            C2uC_all(j,n)=C2uC;
            C2uE_all(j,n)=C2uE;
            C1uC_all(j,n)=C1uC;
            C1uE_all(j,n)=C1uE;

            %   Builds and saves pictures
            else

                disp('"Nao foi calculado porque fLDA < 30 Hz"')

%**************************************************************************
            %   keep all the functions of this point in arrays of cells
            t{n}{j} = NaN;
            x{n}{j} = NaN;
            % longitudinal
            U_Tseries_all{n}{j} = NaN;
            u_Tseries_all{n}{j} = NaN;
            uref_all{n}{j}=NaN;
            AC11adim_all{n}{j} = NaN;
            S11_all{n}{j} = NaN;
            S311_all{n}{j} = NaN;
            kw_all{n}{j} = NaN;
            spectra_uWK_all{n}{j} = NaN;
            spectra_uWHmm_all{n}{j} = NaN;
            spectra_uPer_all{n}{j} = NaN;
```

```
spectra_uY_all{n}{j} = NaN;
spectra_uPer1_all{n}{j} = NaN;
freq_uWK_all{n}{j} = NaN;
freq_uWHmm_all{n}{j} = NaN;
freq_uPer_all{n}{j} = NaN;
freq_uY_all{n}{j} = NaN;
freq_uPer1_all{n}{j} = NaN;
Z_all(j,n) = NaN;
fLDA_all(j,n) = NaN;
mean_u_all(j,n) = NaN;
sample_variance_u_all(j,n) = NaN;
m3111_all(j,n) = NaN;
skewU_all(j,n) = NaN;
m41111_all(j,n) = NaN;
kurtU_all(j,n)=NaN;
MacroTu_all(j,n)=NaN;
MacroTu1_all(j,n)=NaN;
MacroTu2_all(j,n)=NaN;
MacroTu3_all(j,n)=NaN;
MacroTut_all(j,n)=NaN;
MacroTut1_all(j,n)=NaN;
MacroTut2_all(j,n)=NaN;
MacroTut3_all(j,n)=NaN;
epsilonNIL_all(j,n)=NaN;
epsilonNIL1_all(j,n)=NaN;
epsilonNIL2_all(j,n)=NaN;
epsilonNIL3_all(j,n)=NaN;
epsilonA_all(j,n)=NaN;
microTuA_all(j,n)=NaN;
microTwA_all(j,n)=NaN;
KolmLA_all(j,n)=NaN;
KolmVA_all(j,n)=NaN;
microTuB_all(j,n)=NaN;
epsilonB1_all(j,n)=NaN;
KolmLB1_all(j,n)=NaN;
KolmVB1_all(j,n)=NaN;
epsilonCa_all(j,n)=NaN;
epsilonCb_all(j,n)=NaN;
epsilonC_all(j,n)=NaN;
microTuC_all(j,n)=NaN;
microTwC_all(j,n)=NaN;
KolmLC_all(j,n)=NaN;
KolmVC_all(j,n)=NaN;
epsilonD_all(j,n)=NaN;
microTuD_all(j,n)=NaN;
```

```
                microTwD_all(j,n)=NaN;
                KolmLD_all(j,n)=NaN;
                KolmVD_all(j,n)=NaN;
                epsilonE_all(j,n)=NaN;
                microTuE_all(j,n)=NaN;
                microTwE_all(j,n)=NaN;
                KolmLE_all(j,n)=NaN;
                KolmVE_all(j,n)=NaN;
                C2uC_all(j,n)=NaN;
                C2uE_all(j,n)=NaN;
                C1uC_all(j,n)=NaN;
                C1uE_all(j,n)=NaN;
                end
                % cleans all variables
                clear point cell elevation point_path nome_fich original_T U_Tseries YYYY
ZZZZ dt fLDA T_equi time u_Tint
                clear mean_u u_Tseries sample_variance_u m3111 skewU m41111 kurtU AC11
AC11adim S11 S311
                clear aux3a_u aux3b_u aux3ma_u aux3mb_u zero_pad derU
                clear h_uWK h_uWHmm h_uY h_uPer Hpsd_uWK Hpsd_uWHmm Hpsd_uPer Hpsd_uY nfft
uref space dl
                clear MacroTaylor_u MacroTu MacroTu1 MacroTu2 MacroTut MacroTut1 MacroTut2
l_end_u t_end_u
                clear epsilonNIL epsilonNIL1 epsilonNIL2 derU2 epsilonA microTuA microTwA
KolmLA KolmVA
                clear microTuB epsilonB1 KolmLB1 KolmVB1 epsilonCa epsilonCb epsilonC
microTuC microTwC KolmLC KolmVC
                clear epsilonD microTuD microTwD KolmLD KolmVD epsilonE microTuE microTwE
KolmLE KolmVE C2uC C2uE C1uC C1uE
                clear Nss eMl eMr NDS311 subVec eps max_plat locusM mleft mright faulty3rd
TOPLOT yuplimit NDS311H subVecH
                clear subspace beps r_coef XtoPlot ybottlimit KC2 faulty2nd KC1 minimo
ponto C2uX C1uX
            end


            save(strcat(results_path{1},'\tudo.mat'))
            close all


        end
        save(strcat(results_path{1},'\velocity.mat'),'t','U_Tseries_all','u_Tseries_all')
        save(strcat(results_path{1},'\general.mat'),'kvisc','Z_all','water_depth','fLDA_al
l')
        save(strcat(results_path{1},'\autocorelation.mat'),'x','AC11adim_all','S11_all','S
311_all')
        save(strcat(results_path{1},'\spectra.mat'),'freq_uWK_all','spectra_uWK_all','freq
_uWHmm_all','spectra_uWHmm_all','freq_uPer_all','spectra_uPer_all','freq_uY_all','spectr
a_uY_all','freq_uPer1_all','spectra_uPer1_all')
        save(strcat(results_path{1},'\mean.mat'),'mean_u_all','sample_variance_u_all','m31
11_all','skewU_all','m41111_all','kurtU_all','uref_all')
        save(strcat(results_path{1},'\macroscale.mat'),'MacroTu_all','MacroTut_all','Macro
Tu1_all','MacroTut1_all','MacroTu2_all','MacroTut2_all')
```

```
      save(strcat(results_path{1},'\dissipation.mat'),'epsilonNIL_all','epsilonNIL1_all'
,'epsilonNIL2_all','epsilonA_all','epsilonB1_all','epsilonCa_all','epsilonC_all','epsilo
nCb_all','epsilonD_all','epsilonE_all')

      save(strcat(results_path{1},'\microscale.mat'),'microTuA_all','microTwA_all','micr
oTuB_all','microTuC_all','microTwC_all','microTuD_all','microTwD_all','microTuE_all','mi
croTwE_all')

      save(strcat(results_path{1},'\kolmogorov_scale.mat'),'KolmLA_all','KolmVA_all','Ko
lmLB1_all','KolmVB1_all','KolmLC_all','KolmVC_all','KolmLD_all','KolmVD_all','KolmLE_all
','KolmVE_all')

      save(strcat(results_path{1},'\constants.mat'),'C2uC_all','C2uE_all','C1uC_all','C1
uE_all')

      status = fclose('all');

      close all

      disp('end')
```